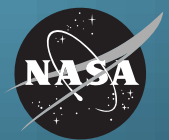*Proceedings of*

NETS-2016

Nuclear and Emerging Technologies for Space

The Von Braun Center
Huntsville, Alabama
February 22-26, 2016

ANS Aerospace Nuclear Science and Technology Division
Universities Space Research Association

About the Meeting

In February 2016, The Aerospace Nuclear Science and Technology Division (ANSTD) of the American Nuclear Society (ANS) held the 2016 Nuclear and Emerging Technologies for Space (NETS 2016) topical meeting at the Von Braun Center in Huntsville, Alabama. NETS is the premier conference for landed- and in-space applications in 2016.

With authors from universities, national laboratories, NASA facilities and industry, NETS 2016 provided an excellent communication network and forum for information exchange.

Topic Areas

NASA is currently considering capabilities for robotic and crewed missions to the Moon, Mars, and beyond. Strategies that implement advanced power and propulsion technologies, as well as radiation protection, will be important to accomplishing these missions in the future. NETS serves as a major communications network and forum for professionals and students working in the area of space nuclear and management personnel from international government, industry, academia, and national laboratory systems. To this end, the NETS 2016 meeting addressed topics ranging from overviews of current programs to methods of meeting the challenges of future endeavors.

Conference Organizers

Omar Mireles, PhD
General Chair
NASA Marshall Space Flight Center
omar.r.mireles@nasa.gov

Lee Mason
Honorary Chair
NASA Glenn Research Center
lee.s.mason@nasa.gov

Mike Houts, PhD
Honorary Chair
NASA Marshall Space Flight Center
michael.houts@nasa.gov

Patrick McClure
Technical Chair, FSP
Los Alamos National Laboratory
pmcclure@lanl.gov

Daniel Cavender
Technical Chair, NTP
NASA Marshall Space Flight Center
daniel.p.cavender@nasa.gov

Sal Oriti
Technical Chair, RPS
NASA Glenn Research Center
salvatore.m.oriti@nasa.gov

Nathan Jerred
Publications
Center for Space Nuclear Research,
USRA
njerred@usra.edu

Margaret Marshall
Publications
Idaho National Laboratory
margaret.marshall@inl.gov

Delisa Rogers
Logistics and Finance
Center for Space Nuclear Research,
USRA
drogers@usra.edu

Wesley Deason
Publications
International Atomic Energy Agency
wdeason07@gmail.com

Chis Morrison
Webmaster
Rensselaer Polytechnic Institute
generalc.intergrity@gmail.com

Jarvis Caffrey
A/V Coordinator
NASA Marshall Space Flight Center
jarvis.a.caffrey@nasa.gov

Session Chairs

Track I: Radioisotope Power Systems
Technical Chair: Sal Oriti, NASA Glenn Research Center

June Sakrajsek	NASA-Glenn Research Center	Ed Lewandowski	NASA-Glenn Research Center
Steve Johnson, PhD	Idaho National Laboratory	Wayne Wong	NASA-Glenn Research Center
Becky Onuschak	DOE-NE 75	Richard Ambrosi, PhD	University of Leicester
Carl Sandifer	NASA-Glenn Research Center	Robert Wham	Oak Ridge National Laboratory
Jean-Pierre Fleurial	Jet Propulsion Laboratory	Tom Sutliff	NASA-Glenn Research Center

Track II: Fission Surface Power

Technical Chair: Patrick McClure, Los Alamos National Laboratory

Susan Voss	Global Nuclear Network Analysis	Tom Godfrey	NASA-Marshall Space Flight Center
Max Briggs	NASA-Glenn Research Center	Steve Clement	Los Alamos National Laboratory

Track III: Nuclear Thermal Propulsion

Technical Chair: Daniel Cavender, NASA Marshall Space Flight Center

Harold Gerrish	NASA-Marshall Space Flight Center	Chance Garcia, PhD	NASA-Marshall Space Flight Center
Michael Eades	The Ohio State University	Glen Doughty	NASA-Marshall Space Flight Center
Jarvis Caffrey	NASA-Marshall Space Flight Center	Jim Werner	Idaho National Laboratory
Vishal Patel	Center for Space Nuclear Research		

Sponsor

Aerojet Rocketdyne is a world-recognized aerospace and defense leader providing propulsion and energetics to the domestic and international space, missile defense and strategic systems, tactical systems and armaments areas, and transformational energy technology solutions to address the world's energy needs. GenCorp is a diversified company providing innovative solutions to its customers in the aerospace and defense, energy and real estate markets.

Additional information about Aerojet Rocketdyne and GenCrop can be obtained by visiting the companies' websites at www.Rocket.com and www.GenCorp.com.

TABLE OF CONTENTS

Mass Optimization of a Supercritical CO2 Brayton Cycle Power Conversion System for a Mars Surface Fission Power Reactor

Kurt E. Harris[1], Yayu M. Hew[2], Kevin J. Schillo[3], Akansha Kumar[4], Steven D. Howe[5]

[1]Department of Mechanical & Aerospace Engineering, Utah State University, Logan, UT 84322
[2]Department of Aeronautics and Astronautics Engineering, Stanford University, Stanford, CA 94305
[3]Department of Mechanical & Aerospace Engineering, University of Alabama in Huntsville, Huntsville, AL 35899
[4]Center for Space Nuclear Research, Idaho National Laboratory, Idaho Falls, ID 83401
[5]Talos Power LLC, Idaho Falls, ID 83402
435-535-1414; k.harris@aggiemail.usu.edu

Abstract. In NASA's Design Reference Architecture 5.0 (DRA 5.0), fission surface power systems (FSPS) are described as "enabling for the human exploration of Mars". This study investigates the design of a power conversion system (PCS) based on supercritical CO2 (S-CO2) Brayton configurations for a growing Martian colony. Various configurations utilizing regeneration, intercooling, and reheating are analyzed. A model to estimate the mass of the PCS is developed and used to obtain a realistic mass-optimized configuration. This mass model is conservative, being based on simple concentric tube counterflow heat exchangers and published data regarding turbomachinery masses. For load following and redundancy purposes, the FSPS consists of three 333 kWe reactors and PCS to provide a total of 1MWe for 15 years. The optimal configuration is a S-CO2 Brayton cycle with 60% regeneration and two stages of intercooling. Analyses are mostly performed in MATLAB, with certain data provided by a COMSOL model of part of a low-enriched uranium (LEU) ceramic metallic (CERMET) reactor core.

Keywords: Mars, FSP, CO2, Brayton, mass

INTRODUCTION

In 2009, the National Aeronautics and Space Administration (NASA) published their Design Reference Architecture 5.0 (DRA 5.0) and stated that surface power on Mars would ideally be through fission power [1]. Their study indicated that nuclear power, over any other technology, would best allow for in-situ resource utilization (ISRU) strategies, reduce power system mass, provide continuous high power generation, and have lower overall cost assuming a complementary lunar system development process.

Decades of work has been done on this issue. In 2001, NASA assessed the performance and masses of Brayton and Stirling nuclear power systems with intended use in space exploration activities, over a wide range of power levels [2]. In 2006, they studied 50 kWe stainless steel systems for Mars applications, and compared power cycle options. A Brayton cycle was shown to have the lowest mass [3].

This study analyzed the power conversion system (PCS) for a fission surface power system (FSPS). The system is intended to generate a total of 1 MW of electric power for 15 years. A separate study into the design of the PCS found that using three separate reactors and PCS generating 333 kWe each allow for redundancy and reduce system mass. Various thermodynamic cycles were considered, leading to the selection of a Brayton cycle. The Brayton cycle system was then rigorously analyzed with varying levels of regeneration, intercooling, reheating, efficiency,

pressure, and temperature. Working fluids were considered, with supercritical carbon dioxide (S-CO2) being selected. A mass model was developed in conjunction with a heat transfer model. The total system mass is the most important figure of merit, reported along with the thermal efficiency of the system. This study complements previous work by more rigorously comparing the various Brayton cycle configurations possible.

METHODOLOGY

Converting the heat from a reactor to electricity can be done using various power cycles, and determining which power cycle to pursue is important. Three options were considered: Rankine, Stirling, and Brayton. Each cycle has advantages and disadvantages, but the most important issues resulted in the selection of a Brayton cycle.

Brayton technology for space applications began in the 1960's under the Brayton Rotating Unit. Since then, many units have been built and tested, resulting in tens of thousands of hours of operation [2]. This past work has led to the development of many compact designs. It is worth noting that Brayton cycles normally rely on the use of relatively inert gases – like carbon dioxide – as the working fluid. This is especially advantageous on Mars, where CO_2 is abundant in the atmosphere and can be used in long-term colonization expansion. Furthermore, Brayton cycles have the advantage of being extremely simple. This simplicity is due to the fact that the cycle may consist of as little as a single phase working fluid with only a few moving parts in the shaft, the turbine, and the compressor. Additional turbines and compressors can be added to a Brayton cycle if desired. And finally, with no phase transition temperature limitations, the turbine inlet temperature can be increased, resulting in higher thermal efficiency. Alternatively, for the same efficiency, the compressor inlet temperature can be raised, enhancing the heat rejection process and reducing mass. Drawbacks to using a Brayton cycle include high pressures and potential complexity from a non-constant heat rejection temperature. However, these problems were deemed relatively minor compared to the advantages offered.

Brayton cycles have been studied using various working fluids, including He, Ar, Xe, N2, H2, and CO2 [4]. To support NASA's long-term plan of colonizing Mars, CO2 was chosen as the working fluid in this study. The advantages include the fact that it can be extracted from the atmosphere once at least one of the three reactors is operational. The CO2 must be shipped to Mars along with the first PCS. Once the first reactor and PCS are operational, the CO2 for the other two reactors can be extracted from the Martian atmosphere. This will reduce the payload mass and cost associated with further launches from Earth. Furthermore, recent work has demonstrated that S-CO2 systems may even be useful in dry-cooling situations on Earth. This technology would also be beneficial on Mars, where water is scarce [5]. Reference properties were downloaded from NIST, and used for all state data [6]. The decision to use the NIST database was made based on previous comparisons of available reference data [7].

The simple Brayton cycle consists of taking a working fluid and putting it through a compressor, then adding heat generated by the core, then passing the fluid through a turbine, and finally rejecting any waste heat. The kinetic energy from the rotating turbine is converted to electricity in a generator, combined in a turbo-generator. Some of the output energy is also used for compression. Actual cycles take into account the isentropic efficiencies of the turbine(s) and compressor(s). Regeneration can also be added to improve the efficiency of the cycle. The net work out of the cycle can be increased using intercooling and reheating between compressors and turbines, respectively [8].

There are two separate loops in this power system. In the simplest version of the first loop, the core heats the S-CO2, which is used as a coolant, and then passes it through an intermediate heat exchanger (IHX) to pass the heat to the power cycle working fluid. If there is any leftover heat in the core fluid, it is then rejected to the ambient environment through an external heat exchanger on the core loop (EHXCL). If there are any reheaters (RHs) in the system, an outlet from the core would enter the first RH, where it would pass heat to the working fluid between expansion stages. A second RH would repeat that process before passing the fluid through IHX, and then through EHXCL. This can be seen in Figure 1, where the RHs are noted to be optional.
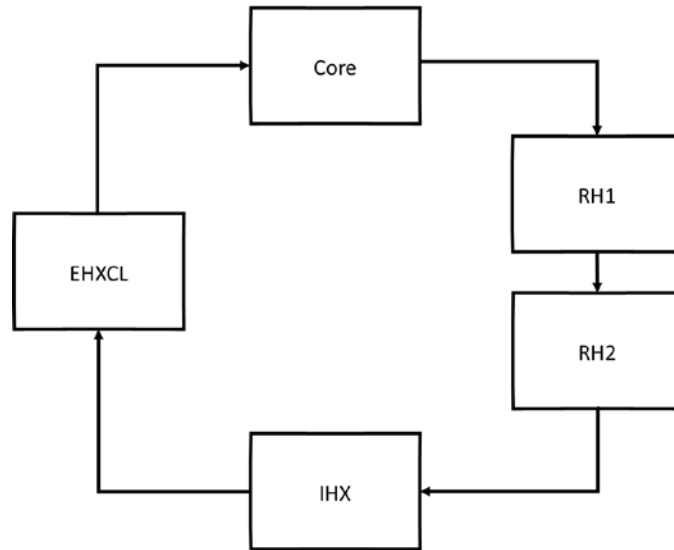
FIGURE 1. Core Loop Consists of a Core, Which Heats a Coolant Fluid, Then Passes It To Reheaters, Then to the Intermediate Heat Exchanger, Then to the External Heat Exchanger for the Core Loop.

In the second loop for the power cycle, the working fluid is compressed, with possible stages of intercooling (IC), then possibly pre-heated by the waste heat from the turbines through a regenerator before entering IHX and being heated by the core fluid. The high pressure, high temperature fluid is then passed to the turbine(s), with possible stages of reheating, and then passed through a regenerator and then the external heat exchanger (EHX) for waste heat rejection. This can be seen in Figure 2.
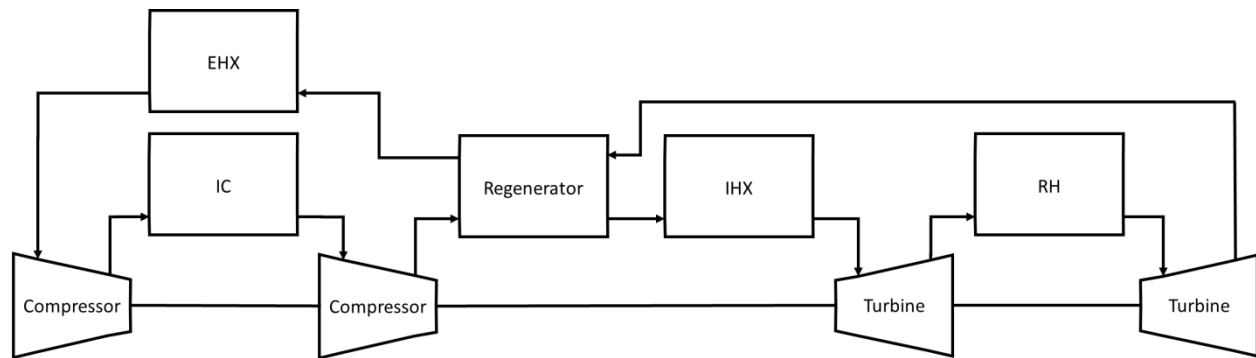

FIGURE 2. Power Cycle Loop Consists of Compression, Intercooling, Regeneration, Primary Heating, Expansion, Reheating, and Primary Heat Rejection.

With regard to heat transfer, losses were assumed to be negligible in the compressors and turbines. Concentric tube counter-flow heat exchangers were used to model the various heat exchangers in the system, except with the exception of the core which was modeled in COMSOL. During cooling processes, a third loop between a heat sink would need to be designed, although that was determined to be beyond the scope of this study. Ideally, the cooling process would be simple and passively safe to avoid potential meltdowns, and utilize local resources to minimize launch mass.

A mass model was also developed based on IEA specifications [9]. Flow was restricted to 3 m/s for S-CO2. Yield stresses were not exceeded for the material selected. The material chosen for piping was MA754, due to its high creep resistance in the presence of high temperature S-CO2, in addition to other desirable properties [7]. This determined the diameters and thicknesses of pipes between and within components. The heat transfer model determined required pipe lengths. With a density of 8.30 g/cm^3 for MA754, an estimate of the mass could be made

for all components making up the entire system. This mass model also included the ~3500 kg core and the S-CO2 in the system, making these estimates conservative. Not all launches will need to include S-CO2.

MATLAB scripts were developed to calculate fluid state properties throughout the thermodynamic cycle. NIST data was downloaded at specific pressures, and contained the fluid properties at various temperatures. The MATLAB script linearly interpolates between temperature points and pressure files to give the most accurate estimate of the fluid state. MATLAB inputs were selected to be the variables shown in Table 1 for thermodynamic inputs in the code. All pressure losses in components and piping were assumed to be zero for simplicity.

TABLE 1. MATLAB Thermodynamic Input Variables for Brayton Cycle.

Core	Turbine	Compressor	Regenerator
Inlet Pressure	Inlet Temperature	Inlet Temperature	Effectiveness
Inlet Temperature	Pressure Ratio	Pressure Ratio	
Outlet Temperature	Inlet Pressure	Isentropic Efficiency	
	Isentropic Efficiency	Number of Intercoolers	
	Number of Reheaters		

For the heat transfer, all components were assumed to be made of the same material, MA754. CO2 was used in all heat exchangers: IHX and RH between core and power cycle, EHX and IC between power cycle and an external heat sink assumed at a constant 242 K and 1.38 MPa (liquid CO2), and EHXCL between the core loop and the external heat sink. An average of one meter of piping was assumed between all components.

RESULTS

The results of the MATLAB code were tested for simple designs, then gradually increased to more complicated configurations. Temperature vs entropy (T-s) diagrams and pressure vs specific volume (P-v) diagrams were generated and plotted to show the cycle and fluid properties. An ideal case is shown in Figure 3, with no intercooling, reheating, or regeneration, and 100% efficient turbines and compressors. A pressure ratio of 2.5 was used, with the low pressure at 7.38 MPa – the lowest pressure CO2 can be at while remaining in the supercritical phase. The core itself ran at 7.4 MPa between 767 K and 910 K.
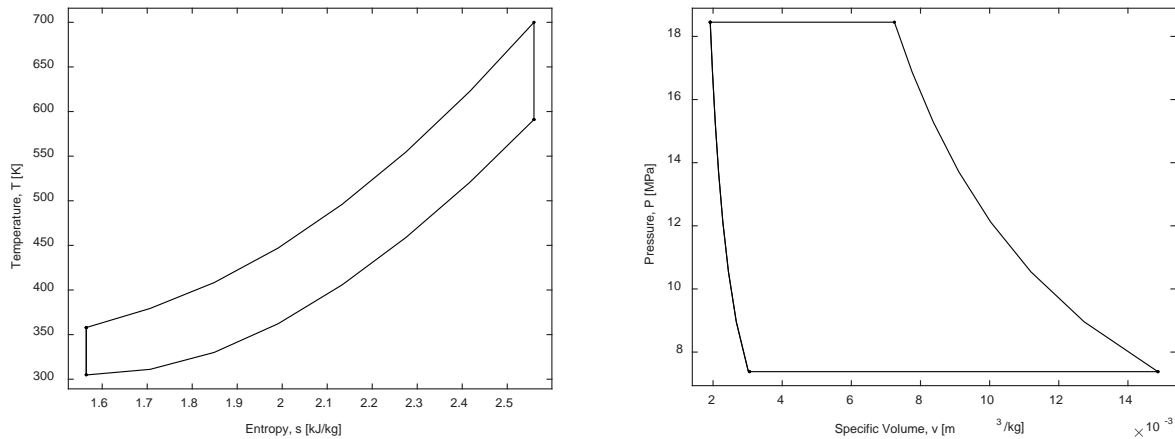

FIGURE 3. T-s and P-v Diagrams for an Ideal Brayton Cycle Configuration with No Regeneration, Intercooling, or Reheating.

A more complex case with two intercoolers, two reheaters, 90% regeneration, and 90% isentropic efficiencies in turbomachinery is shown in Figure 4.
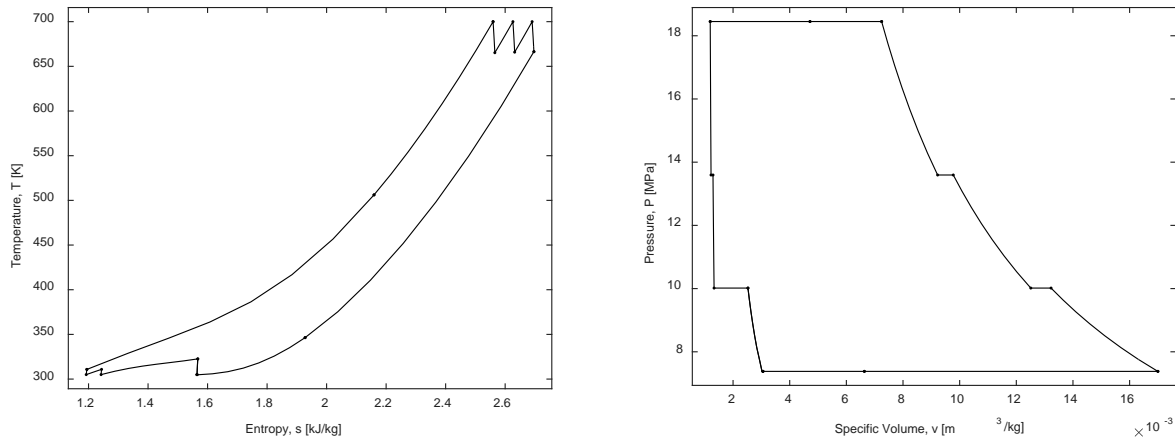
FIGURE 4. T-s and P-v Diagrams for an Ideal Brayton Cycle Configuration with No Regeneration, Intercooling, or Reheating.

With a functioning code calculating variables throughout the Brayton cycle, preliminary work focused on the effect and sensitivity of each input variable on the system mass and cycle efficiency and net work out. In these trade studies, all inputs except one were kept constant. In Figure 5, the effectiveness of regeneration was varied, while the core operated at the conditions previously mentioned. Optimum regeneration (for mass) occurs at an effectiveness of about 60%. The plots also indicate that 100% regeneration would result in infinite mass due to the fact that an infinitely long heat exchanger would be required.

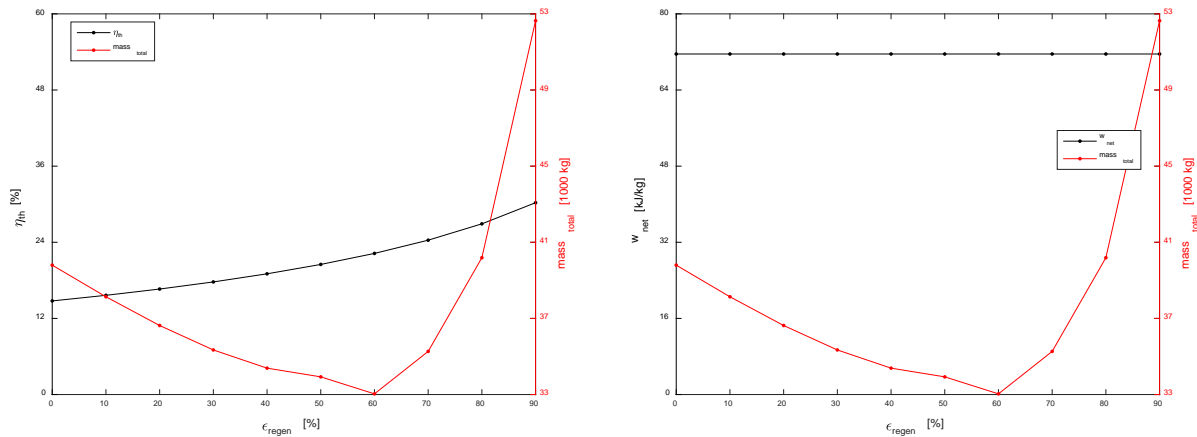**FIGURE 5.** Trade Study of Regeneration Effectiveness. A Mass-Optimum Value Occurs at ~60%.

It can be seen that higher regeneration results in higher thermal efficiency and no change in net work output. And with an optimum value for mass, there is a trade-off after 60% effectiveness. More regeneration results in better efficiency, but higher mass. In Figure 6, two trade studies are shown for intercooling and reheating.

5
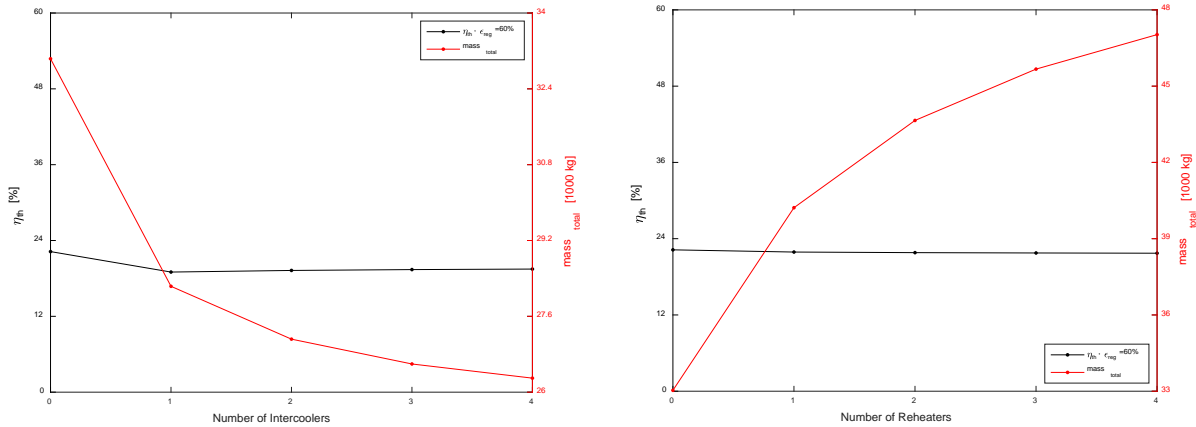
FIGURE 6. Trade Studies of Intercooling and Reheating. Intercooling Decreases Mass, While Reheating Increases It.

It can be seen that intercooling reduces mass, while reheating increases mass. There are diminishing changes in both cases, so adding one or two intercoolers is likely the best realistic option. In Figure 7, a trade study on turbine inlet temperature is shown.
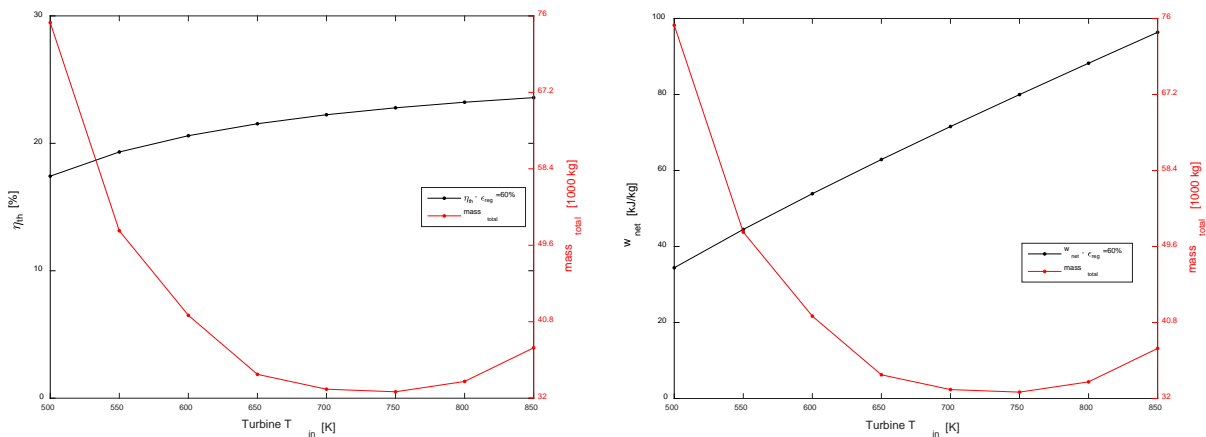
FIGURE 7. Trade Study of Turbine Inlet Temperature. Higher Turbine Inlet Temperature Gives Better Efficiency and Net Work, But There is an Optimum Temperature With Regards to Mass.

This shows that higher turbine temperature is better for both the thermal efficiency and the net work out. However, there is a mass-optimum value at around 700-750 K. In Figure 8, a trade study on compressor inlet temperature is shown.
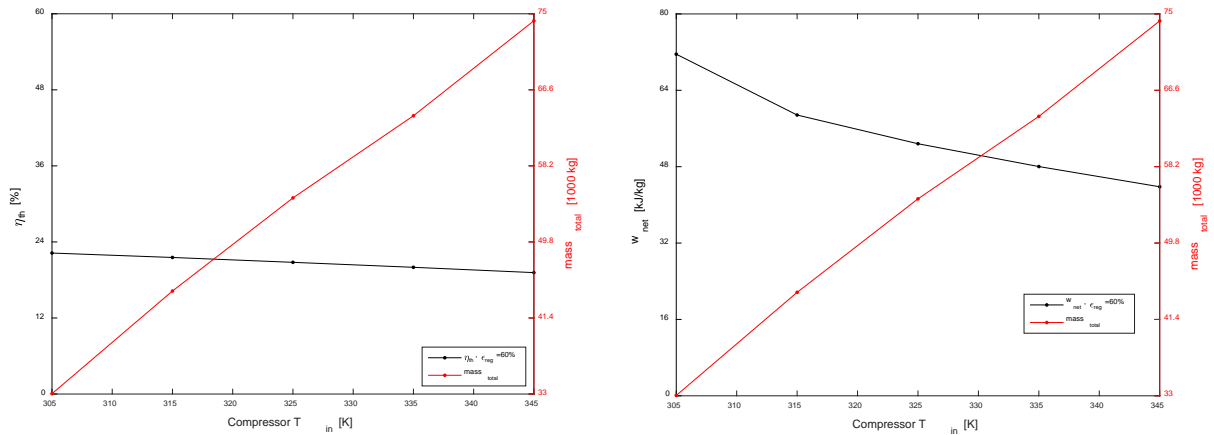
FIGURE 8. Trade Study of Compressor Inlet Temperature. Lower Temperature Results in Lower Mass, Better Efficiency, and Better Net Work Out.

Here, it is seen that low compressor inlet temperature is desirable. The low inlet temperature results in lower mass, higher thermal efficiency, and higher net work out. In Figure 9, a trade study on turbine inlet pressure is shown.
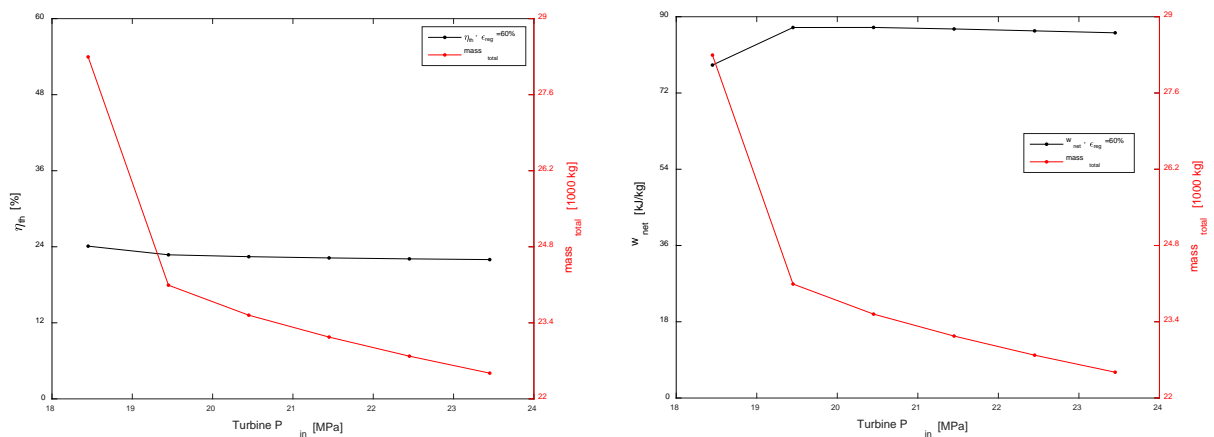
FIGURE 9. Trade Study of Turbine Inlet Pressure. Higher Pressure Results in Lower Mass, With Little Effect on Efficiency or Net Work.

Higher turbine inlet pressure results in lower mass, and does not have much effect on the thermal efficiency or the net work out. In Figure 10, a trade study on pressure ratio is shown.
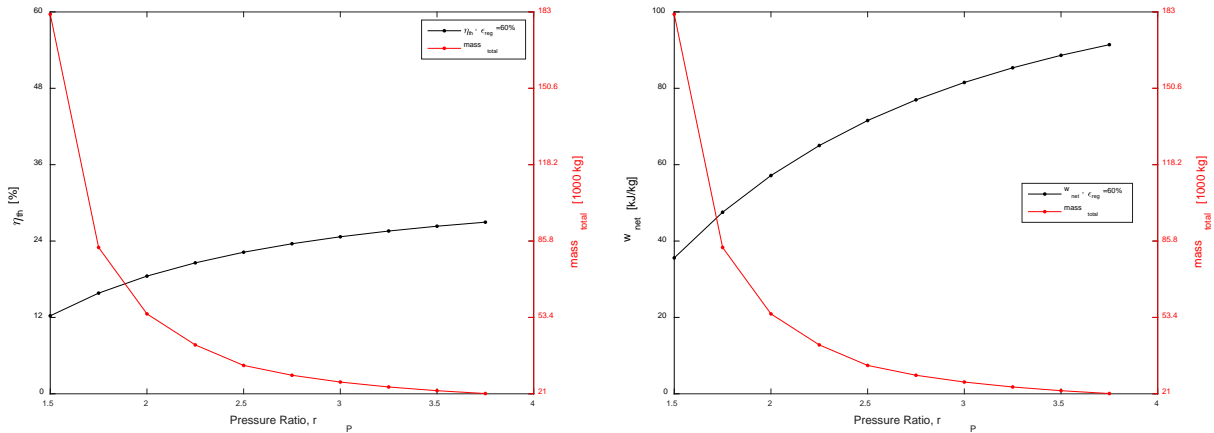
FIGURE 10. Trade Study of Pressure Ratio. Higher Pressure Ratio Results in Lower Mass and Better Efficiency and Net Work.

Higher pressure ratios improve mass, thermal efficiency, and net work. In Figure 11, a study on the isentropic efficiencies of the turbine and compressor is shown.
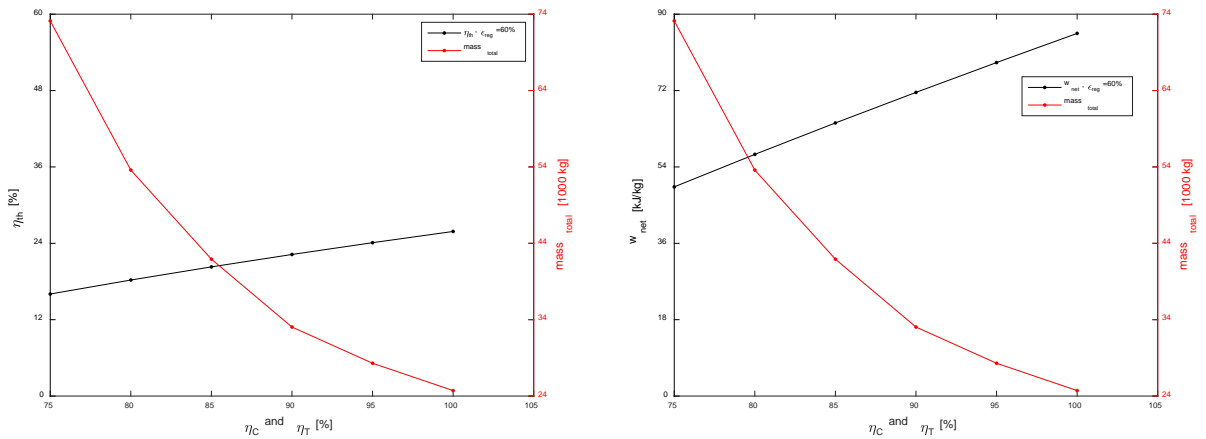
FIGURE 11. Trade Study of Isentropic Efficiencies of Turbines and Compressors. Higher Efficiencies are Better.

Higher efficiencies in the turbines and compressors have a positive effect on mass, thermal efficiency and net work out. A final study was performed looping through nearly a thousand configurations. In Figure 12, these configurations are plotted as mass vs thermal efficiency.
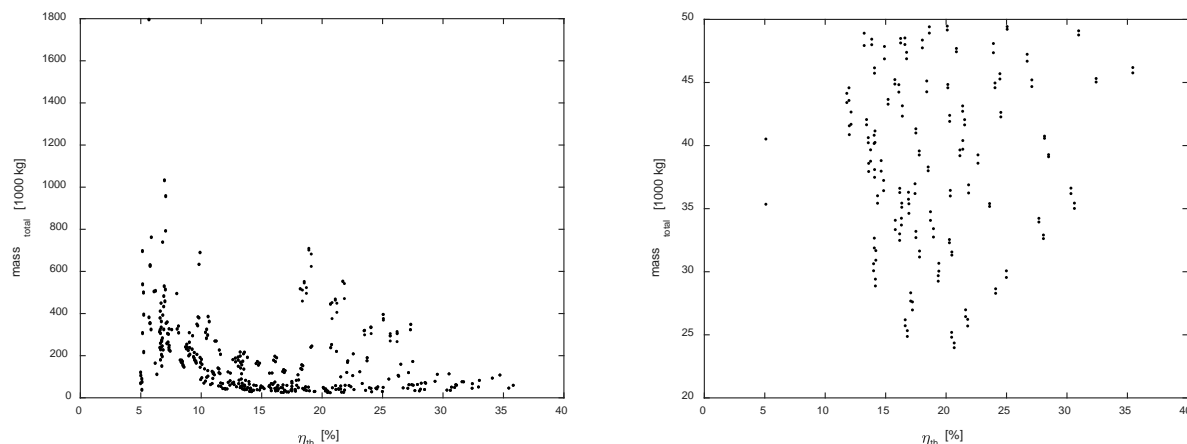
FIGURE 12. Trade Study of All Configurations. On the Left Plot, Mass Seems to Decrease with Higher Efficiency. However, a Tighter Perspective (Right Plot) Reveals No Such Trend.

In general, it seems that higher efficiency results in lower mass. However, feasible configurations that have a total mass less than 50,000 kg don't indicate such an obvious trend. The lowest mass configuration (~24,000 kg) had a thermal efficiency of 20.7%. The core operated between 767 K and 910 K at 7.38 MPa. The turbine fluid entered at 700 K and 18.45 MPa, and was expanded over a pressure ratio of 2.5 at 95% isentropic efficiency. The compressor fluid entered at 305 K and 7.38 MPa, and was compressed over the same pressure ratio at 95% isentropic efficiency. Regeneration was 60% effective. Two intercoolers and no reheaters were used.

CONCLUSION

NASA believes nuclear technology will enable human exploration of Mars. A Mars colony will require the use of surface fission power to heat a working fluid which can be used to generate electricity. Minimizing the weight of the power conversion technology is very important, as this will also minimize the number of launches and the associated costs. The supercritical CO2 Brayton cycle was chosen for long-term application on Mars, as other technologies and fluids may only provide benefit in the short-term. This study provided a heat transfer model and mass model for various Brayton configurations. These models determined the mass-optimal configuration for 15 years of 333.3 kWe of electricity generation. Using three such plants, a total of 1 MWe would provide a power-rich environment for long-term human exploration of Mars.

NOMENCLATURE

NASA	=	National Aeronautics and Space Administration	DRA	=	Design Reference Architecture
ISRU	=	In-Situ Resource Utilization	PCS	=	Power Conversion System
FSPS	=	Fission Surface Power System	S-CO2	=	Supercritical Carbon Dioxide
IHX	=	Intermediate Heat Exchanger	EHXCL	=	External Heat Exchanger on Core Loop
RH	=	Reheater	IC	=	Intercooler
EHX	=	External Heat Exchanger	LEU	=	Low Enriched Uranium
CERMET	=	Ceramic Metallic			

ACKNOWLEDGMENTS

REFERENCES

[1]   NASA, "Human Exploration of Mars Design Reference Architecture 5.0," 2009.

[2]   L. S. Mason, "A Comparison of Brayton and Stirling Space Nuclear Power Systems for Power Levels from 1 Kilowatt to 10 Megawatts," 2001.

[3]   L. S. Mason, "A Comparison of Fission Power System Options for Lunar and Mars Surface Applications," 2006.

[4]   J. Tarlecki, N. Lior and N. Zhang, "Analysis of thermal cycles and working fluids for power generation in space," *Energy Conversion & Management,* 2007.

[5]   T. M. Conboy, M. D. Carlson and G. E. Rochau, "Dry-Cooled Supercritical CO2 Power for Advanced Nuclear Reactors," *Engineering for Gas Turbines and Power,* vol. 137, 2015.

[6]   NIST, "Thermophysical Properties of Fluid Systems," 2011. [Online]. Available: http://webbook.nist.gov/chemistry/fluid/. [Accessed 2015].

[7]   C. Oh, T. Lillo, W. Windes, T. Totemeier and R. Moore, "Development of a Supercritical Carbon Dioxide Brayton Cycle: Improving PBR Efficiency and Testing Material Compatability," 2004.

[8]   Y. A. Çengel and M. A. Boles, Thermodynamics: An Engineering Approach, 2004.

[9]   International Energy Agency, "Upgraded Calculator for CO2 Pipeline Systems," 2009.

Re-Inventing the Light Bulb

Adarsh Rajguru[1], Mikayla Molnar[2], Philip Rexing[2] and Dr. Steven Howe[3]

[1]*Department of Astronautical Engineering, University of Southern California, 854B Downey Way, RRB 225
Los Angeles, California 90089-1192*
[2]*Department of Nuclear Engineering, Missouri University of Science and Technology, 1870 Miner Cir, Rolla, MO
6540*
[3]*Director, Centre for Space Nuclear Research, University Space Research Association, Idaho National Laboratory*
[1]*(213) 819-4536; arajguru@usc.edu*

Abstract. This paper proposes a novel concept of lighting a Mars Habitat using a radioisotope power source. This study is part of a research work that was conducted to investigate a radioisotope power source solution to support the critical life support systems of a human Mars habitat of 6 crewmembers. Adequate, reliable and energy efficient lighting and heating of the habitat were the primary concerns. In order to address these problems, the radioisotope light bulb concept was developed. The study includes the bulb design, heat transfer analysis, thermal radiosity analysis, structural analysis and radiation analysis of the radioisotope light bulb. An Americium Oxide core in a Tungsten Rhenium Cermet was considered as the core for the bulb. A Tantalum coating around the core heats up to temperatures of 1480 K, enabling the material to glow at a "warm white light" spectrum. This is appropriate and psychologically convenient for a healthy work environment inside the habitat. The core is suspended in a Mullite holding cage and vacuum-sealed by an ALON ceramic bulb. Based on the assumption of good thermal insulation of the habitat, a passive heat rejection system from the radioisotope light bulb into the habitat was designed to achieve a steady state temperature of the Tantalum coating at the required 1480 K. The passive heat rejection system was incorporated in the thermal control system design of the habitat in order to maintain the required nominal temperature for the crew. For the "lights off" condition, a ThermoPhotoVoltaic (TPV) cells design was evaluated that would encompass the light bulb. The TPV cells would convert the light energy from the radioisotope into electric power, which would then be channeled into the Power Management And Distribution (PMAD) system of the habitat for storage (via charging batteries) or running electrical appliances. A Monte Carlo N-Particle (MCNP) transport code model was created to study the radiation emitted from the light bulb. The MCNP model helped in polishing the design to meet acceptable radiation dosage for the human crew during the course of the mission. Lighting and heating analysis for operating hydroponics in a Mars habitat were performed to broaden the application of the radioisotope light bulb.

Keywords: Radioisotope, Americium, Plutonium, Photovoltaics and Lighting.

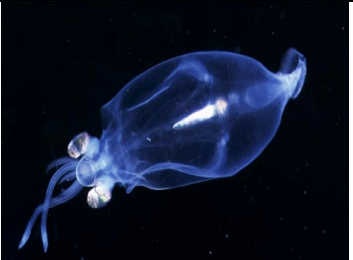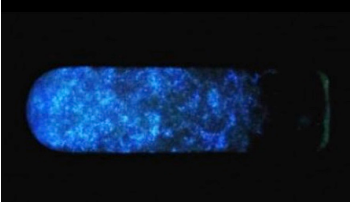## TYPES OF LIGHT SOURCES & SHADES

Types of Luminescence

The type of light sources, which were evaluated initially for this application were the ones that emitted light via luminescence. Luminescence is the emission of light by a substance that's not heated.

Several different kinds of luminescence light sources were investigated for application in the Mars Terrestrial Habitat. These various kinds of luminescence light sources are described in table 1 below.

TABLE 1. Types of Luminescence.

Luminescence Type	Description	Image
Bioluminescence	This is the type of luminescence generated by living organisms. For example a firefly emits light via a chemical reaction within its abdomen that combines oxygen, a cation (usually calcium), Adenosine Triphosphate (ATP) and the chemical Luciferin in the presence of an enzyme Luciferase. However it is short lived.	
Chemiluminescence	Chemiluminescence results from electrochemical or chemical reactions. This is also short lived too.	
Crystalluminescence	Crystalluminescence is produced ocassionally during crystallization. The intensity of light is not good enough for the application being sought.	
Cathodoluminescence	Cathodoluminescence occures when an electron beam impacts on a luminescent material such as phospher. The problem with this kind of luminescence is low intensity and requires an electron beam.	
Electroluminescence	Electroluminescence generates light in response to an electric current passing through some material (basis of Light Emitting Diodes). LEDs were considered for lighting a Martian garden discussed later in this chapter.	
Radioluminescence	Radioluminescence is generated when a radioactive material throws off ionizing radiation such as alpha, beta or gamma rays. A tritium light source was analyzed to evaluate if it could be used on the entire roof of the habitat for providing sufficient lighting. However it was infeasible for the application due to the reasons explained below.	

The half-life of Tritium is 12.3 years and it has low beta radiation energies with an average of 5.7 keV and a maximum of 18.6 keV. The intensity of the light depends on the pressure, tube diameter, phosphor coating and phosphor grain size.

The tubing has to be a specific diameter, because any larger would make the beta particles get absorbed in the gas before reaching the phosphor, making it ineffective. It is the same case for the phosphor coating. However none of these luminescence light sources could supply adequate lighting to the application for which it was being sought. The objective of this research was to come up with an architecture / concept to provide off the grid, adequate, reliable and energy efficient lighting for a human Mars habitat. A static radioisotope power source like a Radioisotope thermoelectric generator (RTG) providing constant electric power to the habitat, which can power the lighting inside the habitat still incorporated the reliance of an electric grid system and a series of LED light bulbs with low reliability. Hence in pursuit of an independent, isolated, multipurpose light bulb, the radioisotope light bulb concept was developed.

As a starting point to proof the physics of such a concept, a light source similar to that produced from a standard 60 – Watt incandescent light bulb was considered for comparison. Lamps and light bulbs have a characteristic called color temperature. The color temperature of a light source is the temperature of an ideal black body radiator that radiates light of comparable hue to that light source [1]. It should be noted that there are several different types of white light. The first type is warm white. Warm white has a color temperature of up to 3000 K and produces a calm, relaxing light. Cool white is the next type of white light and has a color temperature of 3100 K – 4500 K. This produces a friendly, inviting light. Daylight is another type of white light that has a color temperature of 4600 K – 6500+ K, and produces a crisp vibrant light [2]. The type of white light that was aimed for was cool white to provide an adequate visual atmosphere for the astronauts in the habitat.

Another aspect of light that is important to understand is the black body spectrum. This is because an incandescent light source closely resembles that of a black body. A black body absorbs all radiation incident on its surface and emits radiation based on its temperature. It gets its name from the fact that if it does not emit radiation in the visible range, then it appears black due to the complete absorption of all wavelengths [3]. Figure 1 shows the black body spectrum.

Temperature (°C)	Color
480	Barely red in the dark
600	Dark red
800	Cherry red
950	Orange
1100	Orange – yellow
1300	Light yellow
1500	Nearly white

Figure 1: Black-Body Spectrum
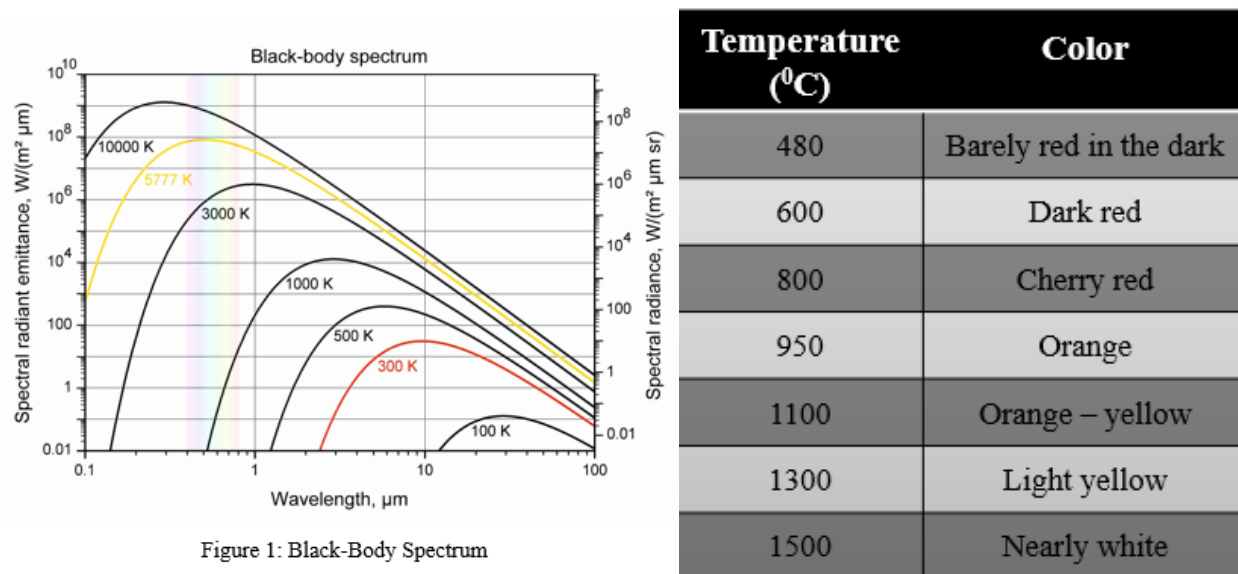
FIGURE 1. Black body spectrum (Left) and Color of metals at various temperature (Right) [3].

The area under these curves represents a blend of all of these wavelengths, so the more visible light present under the curves, the better of mix of colors and the brighter and whiter the light is. The sun is an example of an almost perfect black body.

As seen in figure 1, the graph of the sunlight temperature peaks at right around 500nm in the visible spectrum, which is why the sun we see produces a very crisp white light. The color temperature of a standard light bulb is about 3000 K [3]. This is the color temperature that was aimed to achieve for the radioisotope light source. However, the actual temperature required to achieve in the core is quite different. The table in figure 1 illustrates the color of a metal visible to the eye at different temperatures. The core must heat a tantalum coating up to 1480K in order to produce the desired cool white light. The following section explains the research, design and analysis conducted for an Americium – 241 Dioxide radioisotope light source.

SYSTEM DESIGN, CONFIGURATION AND ANALYSIS

The radioisotope bulb was designed using SolidWorks and the thermal analysis was done in COMSOL. Three different configurations were analyzed. The first had a structural cage for the core with three holder bars, illustrated in Figure 2. This is referred to as Design 1. The second had a structural cage for the core with four bars, as seen in Figure 3. This is referred to as Design 2. The third used a wire through the center of the core to suspend the core in the bulb, illustrated in Figure 4. This is referred to as Design 3.
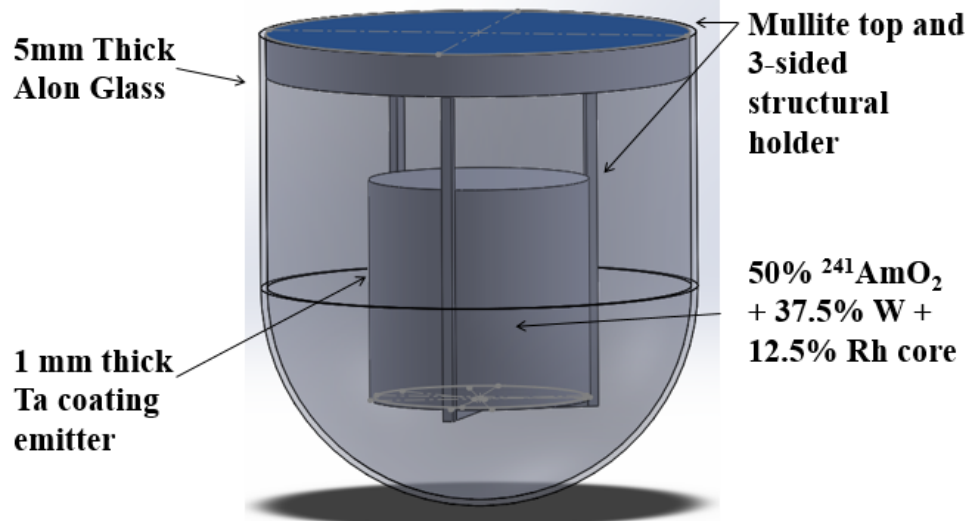
FIGURE 2. Radioisotope Light Bulb Design 1.
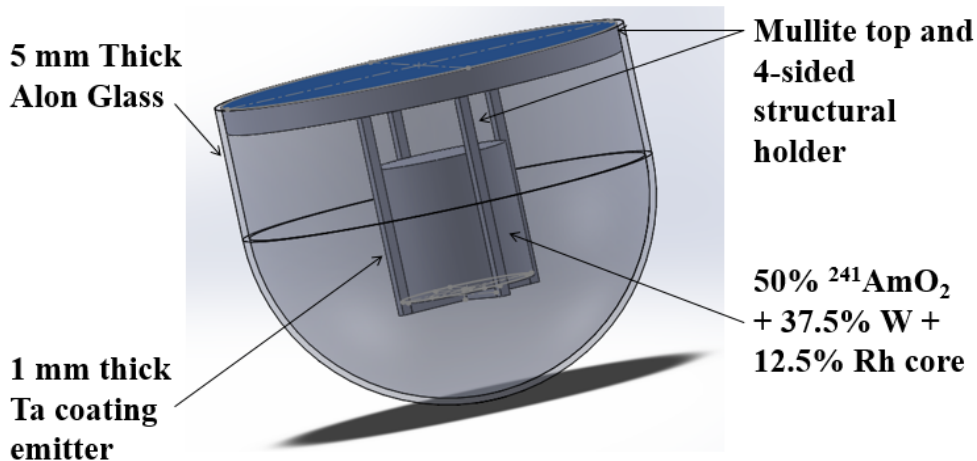
FIGURE 3. Radioisotope Light Bulb Design 2.
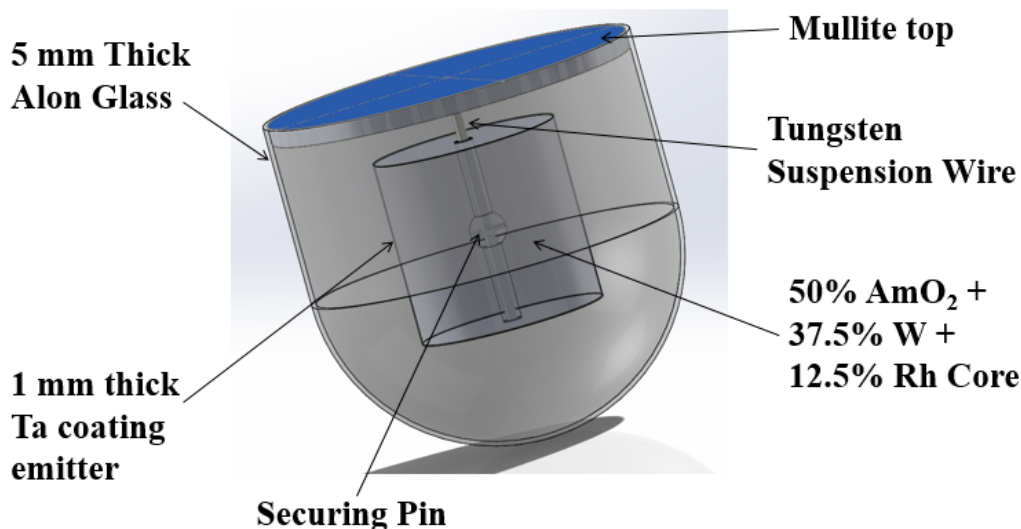
FIGURE 4. Radioisotope Light Bulb Design 3.

All three designs consist of an Americium-241 Dioxide / Tungsten / Rhenium cylindrical core matrix. For each design, the size of the core was analyzed at 10 cm (diameter) x 10 cm (height), 15 cm x 15 cm, and 20 cm x 20 cm. Design 2 was also analyzed with a core size of 25 cm x 25 cm. A 1 mm thick Tantalum coating surrounded the core, which is the material important for the emission of light [4]. The top of the structure is made of Mullite and the bulb is made of ALON glass for all three designs. The cage structure for Designs 1 and 2 are made of Mullite while the wire suspending the core of Design 3 is made of Tungsten, all bolted to the top with tungsten washers and screws [5].

Heat Transfer Analysis

The heat transferred throughout each system was analyzed using COMSOL Multiphysics simulation software. Each design and core size variation was built in SolidWorks and then imported into COMSOL to be analyzed and simulated individually. The results are as followed:

For Design 1, the 10 cm x 10 cm, 15 cm x 15 cm, 20 cm x 20 cm core configurations reached temperatures of 1080K, 1010K, and 1080K, respectively. Design 1's temperature analysis is shown below

FIGURE 5. 10cm x 10cm   **FIGURE 6**. 15cm x 15cm   **FIGURE 7**. 20cm x 20cm
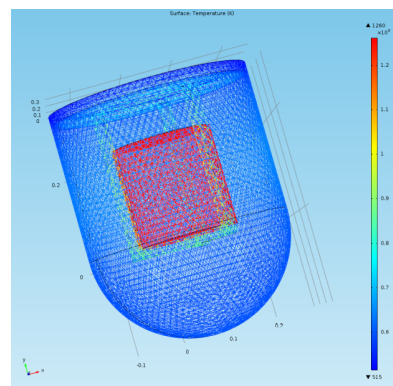
For Design 2, the 10 cm x 10 cm, 15 cm x 15 cm, 20 cm x 20 cm core configurations reached temperatures of 1020 K, 1190 K, and 1300K, respectively. The temperature analysis is shown below:

FIGURE 8. 10cm x 10cm   **FIGURE 9**. 15cm x 15cm   **FIGURE 10**. 20cm x 20cm For
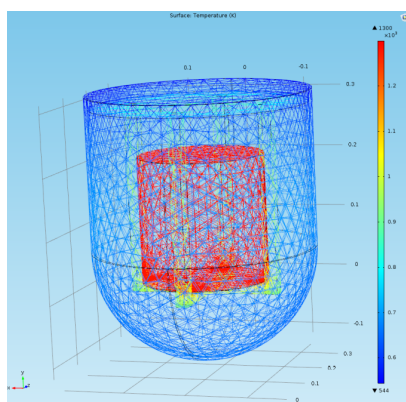
Design 3, the 10 cm x 10 cm, 15 cm x 15 cm, 20 cm x 20 cm core configurations reached temperatures of 1060 K, 1200 K, and 1310K, respectively. The temperature analysis is shown below:
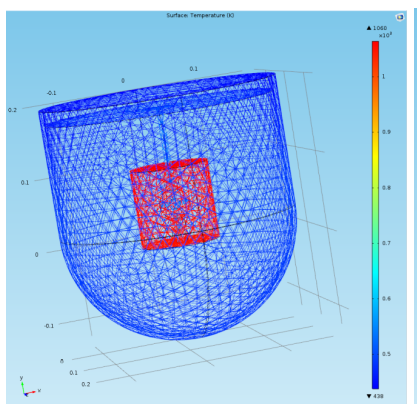
FIGURE 11. 10cm x 10cm   **FIGURE 12.** 15cm x 15cm   **FIGURE 13.** 20cm x 20cm
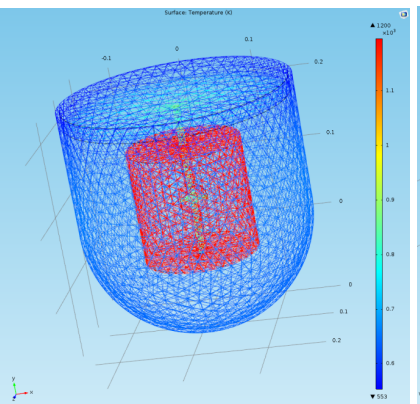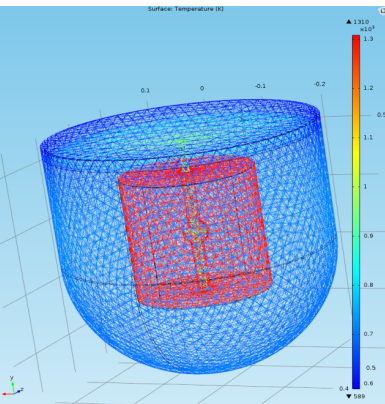
A simulation was run of Design 2 with a core of dimensions 25 cm x 25 cm. This yielded a maximum desired temperature of 1480 K. A standard 60 – Watt incandescent light bulb was also modeled in COMSOL for comparison. The standard bulb reached a temperature of 1530 K from the simulation.
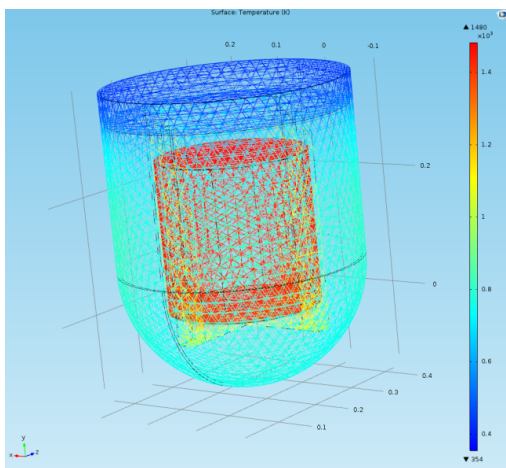
FIGURE 14. 25 cm x 25 cm Design 2 Temperature Analysis   **FIGURE 15**. Standard Incandescent Light Bulb Temperature Analysis
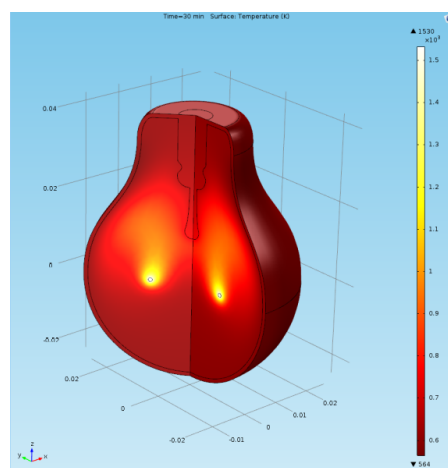
Thermal Radiosity Analysis

In addition to temperature analysis, it was necessary to determine the radiosity (W/m^2) of each design and core size. Conveniently, COMSOL was able to produce these results as well. These are summarized below. For Design 1, the 10 cm x 10 cm, 15 cm x 15 cm, 20 cm x 20 cm core configurations achieved radiosities of 6.68x10^4 W/m^2, 5.95 x10^4 W/m^2, and 8.54 x10^4 W/m^2, respectively.
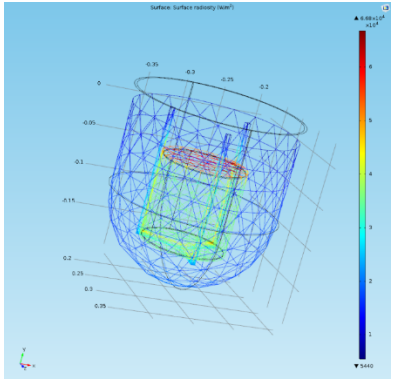
FIGURE 16. 10 cm x 10 cm   **FIGURE 17**. 15 cm x 15 cm   **FIGURE 18**. 20 cm x 20 cm
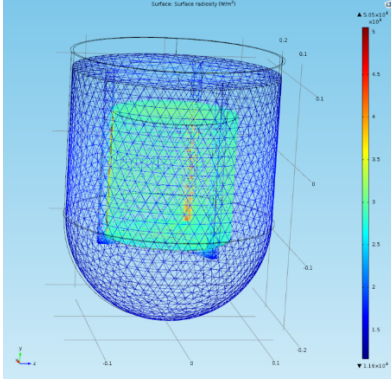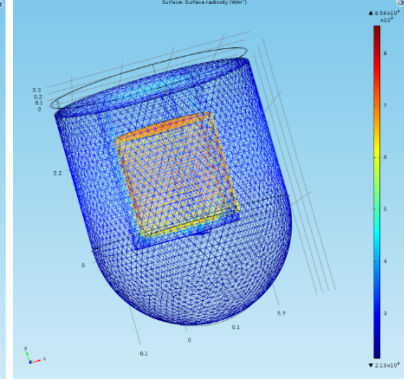
For Design 2, the 10 cm x 10 cm, 15 cm x 15 cm, 20 cm x 20 cm core configurations achieved radiosities of 5.45x10^4 W/m^2, 9.27 x10^4 W/m^2, and 1.37 x10^5 W/m^2, respectively.
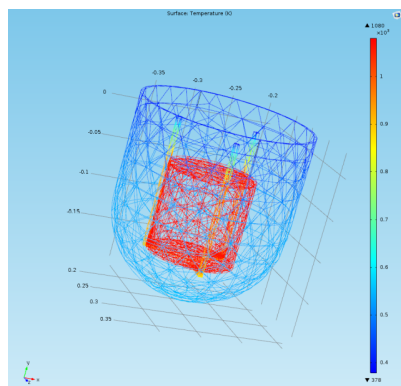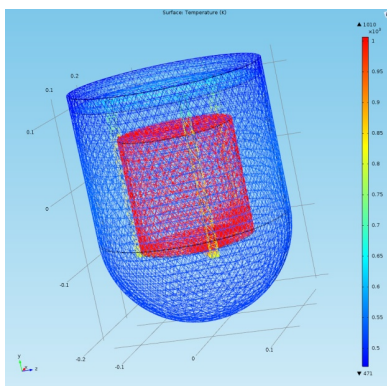
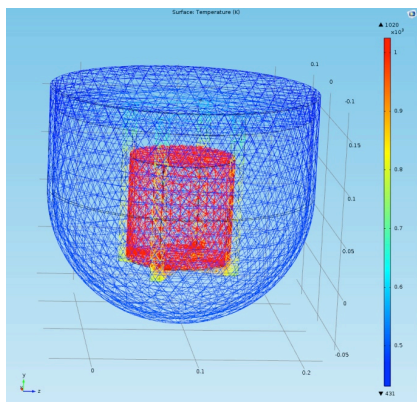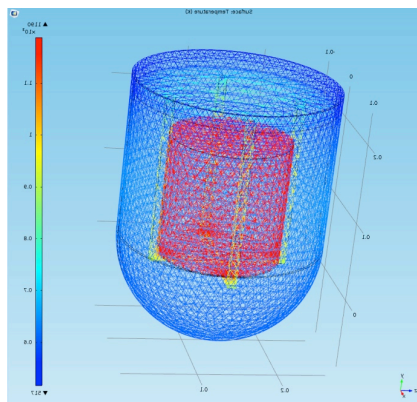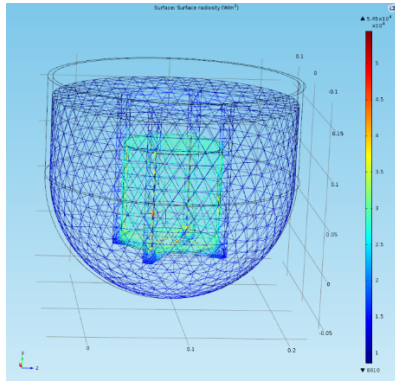

FIGURE 19. 10cm x 10cm   **FIGURE 20**. 15cm x 15cm   **FIGURE 21**. 20cm x 20cm
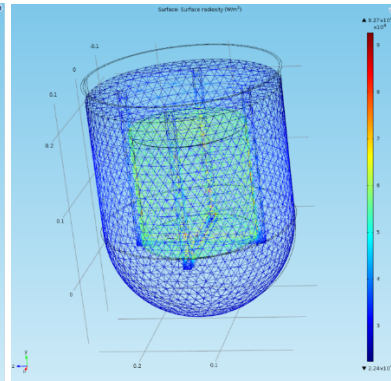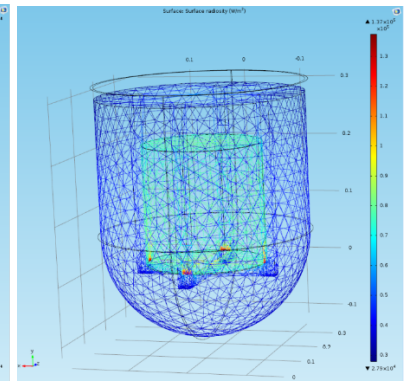
For Design 3, the 10 cm x 10 cm, 15 cm x 15 cm, 20 cm x 20 cm core configurations achieved radiosities of 3.04x10^4 W/m^2, 5.91 x10^4 W/m^2, and 8.87 x10^4 W/m^2, respectively.
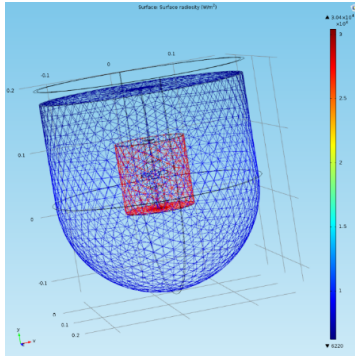
FIGURE 22. 10cm x 10cm   **FIGURE 23**. 15cm x 15cm   **FIGURE 24**. 20cm x 20cm
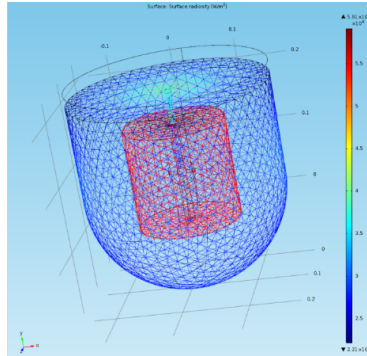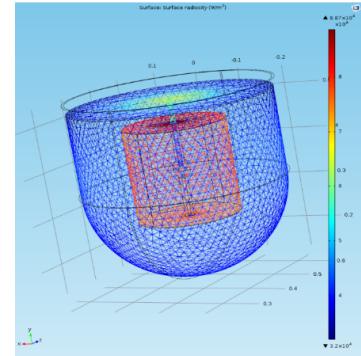
Design 2 with a 25 cm x 25 cm sized core was also analyzed for its radiosity and compared to that of a standard incandescent light bulb. The average radiosity of the radioisotope bulb is approximately 65,000 W/m^2. A standard incandescent has a radiosity of about 6660 W/m^2 generated by COMSOL. When the two are compared, the radioisotope bulb has nearly ten times the amount of radiosity, meaning that it is ten times brighter than the standard 60-watt light bulb.
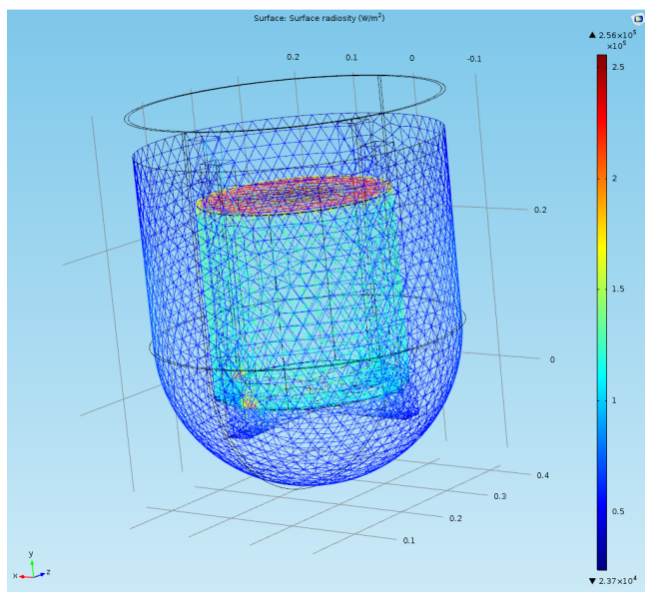
| FIGURE 25. 25 cm x 25 cm | FIGURE 26. Standard Incandescent Light Bulb |
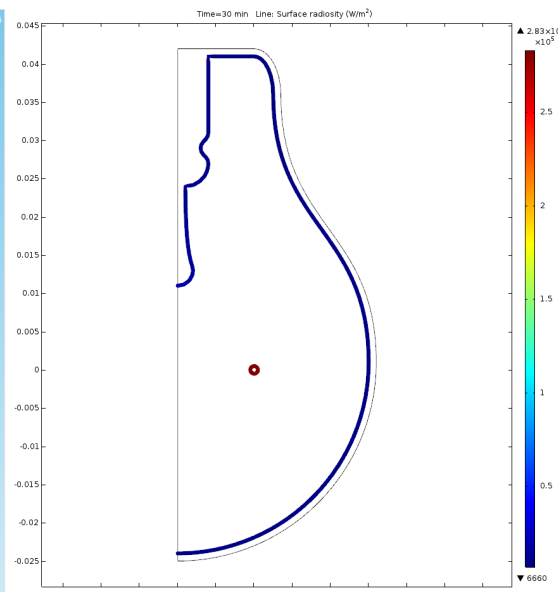
Various designs of the bulb were analyzed in order for the core to reach a thermal temperature 1480 K. As predicted, the design with the single tungsten wire suspending the core yielded the highest temperature for identical core dimensions. For example, for the 20 cm x 20 cm core, Design 1 yielded a temperature of 1080K, Design 2 yielded a temperature of 1300 K, and Design 3 yielded a temperature of 1310 K. Ten kelvin is not a huge temperature difference. However, it is obvious that the 4-sided cage design of Design 2 is much more structurally sound than that of the suspended wire of Design 3. Therefore, Design 2 was chosen as the best design and was then optimized to reach the desired 1480 K.

Radiation Shielding Analysis

To quantify any self-shielding properties of the bulb and provide dose numbers to aid in designing further shielding, MCNP was used to model the radioisotope light. The full geometry of the bulb was detailed in an input file with only small modifications for the sake of simplicity. Primarily, the bulb was made to be cylindrical with no curved bottom, and the support structure of the isotope source was ignored. The porous Mullite base, Americium core, Tantalum coating, and ALON ceramic walls were modeled to be as similar to the COMSOL designs as practical, with material properties matching what would be naturally expected. In initial trials, the void between the source and the glass was modeled to be low-density argon (among some other select gasses); however, in the final design this void was modeled as a vacuum.

A source definition that would model a homogenous radiative source throughout the americium core was created and tally multipliers that would convert surface fluxes into dose rates of rems per hour were included. In total, four separate tallies were used to measure the surface flux for varying distances from the bulb. The first of these tallies was against the exterior side of the ALON ceramic; the second simulated flesh against the ALON glass, the third and fourth simulated flesh at 50 cm and 100 cm respectively. The model was run on Idaho National Laboratory's super-computer.

In total, the simulation ran approximately 10^9 particles to produce consistent results with smaller statistical errors. A basic graph of these results along with a cross-section of the model geometry is shown in Figure 27. The peak at the beginning of the chart is assumed to be due to a minor error within MCNP's calculation process and can be ignored.
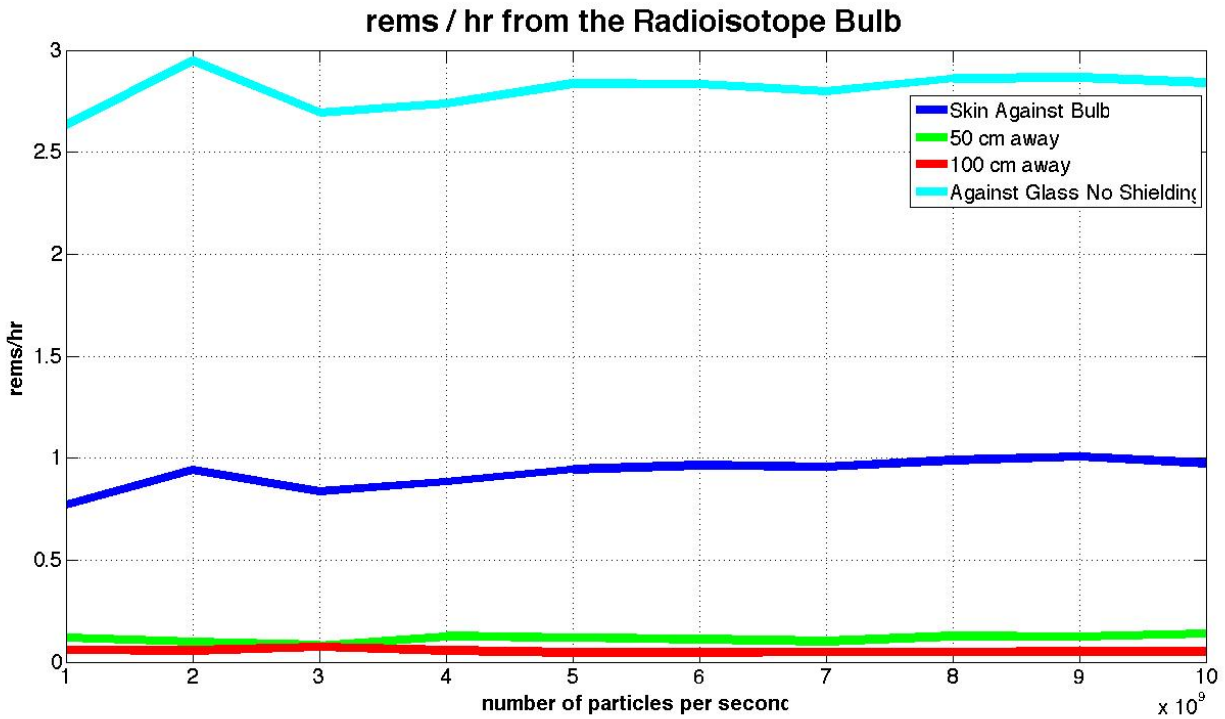
FIGURE 27. Rems / hr dosage prediction using MCNP for the selected Radioisotope Light Bulb design.

To add perspective to the numbers produced, these results are compared in Table 2 shown below. This table also lists currently acceptable exposure limits for crew during spaceflight missions.

TABLE 2. Ionizing Radiation Exposure Limits [7]

Duration of Exposure	Blood Forming Organs 5 cm depth [Sievert]	Eye [Sievert] 0.3 cm depth	Skin [Sievert] 0.01 cm depth	Testes [Sievert] 3 cm depth
Daily	0.002	0.003	6	0.001
30 days	0.25	1	1.5	0.13
90 days	0.35	0.52	1.05	0.18
Annual	0.5	2	3	0.38
Career	4	4	6	1.5

The results that were achieved are not substantially far from the limits listed, but are far above what would be desired in a setting such as a permanent Mars colony. It is expected that dose rates could be reduced greatly by simply increasing the thickness of the ALON ceramic covering the americium bulb.

ELECTRIC POWER CONVERSION EFFICIENCY

It is important to note that once the radioisotope core is fabricated into the light bulb it's "turned on", there is no way of "turning it off". Therefore, we ran into the question of "*how do you block the light when the astronauts are trying to sleep?*" The answer was Thermal PhotoVoltaic (TPV) cells. When the astronauts do not need the light on, they can enclose the bulb with TPV cells. This will do two things:

1. It will block the light from the Radioisotope Light Bulb so the astronauts can sleep
2. It becomes another source of power for the habitat

The TPV cells convert the light from the radioisotope into electric power, which could then be channeled into the Power Management And Distribution (PMAD) system of the habitat for storage (via charging batteries) or running electrical appliances [6]. Table 3 summarizes the performance of the TPV cells in best and worst case scenarios.

TABLE 3. TPV Cells Performance with ^{241}AmO$_2$ + W + Rh Core

Efficiencies of PV cells @ 350 K	Minimum (%)	Maximum (%)
Thermal Efficiency	80	90
Cavity Efficiency	30	40
PV Efficiency	20	25
Total Efficiency	=> 0.8 x 0.3 x 0.2 = 0.048 => 4.8	=> 0.9 x 0.4 x 0.25 = 0.09 => 9
Thermal Power (25 cm x 25 cm Core)	~ 6.736 kW$_{th}$	
Electrical Power	336.8 W$_e$	606.3 W$_e$

CONCLUSION

A radioisotope light source has been designed to provide adequate and reliable lighting for a Mars habitat. The final design of the 25 cm (diameter) x 25 cm (height) Americium-241 Dioxide in a Tungsten Rhenium cermet core encapsulated by a tantalum coating is expected to produce approximately ten times the amount of light than a standard household incandescent light bulb. This radioisotope light source can also be used as a thermal and electrical power source when light is not needed. Because Americium-241 has a half-life of over 432 years, this will also be an extremely long-lasting light source [8].

An in-depth structural analysis still needs to be addressed for the research on this radioisotope light bulb in order to ensure that the bulb would remain structurally sound during takeoff and landing. In addition, the mass of the source can pose a possible problem because the 25 cm x 25 cm core is calculated to have a mass of approximately 193kg. Hence, plutonium may be looked at as a replacement in order to decrease the mass size [6]. Fiber optics may also be analyzed so as to distribute the light to different areas of the habitat and increase the distance between the radioisotope source and the astronauts [9].

ACKNOWLEDGMENTS

REFERENCES

[1] Judd, D. B., MacAdam, D. L., Wyszecki, G., Budde, H. W., Condit, H. R., Henderson, S. T., et. al., "Spectral distribution of typical daylight as a function of correlated color temperature", *JOSA, 54(8), 1031-1040*, (1964).

[2] Westinghouse, "Can color temperature affect my mood?", available online at [*http://www.westinghouselighting.com/color-temperature.aspx*], (2015).

[3] Plank M., "Distribution of energy in the spectrum", *Annalen der Physik, Volume 4, 553-563*, (1901).

[4] O'Brien, C. R., Howe D. S. and Werner E. J., "Advanced radioisotope heat source and propulsion systems for planetary exploration", *Proceedings of International Astronautics Congress*, (2010).

[5] Schneider, et. al., "Structure and properties of Mullite – A review", (2007).

[6] Howe S., et. al., "Design of a Flight Demonstration Experiment for Radioisotope Thermophotovoltaic (RTPV) Power System", (2015)

[7] Eckart P., "Spaceflight Life Support and Biospherics", *Microcosm Press*, (1996).

[8] Oetting, F. L., & Gunn, S. R., "A calorimetric determination of the specific power and half-life of americium-241. Journal of Inorganic and Nuclear Chemistry", *29(11), 2659-2664*, (1967).

[9] Ghatak, A. and Thyagarajan K. "An introduction to fiber optics", *Cambridge university press*, (1998).

Nuclear Thermal Propulsion Integrated Injector-Manifold Development

Travis Belcher[1], Robert Hetterich[2], Matthew Reilly[3], Joaquin Santecchia[4], and Tyler Scogin[5]

[1]University of Texas at El Paso, El Paso, TX 79968
(281)904-0553; travisb117@gmail.com
[2]Lehigh University, Bethlehem, PA 18015
[3]Rowan University, Glassboro, NJ 08028
[4]Arizona State University, Tempe, AZ 85287
[5]Georgia Institute of Technology, Atlanta, GA 30332

Abstract. As research in technology for missions beyond Earth's orbit continues, Nuclear Thermal Propulsion (NTP) is potentially one method to enable deep space propulsion. NTP engines are still in an early stage of research and development, with many new and complicated components that have not yet been developed. One such component is a combined injector-manifold or "Injectifold", which receives H_2 propellant from several components and distributes it for cooling and other duties within the reactor. Having a detailed design and analysis of the Injectifold is a vital part in the development of the engine, but the Injectifold has numerous requirements that are different from standard injectors or manifolds for existing chemical engines. In this work, an Injectifold model was developed using SolidWorks for mechanical design and COMSOL for CFD analysis. A prototype section was manufactured using 3D sterolithography and subjected to cold flow testing using nitrogen as a surrogate propellant gas. It is expected that the design for the Injectifold will continue to iterate in the future, as more tests are carried out and hard data is gathered.

Keywords: Injectifold, Nuclear Thermal Propulsion, Injector-manifold, In-space propulsion

BACKGROUND

Nuclear thermal propulsion (NTP) has been under consideration for use as an in-space stage by NASA since the Apollo program. These rocket engines use the heat from within a nuclear reactor to increase the temperature of a propellant, such as hydrogen (H_2), which is then expanded through a nozzle to create thrust. An NTP engine would have about twice the efficiency of a chemical engine, with a specific impulse (Isp) of around 900 seconds. For reference the RS-25 (SSME) has an Isp of 452 seconds. The NTP engine achieves this higher efficiency by using the lower molecular weight of the propellant that is expelled in the exhaust such as H_2, while a chemical engine uses H_2 fuel and O_2 oxidizer resulting in a heavier molecular weight propellant and a lower Isp [1].

There has yet to be a flight tested nuclear thermal rocket, although extensive research and ground testing was performed in the 1960's for the Rover/NERVA (Nuclear Engine for Rocket Vehicle Application) project, before its eventual cancellation in 1972 [2]. In 2011 NASA began collaborating with the Center for Space Nuclear Research (CSNR) to investigate the use of NTP for a human mission to Mars in the 2030s. Part of this research is the Space Capable Cryogenic Thermal Engine (SCCTE) project, which is a point-design for a 35kN thrust NTP engine, looking at the use of low-enriched uranium in a nuclear thermal rocket. A number of specialized components are in development for the NTP system requirements.

SYSTEM REQUIREMENTS

The proposed NTP vehicle stores liquid H_2 in a cryogenic tank for transport. Figure 1 shows a system schematic of an NTP engine. First, the H_2 comes from the cryogenic tank and goes into a pump at location 2. This pump feeds into a line that splits in two at location 4 in Figure 1, with one line going to a regenerative nozzle cooling line which combines at 17, while the other goes into tie tubes within the reactor. The purpose of this regenerative line is to cool down the reactor control drums along the sides of the reactor core assembly. After coming out of these tie tubes, the propellant is routed through the turbine side of a turbo-pump at location 14. From there, it is then directed to the beginning of the top shield at location 17. This shield attenuates the amount of radiation the crew receives from the reactor during the mission. The radiation shield would consist of boron carbide (B_4C) pellets at a defined packing density to create a torturous path for H_2 to diffuse through evenly. This torturous path is also the mechanism by which the shield mitigates radiation from easily transmitting into the crew compartment, as they must bypass the random locations of the tightly packed B_4C pellets.
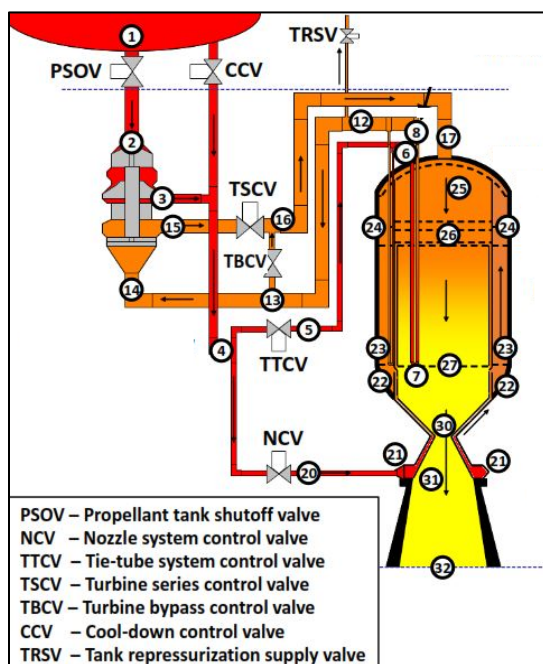
FIGURE 1. NTP Engine Schematic.

While various components for NTP rockets can be drawn from traditional chemical rocket designs, there are a number of specialized components specific to NTP that must be fully designed and tested. One such component is the Injectifold, a combination injector-manifold, located at node 26 in Figure 1. The Injectifold has several functions: First it must direct H_2 from the pump to the tie tubes. The tie tubes contain a Zirconium Hydride ($ZrH_{1.8}$) annulus, approximately 98 cm, which acts as a moderator to thermalize and reflect neutrons back into the reactor core. The tie tube is given in Figure 2. The tie tubes extend the full length of the reactor core and are interspersed in a geometric pattern between the fuel elements.

From the Injectifold the H_2 enters an inner tube, constructed from Zircaloy-4, which runs through the moderator. The H_2 then enters the outer tube and runs up the length of the tie tube, between the outer tube and moderator, finally exiting into another section of the Injectifold. The H_2 acts as a coolant for the moderator and its temperature is raised from 30.7K to 449K. The Injectifold then directs the H_2 to a turbine, where it expands across the stages producing power to run the pump. Upon exiting the turbine, the propellant is directed into the top radiation shield consisting of Boron Carbide (B_4C) pellets. The B_4C pellets work to absorb neutron radiation, but allow the H_2 to still flow through. The torturous path works to mix the H_2, giving it an even temperature cross-section profile. The Injectifold then directs the H_2 to meet up with the hexagonal fuel elements. Each fuel element has 61 through holes for the H_2 to flow through and superheat to a reactor exit temperature in excess of 2500K. The last step is for the H_2 to enter a converging and diverging nozzle and then exit the engine, producing thrust.
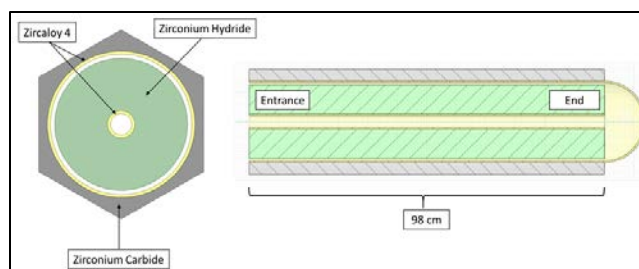
FIGURE 2. Tie Tube Top View and Side Cross-Section View, with the Materials of Each Piece Given.

MODELING AND DESIGN

After a few design iterations and studying heritage injectors, a final design for the Injectifold was realized. Utilizing a modular design with four plates creating a series of passages and plenums, the Injectifold was designed as follows:
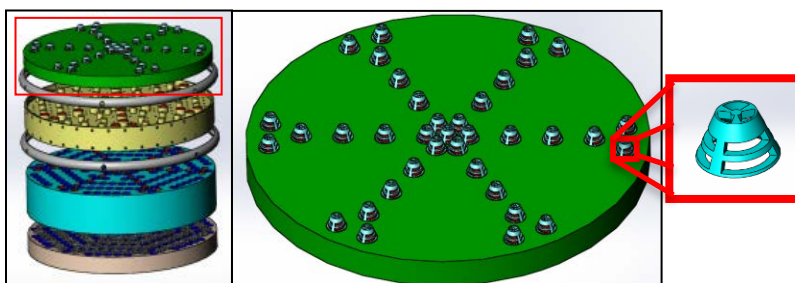
FIGURE 3. Plate 1 with the Shield Masks Installed to Stop the B4C Pellets from Blocking H2 Flow to the Core Shown Next to the Injectifold Exploded Assembly. A Blowup of the Shield Mask is outlined in Red.

Plate 1 - In the current iteration of the Injectifold design, plate 1 acts mainly as a cap for the tie tube inlet plenum formed by plate 2 and contains through holes for H_2 to pass to the core. As seen in Figure 3, plate 1 has shield masks attached over the through holes to stop the B_4C pellets that make up the neutron shielding from blocking the holes.

Plate 2 - The top of plate 2 makes up the plenum that feeds into the inner tubes of the 150 tie tubes. The tops of the tie tube inner tubes would line up with the top surface of the plate. Holes along the sides feed H_2 from a duct system connected to a line from the pump. The red holes seen in Figure 4 represent the through holes for the H_2 from the top shield. The other extrusions with holes are there for hardware to pass through for Injectifold alignment and assembly. The bottom of plate 2 is identical to the top, although the H_2 will flow through the plenum it creates in the opposite direction. When H_2 exits the tie tubes it will move through the bottom plenum into the holes along the bottom outside of the plate. It will then enter a duct system that will run it back to the turbine to power the system.
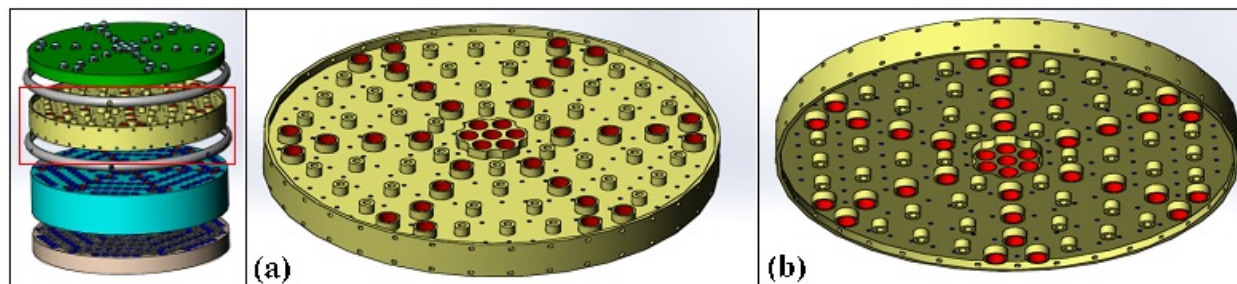
FIGURE 4. Plate 2 Shown Next to the Injectifold Exploded Assembly. (a) The Top Plenum of Plate 2 is for Servicing the Tie Tube Inner Tubes and (b) the Bottom Plenum is for Accepting H2 from the Tie Tube Outer Tubes.

Plate 3 - The function of plate 3 is to ensure that H_2 flow from the top shield to the Injectifold has a uniform velocity profile when it meets the orifice jets to be sent into the reactor core. By having a uniform velocity profile the task of choosing appropriate orifice jets for each fuel element is greatly simplified. The top of plate 3 also acts as the cap for the bottom plenum of plate 2. The top of the outer tubes of the ties tubes would line up with the top surface of plate 3. Two designs were conceptualized, as seen in Figure 5. The red holes represent the 37 through holes from the shield and the blue holes are through holes for the tie tube outer tubes. The first design was inspired by the conical shape of showerheads and was referred to by the team as having a ramp. The second design was a simple flat surface with all 37 through holes opening into a cylindrical plenum.
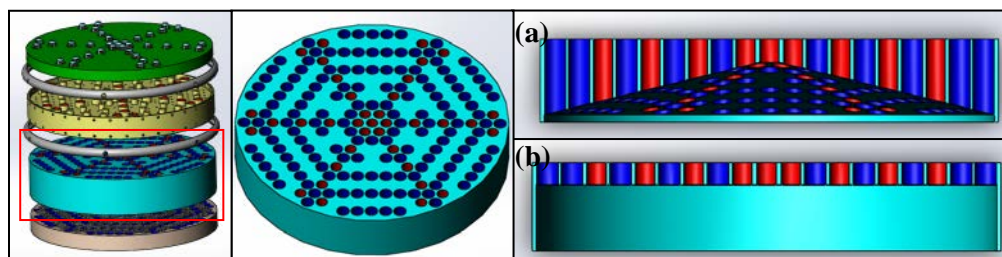
FIGURE 5. Plate 3 with Through Holes for Fuel Element Service in Red and Tie Tube Through Holes in Blue Next to the Exploded Assembly. (a) Ramped Plenum Design Cross-Section. (b) Flat Plane Plenum Design Cross-Section.

Plate 4 - The final plate, plate 4, caps the plenum formed by plate 3. It also has the 151 orifice jets inserted into it. Figure 6 presents plate 3 with the orifice jets inserted and the tie tube through holes to the reactor core shown in blue. A magnified view of an orifice jet cross section is also provided.
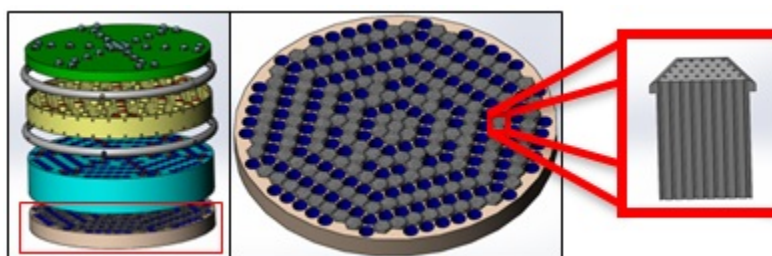
FIGURE 6. Plate 4 with the Orifice Jets for Individual Fuel Element Channel Servicing Installed Shown Next to the Exploded Assembly. A Blowup of a Cross-Section of an Orifice Jet is Outlined in Thick Red.

Since each fuel element in the core has a different power profile, it was suggested that each of the 61 channels on all 151 fuel elements have a custom orifice jet to level out the temperature profile of the reactor. Higher velocity flow would be sent through hotter channels and lower velocity flow through comparably cooler channels. The orifice jets would have to be made from a material, such as tungsten, that could handle sustained contact with the high-temperature fuel elements. Manufacturing these jets would require a high amount of fidelity and a large amount of touch labor due to their lack of uniformity and the accuracy need to line up the jets with the fuel element channels. It will likely prove more practical to have a single custom orifice jet per fuel element with a cavity between the orifice jet and fuel element instead of designing many custom orifice jets directly lined up with each channel. By not having the orifice jets in direct contact with the fuel elements the heat conduction to the Injectifold would be significantly less, reducing the thermal loading on the Injectifold. Figure 7 provides a comparison of the direct contact and individual channel orifice jets versus having a single orifice jet per fuel element and a cavity.
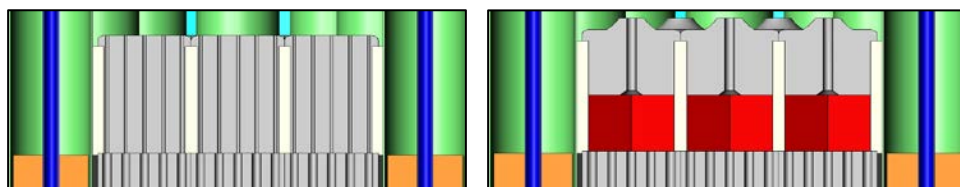
FIGURE 7. A Comparison of Fuel ElemenS Orifice Jets for Each Channel on the Left and Single Orifice Jet for Each Element on the Right.

The plates of the Injectifold are assumed to be manufactured out of an aluminum-beryllium metal matrix composite material. Plates 2 and 3 would be manufactured first. Slotting and through hardware would be used to initially make the two plates concentric and align their complimentary holes. The extrusions for propellant and hardware through holes on plate 2 would be bonded to plate 3 using diffusion welding (DFW). DFW is commonly used throughout the aerospace industry to bond beryllium, zirconium, and titanium, making it an optimal welding process for bonding the two plate's internal features that are in direct contact. Electron beam (EB) welding would then be implemented in attaching the plates along their outer surface.

The fully assembled tie tubes, excluding the ZrC refractory outer shell, would then be inserted and bonded to the two plates. Bonding would be done using brazing with a zirconium-beryllium alloy as the filler metal. The tie tube inner tube would be brazed at the top of plate 2 and the outer tube would be brazed at the bottom of plate 3. All the tie tubes would be installed working from the center of the plates outward.

Plate 4 would be manufactured next and the appropriate orifice jets would be inserted and bonded to the plate using gas tungsten-arc braze welding. Plate 4 would then have to be precision aligned with the plate 2 and 3 assembly and in order to ensure all 150 tie tubes are matched with their appropriate through holes in plate 4. Plate 4 would then be EB welded circumferentially to plate 3, using an appropriate filler metal based on the final material choice for plate 4. The ZrC refractory outer shell would then be slid into place over the tie tube out tubes and DFW would be used to bond the ZrC to plate 4.

Plate 1 would be the final plate manufactured. Slotting and through hole hardware would once again be used to align plate 1 with plate 2. Lastly, the circumference of the two parts bonded at their junction using EB welding. Throughout construction radiographic and ultrasonic testing would be used to check welds for completeness. The final assembly for the Injectifold can be seen in Figure 8.
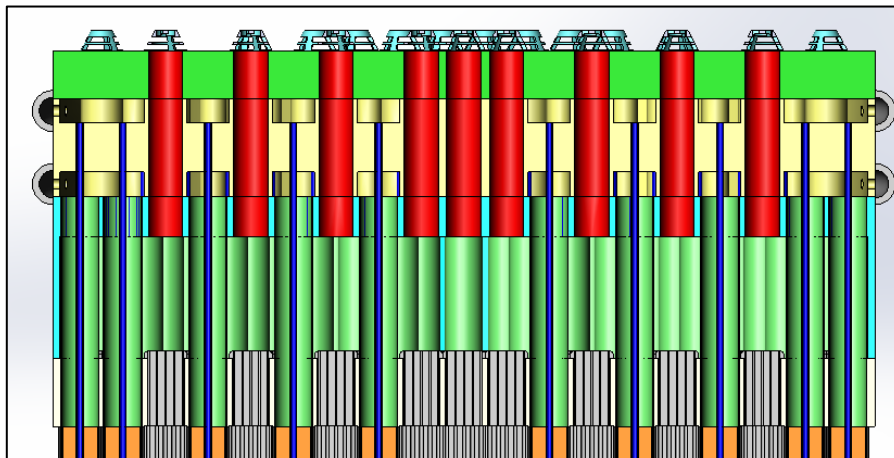
FIGURE 8. Fully Assembled Injectifold with Tie Tubes, Orifice Jets, and Fuel Elements.

COMPUTATIONAL FLUID DYNAMICS ANALYSIS

Once the design for the Injectifold was finalized, a computational fluid dynamics (CFD) analysis was carried out using COMSOL Multiphysics. COMSOL is a powerful CFD tool that was used to generate a theoretical data set that may be seen under expected flow conditions. Since COMSOL models the pathways seen by the fluid using user inputs and fluid boundary conditions, the important shape to model is the cavity that is filled by the propellant during engine operation. Thus, a negative of the model was loaded into COMSOL for plenums 1, 2, and 3 identified as Simulation 1, 2, and 3 respectively. Figure 9 illustrates each simulation cavity within the Injectifold. Symmetry was used in order to model each cavity in terms of a symmetric slice.
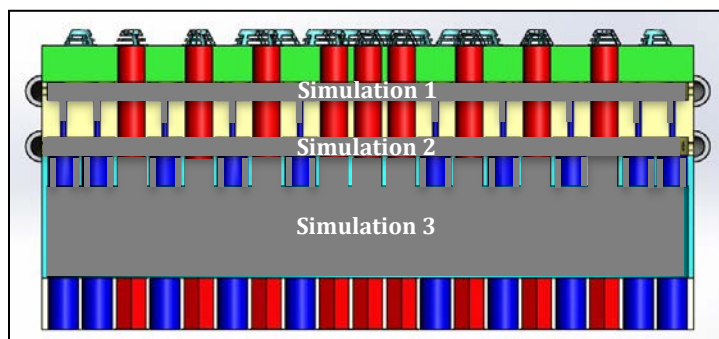
FIGURE 9. Cross-Sectional View of Injectifold with Simulation Cavities Marked.

Simulation 1 was modeled as a $1/12^{th}$ slice of the first plenum with its exit outlets being the inlets to the tie tubes, as seen in Figure 10 (a). As expected, Simulation 1 had the highest pressure and the highest streamline velocities occurring at the plenum inlets on the side of the cavity, approximately 5.0 MPa and 70 m/s respectively. The propellant slowed down to about 10 m/s and distributed as it went into the cavity, then sped back up to 70 m/s as it entered the tie tubes. The pressure of the propellant dropped by about 2.5 MPa as it moved from the plenum inlets to the tie tube inlets.

Simulation 2 was modeled as a $1/12^{th}$ slice of the second plenum so that the inlet of the plenum was the exit of the tie tubes, as seen in Figure 10 (b). Overall, the pressure gradient and the velocity gradient were very similar to that of the first plenum. The velocity varied from 70 m/s at the inlets and outlets of the plenum to 10 m/s inside the plenum, and the pressure dropped from 7.5 MPa at the inlets to about 5.0 MPa leaving the plenum.

Simulation 3 was modeled as a $1/6^{th}$ slice of the H_2 propellant passageways and plenum of plate 3. There are two versions of this simulation, one with a "ramp" that serves as a way for the H_2 to diffuse and allow for mixing before it continues through the next plate to the reactor, as seen in Figure 10 (c). The other, seen in Figure 10 (d), is Simulation 3 without this ramp, so that it is just a cylindrical cavity. Both simulations were run in COMSOL to see which had more desirable fluid flow properties allowing for the better diffusion. In both the ramp and no-ramp simulations the pressure loss was only a few hundred pascals, which is insignificant when compared to the 6.93 MPa inlet pressure. The two versions of Simulation 3 primarily differed when it came to the distribution of the stream velocities at their outlets. Having an even velocity distribution for the outlets of plate 3 is particularly important since plate 3 acts as the injector for the fuel rods of the nuclear reactor. From the simulation it was seen that the ramp simulation had a significantly higher velocity gradient, ranging from 0 m/s to 200 m/s, than the no-ramp simulation, ranging from 10 m/s to 150 m/s. Since pressure loss was negligible and streamline velocity distribution was less severe without the ramp, it was concluded that Simulation 3 without the ramp would be chosen as the test article for a cold flow test.

It should be noted, however, that the simulation for plate 3 was not completely accurate since the outlets were modeled as singular large holes rather than the many smaller holes that would be seen with the orifice jets. This modeling choice was made because COMSOL was not able to handle a simulation with so many small outlets. As a result, much of the flow that came through the inlets went directly through the large outlet holes right below them, starving the outlets that were not directly below the inlet holes. If the outlets were modeled as groups of small holes rather than one large hole, the gas would not all go straight through the outlets directly below the inlets, bouncing

off the material between the small holes, and resulting in better diffusion. Therefore, the results that should be seen in flow testing should be similar to the results seen in the CFD analysis, but with not as severe of a velocity differential.
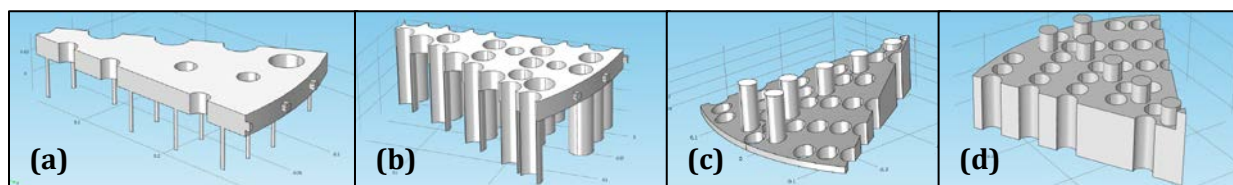
FIGURE 10. Cavities for (a) Sim 1 (b) Sim 2 (c) Sim 3 With Ramp and (d) Sim 3 Without Ramp.

COLD FLOW TESTING

Due to time constraints, a cold flow test was only able to be performed with one plate of the Injectifold. Plate 3 was chosen for testing since it has the vital purpose of feeding propellant into the reactor core and an uneven flow distribution could result in a catastrophic failure of fuel elements. After the COMSOL analysis, it was determined that the no ramp model of plate 3 had a more desirable flow distribution and so the no ramp model was used for testing. A test of plate 3 was devised that could be performed in a couple of weeks and would function as a verification of the COMSOL data, as opposed to a full scale cold flow test. The main objective of the test was to discover if any of the fuel channels being fed by plate 3 of the Injectifold would be starved of propellant while the reactor was operating. In order to achieve this, 3D printing was used to create the test article and off-the-shelf components were used to design the system.

The test article was designed to best replicate the conditions that would likely be present during reactor operations. While it would have been ideal to create a full size model of the Injectifold with flight-like geometry and operating conditions, concessions had to be made due to the budget, the materials, and the current limits of 3D printing technology available. First, nitrogen was chosen as the working fluid instead of H_2 due to the safety issues involved in working with H_2. Eventually H_2 will be used in testing, but because this was only a basic first test, it would be unnecessary and dangerous to waste H_2 when nitrogen is more readily available.

Once the working fluid was agreed upon, it was decided that the two best options for a geometric model would be either a full scale slice of the third plate, or a half scale full plate, due to the maximum size of the 3D printer available. It was decided that a full scale, sliced version of the Injectifold was the best for testing. A few accommodations were made to make the slice easier and safer to test, such as increasing the amount of material in some places and creating interfaces to connect the test article to the rest of the system. Additionally, the 61 holes exiting the Injectifold into each fuel rod were too small for the printer to handle, so they were reconfigured into 7 larger, evenly spaced holes with the same flow area that would be funneled into an outlet plenum. Finally, special features were added to the model so that the polycarbonate sidewalls could be attached, as well as mounting brackets so the test article could be fixed to the test stand. The finalized design for the test article can be seen in Figure 11.
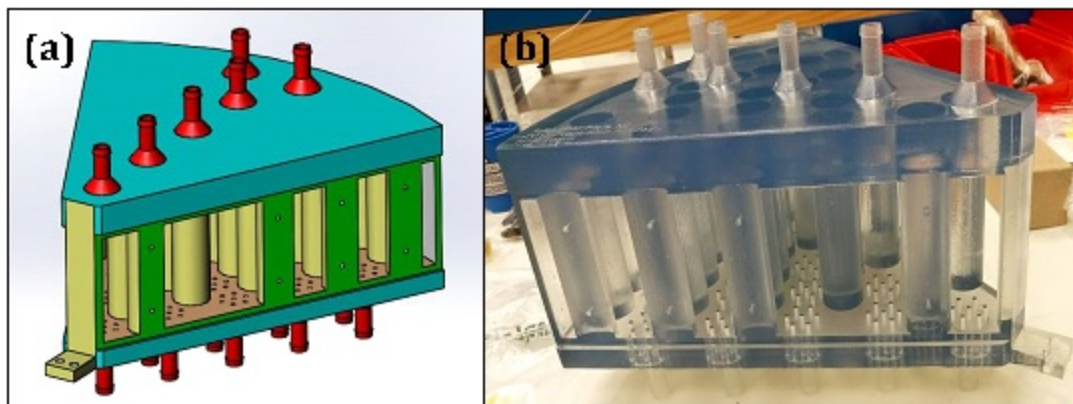
FIGURE 11. (a) SolidWorks Test Article and (b) 3D Printed Test Article.

While finalizing the design of the test article, a test stand was simultaneously being designed to support the required testing. The test stand contained a series of 10 "floating ball" type flow meters in parallel, which could be attached by tubing to any of the test article outlets. The resulting flow measured by the flow meters could then be recorded by hand. The system would use a site nitrogen hookup as an inlet and would exhaust to a fume hood, both located in the lab. High pressure, flexible tubing was chosen to connect all of the components due to its ease of use.

Initiating flow to the test stand was achieved successfully, however, the flow rate from the site nitrogen hookup was insufficient to cause a readable deflection on the flow meters attached to the test stand. After discussing several possible fixes to this problem, it was decided that the best way to proceed was to adopt a new measuring system using a hot wire anemometer to take a reading on each individual outlet as flow was passed through the Injectifold. This would give a precise reading of the velocity of nitrogen from each Injectifold outlet, which could later be converted to volumetric flow rate or used as a basis of direct comparison. Using the anemometer, each outlet was sampled 10 times to mitigate the data being affected by transients and erroneous readings, which was then compiled into Table 1 and analyzed. The data was organized according to the layout seen in Figure 12.
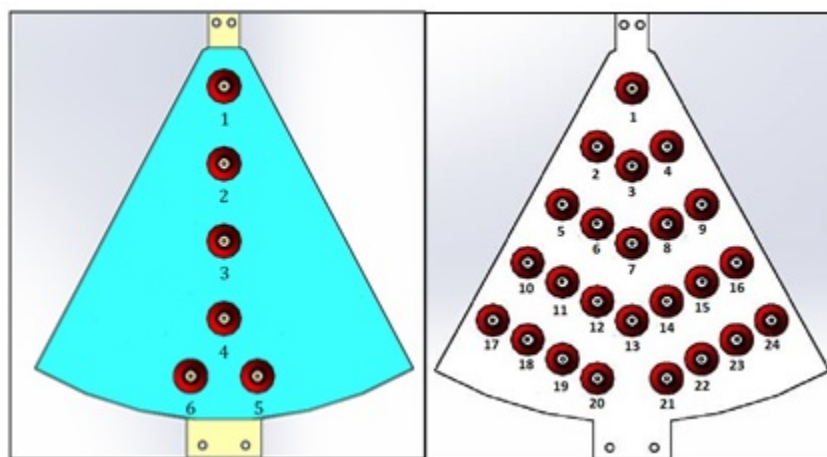
FIGURE 12. Numbering System Used to Track Data for the Injectifold (a) Inlets and (b) Outlets.

TABLE 1. Injectifold Outlet Test Data.

Outlet Number	Average (m^3/s)	Standard Deviation	Percent of Total Flow	Deviation from Total Average Flow
1	2.85	14.13%	4.37%	4.80%
2	2.77	13.00%	4.24%	1.64%
3	2.76	8.97%	4.22%	1.20%
4	2.50	9.08%	3.82%	-8.27%

5	2.74	10.93%	4.19%	0.50%
6	2.89	8.66%	4.43%	6.23%
7	3.09	16.09%	4.72%	13.39%
8	2.84	14.24%	4.35%	4.32%
9	2.68	6.47%	4.09%	-1.74%
10	2.51	12.48%	3.83%	-7.98%
11	2.77	11.32%	4.24%	1.86%
12	2.68	14.59%	4.10%	-1.62%
13	2.62	17.40%	4.01%	-3.68%
14	2.69	18.02%	4.11%	-1.40%
15	2.55	8.94%	3.90%	-6.29%
16	2.73	7.43%	4.17%	0.10%
17	2.80	11.97%	4.28%	2.74%
18	2.50	10.98%	3.82%	-8.27%
19	2.84	11.71%	4.34%	4.25%
20	2.83	12.29%	4.34%	4.07%
21	2.63	13.88%	4.03%	-3.35%
22	2.65	6.89%	4.05%	-2.69%
23	2.59	7.19%	3.97%	-4.82%
24	2.86	11.56%	4.37%	4.98%
Total	**65.36**			

Directly under inlet	Total Average Flow (m³/s) — 2.72
Adjacent to inlet	Average Standard Deviation — 11.59%
2 Away from inlet	Total Average Flow (m³/s) per Outlet — 2.72325
3 Away from inlet	

From Table 1, the "average" column displays the average volumetric flow rate for each outlet after 10 tests. The "standard deviation" column displays the standard deviation of the 10 trials for each outlet. The "percent of total flow" column displays the percent of the total flow through the Injectifold that went to each outlet. The "deviation from total average flow" column displays the percent deviation of each outlet from a perfectly even flow distribution. Total average flow was calculated as total volumetric flow divided by 24, the number of outlets. Although the testing that was performed accumulated valuable results, it is pertinent to mention that two small design flaws were discovered during data review that, though easily fixed, caused a small amount of inaccuracy with the gathered data. The first of these was already mentioned, the original test plan involved using "floating ball" type flow meters to determine the amount of flow through each channel. Switching to the anemometer allowed for velocity data acquisition, but due to the very high sensitivity of the device, it was noticed that it was also picking up other flow velocities in the test area, such as the fume hood exhaust system. This issue will be fixed in the next round of testing by replacing the current flow meters with ones that read lower flow rates. The second flaw occurred when it was noticed that Outlet Channel 7 seemed to consistently have much higher flow rates than the other channels. With a little investigation, the cause stemmed from the fact that Inlet Channel 3 (directly above Outlet Channel 7) was directly in line with the inlet tube from the site nitrogen connection, which created an unrestricted flow region, greatly increasing the nitrogen flow to the outlet channels fed by Inlet Channel 3, shown in Figure 13.
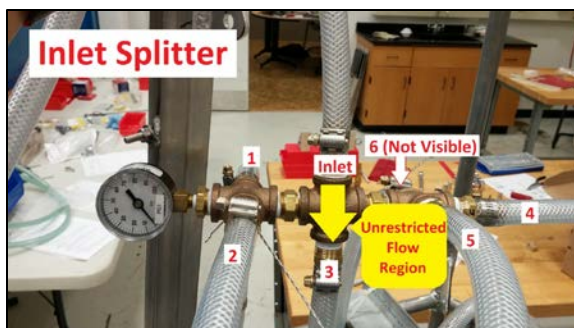
FIGURE 13. The Inlet is Located Directly Across from Inlet Channel 3, Creating an Unrestricted Flow Region.

Once the oversight had been found, the Inlet Splitter was detached from the system and tested to see exactly how much extra flow Inlet Channel 3 was receiving. As seen in Figure 14 (a), Inlet Channel 3 was seeing almost half of the total inlet flow to the test article, which is a huge difference when compared to the meager amount the other flow paths are sharing. Again, the solution to this issue is simple, as a simple reconfiguration of the Inlet Splitter to swap the Pressure Gauge and Inlet Channel 3 should cause the flow coming in to the Inlet Splitter to diffuse more evenly to all of the pathways. However, this mishap actually worked as a proof of concept for the Injectifold design. Even with massively uneven inlet flow to the test article, the design of the Injectifold was able to effectively redistribute the flow and put out relatively even outlet velocities. As seen in Figure 14 (b), a visual representation of the outlet data, any deviation from a perfectly even flow distribution was relatively minimal. The test was viewed as a success because it verified that all of the channels were getting roughly even flow rates and there is no evidence of any excessive fuel channel starvation. There were a few issues with the design of the test stand, but these issues can be easily rectified if more cold flow testing is desired. The next logical steps would be to run a cold flow test similar to this one for plates 1 and 2 of the Injectifold design, and then move forward to creating a combined, full scale model of the Injectifold with a more robust material, such as aluminum, so that cold flow testing with He_2 and then H_2 can be pursued, before eventually running a simulated hot fire of the device.
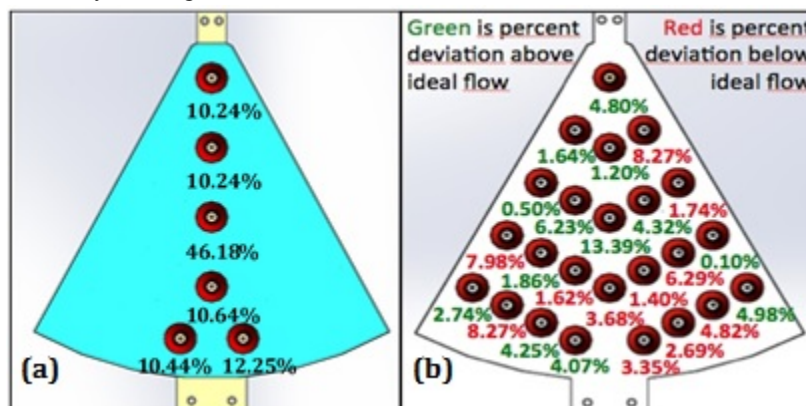
FIGURE 14. This is a Visual Breakdown of (a) the Total flow to each Injectifold Inlet and (b) the Deviation from total average Results Through the Outlets, Depicting the Unusually High Flow Going to Outlet Channel 7.

CONCLUSION

With its pedigree stretching back to the Apollo program, the NTP engine is still a viable technology as an option for deep space exploration. At the component level, many parts from the Rover/NERVA project need to be revisited and redesigned to increase their functionality. The Injectifold is one such component, and after completing a full design iteration, it can be seen that the design tested by the team shows promising results. Using a plate-type, modular design will allow for ease of manufacturability while still maintaining the plenums to direct the flow of H_2 to

support reactor operations. Running the design variants through COMSOL CFD analysis validated the functionality of the Injectifold for its intended purpose, with the "no ramp" version showing better performance than its ramped counterpart. Cold flow testing of the injectifold allowed for a limited view of what more realistic conditions would look like in the third stage of the injectifold and confirmed the CFD analysis that no fuel channels would be starved of propellant flow. All in all, the research and development of the Injectifold was met with an encouraging amount of success, but there is still a great deal of improvement to be done, especially in the area of testing. Unfortunately, time limitations came in to play once the team reached the point that they were ready to test, so only a limited amount of testing on the third stage was able to be performed. Continuing on, further testing needs to be performed on the third stage in addition to the first and second stages in order to fully ascertain the flow performance of the Injectifold.

ACKNOWLEDGMENTS

REFERENCES

[1] "Nuclear Thermal Rocket Propulsion," Space Propulsion & Mission Analysis Office, National Aeronautics and Space Administration, Glenn Research Center. URL: http://trajectory.grc.nasa.gov/projects/ntp/index.shtml, July 2008, Accessed August 4, 2015.

[2] Finseth, J. L., "ROVER Nuclear Rocket Engine Program: Overview of ROVER Engine Tests Final Report," Sverdrup Technology Inc., Huntsville, Alabama, February 1991, Accessed August 4, 2015.

Aluminum-Beryllium Composite Trade Study for Space Nuclear Applications

Robert Hetterich[1], Travis Belcher[2], Matthew Reilly[3], Tyler Scogin[3], and Joaquin Santecchia[4]

[1]Lehigh University, Bethlehem, PA 18015
(516)361-7813; rjh216@lehigh.edu
[2]University of Texas at El Paso, El Paso, TX 79968
[3]Georgia Institute of Technology, Atlanta, GA 30332
[4]Arizona State University, Tempe, AZ 85287

Abstract. With the current drive towards deep space exploration, NASA is investigating nuclear systems as a possible in-space propulsion system for missions beyond low earth orbit. Development of nuclear propulsion is creating a growing need to design engine components made of light-weight materials that still have desirable nuclear properties, such as aluminum-beryllium composites. In traditional aerospace applications aluminum-beryllium composites were used for their light-weight and stiffness, ignoring their nuclear properties. Unfortunately, the major drawback to beryllium is a health hazard due to inhalation of beryllium dust during machining and handling operations known as beryllium poisoning. This deficiency along with the lack of need for light, stiff components in conventional nuclear applications is the main reason that beryllium has seen little development in nuclear and aerospace systems. However, beryllium's light-weight and excellent ability to reflect neutrons combined with the strength and stiffness of aluminum makes aluminum-beryllium composites optimal to use in space-based nuclear applications. In this report a specific example of an aluminum-beryllium composite, AlBeMet® by Materion, was evaluated based on its physical properties for both nuclear and aerospace requirements. The potential advantages and disadvantages of aluminum-beryllium composites are discussed in the context of developing a component for NASA's Nuclear Thermal Propulsion (NTP) engine called an Injectifold. The Injectifold is a combined injector-manifold which directs hydrogen coolant/propellant to different locations in the reactor core while also acting as a neutron reflector. It is recommended that more detailed studies be performed to fully evaluate AlBeMet's® physical properties and viability for space nuclear systems.

Keywords: Aluminum-Beryllium Composite, Injectifold, Nuclear Thermal Propulsion, AlBeMet®

INTRODUCTION

AlBeMet® is the trade name for a metal matrix composite of aluminum and beryllium with very unique properties that make it advantageous to use in space and rocketry applications. Originally conceived by Lockheed in 1963 under their trade name of "Lockalloy," it was used in many aerospace applications for its high strength, high stiffness, and low weight [1]. Unfortunately, the process of creating the material subjects the manufacturing personnel to a condition called beryllium poisoning, which can be fatal. Coupled with the advent of aluminum alloys that are lighter, stiffer, and stronger, Lockalloy was mostly phased out of use in the late 1970's. In recent years, however, an aluminum-beryllium composite was developed by a company called Materion where it received the trade name AlBeMet® (Aluminum-Beryllium Metal). AlBeMet® has helped bring about a resurgence in use of aluminum-beryllium composites due to some of its other attractive properties, such as its good thermal conductivity. Since the majority of its composition is beryllium, a known neutron moderator, it has been hypothesized that AlBeMet® could be used as an effective moderator in a fission reactor. NASA is currently working on a Nuclear Thermal Propulsion (NTP) rocket engine, attempting to revive the heritage Rover/NERVA project. If feasible, a material such as AlBeMet® would be

a huge boon to this project, allowing for the structure of aluminum and the nuclear properties of beryllium in a very lightweight material. The focus of this report is to explore the material properties of AlBeMet® and further discuss its applications in the context of the NTP program.

ALBEMET® MATERIAL PROPERTIES

Physical Properties

AlBeMet® is able to tout such claims as having a much higher stiffness than aluminum at a fraction of the weight due to its unique physical structure. As opposed to the beryllium molecules being a part of the metal lattice, they actually sit inside of the lattice formed by the aluminum, stiffening the lattice, but adding very little additional weight due to their low atomic mass. To illuminate this, Table 1 below shows the difference in physical properties between AlBeMet® and two comparable aluminum alloys, 2024T6 and 6061T6.

TABLE 1. Physical Properties of AlBeMet® Alloy Compared to Common Aluminum Alloys [2].

Physical Properties of AlBeMet® Alloys Compared to Common Aluminum Alloys	2024T6	6061T6	AM162
Density g/cm^3 (Lbs/in^3)	2.77 (0.100)	2.70 (0.100)	2.10 (0.076)
Modulus GPa (Msi)	72 (10.5)	70 (10.0)	193 (28)
Poisson's Ratio	0.33	0.33	0.17
CTE @ 25°C ppm/°C (ppm/°F)	22.9 (12.7)	23.6 (13.1)	13.9 (7.7)
Thermal Conductivity @ W/m°K (BTU/hr Ft° F)	151 (87)	180 (104)	210 (121)
Specific Heat @ 20°C J/Kg°K (BTU/lb °F)	875 (0.209)	896 (0.214)	1465 (0.35)
Electrical Conductivity @ 20°C, % IACS	30	43	49
Damping Capacity 25°C, 500 HZ	1.05x10^{-2}	1.05x10^{-2}	1.5x10^{-3}
Fracture Toughness K$_{Ic}$ Ksi √in (MPa √m)	23 (25)	23 (25)	10-21 (11-23)

Some other physical properties worth mentioning are AlBeMet's® coefficient of thermal expansion (CTE), thermal conductivity, and specific heat capacity. These are the properties that currently make it useful as a material for electrical components, such as heat sinks, where the material needs to be able to absorb and dissipate a lot of heat, but not expand under the heat load to avoid damaging the circuitry around it. In the context of a space nuclear engine, these are very useful properties due to the high heat and energy output of a nuclear reactor.

Nuclear Properties

There has not been testing performed for the specific nuclear role that the Injectifold is intended to perform within the reactor core, but there is a great deal of evidence to support the idea that it should perform as an effective moderator. It has been proven that beryllium is a good neutron reflector due to its relatively low cross-section for neutron absorption, as well as its ability to moderate neutrons [3]. The combination of these attractive nuclear properties and its very low weight make it an ideal material to use for space nuclear applications, and it is currently being considered for a wide variety of components for the NTP project. Since AlBeMet® is a composite as opposed to an alloy, it can be inferred that it will retain the traits of its parent metals, if at somewhat of a reduced capacity. Therefore, AlBeMet® should be able to act as a neutron moderator and reflector, even if it's not at the same level as pure beryllium.

While no research has been done to test AlBeMet's® ability to moderate and reflect neutrons, some testing has been performed to ascertain AlBeMet's® ability to stand up to extreme radiation environments for potential use in Next Generation Nuclear Reactors. From a paper written by researchers conducting tests on composite materials at Brookhaven National Laboratory, "Post-irradiation studies revealed that AlBeMet® is dimensionally stable following irradiation and that it resists embrittlement and degradation even at high proton fluences where materials such as graphite and carbon composites have been shown to undergo serious degradation" [4]. The paper goes on in detail

about how AlBeMet's® ultimate tensile strength actually increases following irradiation, which is common in most metals, but displays no loss in ductility which typically accompanies that increase in strength.

Manufacturing

AlBeMet® is available as raw material for machining in three different ways, based on what sort of shape is needed for the application. These three raw materials are Hot Isostatic Press Billet (HIP'd Billet), Extruded Bar, and Rolled Sheet. The comparison of the material properties of these different raw materials can be seen below in Table 2. AlBeMet® machines very easily, like aluminum, but the beryllium dust that gets into the air during machining can result in a dangerous condition known as beryllium poisoning if it is breathed in. The effects of beryllium poisoning can take anywhere from months to years to emerge in an individual. Some possible effects of beryllium poisoning are cancers, lesions in the lungs, immunological effects, skin allergies, irritation in the lungs, or many other types of lung issues. The danger of beryllium poisoning often differs between individuals and depends on many factors such as length of exposure, frequency of exposure, or type of exposure. Due to the danger of beryllium poisoning during machining, beryllium, beryllium alloys, and beryllium composites are generally only machined to create relatively small objects and must be machined in special facilitities [5].

Additionally, it is possible to form an aluminum-beryllium composite using an investment casting technique known as AlBeCast, however this process is still being developed and not available for widespread use at the time of the writing of this report. For the research into a material to use in the Injectifold, HIP'd Billet and AlBeCast were looked at, as they appeared to be the easiest way to create the Injectifold, however, it should be noted that there has never been a component as large as the proposed Injectifold created using AlBeMet® or AlBeCast, so at this point it would be purely conjecture as to the best way to create the components.

TABLE 2. Comparison of AlBeMet® 162 Varieties [2].

Property	HIP'd Billet	Extruded Bar	Rolled Sheet
Composition	Al-62 wt% Be	Al-62 wt% Be	Al-62 wt% Be
Density g/cm^3 (lb/in^3)	2.071 (0.0748)	2.071 (0.0748)	2.071 (0.0748)
Yield Strength MPa (Ksi)	193 (28)	276 (40)	276 (40)
Ultimate Strength MPa (Ksi)	262 (38)	400 (58)	386 (56)
Elongation %	2	7	5
Modulus GPa (Msi)	193 (28)	193 (28)	193 (28)
Thermal Conductivity at 25°C W/m·K (Btu/hr-ft-°F)	210 (121)	210 (121)	210 (121)
Coefficient of Thermal Expansion at 25°C ppm/°C (ppm/°F)	13.91 (7.73)	13.91 (7.73)	13.91 (7.73)

Additive manufacturing of aluminum-beryllium composites is another manufacturing method to consider, although aluminum-beryllium composites that can be additively manufactured is something that is still deep in development. AlBeMet® can be atomized to a powder of 100 mesh or less than 149 microns, which is within the optimal size range for powder metallurgy (PM) [6]. The powder could be cold isostatically pressed into a green form and then heat-treated at 593°C for 24 hours, so that the particles sinter together. PM has the advantage of producing a near net part.

Producing the plates from selective laser melting (SLM) would require finer powder grades. A layer of powder as thin as 20 microns can be deposited when building up a model [7]. Currently, there are no manufactures that produce such a powder, though with modifications to Materion's gas atomization process for producing AlBeMet® it might be possible for them to generate it. Given the benefits of SLM and the current infrastructure at NASA it could be advantageous to approach Materion about making that a reality. This being said, there has been no studies on the material properties of 3D printed aluminum-beryllium composites since it has not yet been done.

INJECTIFOLD MATERIAL SEARCH

Material Requirements

The need for a material first arose while working on developing a component for the NTP engine called an Injectifold, which is a combined injector/manifold that will sit atop the reactor core and direct propellant to different areas of the system to perform various tasks, such as cooling and injecting propellant. The proposed four plate design for the Injectifold can be seen in Figure 1.
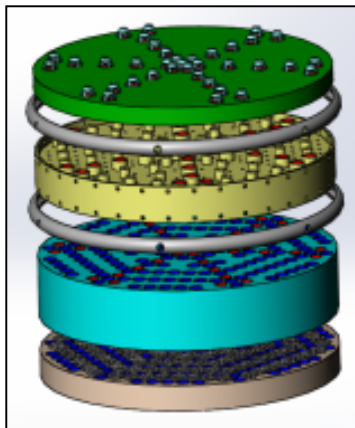
FIGURE 1. Exploded View of the Injectifold Design for an NTP Engine.

After coming up with a design for the Injectifold, an extensive materials analysis was carried out with the goal of specifying candidate materials for the Injectifold based on necessary material conditions. The Injectifold will be operating in a H_2 rich environment near a nuclear reactor, experiencing pressures estimated to range from 11.93 MPa to 6.93 MPa and temperatures estimated to range from 31.7 K to 291 K during steady state operation. Based on these operating conditions, four primary material requirements were specified for the Injectifold:

1.) *The material cannot be susceptible to significant H_2 embrittlement*
    H_2 embrittlement is the phenomena of small H_2 atoms entering the crystal lattice structure of a metal, causing it to embrittle and weakening its mechanical properties. This material requirement is important because the Injectifold will be operating in a pure H_2 environment and can fail due to embrittlement.

2.) *The material cannot be susceptible to significant radiation embrittlement*
    Radiation embrittlement is the phenomena of materials becoming embrittled due to bombardment by neutrons and other types of radiation. This material requirement is important because the Injectifold will be operating directly above a reactor emitting large amounts of radiation, but below the radiation shield so it will deal with a large influx of radiation and can easily fail due to embrittlement.

3.) *The material has to have strong enough mechanical properties to operate under the engine conditions*
    The Injectifold is a vital component of the NTP engine, directing important flows of propellant and coolant throughout the engine, so it is important that the Injectifold does not fail under any conditions.

4.) *The material has to be able to act as a moderator*
    Moderators are an essential component to any type of nuclear reactor. As neutrons are propelled out of the reactor after a nuclear fission reaction, a certain percentage need to be slowed down and reflected back into the reactor in order to fission more uranium and keep the fission process going. Moderators are materials that have atoms similar to the size of a neutron that can effectively bounce the neutrons and reflect them back into the reactor. Although an absence of this property will not cause a failure, it was listed as a material requirement because it would significantly reduce the complexity of the engine and provide weight savings by not needing a separate reflector.

Potential Materials

With these four primary requirements in mind, several commonly used reactor and aerospace materials were selected and analyzed to see how they would hold up to the Injectifold material requirements:

Austenitic Stainless Steels*:* Austenitic stainless steels are not susceptible to H_2 embrittlement (other types of steel are susceptible to H_2 embrittlement) and are not significantly embrittled by radiation under the projected operating conditions [9]. They also have strong enough mechanical properties for the engine's projected operating conditions, but they are not a good moderator and therefore are not an ideal material to use for the Injectifold.

Aluminum 2219*:* Like austenitic stainless steels, aluminum in general is not susceptible to significant H_2 or radiation embrittlement. It is not as strong as stainless steel, but is lighter in weight and still has sufficient properties for the NTP engine's operating conditions [9]. However, like austenitic stainless steel, aluminum has a low neutron scattering cross-section, making it a poor moderator and a poor choice of material for the Injectifold.

Zircaloy–4*:* Zircaloy–4 is not susceptible to significant radiation embrittlement, but is susceptible to significant H_2 embrittlement, according to an interview with Jonathan Lee from the Materials and Processes Laboratory at NASA-Marshall Space Flight Center. In addition to this, it is not a good moderator so it would be a very poor material choice.

Beryllium Copper*:* Beryllium copper is not susceptible to H_2 embrittlement, is not susceptible to significant neutron embrittlement, and has strong enough mechanical properties for the operating conditions of the engine [10]. Beryllium makes for a very good moderator, but unfortunately most beryllium coppers only have a small amount of beryllium (1-4% beryllium, 96-99% copper) so it would not be an effective moderator and should not be used for the Injectifold. This same issue of low beryllium content comes up with other types of alloys with beryllium.

AlBeMet® 162*:* As described previously, AlBeMet® 162 is an aluminum–beryllium metal matrix composite and is not susceptible to H_2 embrittlement, not susceptible to significant neutron embrittlement, has strong enough mechanical properties for the engine operating conditions, and can be used as an effective moderator due to its high beryllium content (62% beryllium, 38% aluminum) [11,12]. These properties are not unique to just AlBeMet®, as other similar aluminum–beryllium composites met the material requirements as well. However, other advantages/disadvantages in reference to the Injectifold were further investigated for only AlBeMet® 162. Although this study focused on specifically AlBeMet® 162, since the majority of the research that was found pertained to AlBeMet® 162, this analysis can be applied to aluminum-beryllium composites with a high percentage of beryllium in general as most of them have very similar properties. For example, another viable aluminum-beryllium composite is Beralcast® by IBC Advanced Alloys, which has similar properties to AlBeMet®. AlBeMet® 140 (40% beryllium, 60% aluminum) was also looked at, but AlBeMet® 162 was further investigated since it would be a more effective moderator due to its higher beryllium content. The entire material property analysis is summarized in Table 3.

TABLE 3. Summary of Primary Requirement Analysis [8-12].

	Hydrogen Embrittlement	Neutron Embrittlement	Act as a Moderator	Mechanical Properties
Aluminum 2219	✓	✓	✗	✓
Stainless Steel	✓	✓	✗	✓
Beryllium Copper	✓	✓	✗	✓
Zircaloy – 4	✗	✓	✗	✓
AlBeMet® 162	✓	✓	✓	✓

ALUMINUM-BERYLLIUM COMPOSITES IN CONTEXT OF INJECTIFOLD

After seeing that AlBeMet® 162 was the only material which met all of the necessary material requirements for the Injectifold, the properties of aluminum-beryllium composites were investigated in more detail as they pertained to the functioning of the Injectifold component. In addition to meeting all of the material requirements, aluminum-beryllium composites offer several advantages:

1. Aluminum-beryllium composites with a large percentage of beryllium are **very light** due to the low density of the beryllium, which saves mass for the rocket engine. Saving mass means more payload or more leeway with other engine components.

2. Aluminum-beryllium composites are also **very stiff,** so that the Injectifold doesn't bend and misalign. This is important because the Injectifold is made up of several plates aligned together.

3. High thermal conductivity, high specific heat capacity, and high melting point provide **favorable thermal properties**. The Injectifold can act as a heat sink for some of the other components, which would be cooled by its large surface area exposed to the H_2 [12]. In addition to acting as a heat sink, a low coefficient of thermal expansion means that there will not be significant misaligning between Injectifold plates.

Aluminum-beryllium composites have many advantages and seem to be a great material for the application of the Injectifold, however, like any material, there are also some disadvantages of using aluminum-beryllium composites for the Injectifold:

1. Due to danger of beryllium poisoning, aluminum-beryllium composites **can only be manufactured and machined in special facilities** outside of NASA. Since the Injectifold is a relatively complicated component, this will make production of the Injectifold take much longer and be more expensive [13].

2. The material itself is also **expensive**, with AlBeMet® costing about three times the price of titanium (although an exact price was not given).

3. Aluminum-beryllium composites **have not been used for creating anything as large as the Injectifold**. They are currently used for small electronics and raw materials are not currently offered in the sizes needed to machine the plates of the Injectifold [12].

All of the main advantages and disadvantages of AlBeMet® 162 in respect to the Injectifold component can be seen summarized in Table 4.

TABLE 4. Summary of AlBeMet® 162 Advantages and Disadvantages as they Pertain to the Injectifold [12].

AlBeMet® 162 Advantages for Injectifold		
Density	2.10 g/cm^3	Light
Modulus of Elasticity	193 GPa	Stiff
Yield Strength	276 MPa	Strong enough
Melting Point	666°C – 1180°C	Wont melt and can act as a heat sink
Chemical Makeup	62% Be, 38% Al	Moderator
AlBeMet® 162 Disadvantages for Injectifold		
Manufacturing	Special facility	Complicated
Cost	3X cost of Titanium	Expensive
Availability	Only available in small size	Not very available

Based on the disadvantages it would seem that it is not practical, or possible, to use an aluminum-beryllium composite for a complicated part the size of an Injectifold, but some of these problems can be overcome by casting the part rather than machining it. Although aluminum-beryllium composites have been around for many years, a recent development has been forming these composites with an investment cast and then doing small amounts of machining on the cast, two examples being AlBeCast® and Beralcast®, as previously mentioned. Casting each plate of the Injectifold would immediately solve disadvantage #3 because in this case a piece of raw material the size of an Injectifold plate would not be needed. The maximum cast size for Beralcast®, for example, is 0.75 meters wide by 0.85 meters high, which exceeds the size of any single plate in the Injectifold [14]. Casting the part would also significantly reduce the magnitude of disadvantage #1 because it would severely limit the amount of machining necessary on the part and greatly speed up the production process. This being said, casting of aluminum-beryllium composites is still a new process and is still being tested.

When considering casting the part, rather than pure machining, the disadvantages are reduced down to the small amount of machining necessary and the cost of the material/casting, which are outweighed by the advantages of aluminum-beryllium composites. Making the Injectifold out of an aluminum-beryllium composite saves space, decreases complexity, and reduces weight because a separate reflector is no longer needed and because aluminum-beryllium composites are very light compared to other standard metals used in injectors and manifolds. Reducing weight, complexity, and size of the engine can allow for a greater payload or provide leeway for other engine components, which is a huge benefit compared to the cost of the material or casting.

CONCLUSION

Aluminum-beryllium composites are unique materials with favorable properties that make them very useful for space-based nuclear applications and this report looked at one example, AlBeMet® 162, in detail. Not only are aluminum beryllium composites mechanically strong with favorable thermal properties, but they can also act as effective moderators for nuclear reactors. The four most important material requirements for the Injectifold material are that it cannot be susceptible to H_2 embrittlement, it cannot be susceptible to radiation embrittlement, it has to have mechanical properties strong enough for engine operating conditions, and it has to be able to act as a moderator. Of the materials looked at, the only materials that met all of these requirements were aluminum-beryllium composites. In the context of the Injectifold, it was found that aluminum-beryllium composites have several significant advantages and a few major disadvantages, but using an investment cast with the material rather than trying to create the Injectifold using pure machining can mostly cancel out these disadvantages.

In conclusion, it is recommended that investment casted aluminum-beryllium composites be seriously considered as a possible material for the Injectifold of the NTP engine. This being said, further research should be done into the testing, costs, etc. of investment casting aluminum-beryllium composites. IBC Advanced Alloys claims that the properties of Beralcast®, an investment casted aluminum beryllium composite, are almost the same as AlBeMet® 162, but more research should be done into this claim and the properties of the material when used for a larger part [15]. Some areas of future work in materials for the Injectifold are:

1. Investigate soft good materials used to mechanically align the plates.
2. Thermal analysis of an Injectifold made out of aluminum-beryllium composite in COMSOL or another multi-physics platform.
3. Conduct a more in depth cost and weight comparison analysis of using aluminum-beryllium composites vs. other materials.
4. Conduct further analysis of other possible manufacturing methods for aluminum–beryllium composites (e.g. power metallurgy).
5. Further investigate possible materials to use for plate 4 – meant to act as an insulator so that the Injectifold isn't directly touching the uranium - such as refractory metals.

NOMENCLATURE

NTP	= Nuclear Thermal Propulsion	H_2	= Hydrogen
NERVA	= Nuclear Engine for Rocket Vehicle Application	AlBeMet®	= Aluminum Beryllium Metal
COMSOL	= COMSOL Multiphysics®, version 5.1		

ACKNOWLEDGMENTS

REFERENCES

[1] Nekrasova, G.A., and Yatsenko, K.P., "New Light High-Modulus Beryllium-Aluminum Alloys of the Lockalloy Type for Space Vehicles," *Metallovedenic i Termicheskaya Obrabotka Metallov [Translated],* **No. 5**, 55 - 57, (1965).

[2] "AlBeMet® Technical Fact Sheet," *Materion Beryllium & Composites* [online], URL: http://materion.com/ [cited 08 January 2016].

[3] Tomberlin, T.A., "Beryllium - A Unique Material In Nuclear Applications," in proceedings of *36th International SAMPE Technical Conference*, San Diego, (2004).

[4] Simos, N., and Cuppoletti, J., *Metal, Ceramic and Polymeric Composites for Various Uses,* InTech, Rijeka, Croatia, 585-587, (2011).

[5] "HSDB: Beryllium, Elemental," *Hazardous Substances Data Bank*, National Library of Medicine, Last Updated June 2014, Web.

[6] Hashiguchi, D., Ashurst, A.N., Grensing, F.C., and Marder, J.M., "Aluminum-Beryllium Alloys for Aerospace Applications," *Materion Beryllium & Composites* [online], URL: http://materion.com/ [cited 06 August 2015].

[7] Greenemeier, L., "NASA Plans for 3-D Printing Rocket Engine Parts Could Boost Larger Manufacturing Trend," *Scientific American* [online journal], URL: http://www.scientificamerican.com/ [cited 06 August 2015].

[8] Michler, T., and Naumann, Jörg, "Hydrogen environment embrittlement of austenitic stainless steels at low temperatures," *International Journal of Hydrogen Energy,* No 33, 12 Feb. 2008, pp. 2111-2122.

[9] Gangloff, R., and Somerday, Brian, "Gaseous Hydrogen Embrittlement of Materials in Energy Technology", Vol. 1, Woodhead Publishing, Philadelphia, 2012, pp. 708 – 751.

[10] Raymond, L., "Hydrogen Embrittlement Testing," *Seventy-fifth annual meeting of the American Society for Testing and Materials,* Issue 543, ASTM International, Los Angeles, CA, 25-30 June 1972, pp. 190.

[11] Levoy, N., "Ductile – Ductile Beryllium Aluminum Metal Matrix Composite Manufactured by Extrusion," *Nuclear Metals, Inc.*, Jun. 1995.

[12] Speer, W., and Es-Said, O., "Application of an Aluminum – Beryllium Composite for Aerospace Components," Mechanical Engineering Dept., Loyola Univ., Los Angeles, CA, 2003.

[13] Agency for Toxic Substances and Disease Registry, "Beryllium Toxicity," *Case Studies in Environmental Medicine,* 23 May 2008.

[14] "An Advanced Materials Company Providing Application Specific Material Solutions for its Customers," *IBC Advanced Alloys Corp.* 2015.

[15] Say, C., Duich, J., Huskamp, C., and White, R., "Cost Effective Aluminum Beryllium Mirrors for Critical Optics Applications," *IBC Advanced Alloys Corp*, September 2013.

Multi-Mission Radioisotope Thermoelectric Generator Experience on Mars

Eric G. Wood[1], Jennifer A. Herman, Ronald A. Hall, Andrew W. Mitchell,
Paul M. Stella and Thomas I. Valdez

[1]*Jet Propulsion Laboratory, California Institute of Technology, 4800 Oak Grove Drive, Pasadena CA 91109*
818-354-8984; Eric.G.Wood@jpl.nasa.gov

Abstract. The Mars Science Laboratory (MSL) Curiosity rover has been operating on Mars using the F1 Multi-Mission Radioisotope Thermoelectric Generator (MMRTG) for over one and one-half Mars years (over three Earth years). During this extended period, Curiosity has provided a wealth of information about operating with a MMRTG in the Mars surface environment. This paper discusses MMRTG performance over the life of the mission as affected not only by expected radioisotope degradation, but also by the thermal environment, including seasonal, wind, and time-of-sol effects. Additionally, issues related to MMRTG internal shorts will be discussed including detection, impacts on operations, and clearing the shorts.

Keywords: RTG, MMRTG, Mars, Surface, Operations, MMRTG internal short.

INTRODUCTION

The Curiosity Mars rover is the first space application of the Multi-Mission Radioisotope Thermoelectric Generator (MMRTG). Curiosity has been operating on the Martian surface for over 1230 sols which is 1.8 Martian years (equivalent to 3.4 Earth years). The MMRTG has provided consistent and predictable power, simplifying mission planning in a way that solar-powered missions cannot; however, degradation over time beyond initial expectations has occurred. Furthermore, some internal shorting has also been detected but has little impact on output power.

In this paper a brief description of the design of the MMRTG is provided, as well as some description of the integration of the MMRTG with the Curiosity rover. A brief outline of the modeling of the MMRTG is given, including discussion of the degradation rate. Finally, there is a description of the internal shorting and its impact on operations.

MMRTG DESIGN

The MMRTG design is similar to other RTGs, incorporating a radioisotope heat source that provides a heat flow through an array of thermoelectric (TE) couples. Electrical current is generated in the couples due to the Seebeck effect. The radioisotope heat source consists of eight General Purpose Heat Source (GPHS) blocks, each containing Pu^{238} in the form of plutonium dioxide. See Figure 1 for an overview of the MMRTG construction.
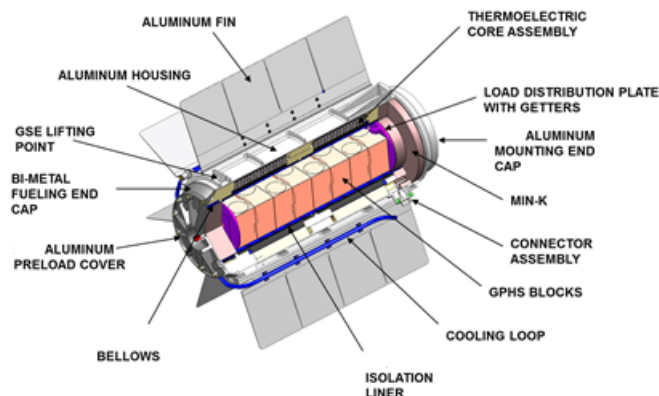
FIGURE 1. MMRTG Cutaway View [1].

The heat from the GPHS blocks radiates onto the Thermoelectric Core Assembly (TCA). See Figure 2 for an exploded view of the TCA. In the TCA, heat first enters the Heat Distribution Block (HDB), where it is conducted to the thermoelectric module and thence to the hot-side of the couples. The couples sit in recesses in the module bar where they are spring loaded to press against the HDB. Heat exits the couples on the cold side into the module bar and is then conducted to the case, where it is rejected by the fins.
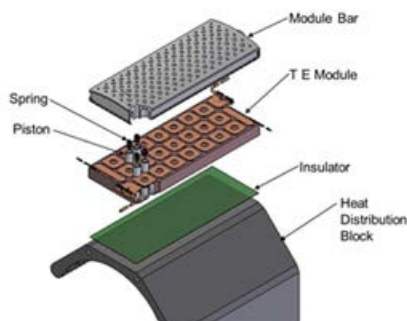
FIGURE 2. Thermoelectric Core Exploded View [1].

Thermoelectric Couple Design

Each TE couple, see Figure 3, consists of two legs. The N-type leg generates current in the same direction as the heat flow and the P-type leg generates current in the opposite direction. The P-type leg is divided into two segments, each optimized for a particular temperature range. The legs of each couple are electrically connected in series at the hot side, and connected in series at the cold side with other couples in a string. There are two strings in the MMRTG with cross strapping between couples for redundancy.
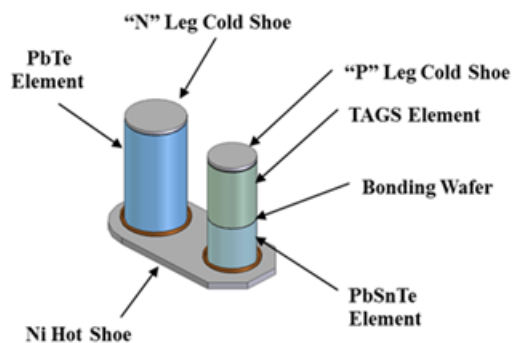
FIGURE 3. MMRTG Couple Construction [1].

MMRTG INTEGRATION INTO MSL ROVER

Mechanical and Thermal Integration

The MSL MMRTG is mechanically attached to the rear of the rover at an angle as shown in Figure 4. The MMRTG's angle with respect to the vehicle is a product of desired dust mitigation, rover arm ballast, and the ideal configuration for integrating the MMRTG through the back shell of the spacecraft at the launch pad, after spacecraft integration.
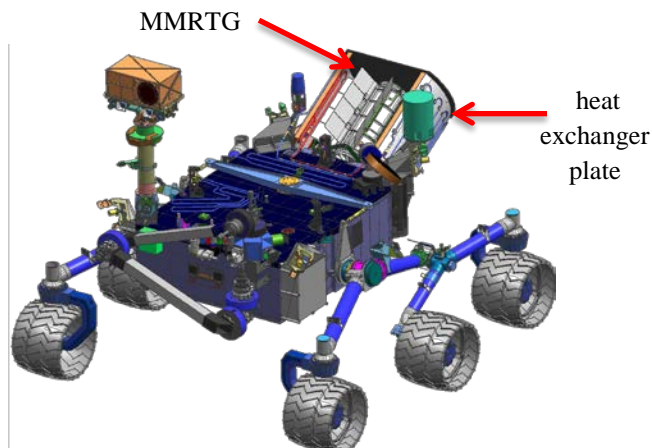
FIGURE 4. MMRTG Integrated with MSL Rover [2].

Rover electronics are kept warm using the waste heat from the MMRTG, which is captured by heat exchanger plates. A thermal fluid loop is routed across the heat exchanger plates and into the rover electronics mounting plate in the rover body. The affects of wind on the temperature of the MMRTG were reduced through the addition of a fabric baffle on the back of the MMRTG.

Electrical Integration

Electrically, the MMRTG is connected to the floating power bus, with the MMRTG case connected to the rover chassis. This floating power bus is created by isolating it from the 24 to 32.8 volt primary bus high side and low side through 5 kΩ resistors as shown in Figure 5. The power bus measurement with respect to the primary power bus low side is what the engineering operations team calls the "bus balance voltage" and is used to detect any MMRTG chassis shorts. Five shunt stages, mounted on the heat exchanger plates, facilitate power bus voltage regulation by shunting away excess MMRTG power.

In addition to the circuity shown, there is also the capability to command a "Battle Short," which effectively connects the chassis (SPG in the diagram) to the primary bus return. This is useful in clearing MMRTG internal shorts, as will be discussed later.
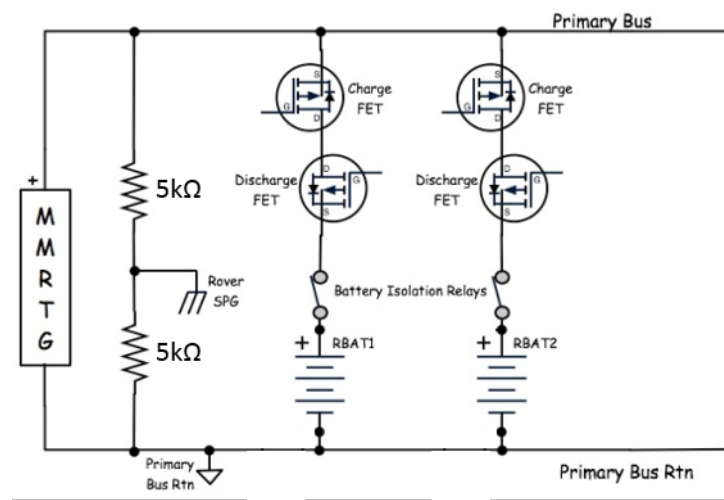
FIGURE 5. Floating Power Bus design [3].

MMRTG MODELING

JPL uses an in-house tool, the Lifetime Performance Prediction Model (LPPM), to model MMRTG performance. LPPM is a FORTRAN-based, parametrically-driven general RTG simulation. LPPM supports a configurable steady-state thermal model. It computes generator performance by aggregating up from a model of a single average TE couple. It is designed to simulate performance over the lifetime of any cylindrical RTG. In addition, to assist in the design of new RTGs, it can calculate overall RTG dimensions and mass. In this case, the LPPM parameters have been configured to describe the Flight Unit 1 (F1) MMRTG in use by MSL.

TE Performance Modeling

TE couple performance is computed by dividing each TE segment into 26 sub segments. The temperature of each sub segment is computed and the applicable Seebeck coefficient, thermal conductivity and electrical resistivity are obtained from TE property tables specific to each TE material, based on temperature and generator heated hours (lifetime). The tables are developed from lifetime testing of TE material samples.

Degradation Modeling

LPPM supports modeling of several generator degradation mechanisms: radioisotope decay, TE material property changes over time at temperature, sublimation of TE materials and degradation of surrounding insulation due to deposition of sublimed materials. Radioisotope decay modeling simply uses the initial heat and the half-life of the radioisotope source to compute the heat generated at a given time in the future. TE material changes are incorporated into the TE property tables mentioned above. Sublimation at the sub segment level can be simulated as a cross-section area loss as a function of time at temperature. Property changes of surrounding insulation is computed as a function of couple weight loss due to sublimation; however, due to lack of test data and the small impact that sublimation has on generator performance, the sublimation mechanism was not incorporated into the MMRTG configuration of the LPPM.

The MMRTG output power has degraded at a higher rate than was originally expected. Analysis of results from the engineering unit (EU) have shown this to be due to increased internal electrical resistance and, to a lesser extent, increased thermal resistance. The EU is a highly instrumented, electrically-heated version of the MMRTG that is undergoing life testing. The current hypothesis is that this is occurring at the hot end of the couples. To handle this, an additional time-based straight-line empirical degradation was added to the model by adding additional (extraneous) electrical resistance at the hot end of the TE couples. The magnitude of this degradation is computed by fitting an exponential decay curve to actual output power and also to the modeled output power. The two exponentials are compared and adjustments are made to the beginning and ending values of the extraneous resistance until the decay curves are identical, see Figure 6.

To deal with this issue, a proposed enhanced MMRTG (eMMRTG) is being developed for future missions that would address the hot side electrical resistance degradation issue, as well as providing improved efficiency and significantly greater end-of-mission power through the use of more advanced TE materials.

Degradation Rate

As of this writing, the exponential degradation rate (r) for the generator is 4.62%, using an epoch time of MSL Sol 0 T 00:00:00 and a P_0 value (initial power) of 113.87 W.

Equation (1) can be used to estimate the power at some future date.

$$P(t) = P_0\, e^{-rt} \tag{1}$$

Equation (2) can be used to compute time in Earth years given a Mars sol number.

$$t = Sol * 1.02749 / 365.25 \tag{2}$$
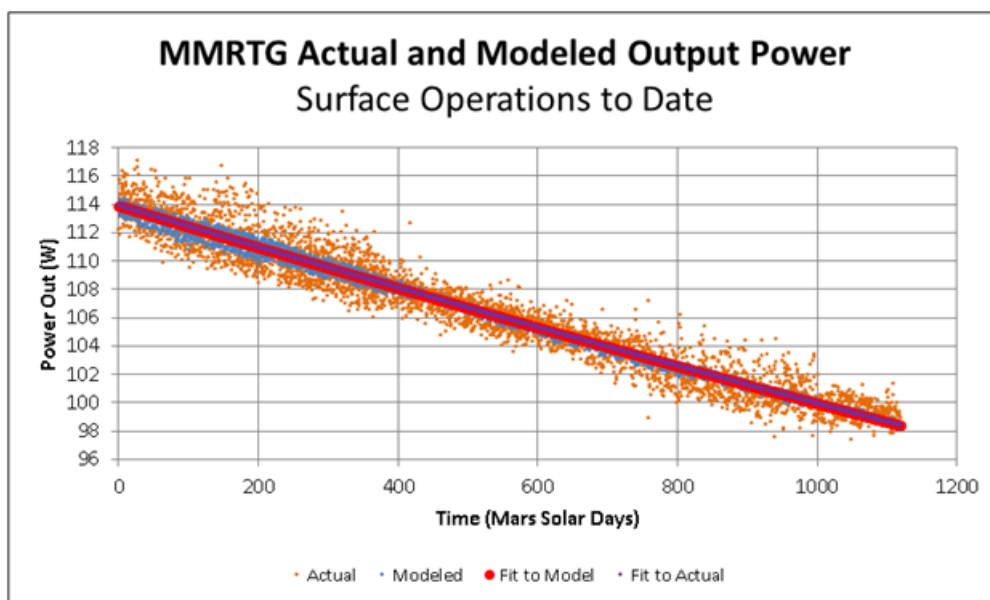
FIGURE 6. MMRTG Actual and Modeled Output Power [4].

Drawback of Steady-State Thermal Model

LPPM uses a steady-state thermal model. This has the benefit of simplifying the parameters needed to create a configuration. Its downside is that the model does not respond to environmental temperature changes in a way similar to the actual generator. This has been evident during surface operations when the wind picks up. The actual generator gets a temporary performance boost when the wind cools the generator's fins, creating a larger temperature drop across the couples that can persist for some minutes. As the cooler temperature permeates the generator, reducing the temperature differential, the performance boost slowly disappears. A similar, but opposite process occurs when the wind subsides. By contrast, since the model is steady-state, the suddenly cooler or warmer fin temperature is assumed to instantly permeate the generator, producing little if any change in performance. In looking at **FIGURE 6**, one can see that the scattering of the actual output power is much broader than the modeled output power. This is due to the steady-state nature of the model. However, the average power output of the model matches the actuals quite well.

MMRTG INTERNAL SHORTING

The MSL Fault Protection (FP) software tracks telemetry and responds when telemetry is outside expected operational ranges. Bus balance voltage telemetry is used to detect electrical shorts from chassis to power bus or power bus return on the rover. If the bus balance voltage is out of range, then the FP software raises a fault and ceases scheduled mobility activities. Understanding and crafting effective operational policies for handling bus balance voltage anomalies is crucial for the mission.

On mission sol 456, MSL engineering operations staff observed an unexpected shift in bus balance voltage telemetry: the balance voltage shifted from its nominal ~11 volts to ~4 volts. Further review of telemetry indicated that balance voltage had intermittently shifted from nominal to ~4 volts several times over the previous sol, before "settling" into a continuous value of ~4V. Note: only by having the balance voltage sense circuitry/telemetry can

MSL sense this internal short. Responding to the anomaly, the power engineering operations team immediately investigated potential operational causes of the short, as well as brought in RTG domain experts with particular knowledge of the behaviors of the RTGs used on NASA's Cassini Saturn orbiter.

The investigation team considered two classes of shorts to determine the root cause of the balance voltage shift: a "soft" short to chassis of about 1 kΩ between power bus return and chassis, and a hard short to chassis of a 0 to 4 V source, consisting of 0 to 1 kΩ. Based on the operations plan at the time of the observed balance voltage shift, the team conducted diagnostic activities to ferret out potential causes related to these two classes of shorts, ultimately observing that telemetry revealed a measurable drop in MMRTG current at the exact time the bus balance voltage shift occurred.

The working hypothesis is that an internal low impedance short on the MMRTG is the only credible root cause of the anomaly. MSL has determined that there is no impact to nominal operations with the short in place, as all electronics and instruments were designed and tested to work with any chassis voltage from the bus return to power bus voltage, with one exception. That exception is using the drill percussion mechanism with the battle short enabled. The sol 456 MMRTG short spontaneously cleared on sol 461 when the rover was asleep.

Over the sols since the first MMRTG short, MSL engineering operations has learned to evaluate telemetry to quickly and accurately identify an internal MMRTG short and explicitly clear a persistent soft short. Over this same period, the frequency of shifts in bus balance voltage has increased, but the balance voltage shift itself has remained fairly consistent.

Key observations:
- It is important to develop a procedure and supporting tool to assist
- Bus balance voltage shifts from its nominal value of ~11 volts to ~4 volts
- MMRTG current drop while the short is cleared is always very small
- Some MMRTG shorts events clear spontaneously, but most are cleared explicitly by using the battle short
- Having the ability to sense and clear an internal MMRTG short has proven invaluable in evaluating MMRTG behaviors and allow for even rudimentary investigations thereof.

Since the sol 456 MMRTG short, MSL has observed that the bus balance voltage shift is associated with an MMRTG short on the sol ranges listed below (see also Figure 7). For many of these, the short may have been intermittent. Usually the MMRTG short is observed for a few sols before it is cleared by battle short.

- 456 to 461   spontaneously cleared
- 816 to 836   explicitly cleared using the battle short checkout sequence
- 1084 to 1085   spontaneously cleared
- 1089 to 1092   spontaneously cleared
- 1158 to 1167   explicitly cleared using the battle short checkout sequence
- 1173 to 1182   explicitly cleared using the battle short checkout sequence
- 1186 to 1192   explicitly cleared using the battle short checkout sequence
- 1204 to 1223   explicitly cleared using the battle short checkout sequence
- 1233 to 1239   explicitly cleared using the battle short checkout sequence
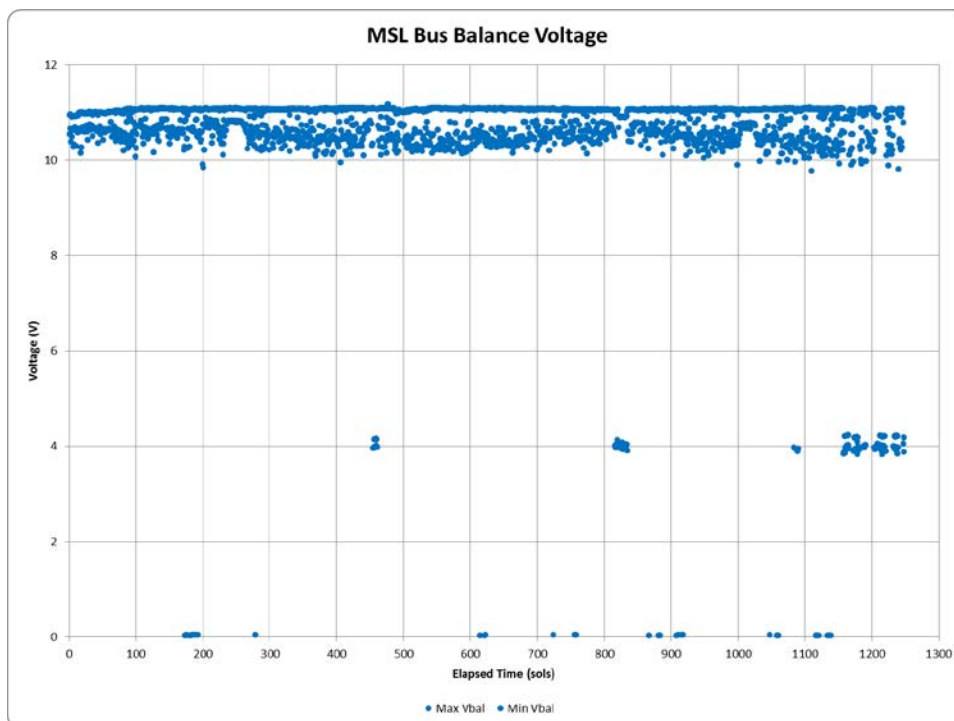
FIGURE 7. MSL Bus Balance Voltages

Possible Causes of Internal Shorts

The definitive cause of the internal MMRTG short has not been determined. The leading theory is that conductive material is sublimated and circulates within the MMRTG until it reaches a location within the stack where conditions are right for condensation, causing a leak path to the generator case, which is connected to the rover chassis. This condensation appears to occur at essentially the same location, as evidenced by the balance voltage shift *to* ~4 volts for each event. When the short does clear, it doesn't completely dissipate all condensation buildup; hence, relatively little additional condensation can cause a short to reform at the same location. One likely location for the short is from a TE couple to the module bar.

Clearing the MMRTG Short

MSL has a dedicated switch that is invoked to connect the power bus low side to the rover chassis. In MSL parlance, "invoking a battle short" closes this switch prior to using the percussive drill to minimize noise in the power bus. MSL has exploited this "battle short" activity to drive current through the MMRTG soft short and clear it.

Impact on Operations

Initially, the impact of the first MMRTG internal short on mission operations was significant; the project placed science operations on hold while the unexpected shift in bus balance voltage was under investigation. A week later, the project decided to attempt to clear the MMRTG short with the battle short activity, but the MMRTG short cleared spontaneously before the battle short could be used. Four hundred sols later, when the MMRTG short appeared again, the project had a better understanding of the issue and was able to eventually clear the MMRTG short with the battle short.

48

To date, there have been over nine instances of the MMRTG short. The MMRTG shorts have become more familiar to the power subsystem operations team - it is now standard procedure for the power operations team to monitor the MMRTG short for a few sols and then request the battle short.

CONCLUSION

The overall use of a MMRTG for surface operations on Mars has been a great success, notwithstanding the elevated degradation rate. To date, power availability has generally <u>not</u> been a limiting factor in operational planning. Internal shorting has not had a significant impact on operations and is expected to continue as it has on other RTG-powered missions.

NOMENCLATURE

$P(t)$	=	MMRTG output power at time t	r	=	Exponential degradation rate.
P_0	=	MMRTG output power at the epoch time	t	=	Time in Earth years
Sol	=	Martian solar day number based on mission landing day (sol 0)			

ACKNOWLEDGMENTS

REFERENCES

[1] Teledyne Energy Systems, Boeing, MMRTG – Preliminary Design Review, 2004
[2] Beatty, J., "MMRTG Interface Control Document (ICD) Rev. A," *JPL Document Number D-27138 Figure 2.2-2 "Rover Traverse Configuration",* Pasadena, CA, 2011.
[3] Jones, L., Mitchell, A., "MSL Power and Power and Analog Module (PAM) Functional Design Description Rev. E," JPL Document Number D-34194 Figure 4-12 "Power bus and example power switch cross strapped to single load", Pasadena, CA, 2015
[4] Wood, E., "MSL MMRTG Performance Summary and Predict: Martian Surface FY16Q1," JPL Interoffice Memorandum IOM-3466-16-001, Pasadena, CA, 2016.

DEMOCRITOS: Development Logic for a Demonstrator Preparing Nuclear-Electric Spacecraft

Mr. Stéphane Oriol, Mr. Frédéric Masson [1]
Mr. Tim Tinsley, Dr. Richard Stainsby, Ms. Zara Hodgson [2]
Dr. Emmanouil Detsis, Dr. Jean-Claude Worms [3]
Academician Anatoly Koroteev, Dr. Alexander Semenkin, Dr. Alexander Solodukhin [4]
Dr. Frank Jansen, Dr. Waldemar Bauer [5]
Ms. Simona Ferraris, Ms. Maria Cristina Tosi [6]
Mr. Michel Muszynski, Mr. Francois Lassoudiere [7]

[1]CNES, launcher directorate, 52 rue Jacques Hillairet, 75612 Paris Cedex, France
[2]National Nuclear Laboratory, Sellafield, CA20 1PG, United Kingdom
[3] European Science Foundation, Strassbourg, 67080, France
[4]Keldysh Research Center, Moscow, 125438, Russia
[5] DLR Institute of Space Systems, Bremen, 28359, Germany
[6] Thales Alenia Space, Torino, 10146, Italy
[7] Airbus Safran Launchers, Vernon, 27208, France

Abstract. The DEMOCRITOS project aims at preparing demonstrators for a mega-watt class nuclear-electric spacecraft. It is funded by the European Community through the Research & Technology program "Horizon 2020". The resulting European and Russian cooperation includes the following partners: the Nuclear National Laboratory – NNL (U.K.), the German Aerospace Center – DLR (Germany), the Keldysh Research Center – KeRC (Russia), Thales Alenia Space Italia – TAS (Italy), Airbus-Safran Launchers – ASL (France), the European Science Foundation – ESF, (France) and the Centre National d'Etudes Spatiales – CNES (France). The Instituto de Estudos Avançados – IEA (Brazil) has joined the project as an observer. DEMOCRITOS is the follow-up to the MEGAHIT project.

In this paper we will present the development logic for a ground demonstrator, whose target is to test end-to-end nuclear-electric propulsion, with the nuclear core replaced by a conventional heater. We will first justify the need for a ground demonstrator, and we will introduce our reference vision: the general architecture and the definition of each sub-system, together with the technologies considered. We will then detail the test objectives and the requirements for the test bench. Our target is to test a 200 kWe conversion loop (closed Brayton cycle), linked to a lower power heat-pipe radiator and electric thrusters. As the ground demonstrator should be modular, several technologies could be tested for each subsystem (kit approach), particularly for electric thrusters. Given the technology and test benches already available in Europe and Russia, we believe it is possible to conduct a first test campaign in 2023 giving the required representative demonstration of an INPPS flagship (International Nuclear Power and Propulsion System).

Keywords: Nuclear, electric, space propulsion, DEMOCRITOS, INPPS.

CONTEXT

Powering spaceships with nuclear fission could significantly increase payload masses and shorten space journey duration, thus facilitating future missions with high power needs, such as deep solar system exploration, Moon and Mars cargo missions, or Earth protection related to asteroids. The 1 MWe nuclear-electric spaceship stands out as one of our promising long-term targets, for which the forerunner MEGAHIT project laid out a global roadmap, along with various reference systems architectures, a technological trade-off and a maturation action plan.

The DEMOCRITOS project puts forward a ground demonstration system and associated test campaigns as part of the maturation action plan. It defines a ground demonstrator with 200 kWe power in order to study the following subsystems: thermal control, power conversion, power management, electric thrusters, propulsion and structures [1].

We will now present the development logic for this ground demonstrator, starting with the targeted spaceship, followed by the need for demonstration, the demonstrator's architecture, our design priorities and our technological roadmap, concluding with the test facilities requirements and test campaign objectives.

MANY MISSIONS, ONE SPACECRAFT

Main missions

Our aim is to design a spacecraft able to fulfil a large number of diversified missions, including cargo missions to the Moon and Mars, asteroid deflection and outer solar system missions. We will investigate how such a spacecraft could be adaptable in a kit approach logic, for example with additional propellant tanks.
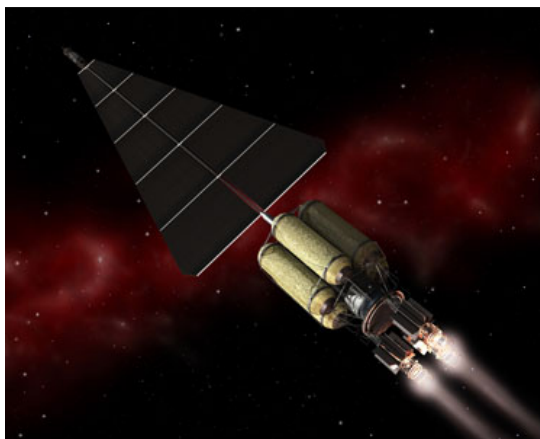
FIGURE 1. Reference spaceship design: 1 MWe nuclear electric, 10 years operational lifetime (5 years at full operational power) ©*Courtesy CNES*.

TABLE 1. Several missions are considered in the DEMOCRITOS project, based on a 1 MWe / 20 t vehicle:

Mission	Cargo to Mars	Outer solar system missions	Lunar orbit tug	NEO asteroid deflection
payload and mission duration	15 t in 400 days (per round trip)	Europe: 3-10 t in 3 years Titan: 3-12 t in 3.5-6 years	650 t in 10 years (~15-20 t round trips)	Apophis example: if the spacecraft left Earth in 2021 it would reach Apophis in 200 days and deflect it by 1 million km before it reaches Earth just by staying 300 m away from it.
Total number of cycles	8 cycles (4 round trips)	Less than Mars mission	30-40 cycles (20 round trips)	Less than Mars mission

General presentation of the INPPS

Aboard the INPPS flagship, a nuclear reactor produces thermal power converted into electrical power which is managed by PMAD system (power management and distribution) and finally powering some electric thrusters. These thrusters could be ion or Hall Effect thrusters, fed with propellant such as Argon or Krypton. A huge (!) heat pipe radiator provides the cold sink necessary for the thermodynamic cycle to evacuate the extra heat.

The fission nuclear reactor produces up to 3.3 MWth, and 6 parallel conversion loops of 200 kWe each are necessary to meet the 1 MWe target. Each conversion loop will normally function at ~85% power, but if one of them should fail, the 5 remaining loops would power up to 100% in order to maintain the needed 1 MWe for thrust.

THE NEED FOR A GROUND DEMONSTRATOR

The "ground demonstrator" is an essential element of our roadmap towards a 1 MWe nuclear-electric spaceship.

Its ambition is to test the whole system end to end, in the most representative environment possible, with the clustered electric thrusters linked to the electrical power source. In the DEMOCRITOS "ground demonstrator" the nuclear core is replaced by a representative heater. The nuclear core and robotics will be part of later demonstration programs.

The ground demonstrator is indispensable for two main reasons. The first is to characterize each subsystem. The second is to demonstrate that all subsystems can work together as an overall system. We especially need to demonstrate the ability to start and shut down, bearing in mind that every subsystem would have very different response times: 0.05 s for PMAD, 1 s for the thermodynamic loop, several hours for the nuclear core.

We need to mature challenging technologies, the top priorities being:
- to test a closed Brayton cycle up to 200 kWe, (the US report 60 kWe tests) and to couple such a power full cycle with electric thrusters (the US published 2 kWe coupled tests). Moreover, clusters of high-powered electric thrusters (~20 kWe each) have never been tested in Europe,
- to operate at a very high temperature, with long duration, no maintenance and multiple restarts. High temperatures have the advantage of making the nuclear-electric spacecraft light and compact, thus competitive. The 1300 K reference point is a compromise between performance and feasibility, and will be particularly challenging for the turbine (blades and rotating parts), heat pipes and the electronics,
- deployment of integrated structures (e.g. boom, radiator and thruster assembly).

GROUND DEMONSTRATOR: REFERENCE ARCHITECTURE

Power Levels

The ground demonstrator is down-sized compared to its 1 MWe target both in terms of cost and feasibility. However, **one 200 kWe conversion loop** is anticipated for demonstration, fed by a **hot source of 650 kWth**. **PMAD will be at 200 kWe**.
A consistent heat pipe radiator (250 m^2 for ~450 kWth dissipation) would not fit into the test facilities nor the budget, so it needs to be drastically downsized to a **1 to 3 m^2 heat pipe radiator**, and completed with heat exchangers provided by the test facility.
Testing electric thrusters requires a high level of vacuum, which is most difficult for higher thrust power. **A 40 kWe cluster of thrusters** will be tested, based on the remarkable capacities of the KeRC existing test bench.

Overall Monitoring

The demonstrator's autonomous On Board Computer will supervise the system's self- regulation, data collecting and failure management. The test bench will be interfaced directly with the On Board Computer and safety redlines enabling Control & Command operations (starting, operating point changes and stopping) and safety.

Fluid Loop

The heat generator is a non-nuclear device that can simulate nuclear core behavior regarding temperatures and exchange coefficients with the fluid for stabilized phases and various transient profiles including starting, stopping, operating point changing. There will be no simulation of the internal functional parameters nor the radiation.

The fluid loop uses a mix of gaseous Helium-Xenon (~35% He, ~10 $kg \cdot s^{-1}$ mass flow rate) in a Brayton power conversion cycle. It is pressurized through a compressor, heated through the nuclear core simulator, expanded through a gas turbine, cooled through a heat pipe radiator (and bench auxiliary exchangers) before getting back to the compressor. The expansion in the turbine generates mechanical work on a rotating shaft. The whole fluid loop is regulated by monitoring the quantity of the Helium-Xenon mixture in the loop. By-pass and safety valves are added to manage power discharge, for example during transient phases or unexpected behavior.
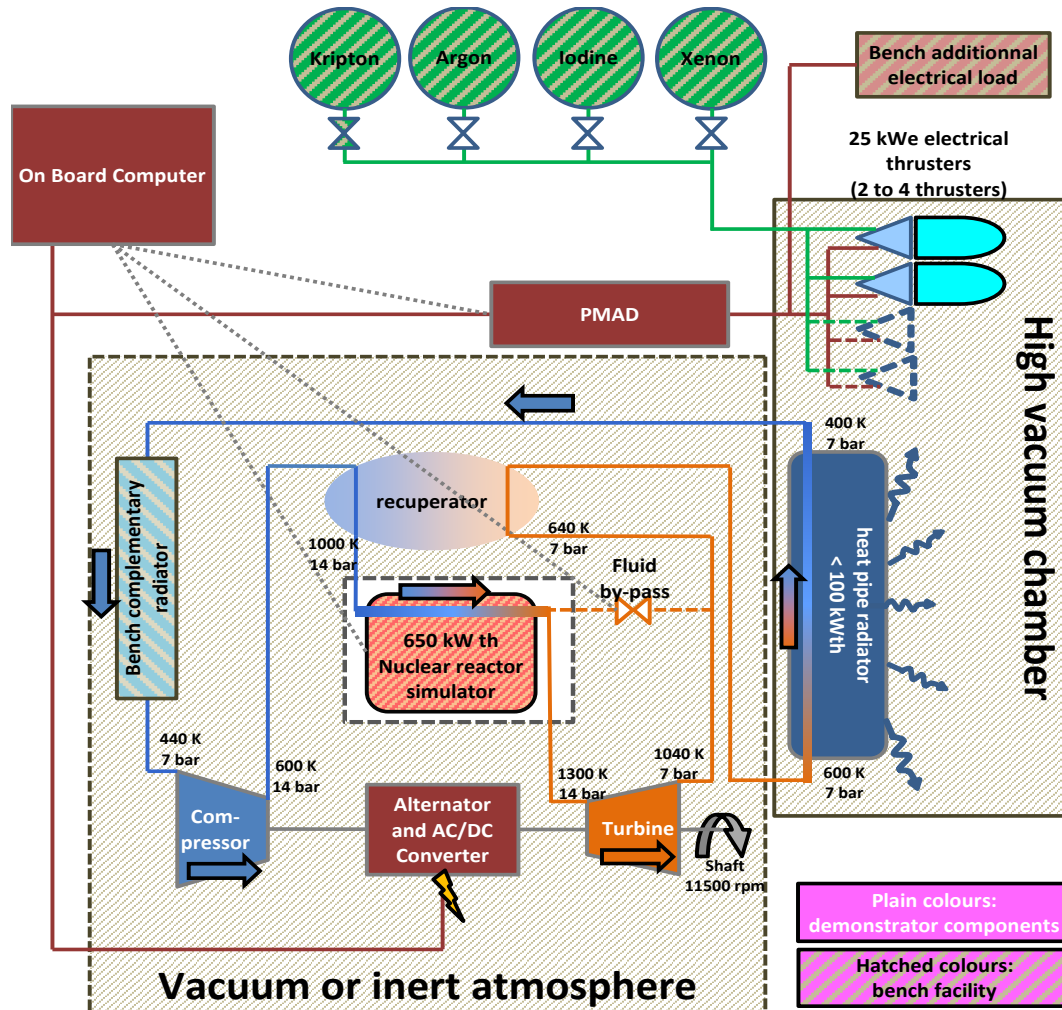
FIGURE 2. Overview of the DEMOCRITOS test architecture

PMAD

The main function is to convert electrical power into 400 A and 500 V DC and convey it to the electric thrusters. PMAD also starts the turbo machinery, manages changes of operating points, and monitors different sensors.
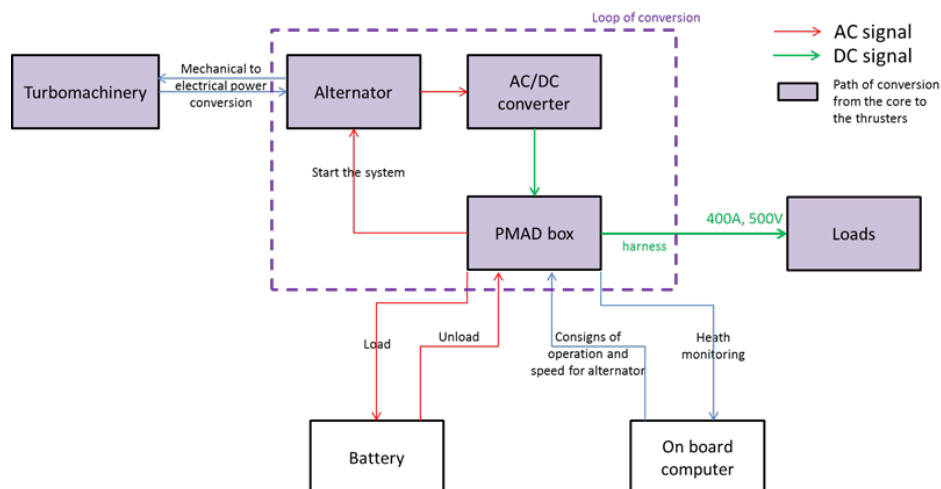
FIGURE 3. PMAD interfaces consist of a mechanical electrical conversion loop, of electrical loads and batteries. PMAD is controlled by an on-board computer.

Electric Thrusters

A cluster of two thrusters, within a power range of 20-25 kWe, will be tested, with their own PPU (Power Processing Unit) converting electrical power from PMAD into electrical power suitable for the thruster. Such systems are scheduled in Europe by 2023. Both Hall Effect and Ion Grid technologies will be demonstrated with various propellants. The test bench provides means to dissipate remaining electrical power through a thruster simulator (electrical load).
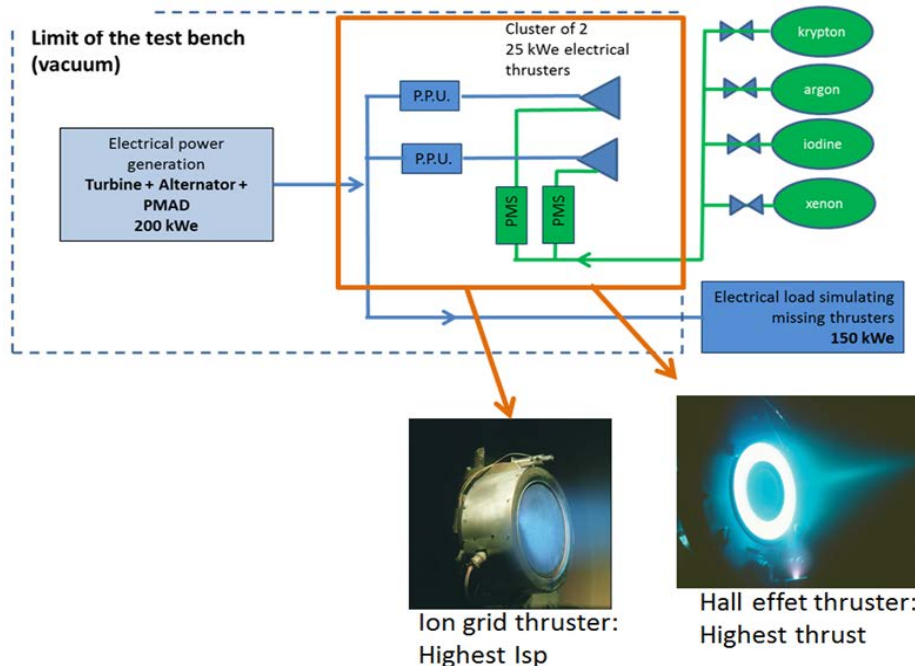
FIGURE 4. The DEMOCRITOS modularity enables us to test thrusters with several propellant and technologies.

DESIGN STRATEGY AND PRIORITIES

The purpose of the demonstration is to test and characterize an overall system, after each subsystem has been tested through individual Factory Acceptance Tests. Our design priorities will be:

- **Functionality, representativeness and safety**: the first key to success is to avoid hazards on the test bench and the demonstrator, then to gradually reach the tests' objectives, from the safest to the most challenging,
- **Cost**: this first step in development has to be at least « affordable »,
- **Planning**: 2023 is the target for the ground demonstrator's first operational test,
- **Performance**: a nominal power between 50 kWe and 200 kWe should be a reasonable target, depending on the test bench capacity,
- **Modularity and growth potential**: the ground demonstration should start in 2023 using off-the-shelf technologies while keeping up with new breakthroughs,
- **Duration**: at least 10 start/shut down cycles,
- **Synergies**: with other aeronautical and space applications.

Representativeness of the systems regarding mass and space environment compatibility would be preferable but not a requirement. However, aspects such as micro-gravity, full scale systems and the nuclear and electromagnetic environment need to be considered in the system's development.

ROADMAPS AND SELECTED TECHNOLOGIES

At least two ground test campaigns are planned. The first in 2023: tests will demonstrate that the system is safe and functional in a steady state and during on off transients. Technologies are already mature in 2015 or scheduled to be so by 2023 will be used. Lower temperatures than the 1300 K baseline would be acceptable.
The second in 2028: more advanced technologies should be tested. The temperature baseline should meet a 1500 K and the demonstrator should meet performance requirements for a competitive spacecraft.

Nuclear Reactor Simulator

A simple electric heater or boiler could simulate a first-version core reactor (delivering 650 kWth at 1300 K, 14 bars), then a more powerful one (650 kWth, 1500 K, 14 bars). The main requirements for this heater will be its capacity to simulate reaction times with a representative thermal behavior. The first start-up transient should last from 24 to 48 hours; whereas the following restarts would take about 5 hours; and shut down transients from 100% to 7% should last no more than a 1 s, then 24 hours from 7% to 1%.

Power Conversion Fluid Loop

A closed Brayton loop was chosen for the power conversion fluid loop, with a turbo-compressor driving an alternator. A moderate 11500 rpm rotational speed will limit high cycle fatigue. The main challenges are:
- a turbine able to sustain 1300 K, with a growth potential of 1600 K during 5 to 10 year period,
- bearings able to resist 5 to 10 years without maintenance,
- tightness systems preventing helium leakage for 10 years.
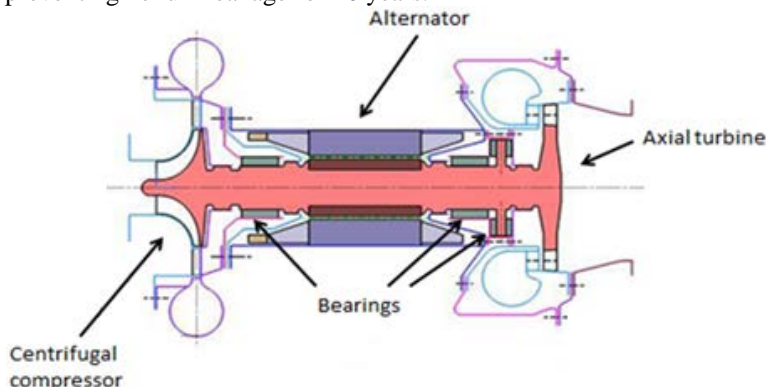
FIGURE 4. The Turboalternator preliminary design includes a direct drive alternator in between the compressor and the turbine. **©Courtesy** *SNECMA Safran group*.

For the first campaign, we will use technologies developed for other industries: aeronautics for the turbine, power plants for the bearings and nuclear plants for helium tightness. The second campaign would need major innovation such as new monocrystal or ceramics turbine blades, new hybrid hydrostatic/dynamic bearings or improved Helium tightness systems.

Existing alternator technologies would be fine provided its temperature is cool at a reasonable 250°C by tapping-off fluid from the conversion loop. A variable reluctance alternator with additional excitation coil appears to be an acceptable compromise, less efficient than a permanent magnet technology, but more convenient to integrate.

PMAD

Operating points are set and commanded by the On Board Computer, which also manages PMAD power needs and fault detection. PMAD electronics then elaborate a speed strategy for the alternator, based on OBC commands. PMAD AC/DC converter converts alternative power from the alternator into a continuous signal. The Harness drives this DC power to the loads. Finally, the power processing unit (PPU) placed just after PMAD sends to the electric thrusters a signal which is regulated in terms of current, voltage, shape and transient behavior. As an example, Snecma's PPS20k needs a 20 kW PPU to work.

By the early 2020s, it is fairly sure that current electrical components will be obsolete. Moreover, further development will be needed to design the spacecraft's electric circuit based on our 2020s demonstrations. Therefore, COTS components can be used for the first demonstration tests. In a second stage, advanced technologies should be tested to be assessed before starting development.

Our challenge? Miniaturization for lighter electronics, higher functional temperatures and heat dissipation, electric conversion management at interfaces, cable isolation and superconductivity, electric storage such as supercapacitance or regenerative Fuel Cells.

Radiator

Radiators provide the Brayton cycle cold source. Optimization is crucial for such voluminous and heavy equipment. To get a compact radiator, we need a high fluid temperature and a wide temperature gap between hot and cold sources. The chosen compromise is a demonstration radiator with a 600 K inlet temperature and a 400 K outlet.

Our baseline is a high temperature heat pipes, with forced circulation to evaporators between the He-Xe loop and heat pipes, with thermal insulation to insure efficiency and protection for payloads and thrusters, and with supporting structures including a large deployment mechanism. For cost optimization, we've decided to downscale the radiator to a one or two square meters and to test the heat collection and rejection capacity in a vacuum chamber during the first demonstration campaign.

The main demonstration objectives consist of the wide temperature operability up to 600 K and restarting ability after a long shut-down in a cold environment, as well as technological modularity. In the second step, demonstration should concern larger areas of radiation and higher temperatures. Large deployment systems and microgravity behavior may be tested in later development phases.
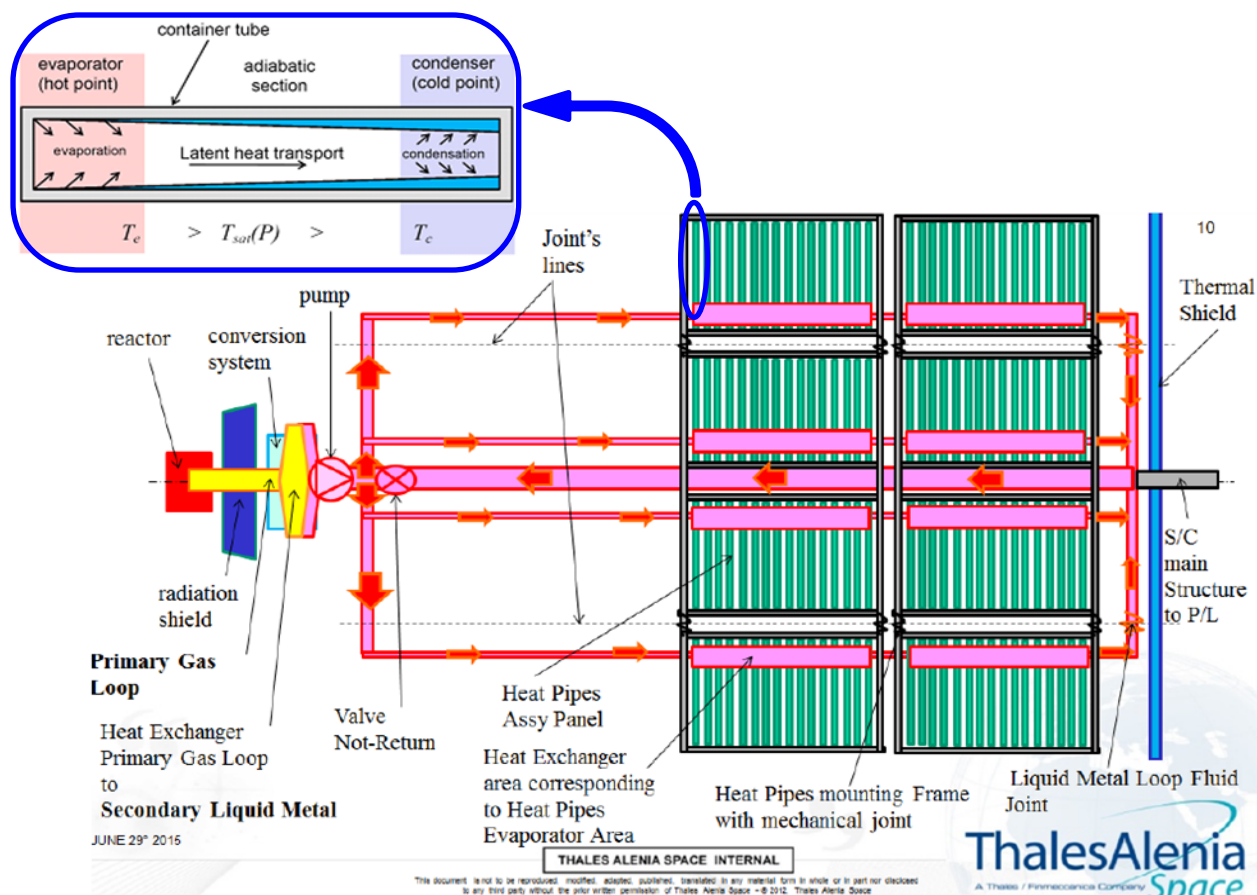
FIGURE 5. The radiator architecture uses a liquid metal loop through high temperature heat pipes fed with Halide and with walls made of titanium or superalloys. **©Courtesy *THALES ALENIA Space*.**

Cluster of Electric Thrusters

The cluster of electric thrusters will have two 25 kWe thrusters working in continuous mode. For the first test campaign (2023), the Hall Effect thrusters SNECMA PPS20k and the Grid ion thrusters KeRC IT-500 should be available and would run with krypton, as well as argon or xenon used as propellants.

TABLE 2. The Trade Off indicates krypton as the reference propellant, because it is a good compromise in terms of cost and performance:

	Price	Availability	Maturity	Isp	Thrust	Anode efficiency	Storage
Xenon	Very expensive 1000 €/kg	Scarce (~20 t/year)	High	Ref	Ref	65%	Easy! Supercritical at 293 K 1100 kg/m^3
Krypton	Between Xe / 2 and Xe / 7	Xe × 10	Medium	Ref × 1.25	Ref × 0.8	65%	More or less easy: supercritical at 208 K 900 kg/m^3
Argon	Xe / 25	Abundant	Medium	Ref × 1.8	Ref × 0.6 Could increase with amperage	50-55%	Difficult: supercritical at 153 K 550 kg/m^3
Iodine	Between Xe / 8 and Xe / 50	Abundant	Low	Ref	Ref	Similar to Xenon	Easy: Liquid at 390 K. High density if solid: 5000 kg/m^3 But: safety constraints
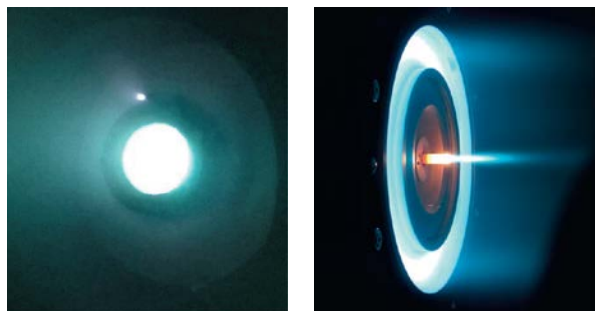
FIGURE 6. DEMOCRITOS aims at testing both IT-500 grid ion thruster (left ©*KeRC*), and the the Hall Effect thruster PPS20k (right ©*SNECMA Safran group*), should help towards their qualification.

Our demonstration will focus on high voltage regimes for Hall Thrusters, clustering effects, propellant long life storage and feeding system. A second test campaign (2028) would give the opportunity to test bigger clusters, higher power thrusters or new technologies such as VASIMIR or MPDT.

Structures

The 1 MWe nuclear electric spacecraft will be large and massive. Therefore it is expected to be launched into orbit in parts and then to be assembled in space. A ground demonstrator can be a chance for testing technological solutions, especially regarding complex connections for fluid loops, electrical circuits, robotic automation or deployment.

TESTS CAMPAIGNS

Test Objectives

For the first test campaign, our priority is to demonstrate the consistency and functionality of the global system comprising heater + conversion loop + PMAD + radiator + thrusters. The system will:

- sustain a steady state for long operational duration at different power levels (duty cycle: 50% up to 90%),
- enable a start and shut down cycle many times (40 cycles are required for a lunar mission),
- sustain failure tolerance remaining in safe conditions in all modes.

We will characterize performances for each component, and also for the overall system: power, efficiency, thermal and electric losses, gaseous tightness, thrust, specific impulse and ageing. Furthermore, early tests will be carried out to assess the system's robustness according to the dispersion of physical parameters. This should be done in environmental conditions representative of space when necessary. No doubt exploring the system's thermal behavior will require specific conditions: a high vacuum level and low temperatures.

More severe conditions may also be necessary to accelerate ageing effects and to demonstrate a strong resistance of the subsystems. For example, cracking phenomena on the turbine blades are relatively easy to amplify, simply by increasing the inlet temperature: a 50 K increase can speed up ageing by a factor of 1000. As for the electronics, equivalency formulae can be used to accelerate temperature and humidity effects and be representative of a complete ten years life cycle. As for the electric thrusters, ageing can to be accelerated by increasing the propellant flow rate but this is very limited and additional tests would be needed outside the ground demonstration.

The second test campaign would integrate innovative technologies, in order to participate to their characterization and qualification, and of course demonstrate that they improve our demonstrator's performances. In parallel, other demonstrations might be necessary to prepare the spacecraft, such as a dedicated nuclear core, Zero-G flights or in ISS experiments for microgravity purposes, thermal ageing of specific materials, structures' automatic deployment and assembly.

Test Bench

The DEMOCRITOS test bench is supposed to accommodate the whole ground demonstrator and tooling. As one big vacuum chamber wouldn't be financially sustainable, we expect to use half a dozen specialized test areas, interfaced with each other in order to maintain system overall representativeness.
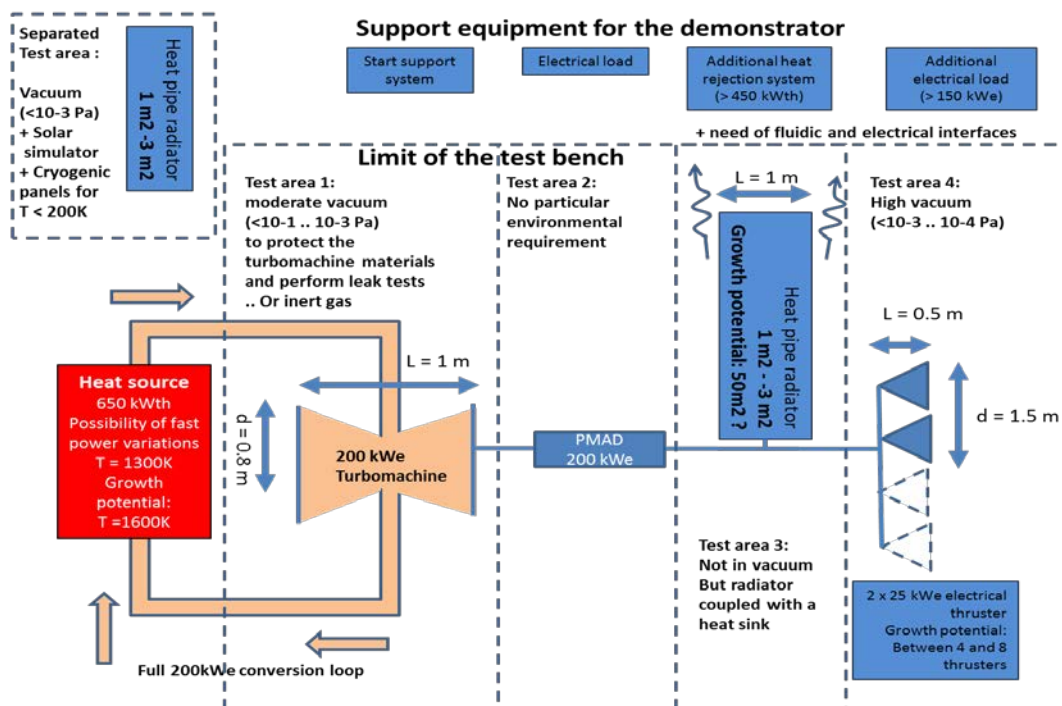
FIGURE 7. The DEMOCRITOS test bench could consist of three vacuum chambers and other specialized areas allowing tests' customization according to technological purposes [2].

CONCLUSION

The DEMOCRITOS project results from a cooperation between Europe and Russia to lead the way towards the first demonstration of a nuclear electric space propulsion system – the INPPS flagship. It has identified potential missions for a nuclear electric spacecraft, an architecture for a downscaled ground demonstrator, a strategy for technical designs and demonstration priorities, a general roadmap for two test campaigns, together with associated objectives and test bench needs.

The project can now start a conception process in order to achieve a preliminary definition for the demonstrator's subsystems: mainly the turbocompressor, alternator, radiator, PMAD, cluster of thrusters, structural architecture and mechanism. The main challenges concern the mechanical constraints due to high temperatures and how to find a way to simulate a 10 year life cycle with a limited test time.

International space community is invited to join the INPPS flagship concurrent engineering study of DEMOCRITOS project in summer 2016 [3].

ACKNOWLEDGMENTS

REFERENCES

[1] Masson F., Ruault J-M., Worms J-C., Detsis E., Beaurain A., Lassoudiere F., Gaia E., Tosi M.C., Jansen F., Bauer W., Semenkin A., Tinsley T., Hodgson Z., *Democritos: preparing demonstrators for high power nuclear electric space propulsion*, NETS (2015).

[2] Lovtsov A.S., Shagayda A.A., Muravlev V.A., Selivanov M.Y., *Ion Thrusters Development for a Transport and Power Generation Module Project,* in proceedings of *34th International Electric Propulsion Conference* and *30th International Symposium on Space Technology and Science* Hyogo-Kobe, Japan (2015).

[3] Jansen, F., Bauer W., Masson F., Ruault J.-M., Worms J.-C., Detsis E., Lassoudiere F., Granjon R., Gaia E., Tosi M.C., Koroteev A.S., Semenkin A.V., Tinsley T., Hodgson Z., Koppel Ch., *DEMOCRITOS Demonstrators for Realization of Nuclear Electric Propulsion of the European Roadmaps MEGAHIT & DiPoP* (IEPC-2015-91079), in proceedings of *34th International Electric Propulsion Conference and 30th International Symposium on Space Technology and Science Hyogo-Kobe, Japan (2015).*

Space Propulsion Optimization Code Benchmark Case: SNRE Model

Vishal Patel[1,2], Michael Eades[1,3], Claude Russell Joyner II[4]

[1]*Center for Space Nuclear Research, 995 University Blvd., Idaho Falls, ID 83401*
[2]*Department of Nuclear Engineering, Texas A&M University, College Station, TX 77843*
[3]*Nuclear Engineering Program, The Ohio State University, Columbus, OH 43201*
[4]*Aerojet Rocketdyne, P.O. Box 109680, West Palm Beach, Florida 33410, USA*
832-334-9762; vkp93@tamu.edu

Abstract. The Small Nuclear Rocket Engine (SNRE) was modeled in the Center for Space Nuclear Research's (CSNR) Space Propulsion Optimization Code (SPOC). SPOC aims to create nuclear thermal propulsion (NTP) geometries quickly to perform parametric studies on design spaces of historic and new NTP designs. The SNRE geometry was modeled in SPOC and a critical core with a reasonable amount of criticality margin was found. The fuel, tie-tubes, reflector, and control drum masses were predicted rather well. These are all very important for neutronics calculations, meaning the active reactor geometries created with SPOC can continue to be trusted. Thermal calculations of the average and hot fuel channels agreed very well. The specific impulse calculations used historically and in SPOC differed so mass flow rates and impulses differed. Modeling peripheral and power balance components that do not affect nuclear characteristics of the core is not a feature of SPOC and as such, these components should continue to be designed using other tools.

INTRODUCTION

The SNRE was the last engine studied in the Rover/NERVA program in the early 70s. It was meant to be an engine that incorporated all lessons learned during the NERVA program to produce a state-of-the-art NTP design. The program was unfortunately canceled before the SNRE could be built, though a relatively mature design was developed. As such, the SNRE design is a prime candidate for validating new design tools by modeling the SNRE in the new tool. The goal of this paper is to present results of modeling the SNRE within the SPOC tool to further validate the use of SPOC for new NTP designs.

SPOC

The SPOC tool [1] creates optimized NTP designs by performing parametric design analysis given some system constraints, typically core pressure, reactor thrust, and maximum allowable fuel temperature. SPOC creates MCNP inputs based on highly customizable user inputs, and then analyzes MCNP outputs for all relevant performance criteria. The tool is setup to accept different fuel forms, as long as they are NERVA-derived fuel elements (hexagons of any size with any number of variably sized coolant channels). This means LEU and HEU fuel versions of carbide and cermet fuels can easily be modeled. Other more exotic fuel types can also be added with little effort. An average and hot channel analysis is used to determine fuel element temperatures by using power profiles found through MCNP.

SPOC focuses on the nuclear core geometry and as such was not built to be as flexible in modeling core peripheral elements. Most non-nuclear parts of the core are created based on HEU cermet reactors where the fuel was used as support instead of tie-tubes. This means the SNRE cannot be exactly modeled with SPOC without updates. Fortunately, the non-nuclear components do not have much impact on calculations performed in SPOC.

ESTABLISHING A BASIS OF COMPARISON

Core dimensions were taken from the SNRE final report [2] and input into SPOC. The report estimates masses for each component and SPOC calculates masses for each modeled component. The dimensions of the SNRE were not well documented in the report (e.g., in one clearly labeled diagram) but they could be determined from component descriptions in the final report. The SNRE core dimensions used in the SPOC model are listed in Table 1.

Masses reported in the general results section of the SNRE final report are lumped in large "bins", so a component-to-component comparisons cannot be made. Within the component level descriptions, mass estimates are generally available, so they are used for comparison. Hardware that is not modeled in SPOC is not included in the SNRE mass descriptions so that the best comparison can be made. This is stated because previous SNRE comparisons in literature tend to use the larger mass bins reported in the SNRE final report. This can lead to error canceling where some subcomponents are over-estimated and others under-estimated, but the sum of the components is seen as correct.

TABLE 1. SNRE Component Description and Engineering Characteristics.

Component	Dimension (cm)
Fuel:	
Fuel flat to flat	1.91
Coolant Channel Pitch	0.41
Coolant Channel Radius	0.13
Element coating Thickness	0.005
Channel coating Thickness	0.01
Fuel Height	89
Tie-Tube:	
H Supply Channel Outer Radius	0.2095
Supply Channel Clad Outer Radius	0.2605
ZrH1.8 Outer Radius	0.584
H Return Channel Outer Radius	0.678
Return Channel Clad Outer Radius	0.705
ZrC Insulator Outer Radius	0.8065
Flat to flat	1.91
Core Periphery:	
Outer Radius of Fueled Region Making up Insulator	29.5
Outer Radius of Slats	32.76
Inner Radius of Reflector	33.65
Outer Radius of Reflector	48.35
Outer Radius of Vessel	48.93
Control drum Inner Radius	6.15
Control drum Outer Radius	6.35
Component:	**Total**
Fuel Elements	564
TT Elements	241
Coolant Channels per Element	19
Control Drums	12

SPOC Modeling Deficiencies Identified

SPOC focuses on neutronics, which generally requires only modeling major system components that are external to the active core. This means hardware such as turbines, pumps, electrical systems, actuators, etc. are not modeled. Mass estimates for these components are therefore not available from SPOC. The fuel and tie-tubes were well

modeled, but the core periphery, reflector, support plate, pressure vessel, and radiation shield all had small issues that will be described in this section.

The most flexible part of SPOC is the fuel element / tie-tube configuration modeling (materials, densities, layout, dimensions, etc.). This is the most neutronically important part of the engine. The peripheral components such that the insulator, wrapper, and slats with tie tubes just outside of the fuel elements are not as flexible, and cannot be accurately modeled in the current version of SPOC. The exact differences can be seen in Fig. 1.
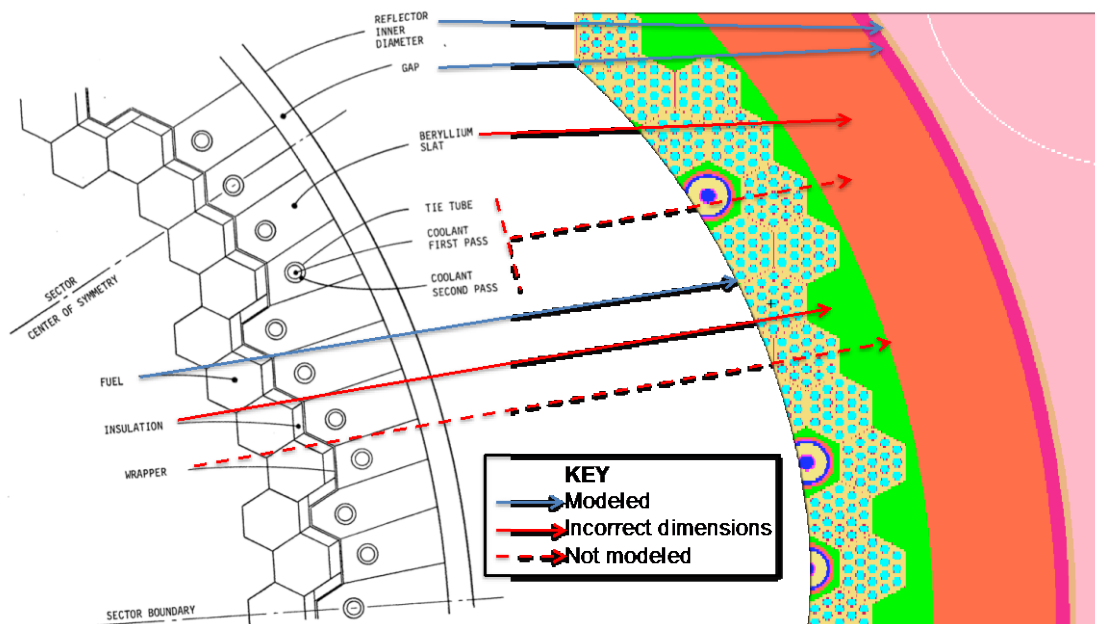
FIGURE 1: SNRE (left) / SPOC (right) Core Periphery Comparison.

The SNRE reflector has coolant channels to cool the reflector and control drums. These channels are also not modeled within SPOC because they should be unique to the design as the channel characteristics depend on the cooling requirements, whereas SPOC attempts to find point designs to perform further analysis on. SPOC focuses on characterizing large design spaces so the details of the reflector coolant channels are ignored. To mimic the presence of coolant channels in the reflector, a simple analysis of comparing criticality between the as modeled SNRE and the SNRE with 90% of the reflector thickness reveals a loss of 1205 pcm of reactivity. The smaller reflector reactor still has a good criticality margin.

The support plate in SPOC is not modeled exactly as the SNRE so a comparison could not be made here either. The support structure in SPOC currently assumes the tie-tubes are not the main support structure because SPOC was initially designed for cermet reactor design, which allows for the fuel to be the support structure. However, geometrically similar to the SNRE support plates above the axial core can be modeled in SPOC. The only difference between the SNRE plate and the SPOC model is that the fuel coolant channels are modeled as a feed-through in SPOC whereas there is an entrance plenum with one large coolant channel in SNRE.

The SPOC pressure vessel region around the active core is modeled to the SNRE specs; however, the SNRE pressure vessel thickens at the bottom and top ends near the nozzle and turbo-machinery respectively. The thicker portions are not modeled in SPOC. SPOC also encloses most components of the rocket in the vessel, which is likely not representative of a realistic design.

The internal radiation shield can be modeled in SPOC as two plate-like regions above the upper hydrogen plenums. Each plate has coolant channels similar to the fuel element channels. The cooling requirement of the shield is

different than the fuel elements. This presents another small issue in SPOC. SPOC is not meant for shielding analysis but could be used in the tool chain required for such analysis.

The SNRE final report's fuel loading method was used to radially load the fuel with different uranium loadings. No axial loading was performed for the SNRE, mainly because the fuel extrusion process did not allow for axial loading control. The fuel is loaded by taking a digitized version of the radial power profile reported, inverting it and then renormalizing the inverted profile such that the maximum value lies at 0.64 g/cc.

The SNRE control drums were an unfinished design so a detailed model was not reported. It is known that the control material was BCu, but the stoichiometric ratio is unknown. A phase diagram of the material was found in [3], and the BCu was modeled with 10 a/o B and the remainder Cu. Both natural B and 90% enriched ^{10}B was modeled in SPOC. The natural B system gave a control drum swing of 9$, but neither drum material could keep the core subcritical when drums were fully inserted. It was deemed that this issue could not be resolved without further research but because the drum design was reportedly incomplete, the issue should not be further investigated. However as a compromise, during all analyses the drums were turned such that the radial power peaking factor was approximately 1.2 in an attempt to get the correct power profile shape. B_4C was used in the drums of the following SPOC analysis to allow for drums that are about 60 degrees out when the radial peaking factor was 1.2 to match SNRE reports.

SNRE RESULTS COMPARISON

The SNRE was modeled in SPOC using the dimensions of Table 1 and is introduced as the SNRE-TNG here. Mass estimates from SPOC are shown in Table 2. To recap, some of the known differences between the SNRE final design report model and SPOC are:

Not Included in Model
- Insulator/Wrapper
- Support Plate
- Tie-Tubes in Slats
- Coolant Holes in Reflector

Not Modeled
- Slats
- Pressure Vessel
- Shield

It can be see that the fuel elements are well estimated. The tie-tube elements are a bit off, likely due to the ZrC density used in SPOC (60%), which is slightly off. The Be reflector in SPOC is over-predicted, but adding coolant channels in the reflector should being that mass down. The control drums are a bit large in SPOC. The SNRE final report includes the tie-screw in the control drum and coolant channels in the drum and reflector. The slats (known to be incorrectly modeled) are reported to show it is under-estimated by a factor of two. This mass would increase if the insulator was modeled properly. The pressure vessel is unpredicted, but also incorrectly modeled. Of the four components SPOC was designed to model for neutronic concerns, the total mass calculated are similar.

TABLE 2. SNRE Masses Comparison (Units in kg).

Component	SNRE	SNRE-TNG
Fuel Elements	433.0	437.57
Tie-Tubes	240.97	223.74
Be in Reflector	301.83	336.22
Control Drums	184.1	213.80
Total (above)	1160.0	1211.0
Slats	35.37	16.39
Pressure Vessel	150.2	87.65

Power profile

The power profile was reported in the SNRE final report as a typical cosine shape with an offset. This profile is compared to the profile found with SPOC in Fig. 2. The SPOC profile is peaked slightly closer to the core inlet than the SNRE. This is likely due to BeO filler that is used between the hydrogen plenum and core inlet to allow for a sensible geometry in SPOC. This material should be changed to something with less reflecting properties in SPOC, or the geometry modeled correctly to remove the need for this filler in SPOC. The calculation accuracy of design tools for the SNRE could also be the cause of this difference. In general, the shapes agree rather well, especially considering the good alignment in thermal characteristics shown later.
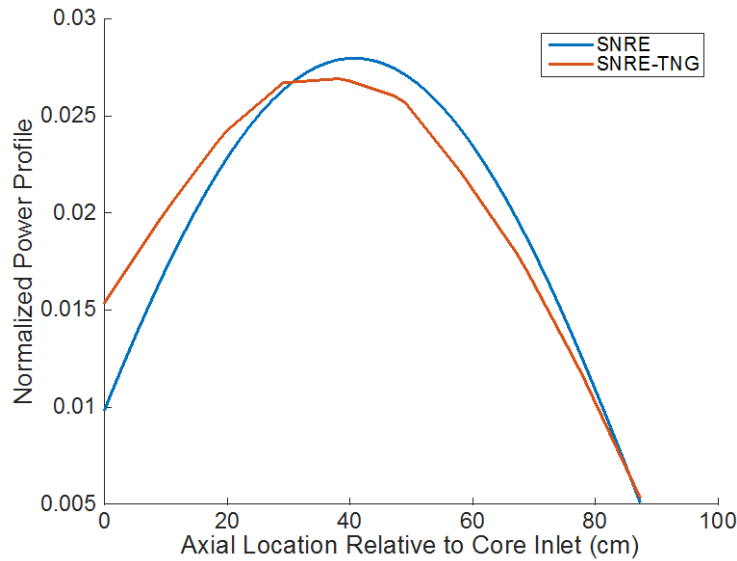
FIGURE 2. SNRE and SNRE-TNG (modeled) Power Profile Comparison.

Neutronic Characteristics

Historical calculations were performed with approximate models of core neutronics. Most analyses were performed using 1D discrete ordinances (S_4) with 25 energy groups combined with axial buckling factors to approximate leakage. Two-dimensional calculations were performed for control drum analysis. The approximations induced by these methods are large enough that it is not expected that they would agree well with full transport calculations. The reported results should not be used like benchmarks. However, results should be expected to agree well within reason, e.g., supercritical eigenvalues from historical and present calculations.

Table 3 compares historical SNRE calculation with modern MCNP calculations. All results agree within reason except for the control drum swing, but that was explained at the end of subsection "SPOC Modeling Deficiencies Identified". The reported reactivities are reported in units of dollars using the SNRE reported delayed neutron fraction. All MCNP calculations had the drums at about 60 degrees so the radial power peaking factors matched.

TABLE 3. SNRE Neutronic Comparisons

Comparison	SNRE	MCNP
k_{eff}	1.058	1.04960 ± 0.00059
Delayed Neutron Fraction	0.0075	0.0071 ± 0.00028
1 cm Reflector Worth ($)	1.2	0.79 ± 0.03
Cold to Hot ($)	-0.4	-0.3 ± 0.04
Control Drum Worth ($)	8.9	18.20 ± 0.03

The criticality eigenvalue reported in SNRE likely assumed no control material such that the core size could be determined from 1D results. Specific eigenvalues for higher fidelity analyses were not reported. The delayed neutron fraction from historical calculations likely used a thermal weighted spectrum for ^{235}U, whereas MCNP calculates the adjoint weighted delayed neutron fraction. The temperatures assumed in cold to hot worth calculations were not reported. The MCNP calculations used temperature profiles from SPOC results with 10 axial bins.

Thermal Characteristics

The SNRE design report addresses cooling issues in all parts of the reactor. Some of the main results are for average and peaked fuel channels to verify the characteristics are in design bounds. These results are then used to determine rocket characteristics, which are needed for mission analysis. Two SNRE design points are reported, the main design is for an 875 s / 16406 lbf (isp/thrust) engine while an alternative design is for 850 s / 16118.8 lbf (isp/thrust). SPOC was used to determine average and hot channel thermal profiles using SNRE reported core inlet conditions, thrust levels, and maximum allowable fuel temperatures. The hot channel was assumed to generate 1.2 times the heat of the average fuel channel and have 1.2 times the average hydrogen mass flow rate. Results are summarized in Table. 4.

The average and peaked core outlet temperatures for the design point and alternative design are both well predicted by SPOC. However, the specific impulse (Isp) predicted between the two design analyses is different. In the SNRE design report, the Isp was calculated from the chamber temperature, which was slightly cooler than the fuel exit temperature. This small temperature difference does not account for the relatively large difference in Isp predictions.

SPOC Isp calculations are based on CEA with a 97% nozzle/chamber/throat efficiency and a normalization to a TDK calculation, whereas the SNRE reports used 1D analysis with approximations from bell nozzle analysis and estimated losses from the regeneratively cooled nozzle and viscous wall effects. The SPOC calculations are considered to be more accurate than the SNRE calculations.

TABLE 4. Thermal Performance Comparison.

	Alt	SPOC Alt	Rel Diff (%)	Design	SPOC Design	Rel Diff (%)
Thrust (lbs)	16118.8	16118.8	(Input)	16406	16406	(Input)
Specific Impulse (s)	860	886.37	3.07	875	899.90	2.85
Core Inlet Temperature (K)	356.4	356.4	(Input)	372.1	372.1	(Input)
Max Temp of the Average Channel (K)	2790	2790	(Input)	2850	2850	(Input)
Max Allowed Matrix Temperature (K)	2860	n/a	n/a	2920	n/a	n/a
Fuel Exit Gas Temperature (K)	2670	2674.16	0.16	2730	2735.42	0.20
Peaked FE Max Temperature (K)	2810	2801.92	0.29	2865	2861.85	0.11
Chamber Pressure (MPa)	3.07	3.65	18.99	3.1	3.64	17.42
Core Pressure Drop (MPa)	0.9	0.35	61.45	0.9	0.36	60.02
Mass Flow Rate (kg/s)	8.51	8.25	3.10	8.51	8.28	2.75
Hydrogen flow per element (kg/s)	0.0147	0.0146	0.54	0.0147	0.0147	0.29
Power per element (MW)	0.63	0.56	11.09	0.65	0.58	11.05
Thermal Power (MW)	354	345.34	2.45	367	357.49	2.59

Color Key

	No differences if No Color
	Modeled well
	Differences explained in text
	Differences attributed to Isp models

The pressure drop in SPOC is well under-predicted when compared to the SNRE reports. The different Isp's for similar core outlet temperatures will result in different mass flow rates of hydrogen to achieve the same thrust, as shown in Table 3. SPOC predicts a higher Isp so a smaller mass flow rate is needed to achieve the same thrust. This smaller mass flow rate is one contributing factor the smaller pressure drop observed in SPOC. Furthermore, SNRE

reports core inlet pressures, not fuel element inlet pressure, which is what SPOC uses. The geometric form loss of going from a single large channel to the 19 fuel element channels is not calculated in SPOC and is not reported in the SNRE final report but is lumped in to the core pressure drop reported. These two effects likely explain the observed differences in pressure drop.

The total power reported by SPOC is the total power needed to close the cycle and is calculated using a simple enthalpy balance from the tank to core outlet to determine the heat input required. This calculation is used because a power balance is not currently available in SPOC to account for neutron and gamma heating in core structures. It is assumed that 14 MW of heat is regenerated in nozzle such that the heat input found in the previous calculation minus the 14 MW from regeneration is the total core power. Using just the core power from SPOC thermal analysis, the fission power is 326 MW so the total power calculation performed here is reasonable.

A peculiarity was found in the SNRE reported total core flow rate and the fuel element flow rate. If the core flow rate reported is used to calculate the fuel element flow rate, the resulting value does not equal the reported fuel element flow rate. The same is true when doing the reverse calculation of using the fuel element flow rate to determine the total mass flow rate. These calculation results are shown in Table 5. It is unclear as to why this is the case. A hypothesis is that there is an assumed hydrogen leakage term somewhere in the SNRE calculations.

TABLE 5. Mass Flow Rate Inconsistencies in SNRE Final Design Report

Comparison	Alt	Rel Diff Alt (%)	Design	Rel Diff Design (%)
Element for rate from total	0.0151	2.64	0.0151	2.64
Total flow rate from element	8.29	2.58	8.29	2.58

SPOC Changes Needed to Model SNRE with more Fidelity

SPOC was found to predict the fuel, tie-tubes, reflector, and control drum masses rather well. These are all very important for neutronics calculations so the active reactor geometries created with SPOC can continue to be trusted.

Peripheral components, originally modeled for cermet reactors, are modeled correctly, but are not robust in nature to model the SNRE. Some SPOC upgrades that would allow for more flexibility in peripheral core modeling are itemized below:
- Channels in reflector and control drums
- Core insulator that straddles the edge fuel element shapes rather than fill a large cylinder
- Coolant tie-tube holes in the slats
- Upper fuel region using one large coolant pipe instead of separate channels will allow for an SNRE support plate to be modeled

These components, for a new NTP design, should be designed based on thermal and structural considerations.

The extra components such as valves, actuators, and turbo-machinery should continue to not be modeled, as the neutronic effect is negligible. However, if neutron-streaming pathways can be identified, the lines feeding different components should be modeled (e.g., coolant channels in reflector and shield). For simple initial estimates, sizing correlations can be implemented based on the power cycle found in SPOC, though the current power cycle is still being revised.

CONCLUSION

The Small Nuclear Rocket Engine was modeled in CSNR's Space Propulsion Optimization Code to create the SNRE-TNG. The goal of this study was not to model the SNRE perfectly, but rather show off current capabilities of SPOC. Though many of the components of the SNRE could not be modeled exactly in SPOC, the modeling differences did not lead to large differences in performance parameters such as thrust, coolant outlet temperatures, and maximum fuel temperatures. Deficiencies of SPOC were identified that would allow for better modeling of the SNRE. SNRE design parameters were also listed in convenient tables for future studies. The major takeaway from this study is that the SNRE can be reasonably well modeled within SPOC, so other core designs produced by SPOC should also be considered well modeled.

REFERENCES

[1] Husemeyer, P., Patel, V., Venneri, P., Deason, W., Eades, M. and Howe, S., "CSNR Space Propulsion Optimization Code: SPOC," in "Nuclear and Emerging Technologies for Space", Albuquerque, NM, Feb. (2015).
[2] Durham, F. P., "Nuclear Engine Definition Study Preliminary Report, Volume 1 – Engine Description," Los Alamos National Laboratory, Report LA-5044-MS Vol 1, Los Alamos, NM, Sept. (1972).
[3] D. Chakrabarti and D. Laughlin, "The B-Cu System," Bulletin of Alloy Phase Diagrams, Vol. 3 No. 1 (1982)

Development of a Sliding and Compliant Cold Side Thermal Interface for a Thermopile Inside a Terrestrial Mini-RTG

Nicholas R. Keyawa, Poyan Bahrami, Gabriel Molina, Velibor Cormarkovic, Samad Firdosy, Richard Ewell

Jet Propulsion Laboratory, California Institute of Technology, Pasadena, CA 91109
Phone: +1-818-354-4355, E-mail: Nicholas.r.keyawa@jpl.nasa.gov

Abstract. Radioisotope Thermoelectric Generators (RTGs) could be an ideal power source for potential applications in remote areas on Earth that require little to no maintenance and stable electrical power over the course of decades. As thermoelectric technology improves, RTG designs are pushing the boundaries in how small they can become in order to meet applications that would require a few watts of electrical power in tight and compact areas. Due to the compact nature of these Mini-RTG concepts, an innovative cold-side thermal interface is required for the thermoelectrics in order to minimize the temperature difference between the thermoelectrics and the thermal sink to optimize the performance of the generator. During assembly, the insertion of the thermoelectrics into the Mini-RTG would require that the cold-side thermal interface slide while maintaining good thermal contact once fully inserted and assembled. In addition, the cold-side thermal interface needs to provide compliance in order to minimize load stresses in the thermoelectrics due to environment vibrations and shocks from potential dropping/handling. In order to assess the performance of the cold-side thermal interfaces, an Electrical Power Demonstrator (EPD) for a Mini-RTG concept was designed and fabricated to mimic the thermal performance of a 1/8th section of the generator. In addition, a Thermal Contact Resistance Measurement (TCRM) Fixture was designed and developed to more rapidly assess the thermal performance of various cold-side thermal interface candidates. The cold-side interface is required to operate at around 170°C, and provide a temperature delta of less than 20°C between the cold side of the thermopile and the contact wall, assuming about 2.2 W/cm^2 of heat transfer through the thermopile. Two potential cold side thermal interfaces were tested: a stainless steel flat spring, and a carbon velvet thermal pad. Each interface was tested using the EPD and TCRM fixture. For testing with the EPD, various aerogel insulation and thicknesses were explored, in addition to operation in both high vacuum and argon cover gas. Results indicate that the carbon velvet thermal pad is the more promising cold-side thermal interface. For future work, the physical properties of the carbon velvet thermal pad are to be adjusted to optimize the thermal performance for this unique potential Mini-RTG application. In addition, bonding techniques of the carbon velvet thermal pad to the cold side of the thermopile are to be further developed.

Keywords: Cold side thermal interface, thermopile, Mini-RTG concept, carbon velvet thermal pad, electrical power demonstrator, thermal contact resistance

ELECTRICAL POWER DEMONSTRATOR

The Electrical Power Demonstrator (EPD) is a fixture which thermally matches the characteristics of the Mini-RTG. In order to accomplish this within a reasonable budget, the EPD is modeled after a 1/8th section of the Mini-RTG. In order to simplify machining, the chamber size was adjusted to generate a trapezoidal prism that will house a heat source within its cavity. This EPD is utilized to verify the thermal performance of the overall Mini-RTG, optimize the Mini-RTG dimensions, and validate the performance of a cold side thermal interface design for the internal thermopiles.

Electrically Heated Heat Source

In order to perform repeatable thermal testing, the heat source of the EPD is electrically heated. Due to its size, a single 0.635cm diameter cartridge heater is used to electrically heat the EPD. The initial design specification stated that the hot side junction of the thermopile of the Mini-RTG could be as high as 600°C, and the radioisotope material is to produce a maximum of 10W of heat. In order to meet these thermal requirements for the EPD, a high power density cartridge heater was chosen that can operate at a maximum temperature of 815°C in vacuum argon, and can generate 150W of heat. Figure 1 shows the heat source. In order to simplify machining and allow the cartridge heater to be replaced, the two ends of the Mini-RTG heater housing are designed as lids that are attached using #0-80 stainless steel screws. The housing and lids are made out of 303 stainless steel. In addition, the heat source length and shape were determined based on the geometry constraints of the Mini-RTG design concept, and optimized to maximize the power output of the thermopiles for a given source of radioactive material.

FIGURE 1. The heat source (with removable lids) utilizes a single 0.635cm diameter cartridge heater to apply heat to the EPD.

Thermopile Simulator

For the initial thermal testing of the EPD, a thermopile simulator that closely matched the dimensions and thermal performance of the actual thermopile was required. To accomplish this, the thermopile is thermally represented by a macor ceramic material. The cross-sectional area, overall length, and surface contact of the macor ceramic thermopile simulator are sized to provide a similar heat flow (taking into account the Peltier and Seebeck effect) that one would see from an actual thermopile, as shown in Figure 2. The thermopile simulator is designed with two #0-80 clearance holes to allow the component to be attached to the Mini-RTG heater housing, which is similar to one of the design options on how the actual thermopile is to be attached to the heater housing.
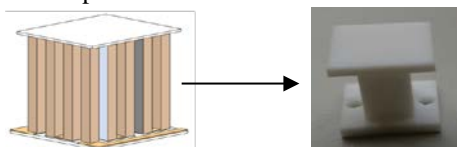
FIGURE 2. Using the thermal properties of the Thermopile (left), a macor ceramic (right) is sized to the approximate dimensions that will match the thermal behavior of the Thermopile.

Heat Source Integration and Aerogel Insulation

Once the heat source is assembled with the thermopile simulator and cold side interface (to be discussed in a later section), the heat source assembly needs to be integrated inside the cavity of the EPD. The heat source is suspended inside the cavity of the EPD utilizing small stainless steel wire ropes. In order to accomplish this, the assembly fixture shown in Figure 3 is used to insert and wire the heat source. A sleeve that spans the length of the cavity is used to guide the heater housing. Attached to the sleeve is a bracket with an attached 0.635cm diameter rod. The heat source (with the stainless steel wire ropes and thermopile simulator already attached) slides onto the rod, and the entire heat source assembly is gently slid into place. The already attached stainless steel wire ropes (shown in yellow) are then wired through the available holes, twisted tight, and set in place with locking screws. Once the guy wires on both ends of the heat source assembly have been made taught, the assembly fixture is pulled out.
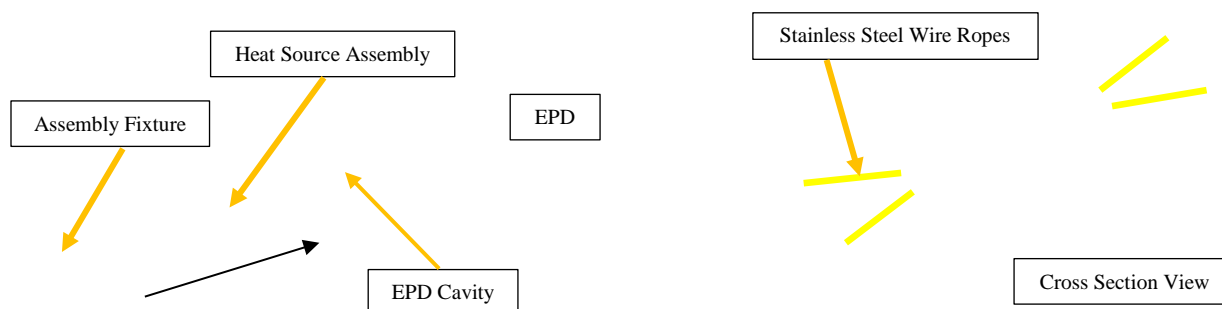
FIGURE 3. The integration and assembly of heat source assembly into the cavity of the EPD.

Once the heat source assembly has been installed (with all the appropriate wiring and cartridge heater) into the cavity of the EPD, a cover plate is set in place on the bottom end of the EPD as shown in Figure 4. This allows the cavity to be filled with aerogel. The aerogel acts as a thermal insulator surrounding the heat source assembly, and allows more heat to travel through the thermopile.
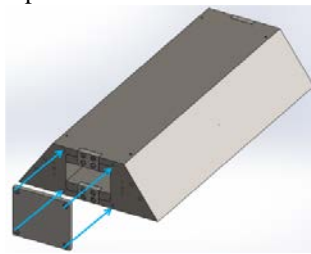
FIGURE 4. A cover plate will be attached to the bottom end of the EPD to allow the heat source assembly to be encapsulated in aerogel.

Aerogel Insulation Thickness Variation: Removable Sleeves

In order to gauge the thermal performance of the EPD at various aerogel thickness dimensions, the cavity is designed to house removable sleeves. These removable sleeves can be sized to a desired thickness and, once installed, they can effectively increase or decrease the width of the EPD cavity as shown in Figure 5. The width of the cavity can be varied anywhere between 2.54cm to 1.75cm. This provides insight during thermal testing as to the optimal cavity size for the EPD, and ultimately for the actual Mini-RTG concept.
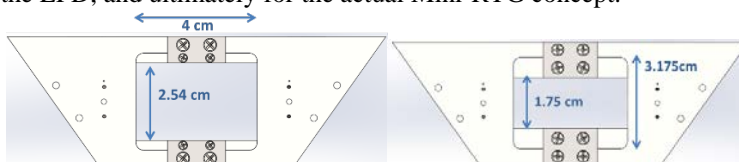
FIGURE 5. Removable sleeves span the length of the EPD, and can vary the thickness of the aerogel by adjusting the width of the EPD cavity.

Cold Side Heaters

In order to control the cold side temperature of the thermopile simulator, two polyimide film heaters are placed on the two surfaces of the EPD that represent the external surfaces of the Mini-RTG, as shown in Figure 6. The desired cold side temperature of the thermopile is to be about 170°C. In order to achieve this temperature, the film heaters were sized to 0.4W/cm^2 with a maximum operating temperature of 200°C.
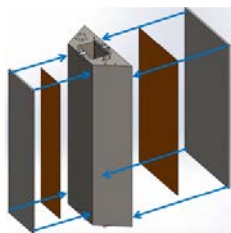
FIGURE 6. Metal plates compress and hold the polyimide film heaters up against the walls of the EPD that represent the exterior walls of the Mini-RTG.

EPD Testing Apparatus

Once the EPD is fully assembled, the fixture is placed on top of the copper plate of the testing stand within a vacuum chamber. As shown in Figure 7, the EPD has four guide brackets that will slide and attach to two guide rods mounted to a base plate. This fixture is placed on the testing stand, where all heater wires and thermocouples will attach to the ceramic standoffs. The copper test plate resides within a bell jar vacuum chamber as shown in Figure 8. The heater and thermocouple wires run through a vacuum rated feed through, and are wired to an instrument rack for data acquisition and temperature control.
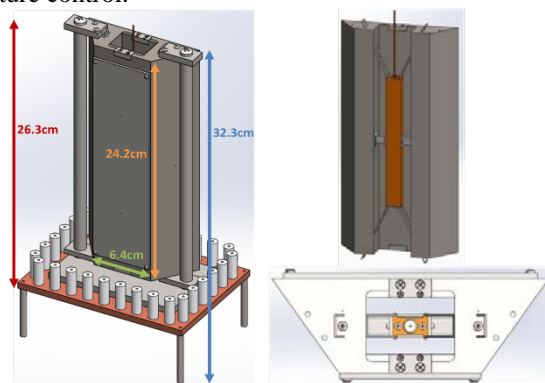
FIGURE 7. The fully assembled EPD is mounted onto the test plate using four brackets and two guide rods mounted to a base plate (left).

FIGURE 8. The copper test plate resides within the vacuum chamber bells jars, and is wired to an instrument rack for data acquisition and temperature control.

Temperature and Power Measurements

To monitor the thermal and power performance of the EPD, sixteen thermocouples are placed throughout the fixture. The type of thermocouples that are used are K-type quick disconnect thermocouples with a 20 mil sheath. The thermocouple sheaths are snug fit into 20 mil holes that were drilled into the desired locations on the EPD. See Figure 9 and Table 1 for the locations of each of the thermocouples on the fixture. In addition, the power from the hot and cold side heaters is monitored during testing. DC power supplies are used to provide constant power to the electrical heaters, and are set to provide a constant heat ranging from 2W to 10W.
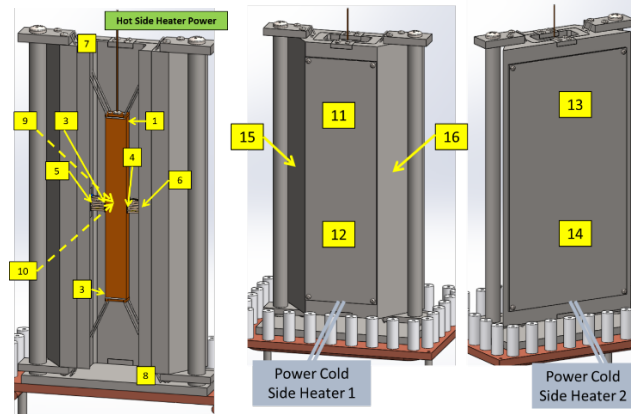
FIGURE 9. The marked locations of all 16 thermocouples on the EPD.

TABLE 1. Location description of thermocouples on EPD

Thermocouple #	Location on EPD
1	Top of heat source container
2	Bottom of heat source container
3	Hot junction of Thermopile Simulator 1
4	Hot junction of Thermopile Simulator 2
5	Cold junction of Thermopile Simulator 1
6	Cold junction of Thermopile TSIM 2
7	Top of Chamber (close to guy wire)
8	Bottom of Chamber (close to guy wire)
9	Midway within Chamber (back wall)
10	Midway within Chamber (front wall)
11	Top of small film heater
12	Bottom of small film heater
13	Top of large film heater
14	Bottom of large film heater
15	Left Side of Chamber
16	Right Side of Chamber

THERMOPILE COLD SIDE THERMAL CONTACT INTERFACE

In order for the actual thermopile to obtain the desired temperature gradient across the thermoelectrics and maximize electrical power output, a good thermal contact interface between the cold side of the thermopile and the interior wall of the Mini-RTG is required. Due to the assembly procedure of the Mini-RTG, the thermal contact interface needs to be able to maintain good thermal contact with the wall while sliding along the wall's surface. In addition, the interface must isolate the thermopile from the vibrations and shock that the Mini-RTG may experience during handling and operation, in order to minimize shear loads on the thermopile. In addition, the thermal contact interface needs to bridge the gap between the cold side of the thermopile and the interior wall of the EPD that is on the order of 0.75mm to 2mm. The thermal requirements for the thermal contact interface are as follows (for vacuum or argon operating environment):

- The nominal hot side temperature of the thermopile is expected to be about 350°C.
- The temperature difference between the cold side of the thermopile and the interior wall of the EPD is to not exceed 20°C.

- The nominal wall temperature is expected to be about 150°C, which means that the desired cold side temperature of the thermopile is to be no hotter than 170°C.
- The heat flux through the thermopile is on the order of 2.2W/cm^2.
- The thermal contact resistance of the cold side interface is to be less than or equal to 9.1 K-cm^2/W, based on the desired heat flux and temperature gradient.
- For the Mini-RTG application, the thermopile is going to be subjected to gamma radiation for about 20 years for a total of 1 Giga Rad of radiation.

Using the above requirements, two potential cold side thermal contact interfaces were pursued: A metal flat spring and a carbon velvet thermal pad.

Metal Flat Spring

A first iteration design approach for the cold side thermal contact interface was a custom flat spring as shown in Figure 10. In order for the legs of the flat spring to maintain full contact with the surface under operational loads, the legs were given a slight bend. The springs were fabricated out of 302 stainless steel at Microphoto Incorporated.
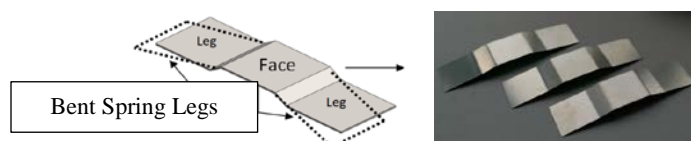
FIGURE 10. The 302 stainless steel flat spring was designed with an additional bend to the legs in order to achieve full flat contact with the surface at operational loads.

In order to test how well the metal flat springs perform thermally in the EPD, the springs need to be bonded to the thermopile simulator. A graphite fixture is utilized to bond the thermopile simulator as shown in Figure 11. The bottom face of the flat spring is placed on top of a square piece of graphite (with a layer of graph foil in between to prevent bonding), in order to apply sufficient loading to the macor thermopile without fully compressing the flat spring. The braze foils chosen to bond the macor to the flat spring are CuSil and Ti since they compensate for the CTE mismatch between the macor and 302 stainless steel. After placing the CuSil between the macor and the flat spring, the top graphite plunger is placed on top with a moly weight. The graphite fixture and moly weight are placed in the braze furnace, a high vacuum is pulled, and the chamber is slowly heated to 825°C. The high temperature is held for about 10 minutes, and the chamber is then slowly cooled.
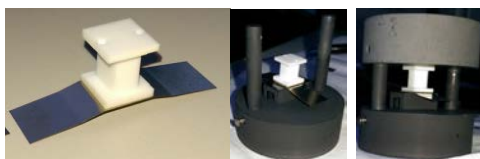
FIGURE 11. A graphite fixture is used to braze the thermopile simulator to the 302 stainless steel flat spring.

After successfully brazing the thermopile simulator to the metal flat spring, the thermopile simulators are attached to the heat source using #0-80 screws and are inserted into the EPD chamber as shown in Figure 12.

FIGURE 12. The heat source with the thermopile simulators and bonded metal flat springs being inserted into the EPD chamber.

Carbon Velvet Thermal Pad

The second iteration design approach for the cold side thermal contact interface was a carbon velvet thermal pad from Energy Science Laboratories Inc. (ESLI), shown in Figure 13 [1,2]. The carbon velvet thermal pad has nano carbon fibers attached to a thin carbon sheet that allows for excellent thermal contact on sliding interfaces.

FIGURE 13. The carbon velvet thermal pad consist of carbon fibers (left) that are attached to a thin carbon sheet (center) which allow for excellent thermal contact while providing spring loaded compliance on a sliding interface.

The carbon velvet pad has the capability of being tailored to obtain desired thermal contact characteristics. Properties that can be adjusted include the diameter of the carbon fibers, shape of the carbon fiber contact tip, carbon fiber compact density, carbon sheet thickness, and carbon fiber length. These carbon fiber pads can typically achieve a an optimal thermal contact resistance of 5 K-cm^2/W (under ideal preload in vacuum or argon), which satisfies this Mini-RTG application requirements[3]. A custom carbon velvet pad tailored to this Mini-RTG application will be discussed later in the report as part of the future work. However, for the initial round of thermal testing, ESLI provided two off-the-shelf carbon fiber pads: a 1.75mm thin carbon velvet pad with an adhesive backing, and a 3.5mm thick carbon velvet pad (as shown in Figure 13). Each pad was bonded to the thermopile simulator using a high temperature rated metallic adhesive, as shown in Figure 14.
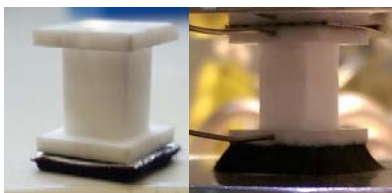
FIGURE 14. Two cold side thermal interfaces were tested with the macor thermopile: a thin carbon velvet thermal pad with an adhesive backing (left), and a thick carbon velvet thermal pad bonded using a metal epoxy.

Once the carbon velvet pads are attached to the thermopile simulator, they would be attached to the heat source and inserted into the EPD as shown in Figure 15.
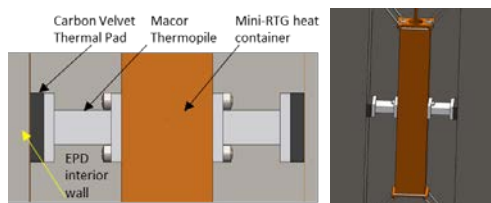
FIGURE 15. The carbon velvet thermal pad interface between the thermopile simulator and the interior wall of the EPD

Thermal Contact Resistance Measuring Fixture

In order to quickly characterize thermal contact resistances of various thermal interfaces for application between the cold side of the thermopile and the interior wall of the EPD, a thermal contact resistance measurement (TCRM) fixture was designed and fabricated as shown in Figure 16. The fixture consists of a manual turning knob which allows the user to controllably lower the hot side cartridge heaters and representative interface onto the test sample. A load cell is available to allow the user to set the desired compressive load onto the test sample. There are twelve holes available to insert thermocouple wires (T1-T12) in order to accurately quantify the heat flux traveling through the test sample.
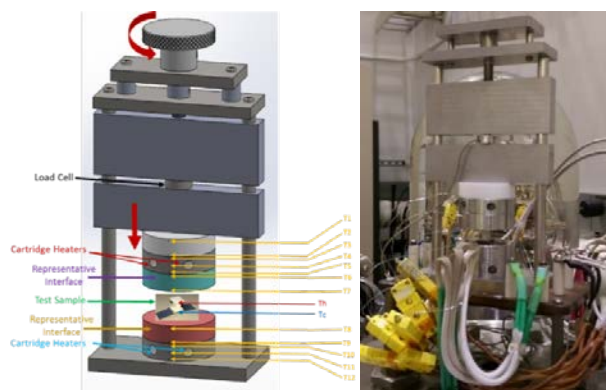
FIGURE 16. The thermal contact resistance measuring fixture schematic on the left and fabricated/instrumented fixture on the right.

Using this fixture, three macor thermopiles with different cold side interfaces were tested. The three interfaces are the stainless steel flat spring, the thick carbon velvet thermal pad, and a thin carbon velvet thermal pad with an adhesive backing, as shown in Figures 11 and 14. For each test sample, the fixture was wrapped in a high purity alumina cloth for heat insulation to reduce heat losses and to more accurately determine heat flux, as shown in Figure 17. Each test sample was instrumented with thermocouples and cartridge heaters, where the hot junction temperature was controlled to 200°C.

FIGURE 17. The TCRM fixture instrumented with high purity alumina cloth, and then placed under high vacuum inside a glass bell jar chamber.

Using the temperature measurements above, the thermal contact resistance between the cold side wall and the cold side of the thermopile simulator was calculated. The results are shown in Table 2. Using the TCRM fixture, the results indicate that the carbon velvet thermal pad has a much lower thermal contact resistance compared to the stainless steel flat spring: 159 K-cm^2/W versus 764K-cm^2/W. Furthermore, when the load was increased for the thick carbon velvet sample (2.2N to 4.5N), the thermal contact resistance increased, suggesting that more load does not necessarily mean better thermal contact. Lastly, the results from the thin carbon velvet sample indicated a drastic improvement in thermal contact resistance. When compared to the thick carbon velvet sample at the same load, the thermal resistance decreased from 159 K-cm^2/W to 47 K-cm^2/W. This is a about a 70% reduction in thermal contact resistance.

TABLE 2. TCRM Fixture data with alumina wrap in rough vacuum

Parameter	Flat Spring (2.2N)	Thick Carbon Velvet (2.2N)	Thick Carbon Velvet (4.5N)	Thin Carbon Velvet (4.5N)
Hot Side of Macor Thermopile (deg C)	200	201	201	201
Cold Side of Macor Thermopile (deg C)	137	105	111	67
Cold Side Wall Temperature (deg C)	35	41	34	40
Heat Transfer Through Macor (W)	0.27	0.40	0.38	0.57
Thermal Contact Resistance Between Cold Side Wall and Cold Side of Macor (K-cm^2/W)	764	159	205	47

EPD TESTING AND RESULTS

After assembling the EPD and attaching all thermocouples and the internal cartridge heater, the chamber is filled with aerogel and allowed to cure over a period of approximately seven days. Once the aerogel has fully dried inside the EPD, the EPD is placed into the vacuum chamber where all the thermocouples and heater lead wires are attached to the system (Figure 18).

Once the EDP is fully instrumented into the system, the bell jar is placed over the simulator and a high vacuum to 10^{-6} torr is pulled. Once under high vacuum, the internal cartridge heater is heated using a constant DC voltage and current input. This cartridge heater represents the radioactive heat source in the Mini-RTG, and the electrical heater input is varied to about 5W, 6W, 8W, and 10W to represent potential different heater inputs. In addition, the polyimide film heaters on the external surfaces of the EPD are heated using AC power to bring up the interior wall temperature. Upon heating the internal cartridge heater to the desired heater output, the system is allowed 24 hours to achieve thermal stability before temperature measurements are recorded. In addition, multiple measurements are made at each heater input in order to further verify that thermal stability has been achieved. The results of the initial round of testing using the metal flat spring cold side interface under high vacuum at varied heater inputs are shown in Table 3. This process is also repeated under an argon environment (~1 atm argon), and the results are shown in Table 4. Table 5 shows the results of EPD testing in argon using the thin carbon velvet sample from Figure 14.
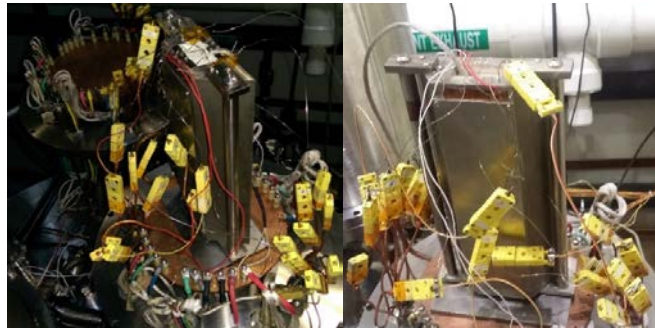
FIGURE 18. A fully instrumented EPD wired into the test chamber.

TABLE 3. Thermal data of the EPD under high vacuum using the metal flat spring cold side thermal

Thermal Parameter	Input Power to Electrically Heated Heat Source (We)			
	DC 14.71V, 0.33A	DC 16.64V, 0.37A	DC 19.13V, 0.44A	DC 21.07V, 0.49A
	4.85W	6.16W	8.42W	10.32W
	Thermal Parameter			
Avg. Hot Side Temp of Macor Thermopile (°C)	318.2	366.95	433.8	488.15
Avg. Cold Side Temp of Macor Thermopile (°C)	218.05	247.55	284.85	319.55
Avg. Inner Wall Temperature (°C)	77.85	89.05	105.1	119.85
Avg. ΔT Across Macor Thermopile (°C)	100.2	119.4	148.95	168.6
Avg. ΔT Across Cold Side and Wall (°C)	140.2	158.5	179.75	199.7
Avg. Q Through Macor Thermopile (W/cm^2)	1.22	1.45	1.81	2.05
Avg. Thermal Resistance of Cold Side Int. (K-cm^2/W)	115.06	109.11	99.19	97.35

TABLE 4. Thermal data of the EPD under argon using the metal flat spring cold side thermal interface

Thermal Parameter	Input Power to Electrically Heated Heat Source (We)			
	DC 14.73V, 0.34A	DC 16.23V, 0.37A	DC 19.13V, 0.43A	DC 21.07V, 0.48A

	5.01W	6.01W	8.23W	10.11W
	Thermal Values			
Avg. Hot Side Temp of Macor Thermopile (°C)	174.15	203.9	264.75	310.3
Avg. Cold Side Temp of Macor Thermopile (°C)	96.4	111.4	141.25	162.65
Avg. Inner Wall Temperature (°C)	36.9	41.0	48.7	53.5
Avg. ΔT Across Macor Thermopile (°C)	77.8	92.45	123.5	147.65
Avg. ΔT Across Cold Side and Wall (°C)	59.5	70.45	92.55	109.15
Avg. Q Through Macor Thermopile (W/cm^2)	0.95	1.12	1.50	1.80
Avg. Thermal Resistance of Cold Side Int. (K-cm^2/W)	62.90	62.63	61.59	60.76

TABLE 5. Thermal data of the EPD under argon using the carbon velvet pad cold side thermal interface

Thermal Parameter	Input Power to Electrically Heated Heat Source (We)			
	DC 14.54V, 0.34A	DC 16.02V, 0.38A	DC 18.17V, 0.44A	DC 20.60V, 0.5A
	4.94W	6.09W	7.99W	10.3W
	Thermal Values			
Avg. Hot Side Temp of Macor Thermopile (°C)	292.8	322.5	368.0	417
Avg. Cold Side Temp of Macor Thermopile (°C)	189.0	194.3	202.2	210.8
Avg. Inner Wall Temperature (°C)	156.15	156.15	156.15	156.2
Avg. ΔT Across Macor Thermopile (°C)	103.8	128.2	165.8	206.2
Avg. ΔT Across Cold Side and Wall (°C)	32.8	38.1	46.05	54.6
Avg. Q Through Macor Thermopile (W/cm^2)	1.26	1.56	2.02	2.51
Avg. Thermal Resistance of Cold Side Int. (K-cm^2/W)	25.97	24.43	22.83	21.76

The results of the EPD testing indicated that the metal flat spring did not provide a good enough thermal contact. For the metal flat spring interface, the temperature difference between the cold side of the thermopile and the interior wall temperature was on the order of 60°C to 200°C (for vacuum and argon environments). In addition, the thermal contact resistances of the metal flat spring cold side interface varied from 60 to 115 K-cm^2/W, depending on if the test was under argon or vacuum. Ideally, the design requires a temperature difference less than or equal to 20°C, and a cold side thermal contact resistance less than or equal to 9 K-cm^2/W. There are two main issues with the metal flat spring design that could be causing this. First, the pressure contact of the flat spring is not sufficient to maintain close contact up against the interior wall of the EPD. Second, aerogel has a viscosity similar to water when it is initially poured into the EPD (before it is cured). This means that the aerogel could easily fill the voids between the legs of the metal flat spring and the interior wall of the EPD, thus creating a poor thermal contact between the two interfaces. In addition, the results show that better thermal contact is achieved in argon compared to vacuum. This is due to the added effect of conduction heat transfer through the argon gas wherever there are voids between two interfaces. In a vacuum, heat transfer can only travel via radiation, which is significantly a much poorer form of heat transfer compared to conduction. However, the results for the carbon velvet thermal interface (Table 5) showed to be much more promising in achieving the design goals. Using an argon environment, the temperature difference between the cold side of the thermopile and the interior wall temperature was on the order of 32°C to 55°C. In addition, the thermal contact resistance of the carbon velvet cold side interface was found to be about 22 to 26 K-cm^2/W. This carbon velvet pad is an off the shelf sample from ELSI and was not tailored to this application. A custom carbon velvet pad would more than likely generate even better results.

Additional testing of the EPD was done to compare various types of aerogel, and at various thicknesses. This led to the design change of using super critical aerogel (which is cured at high temperatures) versus a room temperature cured aerogel. The super critical aerogel provides much better thermal insulation compared to the room temperature aerogel. In addition, the aerogel thickness (dictated by the cavity size of the EPD), was made to be as thick as possible since results showed that the best thermal insulation performance was achieved using the thinnest removable sleeves.

CONCLUSION AND FUTURE WORK

In conclusion, an EPD which thermally represents a section of a Mini-RTG design concept was fabricated in order to test and develop a thermal contact interface between the cold side of the thermopile and the interior wall of the Mini-RTG. Furthermore, a TCRM fixture was designed and fabricated to quickly test various candidate thermal contact interfaces. Two thermal contact interfaces were explored: a metal flat spring, and a carbon velvet pad. Results from both the EPD and the TCRM indicated that the metal flat spring design is not capable of providing a good thermal contact to achieve a temperature difference of less than 20°C. The TCRM and EPD testing revealed that the carbon velvet pad has a much better thermal performance compared to the metal flat spring. For future work, the EPD is to be instrumented and tested with a custom made carbon velvet pad. This test will illustrate how well the carbon velvet pad will perform in a thermal environment similar to the Mini-RTG design concept. Initially, this test was done using an off-the-shelf sample provided from ESLI. Custom carbon velvet pads will be manufactured specifically to meet the design goals of the Mini-RTG concept. In addition, investigation into how to bond these carbon velvet pads to an actual thermopile will be done, and an actual thermopile will be installed into the EPD for thermal and power testing.

ACKNOWLEDGMENTS

REFERENCES

[1] Knowles, Timothy R. "Welcome to Energy Science Laboratories, Inc." Welcome to Energy Science Laboratories, Inc. Energy Science Laboratories Inc., n.d. Web. 04 Dec. 2015. <http://www.esli.com/>
[2] Seaman, Christopher L., and Timothy R. Knowles. "Carbon Velvet Thermal Interface Gasket." Proc. of 39th AIAA Aerospace Sciences Meeting, Reno, Nevada. N.p.: n.p., n.d. N. pag. Print. AIAA-2001-2017.
[3] "VEL-THERMÔ A30B-G2S1: Ultra-high Conductance, Compliant Thermal Gasket." Energy Science Laboratories, Inc., 11 Aug. 1999. Web.

Pyroshock Dynamic Loading Impacts on Thermoelectric Module Assemblies and Bi-Couples in Multi-Mission Radioisotope Thermoelectric Generators (MMRTGs)

Terry J. Hendricks, David J. Neff, Nicholas R. Keyawa, Bill J. Nesmith, Poyan Bahrami, Armen Derkevorkian, Ali R. Kolaini

Jet Propulsion Laboratory, California Institute of Technology, Pasadena, CA 91109

Abstract. Pyroshock testing of the Multi-Mission Radioisotope Thermoelectric Generator (MMRTG) generated undesired dynamic responses during MMRTG qualification unit (QU) and engineering unit (EU) dynamic tests. Pyroshock-driven dynamic responses during testing caused system power output to temporarily decrease by 2-4%, and then fully recover within 10's of minutes after the shock signature subsided. An effort is underway to understand the root causes of the temporary MMRTG power losses, and a detailed system fault tree and associated system analyses have been developed to establish specific root-cause and recovery pathways. Shock-induced loads and accompanying electrical/thermal/structural impacts within the system are currently being modeled. This paper reviews recent findings from MMRTG pyroshock high-frequency wave-propagation dynamic analyses and thermoelectric (TE) bi-couple low-frequency dynamic test results are presented to highlight the potential root-cause mechanisms leading to the power loss and recovery pathways.   SIERRA/PRESTO wave-propagation dynamic analyses have shown that critical MMRTG internal electrical and thermal interfaces are potentially disrupted and rapidly disconnected (within milliseconds) during the transient pyroshock loads. Bi-couple dynamic load testing shows this actually does occur and their electrical and thermal interfaces then do not reversibly recover for relatively long periods of time (10s of seconds), which leads to temporary bi-couple voltage and power losses. The pyroshock dynamic analyses show that this disruption/recovery scenario can be projected to occur across multiple couples of the 768-couple MMRTG due to incident and reflected shock waves throughout a TE module bar assembly. Shock wave propagation impact on MMRTG structural compression components and interfaces, subsequently altering the electrical circuit networks, electrical contact interfaces, thermal networks and interfaces within the MMRTG, is then evaluated and quantified through electrical and thermal modeling to predict potential MMRTG-wide power losses. Results are correlated and tied to system fault tree pathways to identify and prioritize likely causes and recovery mechanisms. This work reviews the latest TE bi-couple testing results obtained from new bi-couple dynamic load testing at representative MMRTG bi-couple temperatures (T_h = 510°C, T_c = 210°C). The new dynamic load test results qualitatively replicate the power loss and recovery profiles and observations originally seen in the MMRTG EU and QU testing under pyroshock environments, and provide new understanding into its potential causes and recovery profile. The combination of computational and experimental techniques is providing new insights to track and predict MMRTG pyroshock effects and impact magnitudes. We also discuss current plans to design and execute a TE-module-assembly pyroshock test to demonstrate pyroshock-driven effects on power at the TE module assembly-level, which will simulate 3-dimensional pyroshock wave propagation into and through the TE module assembly and measure the resultant dynamic effects (i.e., local accelerations/displacements) on TE bi-couples and module power output. Results presented help to understand root causes of the pyroshock anomaly observed during MMRTG shock qualification testing and recommend corrective or mitigating MMRTG design techniques.

Keywords: Pyroshock effects, shock wave propagation, thermoelectric generators, bi-couple dynamic loading

INTRODUCTION

The Multi-Mission Radioisotope Thermoelectric Generator (MMRTG) was built by DoE under a NASA managed contract. A series of MMRTG pyroshock qualification tests, using first an Engineering Unit (EU) and then a Qualification Unit (QU), were performed to qualify this hardware as part of the Mars Science Laboratory (MSL) mission. The first pyroshock simulation test was performed in 2006 and the results from this activity is documented in comprehensive reports [1, 2]. The EU was mounted on a ½" thick large steel plate and the required shock was simulated using primacord detonated on the bottom surface of the plate. Several steps were taken to calibrate the required shock environments using a mass mockup. However, the peak shock level with the EU mounted on the plate exceeded the nominal requirement of 6,000 peak g's above 1,600 Hz and reached close to 20,000 g's at ~3,500 Hz [2], thereby over-testing the EU relative to the multi-mission shock requirement. A significant MMRTG power loss was observed during the EU shock test within a few milliseconds of the pyroshock event, which then recovered several minutes (~10s of minutes) after the pyroshock-driven power-loss event. The concern about the loss of EU power led to performing an additional Qualification Unit (QU) test.
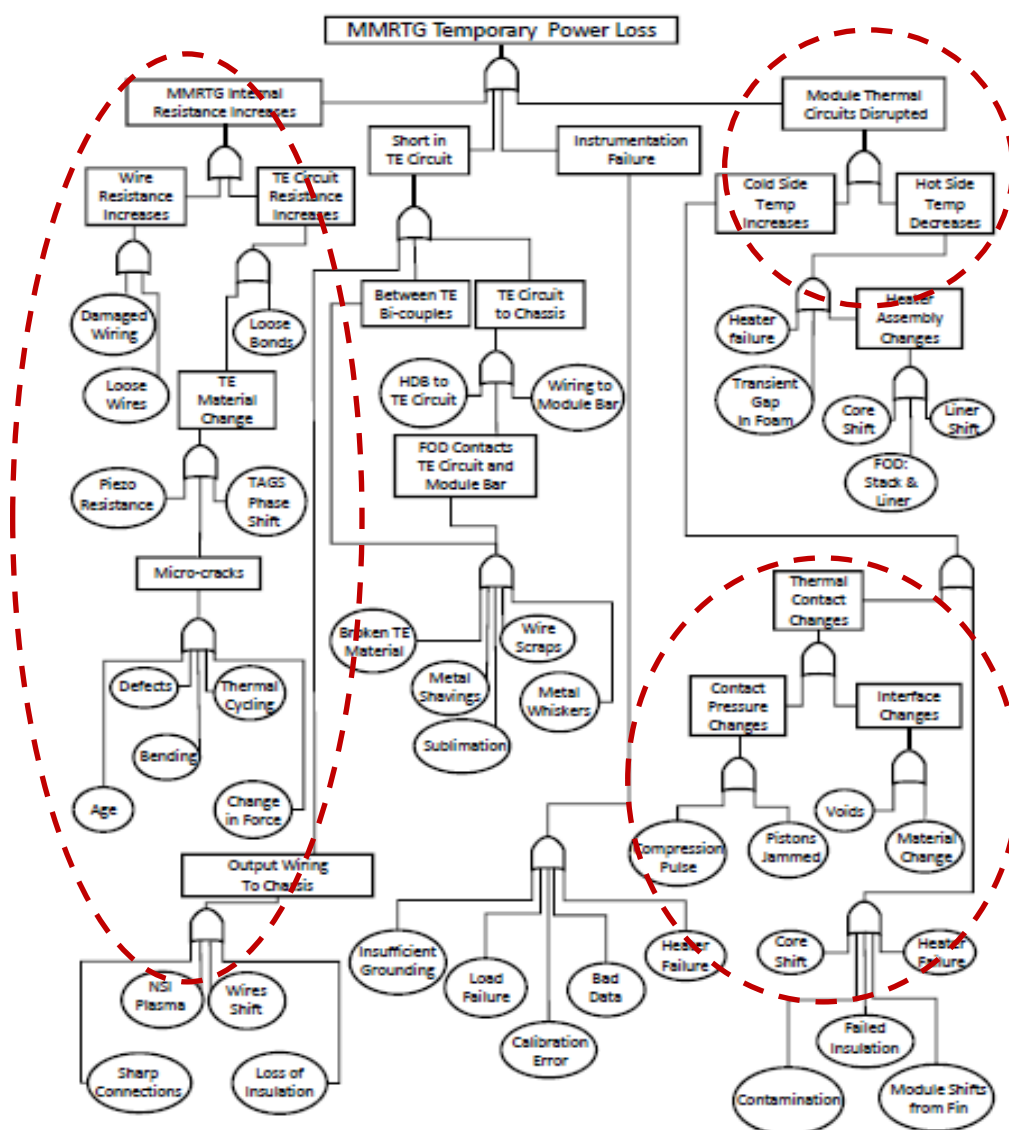

FIGURE 1.   MMRTG Pyroshock-Induced Root-cause Fault Tree Guiding this Study. Red-dotted Regions Show Focus Areas Resulting From and Targeted in this Work.

The QU test was performed at JPL by mounting it on the flight MSL rover chassis [3], where flight-like separation nuts were fired. This test, which was performed at lower shock levels than the multi-mission environment using a flight-like configuration and flight-like separation devices, was intended to gain more understanding about the power drop issue that the generator would experience during the MSL shock environment, The results from the QU pyroshock test confirmed that the generator would respond to a flight level pyroshock event with a temporary power drop, although significantly less severe than that experienced by the EU shock test, and were used to assess flight-readiness hardware risk. Due to the schedule constraint, the root causes of this anomaly were not investigated and MSL was launched with acceptable risk level.

In preparation for the Mars 2020 and future potential missions, the root causes of the MMRTG power drop are being investigated. The first technical paper showing initial progress on root causes was presented at the 2015 NETS (Nuclear and Emerging Technologies for Space) conference in February 2015 [5]. The project team now reports on further highly significant progress made in TE module assembly dynamic modeling, critical low-frequency dynamic testing on bi-couples that has at least qualitatively replicated the power loss behavior observed in EU and QU testing, and begun quantitatively relating the bi-couple level test results to MMRTG-level power losses through mathematical modeling at the bi-couple-level and MMRTG-level.

An updated root-cause fault tree has been created from previous MMRTG pyroshock case studies and test reports. Figure 1 shows the current fault tree with suspect root-cause branches currently being investigated. This was first presented at NETS 2015 [5]. This fault tree shows that the power drops are most likely caused by pyroshock-induced dynamic events that trigger a combination of electrical circuit impacts, thermal network impacts, and/or TE materials impacts which may be interrelated. The current belief is that the pyroshock-induced power drops and recovery occur from a two-step process: 1) An electrically-generated or thermally-caused response in key MMRTG components having a time-constant on the order of milliseconds emanating from a pyroshock dynamic event, followed by 2) A mechanical-thermal recovery response in MMRTG components having a time-constant on the order of 10's of minutes. Work has focused on analytically and experimentally identifying and quantifying dynamic environments that could induce the electrically-generated or thermally-caused response in key MMRTG components. Critical MMRTG components would include the thermoelectric (TE) couples themselves, the couple interconnect materials, the TE couple or TE module electrical connectors and current collectors, the spring-loaded pistons in the TE module bar interfacing on the cold-side, and resulting cold-side and hot-side thermal connections to the TE couples. In order to decipher this potentially complex series of pyroshock-induced dynamic events and resulting electrical-thermal response events causing the power drops, our work focused on employing a combination of SIERRA/PRESTO-based pyroshock dynamic models, bi-couple dynamic testing in a newly-developed bi-couple dynamic load chamber that can provide dynamic loads to bi-couples while simultaneously exposing them to representative MMRTG bi-couple temperature levels and temperature differentials, and analytic power loss results from bi-couple-level and MMRTG-level mathematical models in Matlab/Simulink and Excel. This combination of tools is allowing the team to draw a link between the dynamic causation events and the electrical-thermal responses leading to the observed power drops. Accomplishments and progress this year have now allowed the project team to focus on the red-dotted regions of the root-cause fault tree shown in Figure 1 as the likely causes of the pyroshock-driven MMRTG-level power losses observed in the EU and QU. Instrumentation failure has been eliminated a possible cause due to the repetitive nature of the pyroshock effects in multiple tests and normal successful instrumentation calibration procedures. This technical work follows and complements a most recent technical paper on structural dynamic modeling of the MMRTG TE module assembly given at IMAC-*XXXIV* Conference and Exposition on Structural Dynamics [6].

TE MODULE ASSEMBLY PYROSHOCK DYNAMIC ANALYSIS

Preliminary transient dynamic analysis was initially performed in the low frequency range (i.e., 50-750 Hz) using the MMRTG finite-element model developed in FEMAP/NASTRAN. The results of this analysis were reported in [5]. It was also necessary to analyze and capture the high frequency and shock wave propagation behavior at the MMRTG TE module level to completely investigate critical dynamic effects and behaviors and explore key areas of the fault tree in Figure 1 that could explain the pyroshock-driven MMRTG power loss observations. It is not trivial to capture the structural dynamics due to shock wave propagation within complex contact mechanisms using

traditional finite-element solvers. The challenges are partly due to the high frequency range of interest (i.e., up to 10 kHz), as well as the computational size of the models that is required to potentially capture responses in those high frequency ranges. There is an ongoing effort in the aerospace community to develop viable techniques that could predict the response of complex structural and mechanical systems to shock wave propagation [7, 8]. The authors provide a more comprehensive list of some of the important contributions in this area in [6].

As part of the TE module assembly pyroshock dynamic analysis, a suite of multi-physics numerical solvers known as the SIERRA suite were used. Sandia National Laboratories developed SIERRA Solid Mechanics suite and embedded sophisticated numerical packages to solve complex physical phenomena. For this investigation, a combination of implicit (ADAGIO) and explicit (PRESTO) solvers was used from the SIERRA Solid Mechanics Suite to simulate the dynamic behavior of a TE module assembly when subjected to high-frequency shock loads. PRESTO's explicit dynamics features are designed to solve models having various contact surfaces and subjected to large, suddenly applied loads, such as the TE module assembly under investigation in this paper. More details on the capabilities of SIERRA suite can be found in [9].

Figure 2(a). Before preload

Figure 2(b). After preload

Figure 2(c). Measured acceleration records
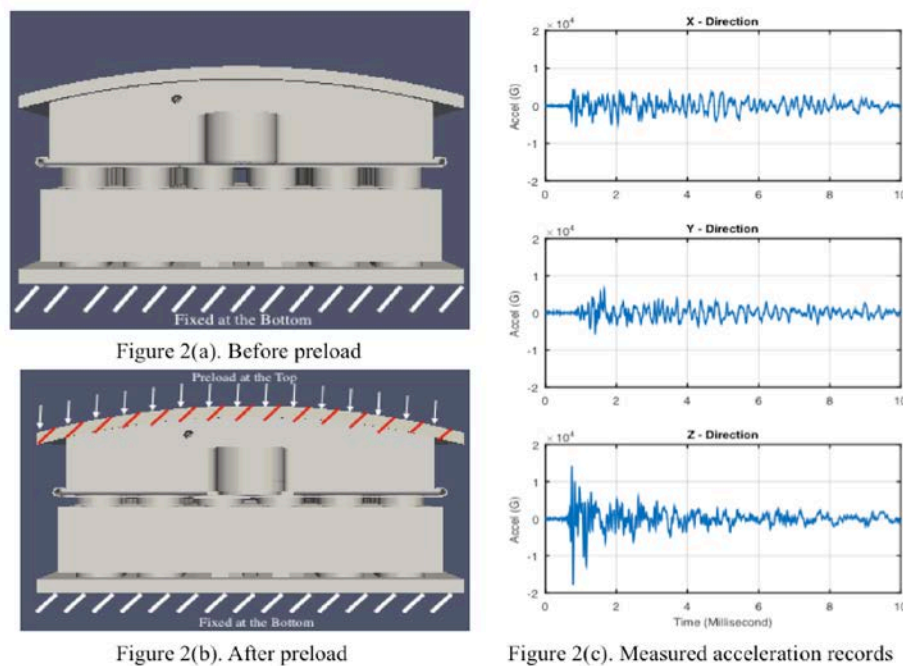
FIGURE 2. Left Column: Side view of the TE module assembly model (before and after the preload). Right Column: Measured acceleration records.

A finite element mesh of the TE module assembly was created using a preprocessor called Cubit. The model was discretized into ~11.5 million elements. The system loading was applied in two steps. The springs within the model were compressed in the vertical direction by applying a quasi-static load to model the pre-load applied to springs in the gravity direction (Step 1). The shock environment was then applied (Step 2) as an input to the model after the application of the preload. Figure 2(a) shows the assembly model before the preload and Figure (2b) shows the assembly model after the preload. The shock input to the model was obtained by recovering the displacement time-history, derived from measured 3-dimensional shock acceleration records from a previous Engineering Unit (EU) qualification test (in all three directions simultaneously). The measured acceleration records are shown in Figure 2(c). The displacement time-histories were applied as inputs to the FE model at the short edge of an interface plate located on top of the TE module assembly to predict the nonlinear dynamic response of the module bar's inner components. The short edge of the top interface plate on which shock loads were applied is highlighted in red lines in Figure 2(b).

Several contact surfaces were modeled with frictional force applied within the inner components of the system. A preliminary coefficient of friction of 0.5 was assumed. The coefficient of friction between the various interfaces of the assembly will be experimentally determined and used for upcoming computational simulations. The quasi-static

preload was applied for the first 5 milliseconds using implicit ADAGIO solver. The shock displacement inputs were applied using the explicit PRESTO solver. Reaction forces at the bottom of the TE model, as well as the Von Mises stresses, at various locations were recovered for the duration of the pyroshock input signatures. Total running time for both implicit and explicit solvers was approximately 60 hours using 3000 processors at NASA AMES Research Center. The quasi-static load was applied to achieve the vertical preload of approximately ~25 N at the bottom of the hot shoes, before the transient shock loads. It is worth mentioning that the input shock signatures were different in all three directions (based on the measured data from the EU and QU shock qualification tests). The signature with the largest amplitudes was in the vertical Z-direction. Peak displacements in the Z-direction were higher by an order of 2 compared to X and Y displacement signatures. Peak amplitudes in X and Y signatures were relatively similar, with slightly higher peaks in the Y-direction. Figure 2(c) shows the measured acceleration datasets.

Figure 3 shows the maximum predicted reaction forces at the bottom of the hot shoes. The maximum values were computed by taking the absolute value of the largest peak in the force reaction time history of each shoe. The left subfigure shows the maximum reaction forces in the X-direction. The X-direction in this analysis is along the short edge of the assembly, highlighted in red stripes in Figure 2(b). The average maximum force, R_x, is 24.6 N, which is very close to the vertical preload applied to springs. The middle subfigure shows the maximum reaction forces in the Y-direction. The Y-direction is along the long edge of the assembly (i.e., into the plane). The results show that average maximum reaction force at the bottom of the shoe, R_y, is 34.1 N, which is expected since the input in the Y direction was slightly higher. The right subfigure shows the maximum reaction forces in the Z-direction. As shown, the average maximum reaction force, R_z, is 143.8 N, which is more than 5 times higher than the initial 25 N preload. The larger reaction forces in the Z-direction are partly due to the initial preload as well as the larger shock input displacement. However, as seen in the figure, some locations (e.g., X2-Y1 and X4-Y1) exhibit forces that are nearly 20 times the initial preload. The high reaction forces may be due to spring dynamics at their resonance frequency and possible impact/contact between the springs and the side walls of the pistons, as observed in this numerical analyses. Ongoing investigation continues to further analyze the observed high reaction forces and correlate them with the input displacement signals. As part of this investigation, a tunable-beam shock test of the TE module assembly is being designed and fabricated, to experimentally validate the numerical results. Further analysis of the results revealed that there were various instances throughout the simulation where the bottom of the shoes offloaded (i.e., $R_z = 0$ N) due to shock wave propagation induced loads. The sudden changes in the reaction forces (i.e., offloading) can potentially cause severe anomalies in the power output of each assembly due temporary loss of electrical and thermal contacts in the TE module assembly. A sample reaction time history is shown in Figure 4. This time history shows the bi-couple experiences several overloading conditions and several complete unloading events during the pyroshock duration. Furthermore, springs that are preloaded inside the assembly, undergo excitation at a resonant frequency of about ~3 kHz during the transient shock load, and tilt sideways from their initial vertical position to make contact with the surrounding piston walls. This spring excitation at the specified resonant frequency is well within the frequency spectrum range of a typical pyroshock environment. Spring resonance itself may also point to a serious design concern. These observations may play important roles in understanding the root causes of the power drop discussed earlier. More details on the results from this analysis can be found in [6]. Findings obtained from detailed, high-fidelity SIERRA/PRESTO numerical analysis were not obvious before the shock qualification tests for the MSL project and could not be obtained from traditional modal-based low-frequency finite element transient analysis approaches. As mentioned earlier, in addition to the promising insights obtained from the high-fidelity wave-propagation dynamics analysis, further analysis and testing are needed as part of a model verification and validation plan. The project team is currently designing a TE module assembly shock test using a tunable beam shock simulation system to verify and validate these results.
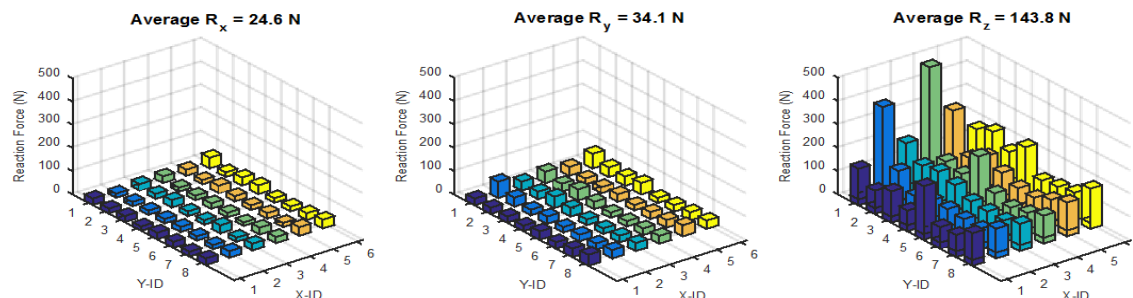
FIGURE 3. Maximum reaction forces at the bottom of the hot shoes in all three (X,Y,Z) directions. Note that in the right subfigure, the initial 25 N preload in the Z-direction is marked on the bottom of each bar.
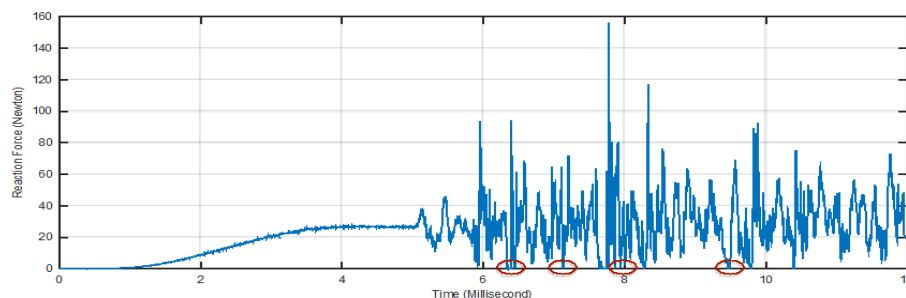
FIGURE 4. A sample reaction force in the Z-direction, captured at the bottom of one of the shoes. Red circles show multiple unloaded conditions.

TE BI-COUPLE TESTING

The pyroshock-driven dynamic vibration of bi-couple springs/pistons at a resonant frequency described in section 2.0 can potentially result in a rapidly varying spring load on individual legs of MMRTG TE couples. Figure 1 hypothesizes that this spring load variation alters couple electrical and thermal contact resistances throughout MMRTG TE modules, thereby resulting in a temporary reduction of MMRTG power output. In order to experimentally investigate this potential causation process an apparatus was designed to dynamically vary the spring load on four bi-couples at MMRTG operating temperatures in an argon cover gas environment. The Dynamic Load Test Station (DLTS) in Figure 5 is capable of monitoring the output power, internal resistance, and gradient temperatures of four independent bi-couples stations while dynamically varying the spring load on each.
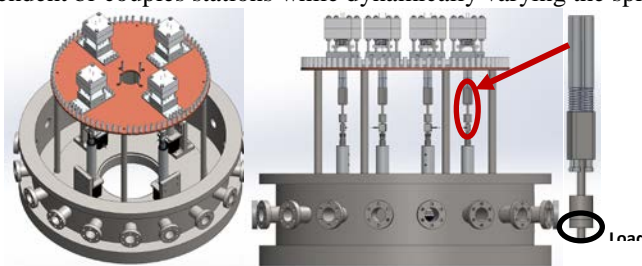
FIGURE 5. The Dynamic Load Test Station.

The Dynamic Load Test Station Design

The DLTS is capable of varying the spring loads of four individual bi-couples with either the same dynamic loads applied simultaneously or different dynamic loads applied on each bi-couple. A load cell in line with the spring piston mechanism (as shown in Figure 5 above), provides the amount of spring load on all 4 individual legs of the MMRTG bi-couple. Each individual bi-couple is supported in a mini module as shown in Figure 6. The mini module

consists of a hot side cartridge heater (capable heating up to 1200°C) surrounded in high purity alumina ceramic (Zircar - ZAL-45AA) for thermal insulation.
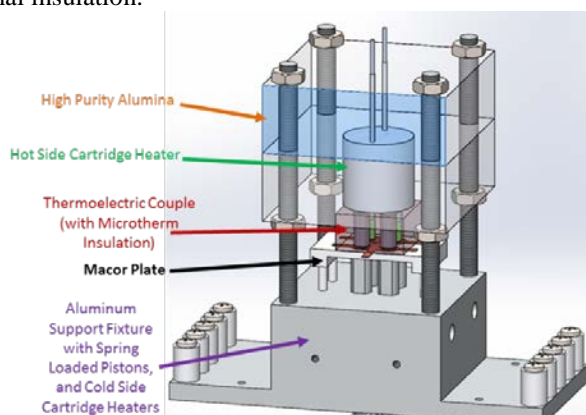
FIGURE 6. The mini module used to support the MMRTG bi-couple.

The MMRTG bi-couples are PbTe, PbSnTe, and TAGS thermoelectric couples surrounded in Microtherm insulation, supported with a hot side heater and bi-couple Macor plate (to maintain thermal contact when the spring loaded pistons are fully retracted). The aluminum support fixture houses cold side cartridge heaters (capable of heating to 600°C). Each mini module is bolted down to a large, round copper support plate (Figure 6), which is cooled with 17°C water flow. Each aluminum support fixture is thermally tied to a cooled copper plate through a Macor block that allows bi-couple cold-side temperatures to stay high enough to accurately simulate MMRTG cold-side conditions.

Test Results

Each bi-couple is instrumented with six thermocouples, and current-monitoring and four voltage-monitoring wires. Data is automatically collected in LabVIEW during testing, where the linear force actuators are controlled to vary and monitor the spring force per TE couple leg, as shown in Figure 5. First tests were done with MMRTG bi-couples heated to a hot junction temperature of 300°C and a cold junction temperature of 150°C. While at temperature, the spring load per TE leg was varied from 13.4N to 0N to 13.4N, with a 1 second hold at 0N. This load profile simulates a condition where the MMRTG TE couples momentarily unloads from the spring loaded pistons, which TE module dynamic analysis has shown to potentially occur during a pyroshock event (see Section 2.0). Voltage and temperature across each leg was recorded during the dynamic change in spring load, and examples of the data collected are shown in Figure 8. All four MMRTG bi-couple tested showed the same voltage and temperature response results.
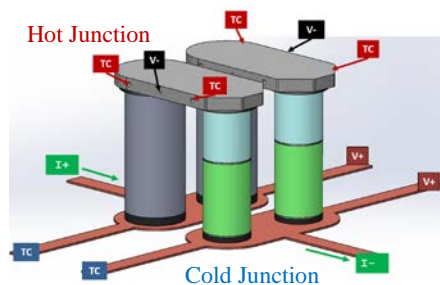
FIGURE 7. The location of wires on the MMRTG bi-couple and the LabVIEW GUI used to collect data.

 Measurements from all four bi-couples (results in Figure 8) indicated that voltages across the legs changed on the order of 0.5mV to 1mV during momentary unloading. In addition, the temperature differential across each of the legs would drop by 1°C to 2°C (the more significant temperature change occurred mostly on the cold side). In addition, the voltage time response across each of the bi-couples qualitatively matches the response seen on the power output of the MMRTG during a pyroshock event. When the MMRTG was hit with a pyroshock, the power

output quickly dropped by 2W to 5W on the order of milliseconds. Eventually the power would recover, but on the order of tens of minutes. This same response of a rapid power drop followed by a slow recovery was seen on all four bi-couples tested at this temperature in the DLTS. Using the voltage and temperature data of all four bi-couples, the resistance as a function of time during the dynamic change in load was calculated. Taking into account the Seebeck effect and Ohms law, the resistance was calculated as:

$$R_{leg} = \frac{\alpha \Delta T - V_{meas}}{0.5I} \qquad (1)$$

FIGURE 8. The voltage, temperature, and resistance data for the N-leg and P-leg of an MMRTG bi-couple at 300°C T_{hj} over time in response to a change in spring load.

where α is Seebeck coefficient, ΔT is temperature across the leg, V_{meas} is measured voltage across the leg, and I is current through the bi-couple. Using Equation (1) and data shown in Figure 8, the resistance as a function of time in response to spring load changes was calculated (see Figure 8). All four bi-couples demonstrated the same behavior with a spike in resistance of 0.2mΩ to 0.4mΩ when compression load was rapidly released on the bi-couple.

Testing at a hot junction temperature of 300°C was an intermediate step to verify the system operation without subjecting the bi-couples to high temperatures. Once the system demonstrated proper function, the hot junction temperature of the bi-couples was ramped up to about 500°C, with a cold junction temperature close to 200°C. These operating temperatures represent the typical hot- and cold-side temperature the bi-couples experience during mission operations of the MMRTG. While at these temperatures, the spring load per TE leg was varied from 13.4N to 26.7N to 0N to 13.4N, with a 1 second hold at 26.7N and 0N. This load profile was made to simulate a more erratic fluctuation of the spring-loaded pistons in the TE module, where the shock wave could cause the springs to apply double the load per leg and then suddenly unload the bi-couple. Voltage and temperature across each leg was recorded during the dynamic change in spring load, and examples of the data collected are shown in Figures 9. All four MMRTG bi-couples tested showed quantitatively similar results and response to the dynamic loading profile.

Measurements from all four bi-couples at 500°C once again indicated that the voltages across the legs changed on the order of 0.5mV to 1mV during momentary unloading. In addition, the temperature differential across each of the

legs would drop by 1°C to 2°C (where the more significant temperature change occurred mostly on the cold side). In addition, the voltage time response across each of the bi-couples qualitatively match the response seen on the MMRTG power output during a pyroshock. In addition, the results indicate that the significant changes in voltage and temperature occur during an unloading event, and not when the load was doubled to 26.7N. The bi-couple voltage and temperature behavior consistently showed a rapid-initial-response (i.e., voltage and temperature differential drop) to a dynamic unloading event, and then a slower recovery response when the load is dynamically reapplied. This behavior demonstrates a common characteristic signature that is qualitatively similar to and replicates that experienced and observed in the MMRTG EU and QU tests. Causes of this characteristic signature are being studied, but it is clear at the bi-couple level that a dynamic unloading event, such as that predicted to occur from a pyroshock-driven input by our SIERRA/PRESTO dynamic models, causes an immediate voltage and power loss that does not "reversibly" recover and leads to longer recovery times.
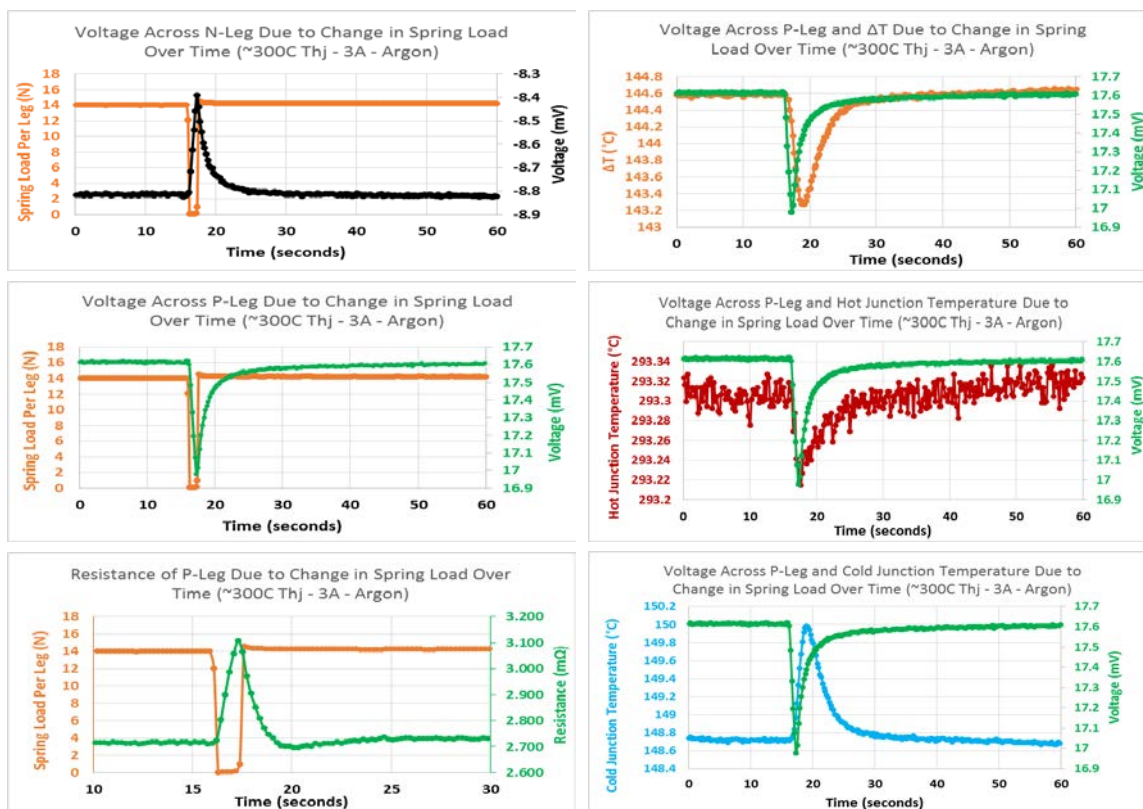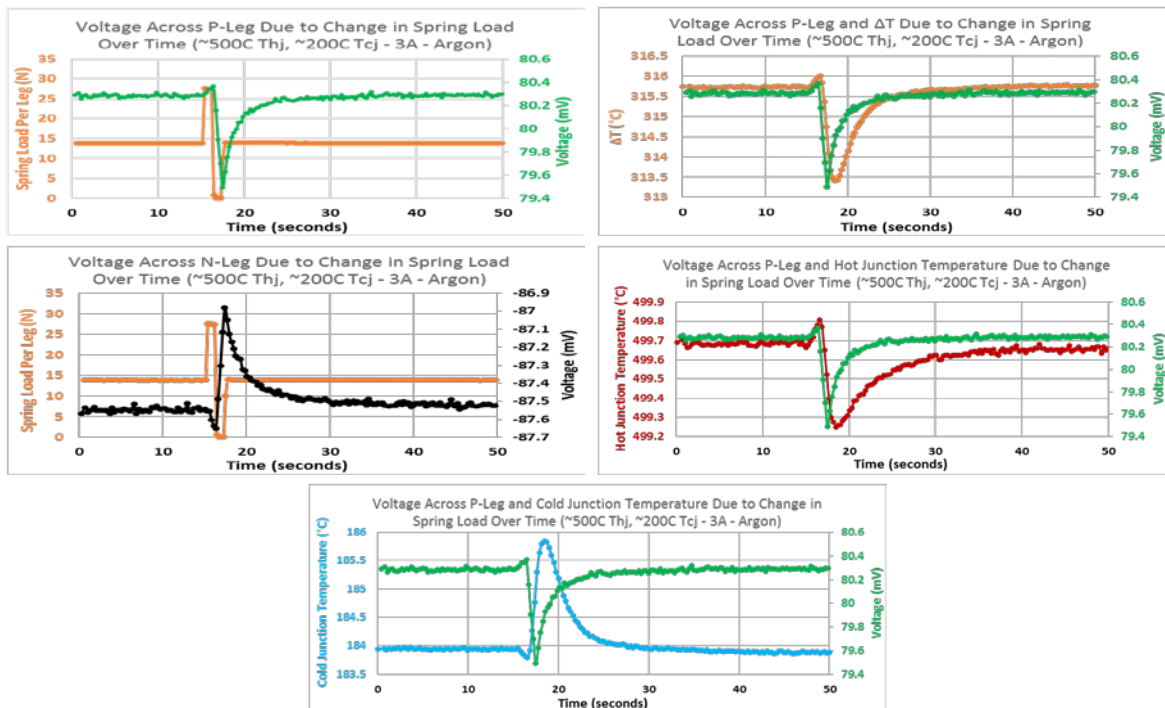

FIGURE 9. The voltage and temperature across an N-leg and P-leg of an MMRTG bi-couple at 500°C T_{hj} over time in response to a change in spring load.

PREDICTED MMRTG POWER DROPS FROM BI-COUPLE RESULTS

One impact of the predicted bi-couple load variations during pyroshock wave propagation is evident in Figure 10 which shows the electrical resistance of the thermoelectric couple as a function of the force against the couples in the Z-direction. In the instance of an offload condition the internal resistance of each couple is at a maximum. The system will also increase in thermal resistance resulting in a reduction in thermoelectric voltage due to the disrupted temperature gradient across the couple. Both scenarios were observed in DLTS testing (see Figures 8 and 9). Two independent electrical analysis models were developed to determine the number of couples experiencing these changes necessary to generate a power drop similar to the ones observed during pyroshock tests.
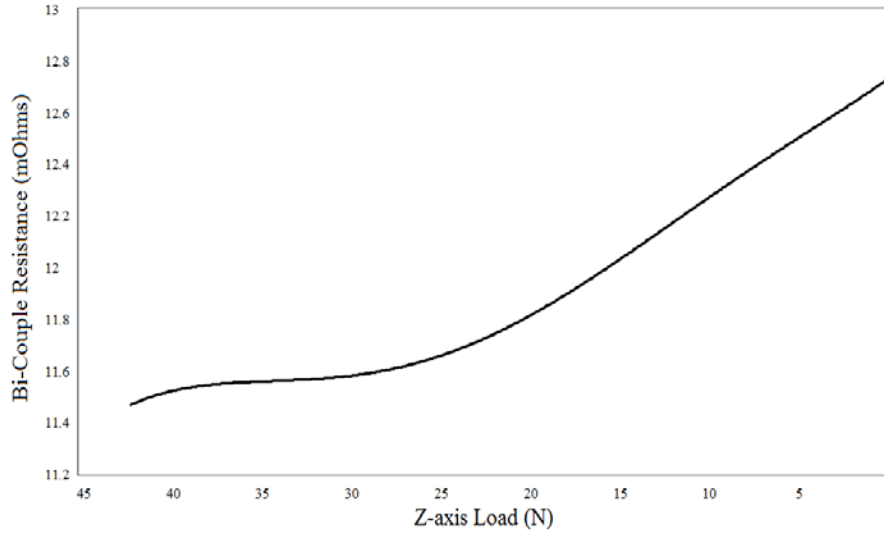
FIGURE 10. Polynomial fit of Bi-couple resistance data at room temperature.

Using MATLAB/Simulink electrical modeling software a couple was represented as two DC voltage sources V_n and V_p with a series resistor R. The magnitude of each voltage is determined by the temperature gradient and Seebeck coefficient of each thermoelectric element. Given the P-leg is segmented, a portion of the overall temperature gradient across the couple was distributed to each segment during calculation. Resistance values were calculated from the combined thermoelectric couple electrical resistivity and verified empirically at room temperature. Values were input into the Simulink model combining two of these parallel circuits to create a bi-couple, then 24 bi-couples combine in series to form a module (see Figure 11), and 16 such modules in series form the full MMRTG.
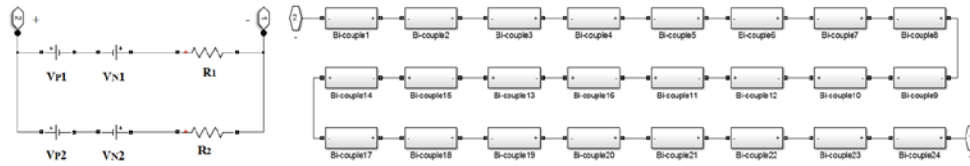
FIGURE 11. Simulink model of MMRTG bi-couple and module.

When a resistive linear load Simulink block was added to the MMRTG model to simulate the electronic load used in pyroshock testing and DLTS observed variations were applied to 50% of the couples, the initial system power loss calculations agreed with test conditions and power losses experienced by the MMRTG (i.e., 2W to 5W) [1]. The results are presented in Table 1.

A second set of calculations were also performed to cross check this model by determining the power of the MMRTG as a function of couple resistance and temperature gradient. MMRTG power can be calculated as follows:

$$P_{MMRTG} = I_{MMRTG}V_{MMRTG} \tag{2}$$

where I_{MMRTG} and V_{MMRTG} are the current and voltage of the MMRTG. These terms can be calculated as follows:

$$V_{MMRTG} = I_{MMRTG}R_L \tag{3}$$

$$I_{MMRTG} = \frac{V_{OC}}{R_{int} + R_L} \tag{4}$$

R_L represents the external load resistance of the MMRTG, R_{int} the internal resistance of the MMRTG, and V_{OC} the open circuit voltage of the MMRTG that is generated through the Seebeck effect. DLTS TE couple testing shows that both variables R_{int} and V_{OC} are directly impacted by changes in the couple spring load. A given percentage of affected couples inside the MMRTG impacts overall power outputs through the following:

$$R_{int} = N_p r_{int} + D_p r_{int}' \tag{5}$$
$$V_{OC} = N_p v_{OC} + D_p v_{OC}' \tag{6}$$
$$N_p = 1 - D_p \tag{7}$$

where N_p is the percentage of couples at nominal parameters, D_p is the percentage of couples incurring a change in spring load, r_{int} is the nominal internal resistance of the MMRTG, r_{int}' is the internal resistance of the MMRTG as a result from changes in couple spring loads, v_{OC} is the nominal open circuit voltage of the MMRTG, and v_{OC}' is the open circuit voltage as a result from changes in couple spring loads.

Open circuit voltages of the MMRTG can be calculated from voltages of each individual couples as shown below:

TABLE 1. MMRTG parameters and change in MMRTG output power based on results from TE bi-couple testing.

Parameters	MMRTG Model Nominal	Change in Hot & Cold Junction Temperatures	Change in Resistance	Simulink Model Nominal	Simulink Model Impacted
Couples At Delta Parameters (%)	0	50	50	0	50
Couples Nominal Parameters (%)	100	50	50	100	50
Hot Side Temp (deg K)	798.15	797.15	798.15	798.15	797.15
Cold Side Temp (deg K)	483.15	485.65	483.15	483.15	485.65
P-Leg Segment Temp (deg K)	673.15	673.15	673.15	673.15	673.15
Delta T (deg K)	315	311.5	315	315	311.5
Number of Couples Per MMRTG	768	768	768	768	768
Load Resistance (Ohm)	6.5	6.5	6.5	6.272	6.533
P-Leg Resistance (Ohm)	0.0087	0.0087	0.009	-	-
N-Leg Resistance (Ohm)	0.0132	0.0132	0.0135	-	-
Ave. Seebeck PbSnTe (V/K) (P-Leg)	0.000195	0.000195	0.000195	.000195	0.000195
Ave. Seebeck Coefficient TAGS (V/K) (P-Leg)	0.000105	0.000105	0.000105	0.000105	0.000105
Ave. Seebeck Coefficient PbTe (V/K) (N-Leg)	-0.0002335	-0.0002335	-0.0002335	-0.0002335	-0.0002335
MMRTG Power (W)	116.220	114.966	114.979	115.801	113.3
Delta in MMRTG Power (W)		1.253	1.241	-	2.501
et Power Drop of MMRTG due to ΔT and ΔR (W)		2.494		-	2.501

$$v_{OC} = N(v_{OCN} + v_{OCP}) \tag{8}$$
$$v_{OCN} = \alpha_{N-PbTe}(T_{HJ} - T_{CJ}) \tag{9}$$
$$v_{OCP} = \alpha_{P-PbSnTE}(T_{HJ} - T_{SJ}) + \alpha_{P-TAGS}(T_{SJ} - T_{CJ}) \tag{10}$$

where v_{OCN} is the open circuit voltage of the n-leg, v_{OCP} is the open circuit voltage of the p-leg, N is the number of couples in the MMRTG, α_{N-PnTe} is the average Seebeck coefficient of the n-leg, $\alpha_{P-PbSnTe}$ is the average Seebeck coefficient of the PbSnTe segment of the p-leg, α_{P-TAGS} is the average Seebeck coefficient of the TAGS segment of the p-leg, T_{HJ} is the couple hot junction temperature, T_{SJ} is the temperature at the segment junction of the p-leg, and T_{CJ} is the couple cold junction temperature. Individual couple resistances lead to the MMRTG internal resistance via:

$$r_{int} = N(r_P + r_N) \tag{11}$$

where r_P is the resistance of the p-leg and r_N is the resistance of the n-leg.

Using equations (2) through (11), assuming the spring load change impact occurs in 50% of the MMRTG couples, and the parameter values listed in Table 1, the calculated net change in MMRTG output power from changes in T_{HJ}, T_{CJ}, and R_{int} as observed during DLTS TE bi-couple testing was approximately 2.5W. These results agree with the MATLAB/Simulink model within 2% using the same parameters (see Table 1). During actual pyro shock testing of the MMRTG qualification unit and engineering units, the generators experienced power drops of 2W to 5W;

suggesting that changes in parameters observed during DLTS TE bi-couple testing are within the range necessary to explain the power drops observed during pyro shock testing.

CONCLUSIONS

Combined analytic dynamic shock wave propagation analysis and experimental bi-couple dynamic load tests presented here is showing a significant connection between pyroshock-driven dynamic effects and observed power losses in MMRTG EU and QU testing. Dynamic modeling work in section 2.0 has demonstrated a highly plausible avenue for bi-couple overloading and unloading. Dynamic modeling has also revealed that the spring/piston natural frequency is approximately 3000 Hz, which lies in the middle of a typical pyroshock frequency spectrum and is, therefore, likely causing significant spring/piston resonant oscillations. Bi-couple dynamic load testing in section 3.0 has also demonstrated that low-frequency dynamic loading and unloading sequences can certainly cause degradation of bi-couple temperature differentials and increasing bi-couple resistances. Pyroshock-driven unloading of a bi-couple shows a characteristic response profile with rapid reduction in bi-couple temperature differential (about 1-2°C) and output voltage and an increase in bi-couple resistance (about 0.2-0.4mΩ) in approximately 100 milliseconds, followed by a relatively long recovery time (i.e., of about 10-15 seconds) to re-establish the original temperatures and voltage output. Bi-couple dynamic load testing has shown this characteristic unloading response profile has occurred on all bi-couples tested to date. This bi-couple behavior during pyroshock-driven unloading qualitatively mimics the power output response to pyroshock events in the full-scale MMRTG tests on the Engineering Unit and Qualification Unit [1, 2]. The magnitude of changes to bi-couple temperature differential and voltage output exhibited in the bi-couple dynamic tests were then used in TE mathematical modeling of power output at the MMRTG system level in section 4.0. Results of this power modeling indicated that the bi-couple temperature differential degradation and resistance increases could lead to MMRTG system level losses of about 2.5 W when applied to only 50% of the MMRTG bi-couple population. This predicted power loss magnitude compares favorably with the power losses experienced in MMRTG Engineering Unit and Qualification Unit pyroshock testing [1,2]. This work indicates a clear connection between pyroshock testing events and conditions, a potential pathway to the resulting MMRTG power losses, and power losses of the approximate magnitude exhibited in MMRTG EU and QU pyroshock testing. Regions of the system fault tree in Figure 1 investigated by this work appear highly relevant to the root-causes of the pyroshock-driven power losses in MMRTG testing. The project is planning future high-frequency shock testing of a representative MMRTG TE module assembly on tunable beam facilities to validate the SIERRA/PRESTO dynamic models and predicted high-frequency pyroshock effects and response down to the bi-couple level within a TE module assembly. After SIERRA/PRESTO dynamics models are validated in room temperature, the impact of bi-couple unloading during shock inputs under inherent MMRTG thermal gradient environments will also be included in the dynamics analysis.

ACKNOWLEDGEMENTS

REFERENCES

[1] Bromberg, M. and Otting, W., "MMRTG EU-ETG Summary Test Report," *Pratt & Whitney Test Report*, TR-00156, S/A #20931, GO #98328, (February 2007).
[2] Chang, J., "EU-ETG Vibration and Shock Test Report," *Pratt & Whitney Test Report*, TR-00152, GO #98328, (March 2007).

[3] Lee, J.T., "Mars Science Laboratory Rover Pyroshock Test Report," *JPL* D-69262, (April 2011).

[4] Baumann, R.C., "General Environmental Verification Specification For STS & ELV Payloads, Subsystems, and Components," *NASA Goddard Space Flight Center*, (1996).

[5] Armen Derkevorkian, Ali R. Kolaini, Nicholas R. Keyawa, David J. Neff, Bill J. Nesmith, Terry J. Hendricks, "Pyroshock Induced Loads Driving Electrical, Thermal, and Structural Impacts in Multi-Mission Radioisotope Thermoelectric Generators (MMRTGs)," *Proceedings of Nuclear and Emerging Technologies for Space 2015 (NETS-2015) Conference*, Paper #5070, Albuquerque, NM, 2015.

[6] Armen Derkevorkian, Lee Peterson, Ali R. Kolaini, Bill J. Nesmith,Terry J. Hendricks, "Development of Multi-Physics Dynamics Models for High-Frequency Large-Amplitude Structural Response Simulation," *Proceedings of IMAC-XXXIV Conference and Exposition on Structural Dynamics,* Paper #87, Orlando, FL, January 2016.

[7] Lee, An Sung, Byung Ok Kim, and Yeong-Chun Kim. "A finite element transient response analysis method of a rotor- bearing system to base shock excitations using the state-space Newmark scheme and comparisons with experiments." *Journal of Sound and Vibration*, 297.3, 595-615, 2006.

[8]   Mace, Brian R., and Elisabetta Manconi. "Modelling wave propagation in two-dimensional structures using finite element analysis." *Journal of Sound and Vibration,* 318.4, 884-902, 2008.

[9] Crane, N.K., "Sierra/SM Theory Manual." No. SAND2013-4615. *Sandia National Laboratories (SNL-NM),* Albuquerque, NM (United States), 2013.

Preliminary Analysis of Low Enriched Uranium (LEU) Ultra High Temperature Nuclear Thermal Rockets Capable of 1100s Specific Impulse

Kelsa Benensky[1,5], Meng-Jen Wang[2,5], Juha Nieminen[3,5], Michael Eades[4,5], and Steven Howe[6]

[1]*Department of Nuclear Engineering, University of Tennessee, Knoxville, TN 37996*
[2]*Department of Mechanical Engineering, Virginia Polytechnic Institute and State University, Blacksburg, VA 24061*
[3]*Department of Astronautical Engineering, University of Southern California, Los Angeles, CA 90089*
[4]*Nuclear Engineering Program, The Ohio State University, Columbus, OH 43210*
[5]*The Center for Space Nuclear Research, 995 University Blvd., Idaho Falls, ID 83401*
[6]*Talos Power LLC, 480 Sunnyside Rd., STE 4, Idaho Falls, ID 83402*

Abstract. The current reference design for a nuclear thermal rocket (NTR) requires a specific impulse (I_{sp}) of 900 seconds, corresponding to six month transit times to Mars. Development of high performance nuclear thermal propulsion (NTP) fuel forms capable of withstanding ultra-high temperatures would enable year-long round-trip missions to Mars with four month transit times. With the addition of enriched hafnium carbide (HfC), solid-solution carbide fuel forms have the potential of operating at temperatures greater than 3400 K and could allow for low-enriched uranium (LEU) engine designs with specific impulse values of greater than 1100 s. This presentation will discuss the operating potential, design methodology, and neutronics studies completed to support the development of a HfC solid-solution NTP fuel form and corresponding engine.

Keywords: Nuclear Thermal Propulsion, Fuel Elements, Hafnium Carbide, Tri-Carbide, Solid Solution Carbide, Low Enriched Uranium

INTRODUCTION

This past summer, it was asked of a group of summer interns at the Center for Space Nuclear Research (CSNR) to perform a preliminary analysis of a solid core nuclear thermal rocket engine capable of 1100s specific impulse to support year round trip missions to Mars and enable four-month transit times and four-month stays on the surface. This paper summarizes the preliminary analysis and efforts of the team over a 10 week summer program. As a preliminary analysis, detailed neutronic or mechanical design is not addressed. This paper is intended to show the limiting system constraints, the expected thermal hydraulic and neutronic characteristics for specified operational conditions, and the material property requirements for the fissile fuel. All criticality calculations were completed in MCNP 6.1 with ENDF-VII/B libraries, while all performance calculations were completed using CSNR's Space Propulsion Optimization Code (SPOC) with hydrogen propellant properties derived assuming chemical equilibrium throughout the reactor core and nozzle.

For an NTP engine, I_{sp} is proportional to the square root of the ratio of propellant exit temperature (T) and molecular mass (M) as demonstrated in equation 1 [1]. For this design, I_{sp} was maximized by increasing the maximum possible operating temperature of the solid core NTR and minimizing the molecular mass of the propellant.

$$I_{sp} = \frac{1}{g_0} \sqrt{\left[\frac{2\gamma}{\gamma - 1} \frac{RT}{M} \right] \left[1 - \frac{p_e}{p_c} \right]^{\frac{\gamma - 1}{\gamma}}} \qquad (1)$$

g_0 - gravitational constant	γ – constant volume specific heat	R – ideal gas constant
T – propellant exit temperature	M – molecular mass	p_e – propellant exit pressure
p_c – chamber pressure		

Engine Design and Reactor Configurations

The engine design is based on ultra high temperature solid solution mixed carbide fuel forms used with a hydrogen propellant. The proposed uranium-zirconium-hafnium carbide or uranium-niobium-hafnium carbide ((U,Zr,Hf)C or (U,Nb,Hf)C) solid solution fuel forms have the capability for both ultra-high temperature melting points and compatibility with the hydrogen propellant over the entire temperature range of operation. If hafnium is enriched in the Hf-180 isotope, fast, unmoderated high-enriched-uranium (HEU) and epithermal moderated low-enriched uranium (LEU) engine designs (19.75% enriched) can be achieved.

The reactor analyzed is a highly un-optimized, preliminary design (figure 1) composed of the active core, 16 control drums (with a B_4C absorber), axial and radial graphite reflectors. Active core length and radius are varied by increasing the fuel element (FE) length and number of elements present within the core. FEs have an extruded hexagonal geometry with coated axial coolant channel holes and surrounded by tie-tube moderator elements (figure 2). Moderator element design was based on previous neutronic optimization studies completed by CSNR [2]. Fuel element designs with a flat-to-flat of 1.905, 2.540, 3.175 cm (0.75, 1.00, or 1.25 in.), with 19, 37, and 61 coolant channel holes respectively were surveyed to determine the configurations with best neutronic and engine performance. Coolant channels in FE design are modeled with radius values varied between a 0.10 – 0.17 cm (0.39 – 0.67 in.) coated with a 0.01 cm (0.04 in.) refractory carbide (ZrC or NbC) cladding.
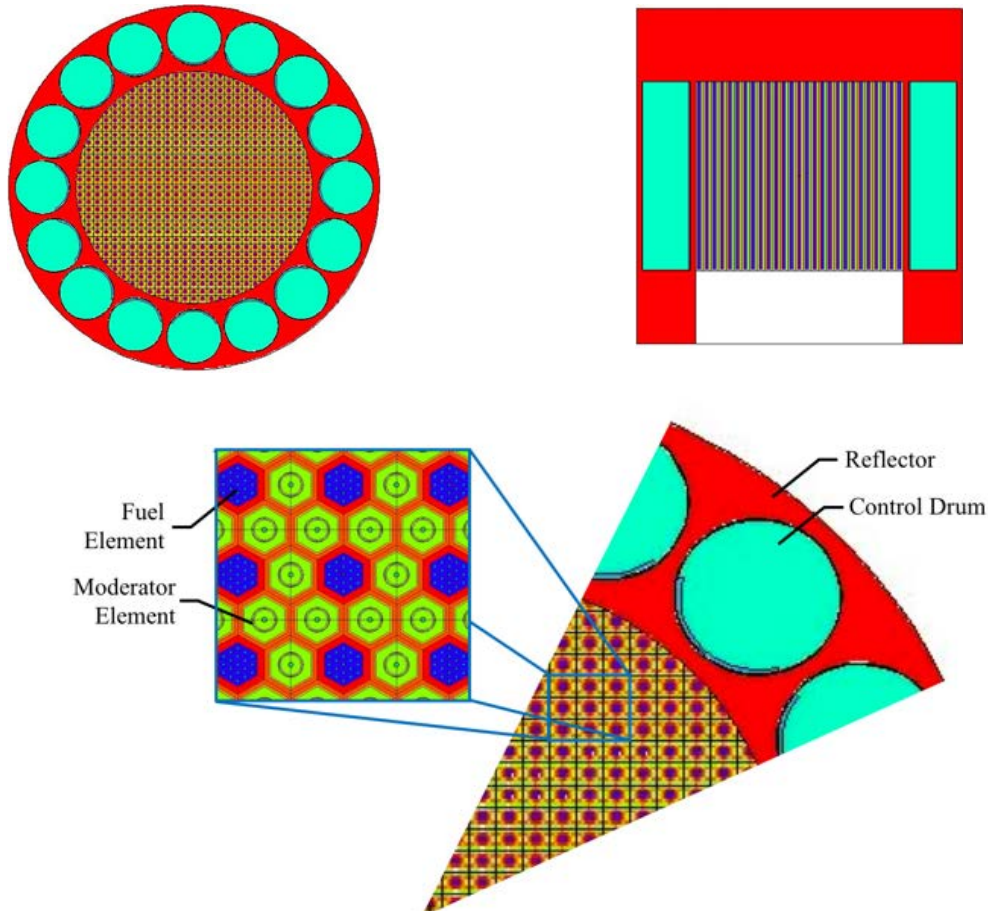
FIGURE 1. Preliminary model used to analyze the ultra-high temperature LEU NTR. The preliminary model is composed of 50 cm thick graphite radial and axial reflectors, 16 control drums with B_4C absorber, and an active core with a 1:3 moderator ratio and LEU all-carbide solid solution fuel. **Top.** Radial (left) and axial (right) projections of the model. **Bottom.** 1/8th Reactor core slice with component descriptions.
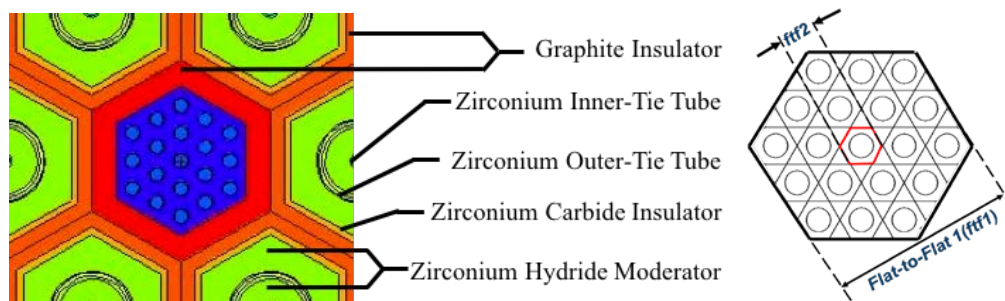

FIGURE 2. A 1:3 moderator ratio is required for the LEU ultra-high temperature NTR. **Left.** Tie-tube component descriptions. **Right.** Fuel elements are classified by their flat-to-flat distance between parallel sides of the extruded hexagonal element (ftf1). For each fuel size, the "flat-to-flat 2" (ftf2) is the distance between coolant channels.

Reactivity and reactor performance calculations suggest that 1.905 cm fuel elements with 19 coolant channels are expected to have the best performance due to smaller fuel element pitch and less parasitic neutron absorption within the moderator elements. A specific impulse value of 1100s is achieved for an active core geometry of 70 cm (28 in.) radius and 130 cm (51 in.) length with a 5 MPa chamber pressure and 3400 K operating temperature. Due to the 1:3 moderator ratio, the LEU design lends better for high thrust, large reactors on the scale of the Phoebus 2A prototype reactor engine tested during the NERVA/Rover program [3]. In this study, an engine capable of 133 kN (30 klbf) thrust is analyzed. This paper will serve to summarize the completed design studies by first explaining the selection of the analyzed fuel form, followed by an overview of the completed neutronic analysis in MCNP using infinite lattice calculations. A description of the thermal hydraulic engine design studies and impact on performance follows. Finally, the report will be summarized with conclusions and suggestions for future work.

FUEL FORM SELECTION

For a solid core NTR, the entire fuel element, consisting of the fuel element matrix and/or fuel compound must remain in a solidus state. In order to achieve the required specific impulse for four-month transit times to Mars, a chamber temperature of at least 3350 K is desired. This exceeds the melting temperature of all tested NTP fuels in past United States programs (Figure 3). Therefore, it was necessary to propose a new fuel form for use in the ultra high temperature LEU NTR. Based on previous NTP development efforts of the United States and former Soviet Union, solid solution carbides were initially analyzed because of their potential to enable the highest operating temperatures, with reported operation of soviet NTP FEs of 3100 K for 1 hour [4]. The team chose an enriched hafnium carbide solid solution fuel due to it's expected exceptionally high melting point (4200 K) and stability in the hydrogen environment.
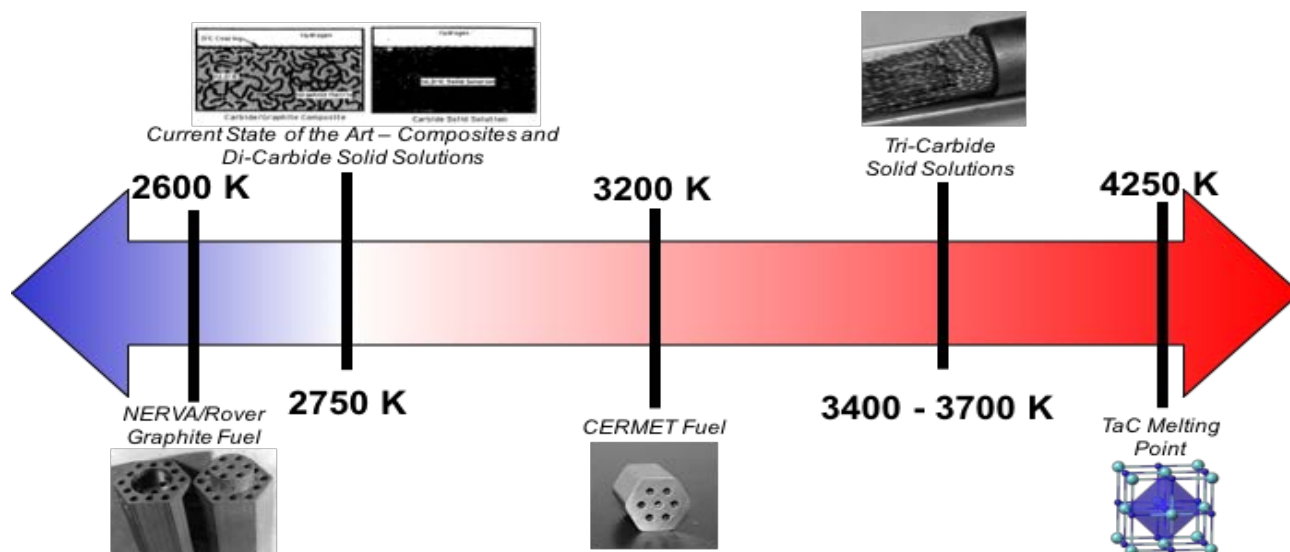
FIGURE 3. Comparison of suggested operating limits of fuels developed in past NTP programs [4,5,6]. Fuels are typically limited by the melting temperature of the uranium fuel compound used.

A solid solution is fuel compound desirable so that lower melting point compounds do not precipitate out of the fuel during operation and cause localized melting. Hafnium carbide and uranium carbide are not mutually soluble below 2273 K. This necessitates the use of a "mediator carbide" such as NbC or ZrC as apart of the solid solution, to form a psuedo-terenary carbide, or "tri-carbide". The tri-carbide mixture has previously been shown to extend the range of solubility of UC, HfC, and ZrC, or NbC and has the potential to increase uranium loading for the fuel [7].

In addition to high melting point, fuel form stability in a hydrogen atmosphere must also be attained. Previous studies [8] have shown that the congruently vaporizing composition (CVC) of prospective constituent carbides in a hydrogen atmosphere governs this stability. CVC is the expected equilibrium ratio of carbon to metal (i.e. C:Hf, C:Nb, C:Zr) at the surface of the fuel exposed to the hydrogen atmosphere and is a consequence of the wide stoichiometry of Zr, Nb, Hf, and Ta with carbon. Melting temperature of the refractory metal carbides is dependent on the carbon to metal ratio (C/Metal ratio). Therefore fuel elements may experience such a ratio shift caused by the transition to the CVC in a hydrogen atmosphere that localized melting at the fuel element surface cam occur. It should be noted that a solid solution uranium-tantalum carbide (U,Ta)C fuel compound was investigated by the former soviet union by the early 1990s [5]. Tantalum carbide is the highest melting point of any known compound and has complete solubility with UC. However, in a hydrogen atmosphere, the CVC limits (U,Ta)C to operation below 3000 K due to the expected surface liquid formation (Figure 4). Therefore, TaC solid solution fuels were not considered in this study in order to increase safety limits when operating the reactor.
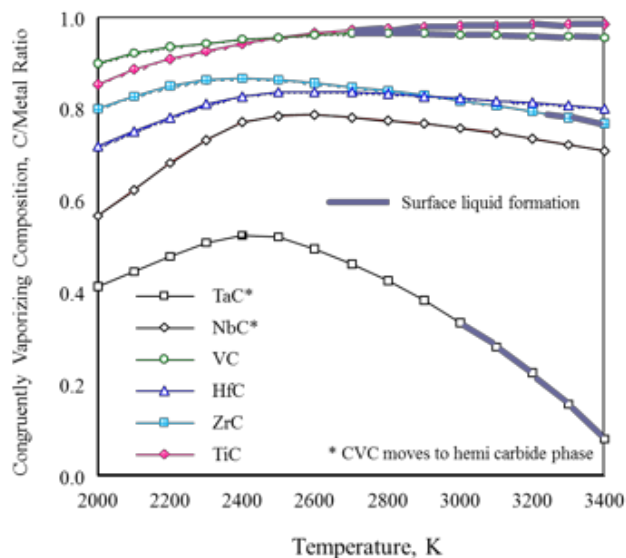
FIGURE 4. The proposed fuel form must have both an ultra-high temperature melting point as well as be stable when operating in a hydrogen environment. **Left.** Prospective solid solution carbides and their reported melting points. **Right.** The CVC of the carbide due to 1 atm hydrogen environment may shift the composition of the fuel element such that localized melting at the fuel element surface may occur [9]. Such is the case for TaC.

NEUTRONIC ANALYSIS

This section will summarize the infinite lattice studies completed within MCNP. Because natural hafnium has a high absorption cross section, achieving enough reactivity to be critical at the operating temperatures was challenging for a LEU engine even with the use of an enriched hafnium isotope. Four studies were completed in the initial infinite lattice studies. First, HEU and LEU fuels were analyzed in both a solid solution "all-carbide" fuel type without a matrix and a composite fuel type comprised of a graphite matrix and inner dispersed web of the solid solution fuel. The effect of constituent carbide content and moderator ratio was assessed for LEU all-carbide fuels. Lastly, the impact of fuel and moderator element geometry and detailed design was assessed in support of the preliminary engine design. For the study, 3000 K was assumed for the fuel temperature; all other materials were modeled at 2500 K. Each case was run for 500 cycles with 5,000 particles per cycle with the first 50 cycles skipped. Fuel temperature modelling was limited by temperature dependent cross sections in MCNP (3000 K). Reactivity may be partially compensated for by the assumed high homogeneous operating temperature of the structural material, however more in depth analysis should take into account a more accurate temperature profile within the elements. Reactivity will strongly be effected by the temperature of the fuel, hydrogen coolant, and ZrH_x moderator. Very high temperature dependent cross sections can be generated in cross section processing programs such as NJOY and used for a more thorough analysis.

Fuel Type Analysis: Moderator and Fuel (UC) Content Studies

Four fuel types were analyzed in the initial infinite lattice calculations. An all-carbide and composite FEs were surveyed for both HEU (97.5% enriched) and LEU (19.75% enriched) fuel forms. For the initial studies, FEs were modelled after extruded hexagonal NERVA/Rover elements with a 1.905 cm flat-to-flat and 19 coolant channels with a 0.10 cm radius. *All-carbide* type FEs are composed of only the solid solution fuel fabricated into a net shape. Previous studies have shown that all-carbide fuels and refractory carbide structural material samples have been manufactured using both hot isostatic pressing (HIP) and spark plasma sintering (SPS) methods [10,11]. *Composite* type FEs are composed of an graphite matrix with a 30vol% inner dispersed fuel-web based on the composite fuels tested in the nuclear furnace (NF-1) during the NERVA/Rover program [4]. The fuel composition was held constant as $(U_{0.10}, Zr_{0.45}, Hf_{0.45})C$, when surveying different FE types. HEU FEs of both types were able to achieve criticality, while LEU fuels were sub-critical without a separate moderator element (Table 1).

Using the same fuels surveyed in the fuel type analysis, all-carbide and composite LEU fuels were arranged in 1:1, 1:2, and 1:3 moderator ratios (figure 5) with moderator elements optimized in past CSNR studies [2]. A comparison of the calculated reactivity (k_{inf}) and respective relative error (σ) for each case is described in Table 1. LEU cases require moderation to achieve criticality and reactivity significantly increases for moderator ratios of at least 1:2. All-carbide fuel elements exhibited the highest reactivity due to increased uranium loading. All-carbide FEs were pursued for LEU engine designs in order to achieve criticality at higher temperatures and finite core sizes due to their greater reactivity.
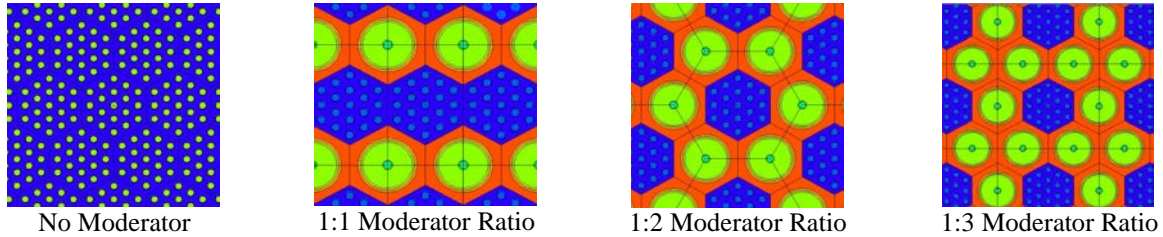

| No Moderator | 1:1 Moderator Ratio | 1:2 Moderator Ratio | 1:3 Moderator Ratio |

FIGURE 5. Schematic of the infinite lattices computed with moderator elements for LEU type engines

TABLE 1. Comparison of calculated reactivity for each fuel element type without moderator and LEU fuel types with moderator elements (($U_{0.10}$, $Zr_{0.45}$,$Hf_{0.45}$)C fuel)

Fuel Element Type	HEU	HEU	LEU				LEU			
	Composite	All-Carbide	Composite				All-Carbide			
Moderator Ratio (F:M)	none	none	none	1:1	1:2	1:3	none	1:1	1:2	1:3
k_{inf}	1.11716	1.41891	0.39751	0.79034	0.80666	0.79909	0.62160	0.72361	0.80384	0.84575
σ	0.00009	0.00009	0.00015	0.00014	0.00012	0.00010	0.00005	0.00010	0.00011	0.00009

In order to increase the reactivity of the all-carbide LEU infinite lattice, the amount of UC in the fuel composition is increased. Compositions of: ($U_{0.10}$, $Zr_{0.45}$,$Hf_{0.45}$)C; ($U_{0.15}$, $Zr_{0.40}$,$Hf_{0.45}$)C; and ($U_{0.20}$, $Zr_{0.40}$,$Hf_{0.40}$)C were simulated (table 2). It was found that increasing UC content is necessary for criticality throughout the mission. However, increased UC content reduces the expected melting temperature of the fuel due to it's lower melting point compared to refractory carbides. Criticality can be achieved for UC loadings of at least 20 mol%, which is expected to correspond to a melting temperature acceptable for engine opperation. Calculations were also performed where NbC was also substituted for ZrC once a finite core size was chosen. The team was concerned that, in the event that cladding or fuel cracking, the surface composition of the fuel (affected by CVC in a hydrogen atmosphere) could lead to localized melting of ZrC. Niobium has a higher melting temperature and greater hydrogen stability, but also has a larger neutron cross section than the zirconium. Increased cross section reduces reactivity and would need to be compensated for in a detailed neutronic optimization.

TABLE 2. Calculated reactivity due to increased UC fuel content for LEU type fuels with 1:3 moderator ratios

Fuel Composition	($U_{0.10}$, $Zr_{0.45}$,$Hf_{0.45}$)C	($U_{0.15}$, $Zr_{0.40}$,$Hf_{0.45}$)C	($U_{0.20}$, $Zr_{0.40}$,$Hf_{0.40}$)
k_{inf}	0.84575	0.98458	1.10395
σ	0.00009	0.00012	0.00012

Fuel and Moderator Element Geometric Analysis

The last variables surveyed for the infinite lattice calculations were the impact of detailed fuel design and element sizing on reactivity. Three fuel form geometries, previously described in the introduction of the paper, were studied: flat-to-flat of 1.905, 2.540, 3.175 cm, with 19, 37, and 61 coolant channel holes respectively. All fuels were composed of LEU, all-carbide solid solutions with 0.10 cm – 0.17 cm radius coolant channels with a 0.01 cm thick refractory carbide (ZrC or NbC) coatings. Fuel form geometries were chosen primarily as feasible designs to manufacture. It was found that increased element sizing led to increased pitch between FEs and greater parasitic

absorption in the moderator, resulting in reduced reactivity (figure 6). The pitch between FEs for the 1:3 moderator ratio layout is twice the FE flat-to-flat. Increased coolant channel radius also reduces the reactivity due to removal of the fuel. For smaller FEs, the reactivity change with increasing radius was smallest due to the smaller number coolant channels per FE (figure 6).
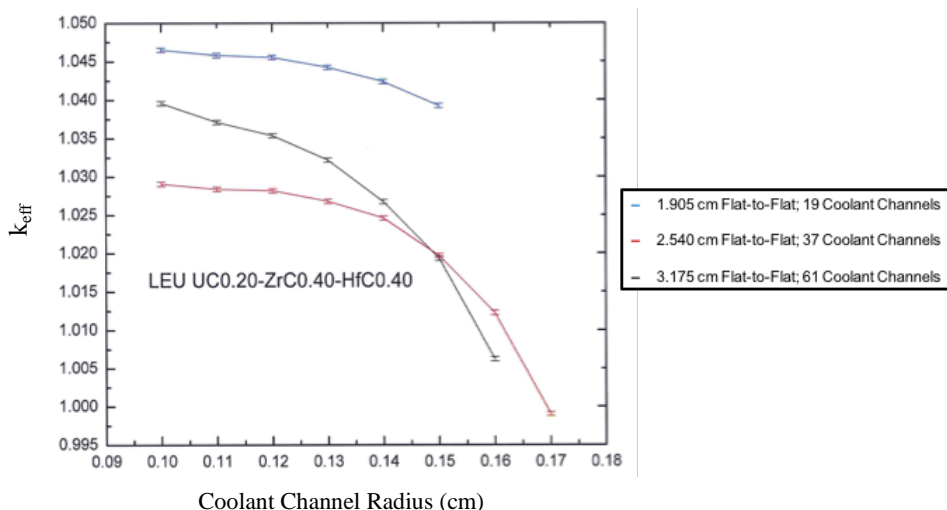

FIGURE 6. Reactivity decreased with increasing fuel element size and coolant channel radius.

Since the zirconium hydride ($ZrH_{1.8}$) moderator melts at relatively low temperatures (1074 K), the ultra-high operating temperature of the fuel increases the possibility of moderator melt. An additional graphite insulator was added to the design around the fuel to reduce the temperature in the moderator element (figure 7). Overall, adding the insulator element decreases reactivity due to a combination of increased fuel element pitch, which increases neutron absorption in the moderator element, and reduced fuel mass. This may also suggest that the current configuration is over-moderated since increase in graphite (a neutron moderator) leads to decreased reactivity.
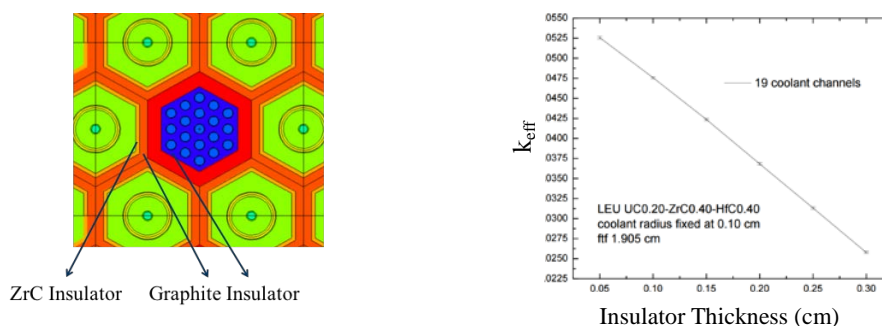
FIGURE 7. If additional insulation is necessary to reduce moderator operating temperature, reactivity will decrease for the LEU all-carbide system with a 1:3 moderator ratio.

ROCKET DESIGN AND PERFORMANCE ANALYSIS

The thermal hydraulics module of SPOC was used to narrow the design space to find the best finite core sizing based on the completed initial infinite lattice calculations in MCNP. The specific module used to calculate thermal hydraulic and reactor performance parameters in SPOC has been explained in previous conference proceedings [12,13]. The highly un-optimized core is calculated to yield I_{sp} values between 1050 – 1150 s for limiting maximum fuel operating temperatures between 3400 – 3500 K (figure 8). The fuel centerline temperature was held below the specified operating temperature and a channel peaking factor of 1.45 was applied to take into account the difference in hydrogen flow between channels. The channel peaking factor of 1.45 is a conservative estimate of flow difference and is dependent on proper orificing of each fuel element channel size to reduce this difference, which results in

increased specific impulse. In this analysis, reactor size (radial, axial), fuel geometry, operating temperature and pressure were varied to optimize the core for maximum engine specific impulse and minimum active core mass for a specified thrust. The thrust level of interest during the program was 133 kN (30 klbf thrust). Once the design space was narrowed, neutronic calculations using the simple reactor model (figure 1) were performed and the results of this analysis are provided below.

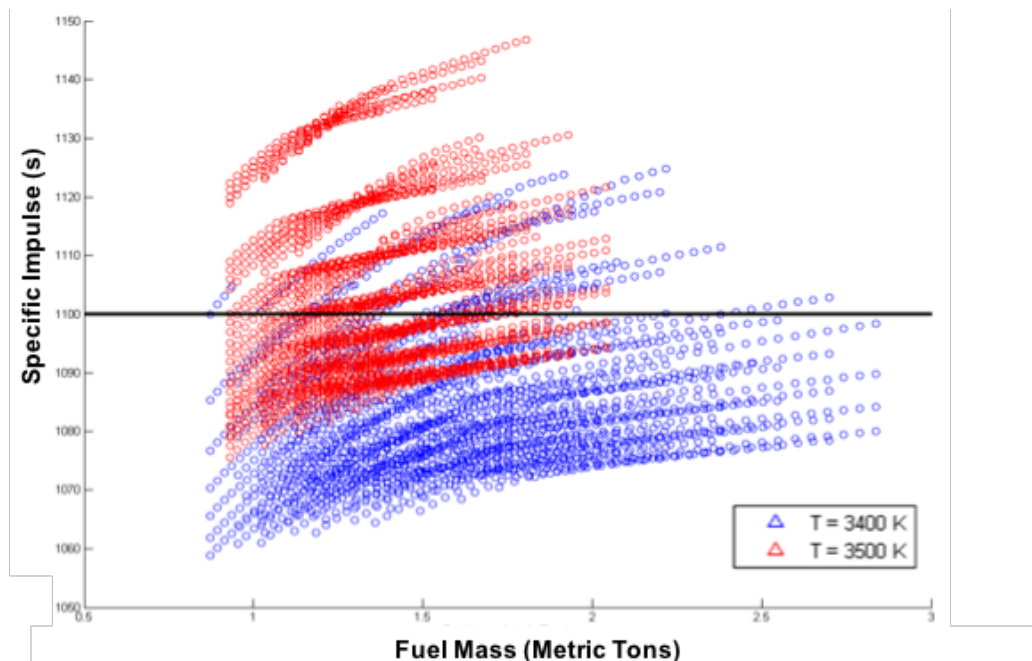**FIGURE 8.** I_{sp} and fuel mass of the NTR engine reactor were optimized initially in the SPOC thermal hydraulics module using a hydrogen propellant. This figure displays the results of the expected reactor configurations if the maximum fuel centerline temperature is held below 3400 or 3500 K with a 300:1 nozzle expansion ratio.

Thermal Hydraulics Results

Four studies were completed in support of choosing the optimal reactor configuration: active core dimensions, fuel form geometry, operating pressure, and maximum fuel centerline temperature. The active core was varied for radius sizes of 55, 60, 65, and 70 cm and lengths of 100, 105, 110, 115, and 120 cm. Fuel geometries were varied with flat-to-flat specifications of 1.905, 2.540, and 3.175 cm with 19, 37, and 61 coolant channel holes. Coolant channels were modeled with radius values between a 0.10 – 0.17 cm with a 0.01 cm coating. Reactor operating pressures between 9.0 and 3.5 MPa were also studied at maximum fuel centerline temperatures of 3400 and 3500 K. Figure 8 plots the results of these studies.

Overall, trends in reactor sizing showed a higher performing reactor with increased mass for larger active cores. Reactor configurations with increased radius produced more power overall and exhibited higher specific impulse values at the cost of increased fuel mass. Increased length also increases reactor power. It was found in this study that increased length had a greater impact on reactor performance, as it increases the area for heat transfer of the coolant channel and increases the probability of hydrogen disassociation at high temperatures and low pressures. Hydrogen dissociation reduces the average molecular mass of the propellant at the outlet. Neutronic studies found that increasing reactor mass adds reactivity to the system due to decreased neutron leakage, which supports a larger sized reactor. However, minimum reactor sizing is desired to reduce the thrust to weight ratio of the highly moderated system.

When surveyed by thermal hydraulic simulations, FEs with larger flat-to-flats and more coolant channels allowed increased propellant flow through the core and resulted in higher specific impulse. However, supporting neutronic simulations showed that increasing fuel element sizing also increased the pitch between elements, leading to more parasitic absorption in the tie-tubes and reduced reactivity. Therefore, unless the moderator ratio is reduced, it is

suggested that smaller flat-to-flat sizes be utilized. The reduced performance in smaller flat-to-flat sizes can be compensated by decreasing coolant channel radius. Decreasing coolant channel radius increases the pressure drop across the coolant channel and increases the probability for hydrogen disassociation and increases reactor performance. For larger core designs and thrust levels, this pressure drop may be too great and require larger coolant channel radius values.

Decreasing pressure also increases expected performance of the reactor. However, in this study, lower chamber pressures also were found to result in a higher relative pressure drop across the core which reduces the number of reactor configurations which meet performance limits. Lower operating pressures necessitate larger cores with increased coolant channels to reduce the pressure drop.

For the case of a 133 kN thrust engine, a reactor design with an active core radius of 65 cm and 130 cm length operating at 5 MPa chamber pressure with fuel temperatures below 3400 K was chosen to achieve 1100 s specific impulse and reduce fuel mass to approximately 1.25 metric tons.

CONCLUSIONS & RECOMENDATIONS

Overall, this study showed that the ultra-high temperature LEU NTR is capable of 1100s specific impulse with necessary neutronic optimization, supporting fuel development and detailed mechanical design. Better performance and smaller sized engines are possible with a HEU fuel form for both composite and all-carbide fuels since moderation is not needed. The thrust to weight ratio on the proposed engines is expected to be very high due to the large required core size to achieve only 133 kN thrust. It is suggested that the ultra-high temperature LEU NTR be used for high thrust applications. Due the required 1:3 moderator ratio, initially a large reactor size necessary to achieve criticality, this reduces the feasibility of the engine for low thrusts. The large baseline engine necessary for criticality has many coolant channels due to the increases presence of fuel elements. For low thrust rates, the propellant flow is too low through the coolant channels to effectively cool the engine. A larger reactor size supports higher thrusts due to the increased number of coolant channels which can handle larger flow rates while maintaining effective heat transfer to preserve high I_{sp}. Reducing the required moderator ratio via neutronic optimization will increase the number of fuel elements within the engine available for heat transfer and allow for higher thrust levels to be reached with the same engine size.

Future studies in MCNP should aim to radially and axially optimize the core power profile in order to maximize reactor performance and heat transfer, as well as decrease reactivity losses due to poor moderation and neutron leakage. A more detailed model of the core should include the expected temperature profile throughout the elements and corresponding temperature-dependent material cross sections. More accurate modelling of the mechanical NTR design will include the addition of: an inner and outer pressure vessel, hydrogen cooling channels and respective coatings within the reflector and control drums. Detailed control drum design is necessary for reactor control to ensure safe reactor start up and shutdown during normal operations and accident scenarios (such as a sea submersion accident).

All in all, the design is based on (U,Zr,Hf)C or (U,Nb,Hf)C tri-carbide solid solution fuel forms which are capable of ultra-high melting temperatures. It will need to be demonstrated that the fuel can be manufactured and assembled into the extruded hexagonal element desired. Thermal mechanical and chemical properties of the fuel including melting point, stability in the hydrogen environment, uranium loading, solubility, mechanical strength, and ductility of the fuel needs to be carefully characterized in order to better predict the performance and safety margins of the reactor. Although previous studies have already demonstrated that fuel and structural materials can be fabricated from the carbide constituents of the fuel, the fuel is expected to be very brittle and may need additional structural support (or housing) within the reactor which will in turn effect reactor reactivity. Due to the brittle nature expected for the all-carbide fuel, fuel manufacturability of net shape fuel elements should be carefully quantified. Fuel element design surveyed in this study was developed based upon past manufacturing limits of the NERVA/Rover program for extruded composite graphite fuel elements. All-carbide manufacturability requires different production processes and feasible manufacturability may be the primary driver for fuel design in this type of engine.

ACKNOWLEDGMENTS

WORKS CITED

[1] McCarty, R.D., Weber, L.A., "Thermophysical Properties of Parahydrogen from the Freezing Liquid Line to 5000 R for Pressures to 10,000 Psia," NBS Technical Note; 617. National Bureau of Standards, Boulder, CO (1972).

[2] Rosaire, G., et. al., *Design of a Low-Enriched Nuclear Thermal Rocket.* Internal Report. Center for Space Nuclear Research, Idaho Falls, ID, (2003).

[3] Finseth, J. L. *Overview of Rover Engine Tests Final Report*. Rep. no. 3 13-002-91-059. Hunstville, AL: National Aeronautics and Space Administration, 1991.

[4] Lyon, L.L. *Performance of (U,Zr)C-Graphite (Composite) and (U,Zr)C (Carbide) Fuel Elements in the Nuclear Furnace 1 Test Reactor*. Rep. no. LA-5398-MS. Los Alamos, NM: Los Alamos National Laboratory, 1973. Print.

[5] Bhattacharyya, S. K. *An Assessment of Fuels for Nuclear Thermal Propulsion*. Rep. no. ANL/TD/TM01-22. Argonne, IL: Argonne National Laboratory, 2001.

[6] Qualls, A. L., and E. F.Hancock. "Recapturing NERVA-Derived Fuels for Nuclear Thermal Propulsion," in proceedings of *47th AIAA/ASME/SAE/ASEE Joint Propulsion Conference & Exhibit.* Tech. no. AIAA 2011-5847. San Diego, CA: (2011).

[7] Rudy, E., et. al., "Über Hafniumkarbid enthaltende Karbidsysteme," *Chemical Monthly*. **91,** 176-187, (December 1959).

[8] Butt, D., et. al. *Vaporization Behavior of Non-Stoiciometric Refractory Carbide Material and Direct Observation of the Vapor Phase using Laser Diagnostics.* Rep. no. LA-UR 93-2943. Los Alamos, NM: Los Alamos National Laboratory, 1993.

[9] Butt, D., "Ultra High Temperature Gas-Solid Reactions Involving Group 4 and 5 Transition Metal Carbides," Presentation. (received 2015).

[10] Knight, T., and Anghaie, S. "Advanced Carbide Fuels for Space Nuclear Thermal Propulsion," in proceedings of *37th AIAA/ASME/SAE/ASEE Joint Propulsion Conference & Exhibit.* Tech. no. AIAA 2001-3510. Salt Lake City, UT: (2001).

[11] Sun, S. K., et. al., "Reactive spark plasma sintering of ZrC and HfC ceramics with fine microstructures," *Scripta Materialia.* **69,** 139-142, (2013).

[12] Husemeyer, P. J., et. al., "CSNR Space Propulsion Optimization Code: SPOC," in proceedings of *Nuclear and Emerging Technologies for Space 2015*. Paper no. 5142. Albuquerque, NM: (2015).

[13] Patel, V., "Temperature Profile in Fuel and Tie-Tubes for Nuclear Thermal Propulsion Systems," in proceedings of *Nuclear and Emerging Technologies for Space 2015*. Paper no. 5110. Albuquerque, NM: (2015).

A Six Component Model for Dusty Plasma Nuclear Fission Fragment Propulsion

Rodney L. Clark[1], Robert B. Sheldon[1,2]

[1]*Grassmere Dynamics, LLC, Gurley, AL 35748-8909 256-776-9471 rod.clark@grassmeredynamics.com*
[1,2]*RB Sheldon Consulting, Huntsville, AL 35803 256-6538592; rbs@rbsp.info*

Abstract. A dusty plasma nuclear fission fragment rocket employs a cloud of nanometer-sized dust of fissionable material inside a magnetized moderator from which the fission fragments (FF) emerge to form the high velocity exhaust. The negatively charged dust, free electrons, and positively charged ions form a 3-component "dusty plasma" that can be confined and manipulated as charged fluid. The FF exit the ~100nm dust with velocities approaching 5% the speed of light, giving this rocket an ISP~500,000 seconds, as discussed previously [1]. Despite 1-10 GW power densities, this ultra-high ISP rocket results in very little thrust, which is only ideal for a distance>100AU mission. The thrust can be increased by expanding the size of the dusty plasma core, however, FF collisions with the dust lower the ISP to ~70,000s and the dust begins to vaporize. In this paper we explicitly backfill the dusty plasma with neutral hydrogen gas to provide a mass-loading of the FF exhaust that increases the thrust, making a variable-ISP rocket. The neutral gas also heats and transfers thermal energy to the dust, which must be accounted for in this design. We model this novel rocket with a six-component dusty plasma, finding the temperature equilibrium between fissile dust, hydrogen gas, free electrons, free protons, FF, and photons. For certain operating regimes, the dusty plasma rocket is competitive with nuclear thermal rockets, but by throttling the hydrogen, can transition to a fuel saving high-ISP engine for interplanetary missions. We consider the potential of using the FF to heat a deuterium-tritium gas mixture to fusion temperatures, but several hurdles must be overcome for this fission-fusion concept to work.

Keywords: Fission fragment nuclear rocket, dusty plasma, thermal equilibrium, variable ISP

THE FISSION FRAGMENT DUST REACTOR

This study examined in some detail the properties of a fission reactor consisting of a dusty plasma consisting of fissionable dust grains embedded in a hydrogen plasma. Such a reactor has been proposed as a source of heated hydrogen propellant in a high Specific Impulse (ISP) rocket engine and as a possible high temperature thermal reactor. The advantage of such concepts arises from the singular properties of dusty plasmas which have been studied extensively in astrophysics. In particular the large surface area of a cloud of fine grain dust particles allows for efficient radiative cooling to the reactor walls which in turn allows the reactor to operate at very high temperatures approaching the melting point of the dust grains.

As shown conceptually In Figure 1, this study examines a fission reactor consisting of a plasma mixture containing fissionable uranium dust, fission fragments, electrons and hydrogen. The entire mixture is contained by a magnetic field and surrounded by a neutron moderating material. When the reactor becomes critical, using an advanced moderator made of deuterated carbon-13, fissionable dust particles begin to emit the fission fragments. The high speed fission fragments interact with and heat the dust and hydrogen gas in the mixture. The fuel of fine dust grains becomes charged as a result of emission of positive charged fission fragments and collisions with electrons and hydrogen ions, which forms a dusty plasma that can be confined and manipulated with external electrostatic fields.

Some of the fission heated hydrogen plasma may be extracted forming a rocket exhaust, or the plasma may be entirely confined to produce power. The primary power output from the Dusty Plasma Fission Fragment Reactor (DPFFR) is copious qualities of Infrared Radiation (IR) incident on the reactor wall. This power is extracted from the reactor through wall cooling loop. The Brayton Cycle could be used to produce electrical power. The criticality of a DPFFR dust reactor has been previous shown using industry standard tools (MCNP) [2].
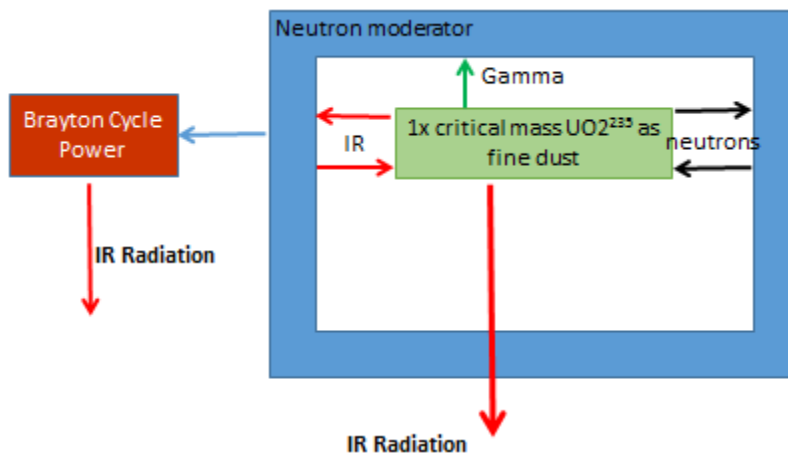
FIGURE 1. Schematic of Dusty Plasma Fission Fragment Reactor Concept.

Figure 2 presents the results of a criticality study using MCNP computer code on two different reactor geometries, a right circular cylinder and a compact spherical torus having equal major and minor radii. The results show the required density of dust grains of three fissionable fuels versus the major radius of the resulting reactor. The larger surface area of the spherical torus shows the benefits of higher reactivity Am fuel compared to U and Pu. These criticality results can be used to size the reactor. As the DPFFR operates at very low hydrogen pressure there is effectively minimal structural loads on the reactor vessel other than to support its own weight and that of the moderator and wall cooling system. The moderator is fixed at 1 meter thickness, which means the radius of the reactor vessel determines the volume of moderator and hence the overall mass of the sytem.

FIGURE 2. Critical Density versus Major Radius in meters for reactor vessel in Cylindrical & Toroidal Geometries.

A simulation of the conditions inside a DPFFR must also consider the effectiveness with which the fission fragments that escape the small dust grains transfer their kinetic energy to other dust grains and to the hydrogen electron plasma. This is the subject of this study.

The Reservoir Plasma Generation

To investigate the heating of hydrogen dust mixture by fission fragments several computer models were used. A Lindhardt-Scharf-Schiott model (labelled M74), 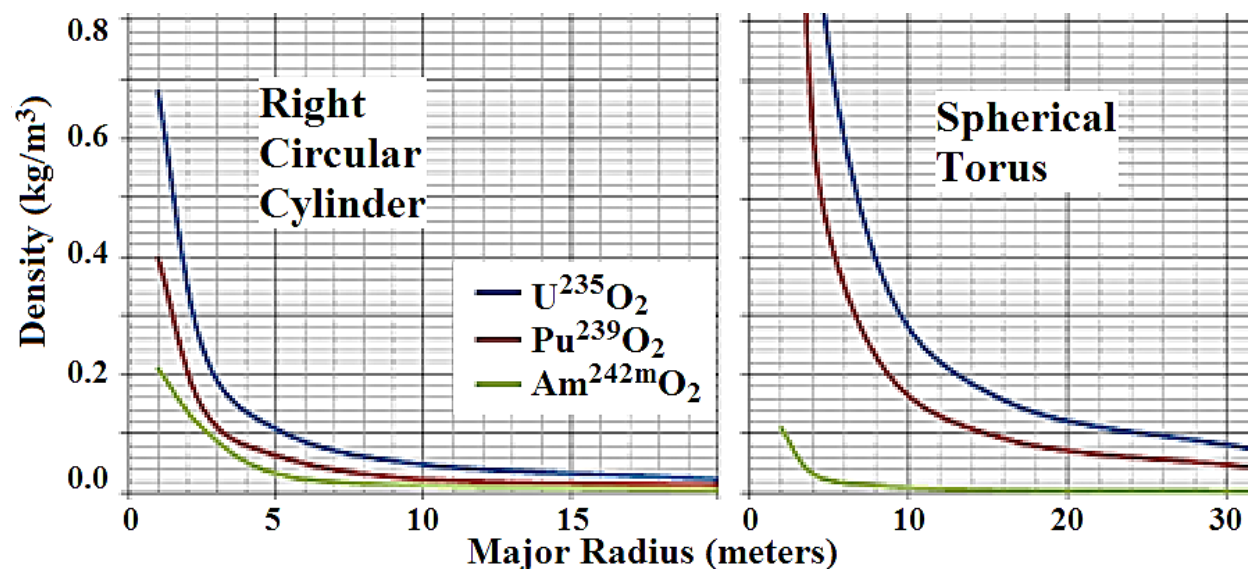the Zeigler SRIM calculation (labelled Tr) and the GEANT4 code (labelled G4) [3], were used to compute the energy deposited by the fission fragments into the fissionable dust, where M74 is fast, SRIM is more accurate at low energies, and GEANT4 at high energies. Figure 3 shows the rate of energy deposition into a Uranium-235 dust cloud in vacuum vs. the fission fragment range in meters. Different colors correspond to different dust densities. Higher dust densities result in shorter ranges.
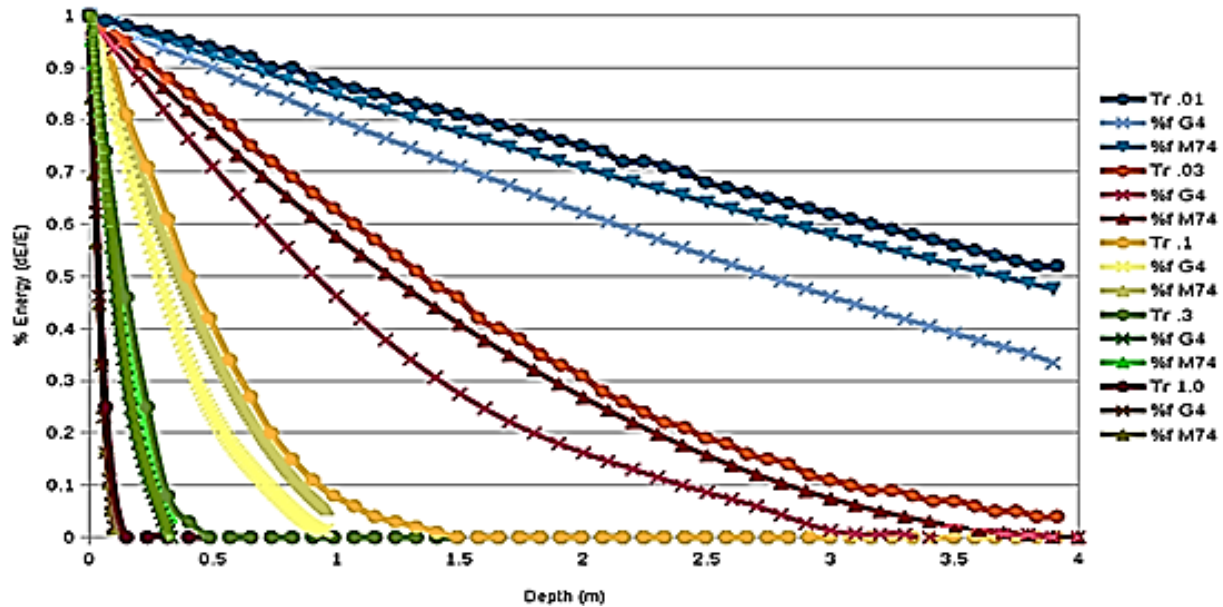
FIGURE 3. FF Energy Loss vs. Range in solid U-235 dust in vacuum at densities of 0.01,0.03,0.1,0.3 & 1.0 mg/cc.

To determine the rate at which the fission fragments heat the hydrogen plasma a third computer model, FF-HEAT, was developed. This computer program is based on the theory of the Coulomb collision integral [4]. The model was validated by comparison with experimental data [5]. Figure 4 compares the predictions of this model to data for various fission fragments penetrating hydrogen plasma, a) Ca-40 below the low-mass FF peak, b) Pb-208 above the high-mass FF peak, and c) Ga-74, d) Kr-84, and Pd-110 lying on the FF mass peak. There is good agreement between the model and data.
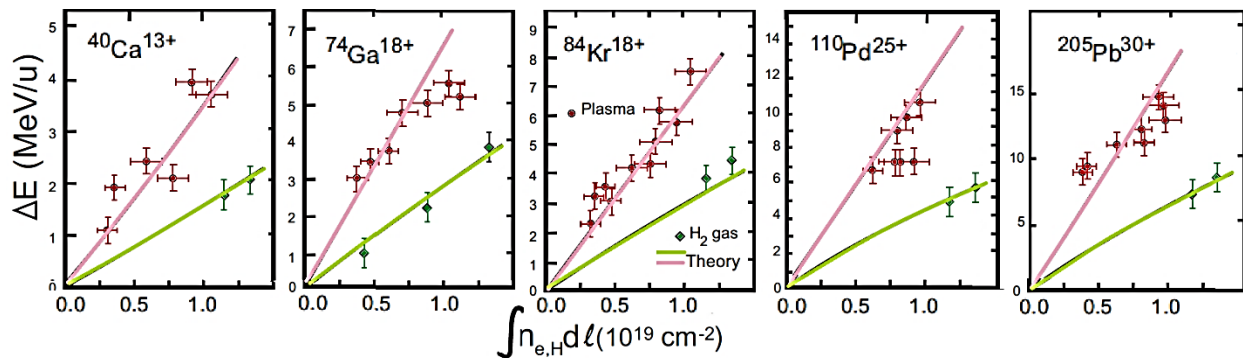
FIGURE 4. Theory & Experiment of the fission fragment energy loss vs. H^+ plasma, Hydrogen gas density [5].

FF-HEAT and SRIM were used to investigate the FF heating of various dust hydrogen mixtures. Using these models various trade studies were performed. Figure 5 shows the fraction of FF energy deposited into a dusty hydrogen electron plasma mixture at a temperature of 252 eV and a density of 1.44×10^{-3} kg per cubic meter for varying dust densities. This figure informs us that mixtures with low dust densities preferentially heat the electrons rather than the hydrogen ions.
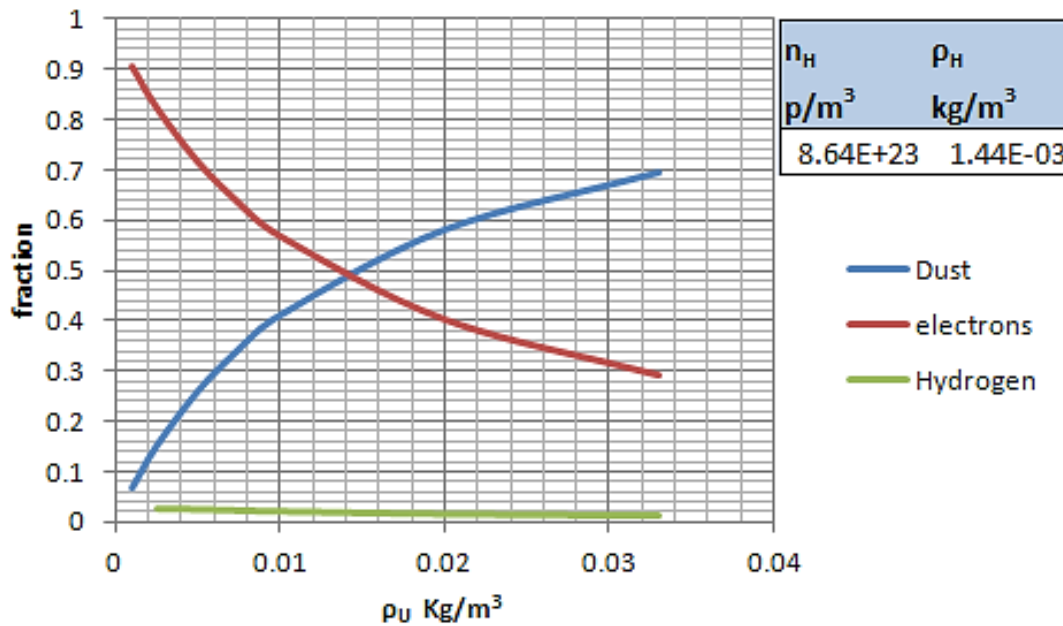
FIGURE 5. Fraction of Fragment Energy Transferred to Plasma versus Dust density T_H =252 eV.

As shown in Figure 6, this energy is quickly transferred to the hydrogen ions under the plasma conditions of interest. Even so the electrons may be hotter than the ions. The final result reached after a few microseconds at most, is that energy transferred to plasma electrons is effectively transferred to the hydrogen.
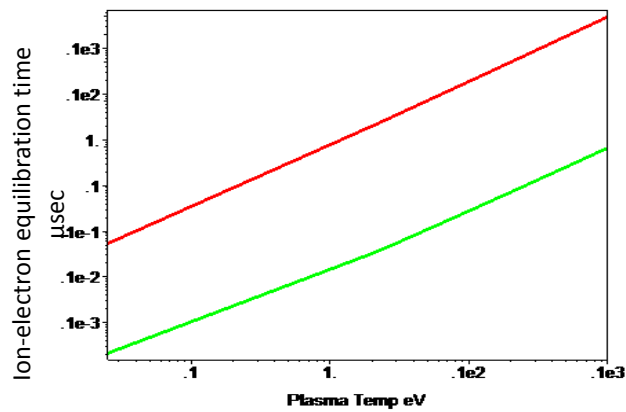
FIGURE 6. Electron- Ion Heat Exchange Time [3].

The trade studies in Figure 7, show low temperature mixtures with low uranium dust density and high hydrogen density are more effective at stopping fission fragments. The lower limit on uranium dust density is set by the requirements of reactor nucleonics given in Figure 2, where the critical dust density as a function of reactor major radius for three nuclear fuels is plotted.
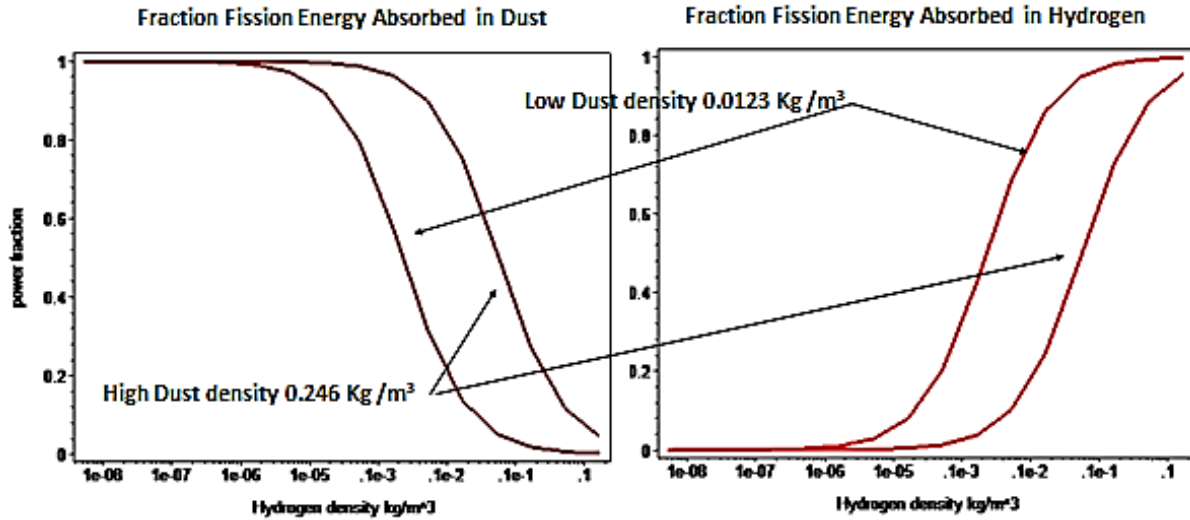
FIGURE 7. Fraction FF energy absorbed in Dust+Hydrogen vs. Density of [H+] for two reactor dust densities.

The upper limit on reactor power is determined by two factors: effectiveness of fission fragment heating and dust cooling. Dust cooling requirements also put constraints on the hydrogen density. For the dust to remain below its melting point, the frictional heat gained from the fission fragments burrowing out to the surface, and the conducted heat gained from the flowing hot hydrogen plasma must be offset by the radiative heat loss by infrared radiation from the dust surface to the reactor walls. For this to happen the plasma must remain transparent to infrared radiation so the particles can see the walls, and the thermal energy transferred to the dust by conduction from the flowing plasma must remain below that which would melt the dust particles. The dust grains might experience mass loss by vaporization, or gain by condensation depending on plasma conditions. Figure 8 shows the factors in determining thermal balance.

$$q_{evaporation-condensation} = \dot{m}Q_{latent\ heat\ of\ vaporization}$$

$$q_{radiation} = \sigma_{sb} 4\pi r^2 (T_{dust}^4 - T_{wall}^4)$$
$$\text{(InfraRed)}$$

$$q_{convection} = h_{convect} 4\pi r^2 (T_{plasma} - T_{dust})$$
$$\text{(Ions + Electrons)}$$

$$q_{fission\ frag} = \frac{4}{3}\pi r^3 Q'''_{fission\ heating\ rate}$$
$$\text{(from SRIM)}$$
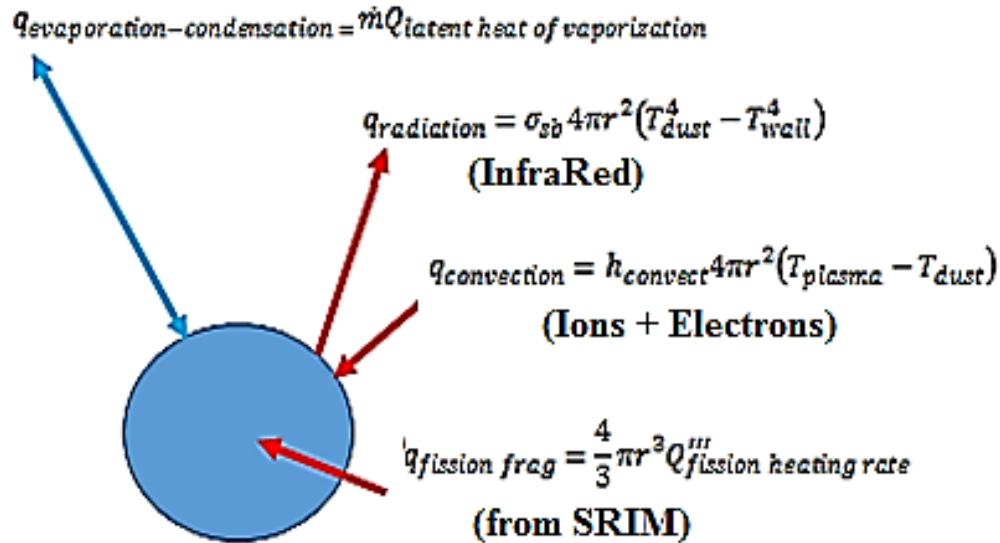
FIGURE 8. Dust Grain Thermal and Mass Transfer Balance Considerations [6].

The Knudsen number is the ratio of the molecular mean free path to the dust particle size. Typical particle size may be 100 nanometers. The molecular mean-free-path is a function of hydrogen plasma density. Free molecular flow applies when the Knudsen number is greater than 10. The hydrogen density at which the Knudsen number equals 10 is 3.73 kg/m^3. At densities below this, the hydrogen plasma acts as a rarified gas with respect to the dust grains. Thus, the rarefied nature of the hydrogen plasma must be considered when calculating heat transfer to the dust from the plasma. Reference [6] is used to calculate the rarefied gas convective heat transfer from the dust to the surrounding hydrogen plasma.
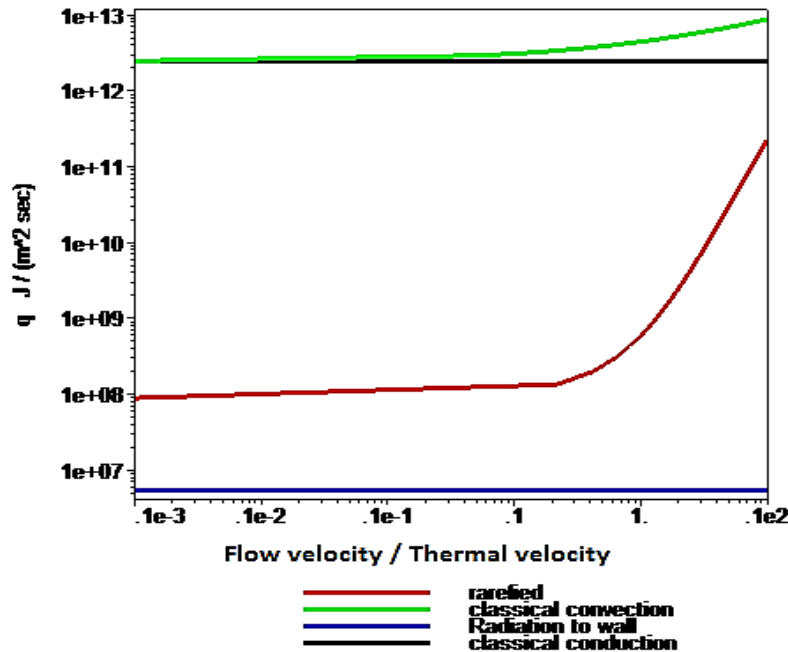
FIGURE 9. Convective Heat Transfer Coefficient for Dust grain in Flowing Hydrogen Plasma [6].

Figure 9 shows the results of this calculation in the case of 100 nm dust grains. The rarefied heat transfer coefficient is much smaller than the atmospheric pressure convective heat transfer coefficient. This result explains how dust can coexist with a hot hydrogen plasma as is commonly observed in reactive ion etching machines and in fusion experiments and other plasma machines. At low hydrogen pressure hot hydrogen can coexist with solid dust particles.
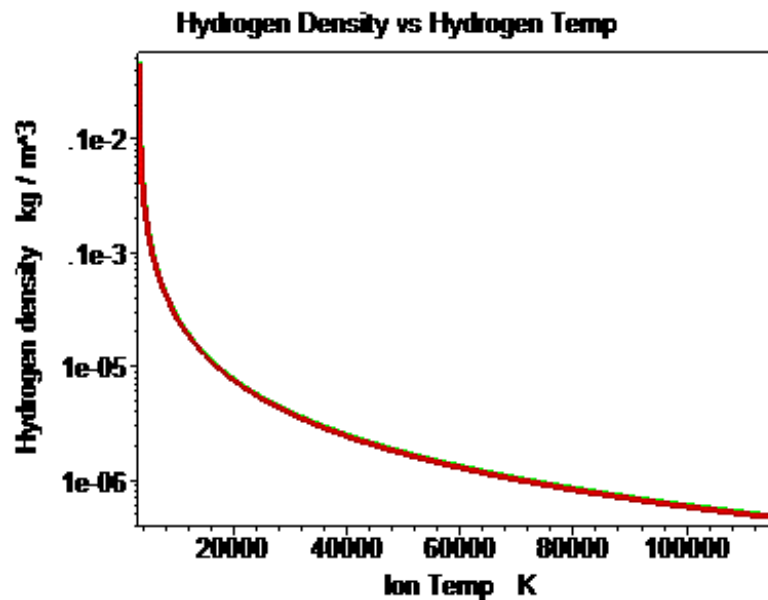
FIGURE 10. [H+] Density vs. Plasma Temperature Required for UO$_2$ fuel dust to remain at 3120K melting point.

Figure 10 show the conditions of temperature and density under which hydrogen can coexist with 100 nm dust grains without the occurrence of melting or vaporizing. It is interesting to see that hydrogen at 100,000 degrees Kelvin can coexist with solid dust albeit at very low densities.

Although hot low density hydrogen can coexist with solid dust it must be demonstrated that fission fragments can raise hydrogen to these temperatures. To this end a multicomponent equilibrium heat transfer model was developed that considered the fission fragment heating of dust, hydrogen and electrons together with the convective heat exchange between these plasma components and with the reactor vessel containment wall. Table 1 shows the particle to particle interactions considered in this model: input on rows, output on columns.

TABLE 1. Matrix elements considered in the exchange of heat between dusty plasma components. Gamma-rays and neutrons penetrate into the moderator and are not included in this equilibrium.

	fission frag ↑	ions ↑	electrons ↑	dust ↑	wall ↑
fission frag →	0	X	X	X	0
electrons →	0	X	0	X	0
ions →	0	0	X	X	0
dust →	0	X	X	0	X
IR from wall to→	0	0	0	X	0

Figure 12 shows a typical result from this simulation. Shown is the hydrogen temperature that can be obtained by fission fragment heating as a function of hydrogen density for two reactor dust densities. Results show that it is possible to heat low density hydrogen well above the dust melting point while retaining solid dust grains, or produce hot dense hydrogen gas at temperatures very close the dust melting point, either of which might be useful for power generation or high impulse rocket thrust.
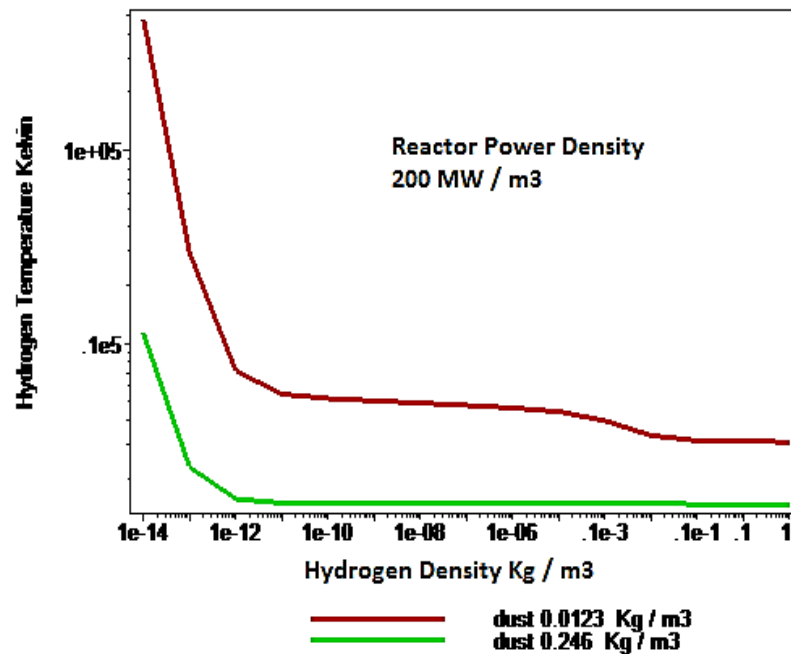
FIGURE 12. Equilibrium H Gas Temperature vs. H Density for two dust densities at same Reactor Power Density.

Charge State Of Fissioning Dust

To compute the maximum dust/hydrogen density, it is necessary to know the charge state of the fissioning dust. Determining this is the subject of another NASA/MSFC-funded project which is attempting an experiment to measure the charge state of a grain of Cf^{252} which is spontaneously fissioning [7]. When the charge state is known it will be possible to determine the maximum hydrogen density at which the dust can remain confined.

$\Phi_{dust} = \frac{q_{dust}}{C_{dust}}$ Dust Potential

$C_{dust} = r \; \exp(- r/\lambda_D)$ Dust Capacitance

λ_D Debye length of plasma

r dust radius

q_{ff} avg. fission fragment charge

q_{ele} electron charge

q_{ion} electron charge

q_{dust} dust charge

n_{ele} electron density

n_{ion} ion density

n_{dust} dust density

T_{ele} electron temperature

T_{ion} ion temperature

$N_{fission}$ total number of fissions / sec

k_B Boltzmann constant

$I_{ions} = H^+ \; ion \; curent$

$I_{electrons} = electron \; current$

$I_{ff} = positive \; current \; of \; Fission \; Fragments$

$$I_{electron} = 4\pi r^2 q_{ele} \; n_{ele} \left(\frac{k_B T_{ele}}{2\pi m_{ele}}\right)^{1/2} \left(1 - \frac{\Phi_{dust}q_{ele}}{T_{ele}k_B}\right) \quad for \quad q_{ele}\Phi_{dust} \leqslant 0$$

$$= 4\pi r^2 q_{ele} \; n_{ele} \left(\frac{k_B T_{ele}}{2\pi m_{ele}}\right)^{1/2} e^{\frac{-\Phi_{dust}q_{ele}}{T_{ele}k_B}} \quad for \quad q_{ele}\Phi_{dust} > 0$$

$$I_{ion} = 4\pi r^2 q_{ions} \; n_{ion} \left(\frac{k_B T_{ion}}{2\pi m_{ion}}\right)^{1/2} \left(1 - \frac{\Phi_{dust}q_{ion}}{T_{ion}k_B}\right) \quad for \quad q_{ion}\Phi_{dust} \leqslant 0$$

$$= 4\pi r^2 q_{ion} \; n_{ion} \left(\frac{k_B T_{ion}}{2\pi m_{ion}}\right)^{1/2} e^{\frac{-\Phi_{dust}q_{ion}}{T_{ele}k_B}} \quad for \quad q_{ion}\Phi_{dust} > 0$$

$$I_{ff} = q_{ff} \frac{N_{fission}}{n_{dust}}$$

FIGURE 13. Dust Grain Charge Balance [8].
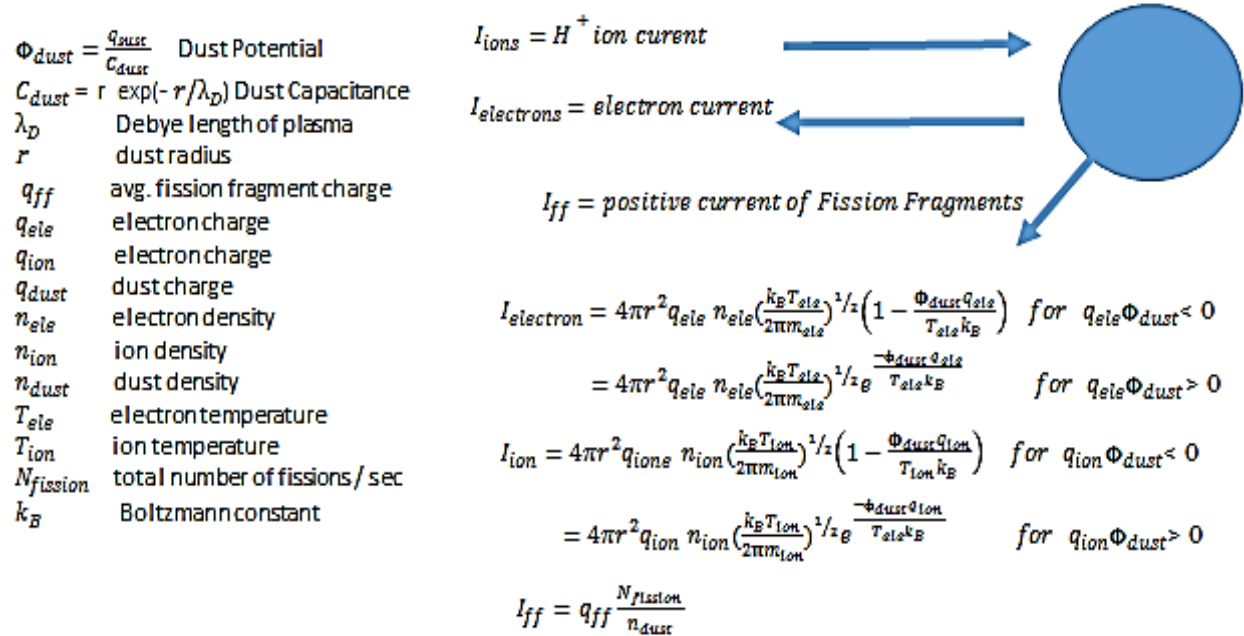
For present purposes the charge state can be estimated by considering the various interactions of the dust grain. Figure 13 shows the balance between positive current from the charged fission fragments leaving the dust grains, negative current of electrons and the positive current of hydrogen ions. Following the discussion in reference [8] an equilibrium charge state model was constructed. The results of this model are shown in Figure 14. It appears that the 100 nm fissioning dust grain has a charge plateau. At high hydrogen ion densities the positive ion current neutralizes the effect of fission negative charging and at low hydrogen densities the charge runs away with no mechanism to neutralize the charge from fission. In between exist a charge plateau of 7 electron charges.
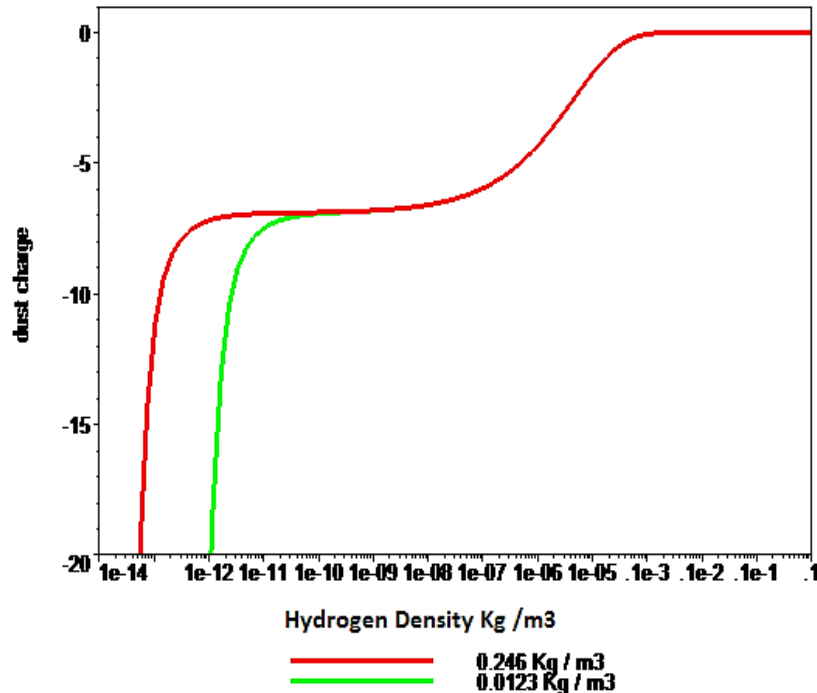

Hydrogen Density Kg /m3

0.246 Kg / m3
0.0123 Kg / m3

FIGURE 14. Dust Grain Charge vs. Hydrogen Density for different Reactor Dust Densities

Packing Density of Fissioning Dust

In order to pack negatively charged dust into a small volume, the hydrogen plasma in the region between dust grains must have enough positive charge to neutralize the repulsion of the dust grains. The radius of a sphere with sufficient plasma inside is called the Debye radius.
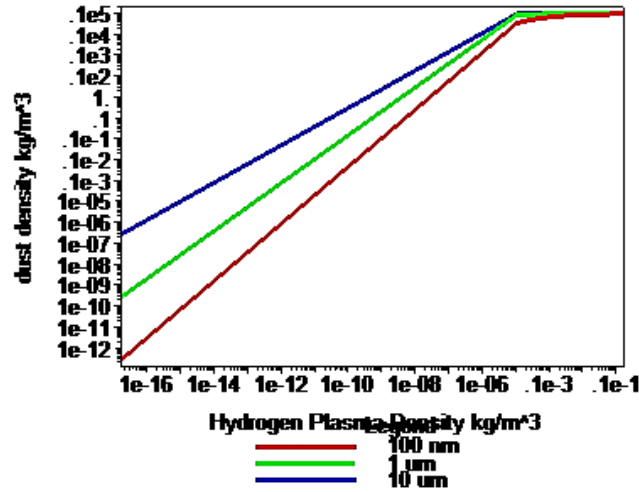

FIGURE 15. Dust vs. H$^+$ density allowing one Debye length between dust particles of three radii.

To prevent agglomeration of the dust grains the average distance between dust grains must be greater than the plasma Debye distance. The maximum dust density for which this condition is true is calculated for various hydrogen plasma densities and shown in Figure 15. Dust grain densities must remain below that shown in the curves for the appropriate grain size to meet or exceed this Debye spacing criteria.

Confinement of Fissioning Plasma

For confinement of the dust in the reactor reservoir, the hydrogen density must be sufficiently low that the drag caused by the flowing propellant does not sweep the dust particle out the nozzle. However as the dust will be charged an electrostatic field can be used to offset the drag force caused by the flow. Figure 16 shows this force balance.

$$F_{drag} = C_d \pi r^2 rho_{plasma} \left(U_{plasma} - U_{dust} \right)^2$$

$$F_{electrostatic} = E_{electric\ field} q_{particle}$$

$E_{electric\ field}$ = Electric Field surrounding dust grain
$q_{particle}$ = Charge on Dust Grain

C_d = Drag Coefficient of Dust Grain
r = dust particle radius
rho_{plasma} = density bulk plasma
U_{plasma} = Flow velocity of bulk plasma
U_{dust} = Flow velocity of dust

FIGURE 16. Dust Grain Force Balance [6].

Following the methods of reference [6] the dust drag coefficient can be computed for various plasma flow velocities. Figure 17 shows the results. From the drag coefficient and the given flow velocity of the hydrogen plasma the strength of the electrostatic field necessary to retain the dust in the reactor vessel can be obtained.
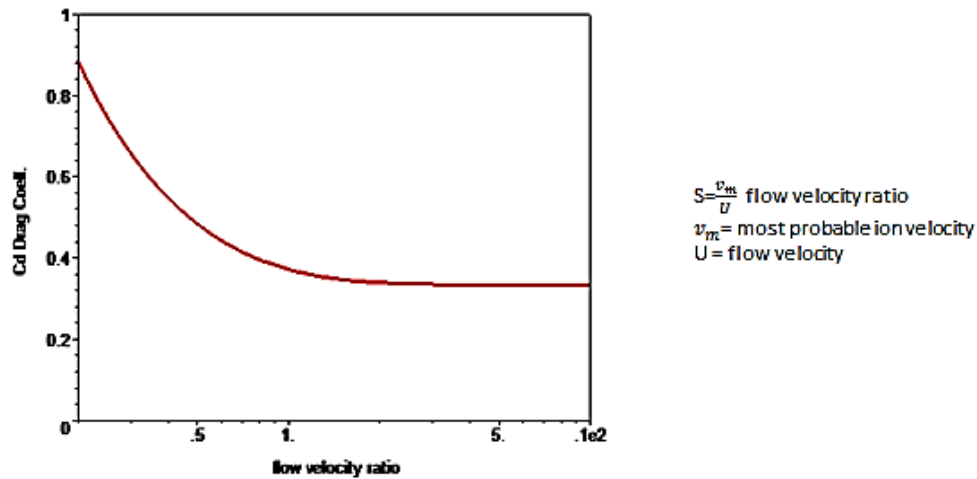

FIGURE 17. Dust Grain coefficient of drag versus velocity ratio[6].

A Fission Fragment Dust Reactor Point Design

All the various aspects of a FFR considered individually above can be combined to develop a first order design of a complete reactor. For simplicity a non-flowing reactor is considered. Hydrogen and dust are confined by the reactor vessel surrounded by 0.5 m thick moderator. A 2.5 meter radius cylinder $U^{235}O_2$ fuel high dust density compact design and a 10 meter radius cylinder radius $Am^{242}O_2$ low dust density design are considered. Figure 2 is used to determine dust densities required for a critical reactor. Hydrogen density and temperature are determined from Figure 12. The grain charge state is taken from Figure 14 and the required dust densities are checked with Figure 15 to verify that the hydrogen and dust densities are compatible with a dusty plasma. Table 2 summarizes these two point designs, where the maximum hydrogen temperature (which gives the maximum thrust ISP rocket) is determined. The moderator mass is calculated from a 1-meter blanket around the exterior of the reactor vessel, so the larger vacuum vessels also have the more massive moderator.

TABLE 2. Two point designs with dust temperature <3120K melting temperature; distance between dust grains is > plasma Debye length; r = 100 nm dust grains; q = -7 charges; reactor power = 200 MW/m^3

Reactor Fuel	Fuel Dens. (kg/m)	Fuel Temp (K)	H Propellant Temp. (K)	H Dens. (kg/m)	Cylinder Size radius, ht (m)	Critical Mass (kg)	Moderator Mass (kg)
$Am^{242m}O_2$	0.0123	3088	4906	$1x10^{-8}$	10, 20	77.28	515,100
$U^{235}O_2$	0.246	1465	1477	$1x10^{-7}$	2.5, 5	24.15	34,500

CONCLUSION

A first order model of a dusty plasma fission reactor is constructed. The model considers the interactions between the various species present in the plasma, fission fragments, 100nm fuel dust grains, electrons and hydrogen ions, to determine the plasma conditions in the reactor. The design obviates the need for an afterburner to mass load the fission fragments by introducing hydrogen gas into the reaction chamber directly. Two point designs meeting all the requirements are considered. Uranium fuel requires a critical mass ~24kg with a high density resulting in relatively low hydrogen temperature. Americium fuel can achieve much lower densities, but then requires such a large size to

achieve criticality that the moderator becomes overly massive. While this low-density reactor achieves better hydrogen temperatures than nuclear thermal propulsion (NTP), with an Isp ~1500 seconds compared to NTP ~900 seconds, the size of the moderator makes it impractical for in-space propulsion. No optimization has yet been performed on this design, so there may yet be a solution that outperforms the NTP in both Isp and acceleration. While not achieving high thrust to mass ratios, these results indicate the feasibility of such reactors as a large IR power source. Higher hydrogen plasma temperatures are achievable for even lower densities, but fusion temperature plasma is not obtained for significant amounts of D-T fuel in this configuration.

ACKNOWLEDGMENTS

REFERENCES

[1] R. L. Clark, R. B. Sheldon and R. O. Werka "Dusty Plasma Based Fission Fragment Nuclear Rocket" in, *Proceedings of Nuclear and Emerging Technologies for Space 2013, paper 6790* February, (2013); and, R. L. Clark and R. B. Sheldon "Dusty Plasma Based Fission Fragment Nuclear Reactor" in *Proc. of 41st AIAA/ ASME/ SAE/ ASEE JPC,* AIAA paper #2005-4460, 2005.

[2] MCNP- A General Monte Carlo N-Particle Transport Code, Version 5, LA-UR-03-1987, Los Alamos National Laboratory April 2005.

[3] M74 (E-DEP-1) //rsicc.ornl.gov/, SRIM, //www.srim.org/ and GEANT4 //geant4.web.cern.ch/geant4/

[4] Wesson John, "*Tokamaks* Third Edition", Oxford University Press, New York, 60-70,(2004).

[5] C. Deutsch , G. Maynard, M. Chabot, D. Gardes, S. Della-Negra, R. Bimbot, M.F. Rivet, C. Fleurier, C. Couillaud, D.H., H. Hoffmann, H. Wahl, K. Weyrich, O.N. Rosmel, N.A. Tahir, J. Jacoby, M. Ogawa, Y. Oguri, J. Hasegawa, B. Sharkov, A. Golubev, A. Fertman, V.E. Fortov and V. Mintsev "Ion Stopping in Dense Plasma Target for High Energy Density Physics," The Open Plasma Physics Journal, (2010), **3**, 88-115; and, C. Deutsch, G. Maynard, D. Gardes, A. Servajean, and B.Kubica, C. Fleurier and D. Hong, *Stopping of multicharged ions in dense and fully ionized hydrogen.* Phys. Rev. A. **46**(8), 15 October 1992.

[6] Eckert, E.R.G and R. M. Drake, *Analysis of Heat and Mass Transfer,* Hemisphere Publishing, New York, 511-521 (1987).

[7] NASA CIF 13-024 Dennis Gallagher - Fission Fragment Dust Experiment Final Report, Dec 2014.

[8] Shukla, P.K. and Mamun, A.A., "Introduction To Dusty Plasma Physics," Institute of Physics Publishing, Philadelphia, **38**, 39 (2002), ISBN 0 7503 0653 X.

A Half-Gigawatt Space Power System using Dusty Plasma Fission Fragment Reactor

Robert B. Sheldon[1,2], Rodney L. Clark[1]

[1]*Grassmere Dynamics, LLC, Gurley, AL 35748-8909 256-776-9471 rod.clark@grassmeredynamics.com*
[1,2]*RB Sheldon Consulting, Huntsville, AL 35803 256-6538592; rbs@rbsp.info*

Abstract. A dusty plasma nuclear fission fragment reactor employs a cloud of nanometer-sized dust of fissionable material inside a magnetized moderator. The negatively charged dust, free electrons, and positively charged ions form a 3-component "dusty plasma" that can be confined and manipulated as charged fluid. The nanometer dust has such a large surface to volume ratio, that it is capable of remaining solid at 3000K while radiating 10-100 GW of radiant power, as discussed in previous work. This ``nuclear light bulb" power source solves the intractable problems of previous designs: confining charged dust rather than hot gas; eliminating the need for quartz windows; and not requiring gas cooling. Unlike previous designs the radiation is in the near-infrared, so that conversion to electricity is inefficient. While Brayton-cycle power converters are often advertised as a space power solution, they require additional radiators and additional mass. Several recent technologies, however, can convert NIR into electric power at improved efficiency and with no moving parts. We model the conversion efficiency of a space system consisting of radiators, moderator, direct fission-fragment converter, and IR converter panels as a viable solution to the growing need for MW space power systems.

Keywords: Fission fragment nuclear reactor, dusty plasma, mass to power ratio, infrared power conversion

INTRODUCTION

This paper complements the paper "A Six Component Model for Dusty Plasma Nuclear Fission Fragment Propulsion" by Clark and Sheldon (CS16) [1], where we look at the advantages of nuclear energy for space electric-power generation. The nucleonics and thermal design of a dusty plasma fission fragment reactor are discussed there, while this paper addresses the application of a DPFFR to a space power system. The two competing technologies for in-space power are currently solar and radioisotope thermal, which we discuss in turn.

While various schemes have been proposed to extract the ~1.3kW/m^2 of solar radiant energy at Earth orbit, the relatively low power density combined with the ~30% efficiency of advanced solar panels, limit spacecraft to <100 kW power plants. Solar power drops another 75% if the spacecraft is to go to Mars, or 96% if it is headed for Jupiter, making solar panels infeasible for outer planet missions, for manned flight, for Discovery class spacecraft using electric propulsion, and in particular, for the VASIMR electric plasma propulsion engine [2].

Currently, missions to the outer planets use radioisotope generators based on Pu238, Sr90, or ESA's proposed Am241 [3]. The power/mass ratios range between 2-5 W/kg, and the efficiency of the current generation of radioisotope thermal generators (RTG) hover around 7%, with improvements using either thermovoltaics or Stirling engines expected to achieve ~20%[4]. In either case, some 80-93% of the heat must be rejected by the in-space radiators, at the relatively low temperatures of the "cold" side, generally around 350K. A 100kWe (electricity generation), would then weigh some 20-50 tons, and must radiate somewhere between 500-2500kWt (heat energy) into space, requiring about 1 ton of radiators, using the numbers from the proposed Prometheus mission to Jupiter[5]. Coupling this power plant to an advanced ion/plasma engine using the published numbers for the

VASIMR-200 electric propulsion engine with 2.5 N of thrust per 100 kWe, produces an acceleration of <0.00001g, which if launched in low earth orbit (LEO), generates such tight spirals that it has trouble escaping collision with the Moon. As the VASIMR website acknowledges, electric propulsion beyond the Moon will require a nuclear reactor power source with a much higher power/mass ratio.

So the critical numbers for space power will be the ability to get > 1kWe/kg, and provide power for typical outer-planet mission lifetimes of 1-10 years.

THE FISSION FRAGMENT DUST REACTOR

From CS16 Figure 2 we show the critical dust density for Am/Pu/U fuels using a 50 cm thick moderator for various reactor radii. Since the hot neutrons are nearly indifferent to size, the larger radii have higher volume (neutron generation) to surface area (neutron loss), and hence lower dust densities. However the larger radii also have greater moderator volume, which at ~1000 kg/m^3 densities, can quickly dominate the mass budget. Using a compact 1 meter radius right-circular cylinder with volume $2\pi r^3$ and area $6\pi r^2$, and using a moderator thickness of 0.5 m with density 1000 kg/m^3, we can comfortably operate at 200 MW/m^3 for a total of 628 MW and moderator mass of 9424 kg. The amount of fuel in the system is negligible, with only 1.25 kg needed for Am242m, and 4.27 kg for U235. Then the thermal power/mass ratio is a hefty, 66 kWt/kg without radiator mass included.

In order to calculate the electric power/mass ratio, the radiator mass must be estimated. For a closed system, the fission fragment (FF) energy goes entirely into the dust, which itself is cooled by radiation, so the output of this reactor is infrared light (IR) from the hot dust, plus some visible light from non-thermal excitations by the fission fragments. From CS16 table 1, the temperature in the reactor at 200 MW/m^3 is about 1400K, far below the ~3000K melting point of the fuel, so that most of the power comes out as long-wavelength IR. The IR can be used in photovoltaic conversion at about 20% efficiency, or, as suggested in a recent patent, [6,7] absorbed by nano-patterned copper panels, where it excites plasmons and is directly converted into electricity at 84% theoretical efficiency. Despite being very large, these efficiencies are very close to direct electrical conversion of the charged FF, as discussed in Clark & Sheldon [8,9], which suggests that there are several ways to achieve these high values. The key point is that the DPFFR is not generating heat but FF and light, with substantial improvement over the thermal Carnot efficiency. Unfortunately, the uncharged fission products are not so easily controlled, so about 15% of the energy is lost in the fission neutrons and gamma-rays, which are principally absorbed by the moderator and will require active cooling.

Using these optimistic numbers, we then have a heat load of 628 MWt*0.15 = 94 MWt heat load into the moderator, plus 628 MW * 0.85 * 0.16 = 85 MWt heat load into electrical converters. The moderator heat load has to be removed at ~500K temperature, or the moderator oil begins to decompose and lose hydrogen. The direct current FF, or the plasmon converters are metal-insulator-metal nanostructures, which decompose near the melting point of the Ag-Au used in their construction, or about 1200K. Since the efficiency of the radiators goes as the fourth power of the temperature, this high a temperature permits the power-converter radiators to be very efficient, so the dominant size and mass will be for the moderator radiators.

Using results from a 2014 PhD on carbon fiber radiator design,[10] we have 0.3 kg/kWt or 300 kg/MWt, which when multiplied by our 94 MWt of waste heat, produces 28,000 kg for the moderator radiator. Scaling by $(85/94)(500/1200)^4$ for the improved efficiency of the higher temperature radiators, we get about 1000 kg for the power conversion radiators. Then the electrical power to mass ratio is 448 MWe/(9424+29000)kg = 11 kWe/kg, certainly enough for VASIMR to escape LEO orbit.

DISCUSSION

Using the unique feature of the DPFFR that the majority of its power is extracted in the IR, we optimistically estimate an 84% electrical power conversion efficiency. But even if this optimism were misplaced, and the efficiency were substantially lower, the high temperature of the FF/IR power converter mitigates the mass of the radiator needed to dissipate the heat load, and therefore softens its impact on the design. For example, using a

pessimistic 50% power conversion efficiency, the radiator mass is increased by only a few tons, and the energy drops to 266 MWe, for a still respectable 6.5 kWe/kg ratio.

A nuclear reactor has a nearly infinite power range that is controlled by managing the neutron density of the core, from a few watts up to Gigawatts. As discussed in the earlier papers, the radiative cooling of a dusty plasma fuel is so efficient that tens of Gigawatts are possible before the fuel melts, which is the limitation of solid core reactors.

The walls of the DPFFR chamber must reflect most of the IR radiation that is emitted by the core, which is another limitation of the design. Typical CO_2 continuous wave (cw) laser mirrors have a damage threshold around 25 kW/cm^2 at 1000 nm IR wavelength, which for our small chamber with 188,500 cm^2, permits a 4.7GW total fluence. So with proper cooling of the moderator and mirrors, this fluence is not the limiting factor. There will also be a large neutron fluence, which is deadly to metallic surfaces, but less dangerous for ceramics and low-Z mirrors such as carbon-fiber based designs. There has been a great deal of work on the 1st wall in tokomak and fusion energy reactors, so we do not think this will be a limitation on the design.

However, the limitation of DPFFR is not a melted core, or an ablated liner, but a vaporized moderator that must surround the core. It is in the moderator that the neutrons lose most of their heat and then reenter the core to generate further fissions. For a ground-based power plant, this is an advantage, because the moderator can be designed to be a much larger volume than the core, and much more easily cooled. But for in-space power, the larger mass of the moderator reduces the power/mass ratio, and so the core must be kept highly compact. This need for a compact moderator, means that the limitation for in-space reactors are the limitations in power flux per area, or power per volume that must be removed. And even if the materials in the moderator can handle the high heat flux, ultimately the radiators have to be designed to remove that heat, which adds mass to the system and reduces the power/mass ratio.

So it is not the energy conversion efficiency, but the moderator that plays the most important role in both the mass of the reactor and the mass of the radiators. It was for this reason that the Prometheus nuclear-electric mission intended for Jupiter used a fast neutron reactor design without moderators that was originally developed for submarines. That design, while mature, was limited by the working temperature of the materials and required a less efficient, Carnot-limited Brayton-cycle converter. Because of this Carnot-cycle limitation, the designers felt compelled to operate the Braytons at a much higher temperature to get the power/mass ratio they needed, and became the justification for cancelling the Prometheus mission. Not until this DPFFR design, could nuclear reactors provide sufficiently high power/mass ratios, where the extra mass of the moderator was traded for a higher efficiency reactor. And if further improvements in the DPFFR moderator can be realized, say, by using higher temperature aromatic ring oils, or hydrogen-doped beryllium moderators, then radiator mass can be reduced further with a direct improvement in the power/mass performance of this space DPFFR.

CONCLUSION

A half-gigawatt design of a dusty plasma fission fragment reactor is used to calculate the power per kilogram of the in-space power plant at a theoretical 11 kWe/kg, or approximately 2000 times better than RTGs. More conservative estimates for the IR to electrical power conversion reduce this number to about 6 kWe/kg, but the real improvements that can achieve 20-100 kWe/kg will come from advanced moderator materials.

ACKNOWLEDGMENTS

REFERENCES

[1]   Clark, R. L. and R. B. Sheldon, "A Six Component Model for Dusty Plasma Nuclear Fission Fragment Propulsion", NETS 2016, this conference.

[2]   Chang-Diaz, VASIMR-200, url= http://www.adastrarocket.com/aarc/Technology, accessed 1/2016.

[3]   Wikipedia, "Radioisotope Thermal Generators" url= http://en.wikipedia.org/wiki/Radioisotope_thermoelectric_generator

[4]   NASA "Radioisotope power systems: Stirling converter technology", url= http://solarsystem.nasa.gov/rps/asrg.cfm accessed 1/2016.

[5]   Prometheus Final Report, 2005, Nasa technical reports server, url= http://ntrs.nasa.gov/search.jsp?R=20060043352 accessed 1/2016.

[6]   Didomenico, Leo D, "Ultra-efficient energy conversion device for converting light to electricity by rectifying surface plasmon polaritons", United States Patent 8866000, 10/2014.

[7]   Sheldon, M. T. et al., "Plasmoelectric potentials in metal nanostructures", Science, 346 (6211), Nov. 14, 2014.

[8]   Clark, R. L. and R. B. Sheldon "Dusty Plasma Based Fission Fragment Nuclear Reactor" in *Proc. of 41st AIAA/ASME/SAE/ASEE JPC,* AIAA paper #2005-4460, 2005.

[9]   Clark, R.L, R. B. Sheldon and R. O. Werka "Dusty Plasma Based Fission Fragment Nuclear Rocket" in, *Proceedings of Nuclear and Emerging Technologies for Space 2013, paper 6790* February, 2013. Clark, R. L. and R. B. Sheldon "Dusty Plasma Fission Fragment Reactor", NETS 2010.

[10] Briana N. Tomboulian, "Lightweight, High-Temperature Radiator for In-Space Nuclear-Electric Power and Propulsion", PhD UMass, 2014.

Status of the Development of Low Cost Radiator for Surface Fission Power - II

Calin Tarau[1], Taylor Maxwell[1], William G. Anderson[1], Corey Wagner[1], Matthew Wrosch[2], Maxwell H. Briggs[3]

[1]*Advanced Cooling Technologies, 1046 New Holland Ave. Lancaster PA 17601*
[2]*Vanguard Space Technologies, Inc., San Diego, CA 92126*
[3]*NASA Glenn Research Center, Cleveland, OH, 44135*
717-295-6066; calin.tarau@1-act.com

Abstract. NASA Glenn Research Center (GRC) is developing fission power system technology for future Lunar and Martian surface power applications. The systems are envisioned in the 10 to 100kWe range and have an anticipated design life of 8 to 15 years with no maintenance. NASA GRC is currently setting up a 55 kWe non-nuclear system ground test in thermal-vacuum to validate technologies required to transfer reactor heat, convert the heat into electricity, reject waste heat, process the electrical output, and demonstrate overall system performance. The paper reports on the development of the heat pipe radiator to reject the waste heat from the Stirling convertors. Reducing the radiator mass, size, and cost is essential to the success of the program. To meet these goals, Advanced Cooling Technologies, Inc. (ACT) and Vanguard Space Technologies, Inc. (VST) are developing a single facesheet radiator with heat pipes directly bonded to the facesheet. The facesheet material is a graphite fiber reinforced composite (GFRC) and the heat pipes are titanium/water Variable Conductance Heat Pipes (VCHPs). By directly bonding a single facesheet to the heat pipes, several heavy and expensive components can be eliminated from the traditional radiator design such as, POCO™ foam saddles, aluminum honeycomb, and a second facesheet. As mentioned in previous papers by the authors, the final design of the waste heat radiator is described as being modular with independent GFRC panels for each heat pipe. The present paper reports on test results for a single radiator module as well as a radiator cluster consisting of eight integral modules. These tests were carried out in both ambient and vacuum conditions. While the vacuum testing of the single radiator module was performed in the ACT's vacuum chamber, the vacuum testing of the eight heat pipe radiator cluster took place in NASA GRC's vacuum chamber to accommodate the larger size of the cluster. The results for both articles show good agreement with the predictions and are presented in the paper.

Keywords: Heat Pipe Radiator, Surface Fission Power, Low Cost Radiator, Single Face Sheet Radiator

INTRODUCTION

NASA Glenn Research Center (GRC) is developing fission power system technology for future Lunar surface power applications. The systems are envisioned in the 10 to 100kW$_e$ range and have an anticipated design life of 8 to 15 years with no maintenance. A nominal lunar fission surface power design has been developed and is shown in FIGURE 1 [2]. The nuclear reactor supplies thermal energy to Brayton (or Stirling) convertors to produce electricity, and uses a heat pipe radiator to reject the waste heat generated by the convertors. The radiator panels must reject heat from both sides to achieve the highest efficiency; therefore, the optimum mounting position is vertical. The radiator panels contain embedded heat pipes to improve thermal transfer efficiency. Since the heat pipe evaporator is on the bottom, the heat pipes are gravity aided and can work as a thermosyphon. This is advantageous because the heat pipe is not required to pump the working fluid back to the evaporator against gravity. Heat is supplied to the heat pipes through a titanium/water heat exchanger that is coupled with the coolant loop in the radiator.

Currently, NASA GRC is developing a Fission Power System Technology Demonstration Unit (TDU) [1, 3]. The TDU is a non-nuclear demonstration unit that will be tested in vacuum to demonstrate the performance of the integrated system. The primary goals for the early systems are low cost, high reliability and long life. To help achieve these goals, ACT, NASA GRC, and VST are developing a single facesheet direct-bond radiator; see FIGURE 2. The radiator will have VCHPs made from titanium that will use water as the working fluid and argon as non-condensible gas (NCG).
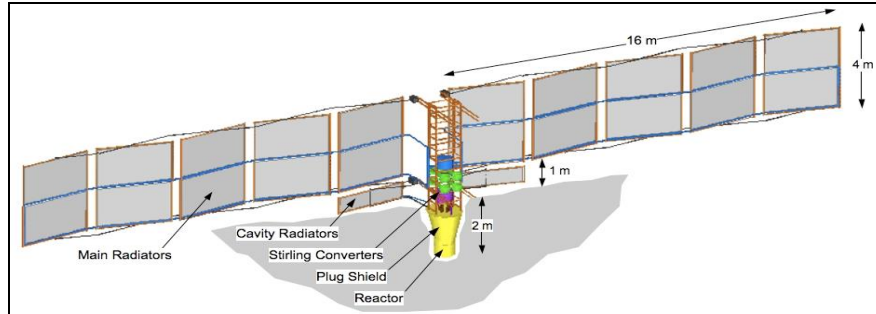

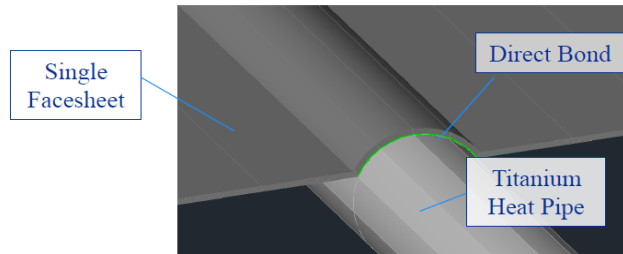**FIGURE 1.** Fission surface power system concept [5]

FIGURE 2. Single-facesheet radiator with direct bonding of the facesheet to the heat pipes [4]

Background

The single, direct-bond facesheet radiator has the advantages of reducing mass and cost of the system by eliminating the graphite foam saddles, aluminum honeycomb, and one of the graphite fiber reinforced composite (GFRC) facesheets, which are present in the previous ACT/VST heat pipe radiators [6].

TABLE 1. Summary of final radiator design.

Geometry	0.75" Cond. OD Design
Evaporator Length (cm)	13
Adiabatic Section Length (cm)	7.62
Condenser Length (cm)	170
NCG Reservoir Length (cm)	7.62
Fin Width Overhang (cm)	12
Total GFRC Area (m^2)	42.36
Total Number of Heat Pipe Modules	96
Total Number of Heat Pipe Clusters	12
Heat Pipe Redundancy Compared to Nominal Radiator (i.e. 36kW, 175K Sink, 400K inlet)	23
% Margin by Area Compared to Nominal Radiator	24
Thermal Performance & Mass	
Total Power Output (kW)	40
Specific Power (W/kg)	609.0
Dry Mass of Single Heat Pipe/Fin Module (kg)	0.685
Total Dry Mass of Radiator System (kg)	65.74

ACT and VST have previously demonstrated the feasibility of the single facesheet radiator by fabricating and testing a small-scale, two heat pipe radiator panel [5]. In a second paper related to this topic [4], the status of the Low Cost Radiator Development was presented where the final design was shown. It was decided that a 0.75 in. (1.91 cm) heat pipe condenser O.D. was more suitable for TDU integration, since it lowers the risk of composite fiber breakage during facesheet direct bonding. The larger diameter pipes also allow for more heat transfer area between the pipes and facesheet, thus lowering the thermal resistance and reducing the necessary number of heat pipes (radiator modules). TABLE 1 summarizes the geometry, thermal performance and mass of the final radiator design.

In addition, the face-sheet/heat pipe interface was also optimized. The wrapping angle of the GFRC around the 0.75 in. (1.91 cm) heat pipe condenser was investigated systematically. Based on thermal performance, a wrapping angle of 151° was chosen. This wrapping angle was the largest among the three wrapping angles that were investigated and presented earlier [4]. The current paper presents a continuation of this development by showing testing results of both heat pipe radiator module and first heat pipe radiator cluster.

HEAT PIPE RADIATOR MODULE TESTING

The development of the Heat Pipe Radiator Module consisted of the following: designing the module and associated heat pipes, developing the direct bond region characterized by the wrapping angle, testing of the heat pipe, developing the testing setup (cold wall) and testing the module. While most of the items mentioned above were discussed and presented in previous papers [4,5], module testing setup and results are presented in this paper.

Heat Pipe Radiator Module

The purpose of the full-scale module development is to validate the heat transport and heat rejection capability of the entire radiator and the ability to start-up from a frozen state. The heat pipe outer surface was primed with BR-127 prior to direct bonding to the GFRC fin. Vanguard Space Technologies, Inc. (VST) fabricated the tool required to make the 0.2 in. (0.508 cm) depth radiator (corresponding to the 151° wrapping angle previously mentioned and described in the previous paper). The fabricated heat pipe radiator module is shown in FIGURE 3a and direct bonding details for both sides of the module are shown in FIGURE 3b and c.
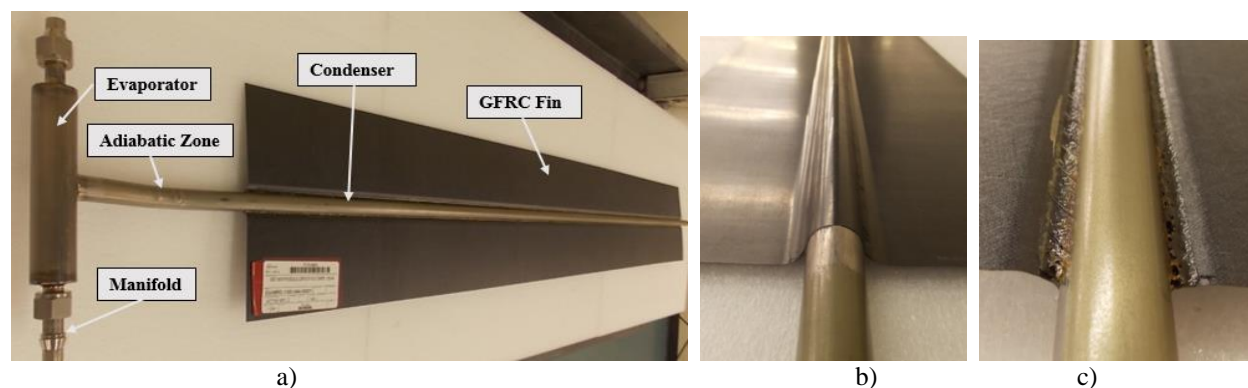

FIGURE 3. a) Fabricated radiator module ready to be tested. Direct bond of GFRC to titanium heat pipe b) Top side and c) Bottom side.

Test Setup

FIGURE 4a shows the testing setup with the module installed inside. The entire assembly is placed in ACT's thermal vacuum chamber for testing as seen in FIGURE 4b. The water line is connected to the manifold and the evaporator is heated by circulating hot water through the manifold, similar to the system will operate in NASA'S TDU. Thermocouples are placed along the entire length of the heat pipe to measure thermal conductivity of the adhesive bond. RTDs are installed before and after the manifold for water temperature measurements. A digital flow

meter is also installed to provide the necessary information for calorimetry calculations to evaluate the power rejected by the radiator module for a given water inlet temperature.
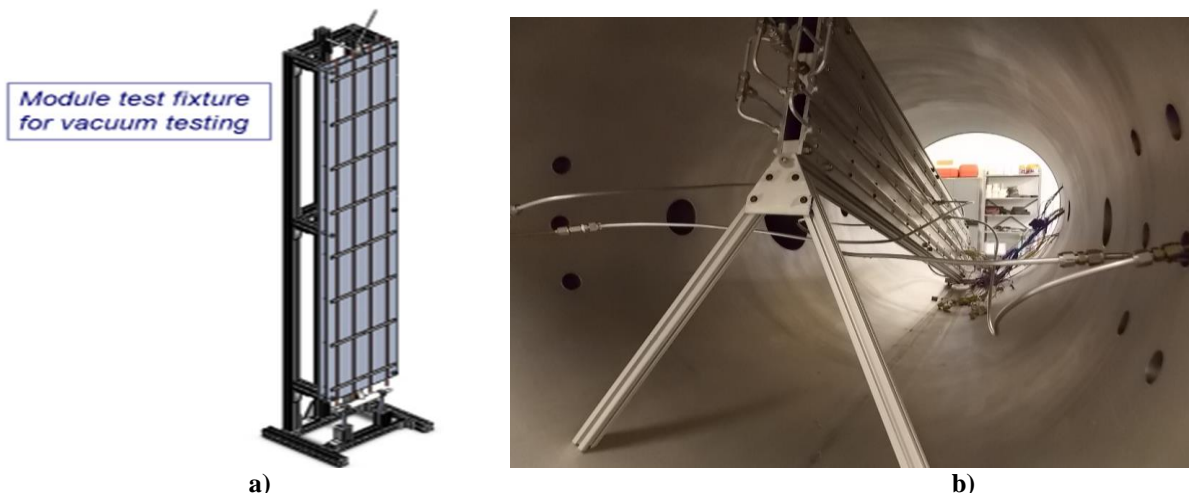

a)   **b)**

FIGURE 4. Fixture for thermal vacuum testing of the radiator module. The evaporator section of the sandwiched module can be seen near the bottom and the reservoir and the fill tube can be seen at the top of the condenser section b) Testing setup and the radiator module assembly as installed in ACT's vacuum chamber for testing.

Testing of the Heat Pipe Radiator Module

VST fabricated the single radiator module with an emphasis on bond development and improving the contact between the GFRC and titanium heat pipes. Thermal lap shear tests were conducted on coupons alongside module fabrication to evaluate bond strength. ACT performed thermal performance testing in both vacuum and ambient conditionsto evaluate the heat rejection capability and integrity of the adhesive bond. Thermal cycle testing was also conducted to determine if the direct bond experiences any degradation caused by CTE induced stresses. Thermal performance testing was repeated to detect and evaluate potential damages or changes to the direct bond joints. After extensive testing, the original evaporator (5.5in (14 cm) long) was cut and replaced with a 7in. (17.8 cm) one to determine the effect of evaporator length on overall thermal performance.

Heat Pipe Radiator Module Testing in Vacuum

The radiator module was tested in vacuum in a gravity aided orientation. However, because of the limited size of the vacuum chamber at ACT (92 cm in diameter), the module was inclined at a ~ 45° angle. Three parameters were varied during testing: sink (cold wall) temperature, water inlet temperature and water flow rate.
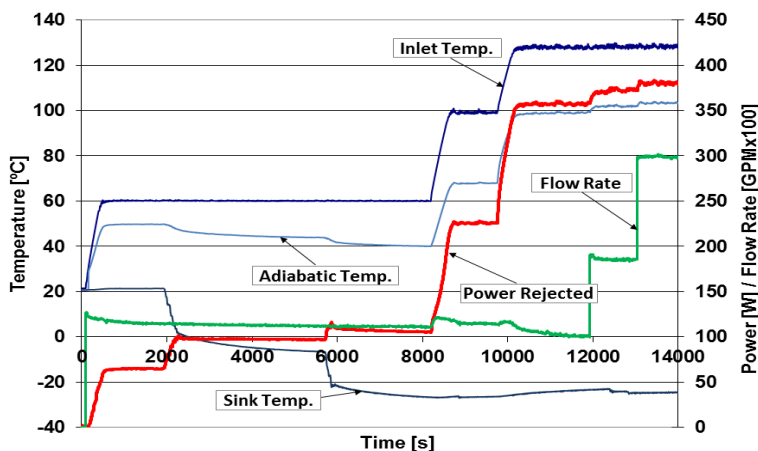

FIGURE 5. Power test before thermo-cycling test.

During the _first testing sequence_, all parameters mentioned above were varied starting with unfavorable values. For instance, the test began with a higher than nominal sink temperature (ambient), a lower than nominal water inlet temperature (60°C), and a lower than nominal water flow rate (1.1GPM). The values and order of these changes was as follows: 1) Sink temperature: ambient, -5°C, -23°C, 2) Water inlet temperature: 60°C, 100°C, 127°C and 3) Water flow rate: 1.1GPM (4.2 L/min), 1.8GPM (6.8 L/min) and 3GPM (11.4 L/min). FIGURE 5 shows the initial vacuum testing of the module where the parameters were changed as previously described. In the end, when all the nominal values were reached, the power rejected by the module was 380W. Note that the predicted radiator module performance in nominal conditions is 416W.

The _second testing sequence_ was thermal cycling in vacuum. Three cycles were performed by simultaneously changing sink temperature (between ambient and -165°C), water flow rate (between ~ 1.254GPM and 0) and water inlet temperature (between 25°C and 122°C). All the cycles are shown in FIGURE 6 where it can also be noticed that the resulting power during the thermal cycling test was between 0 and 360W.
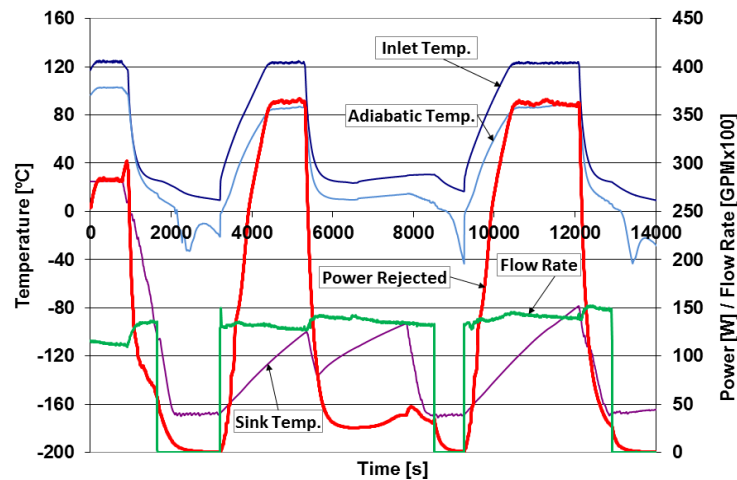

FIGURE 6. Thermo-cycling test.

The _third testing sequence_ was a simple power test (also in vacuum) to check the integrity of the direct bond after the thermal cycling sequence. As seen in FIGURE 7, the power rejected by the radiator after the thermal cycling was 380W, which is equal to the power rejected before the thermal cycling in similar conditions (i.e. similar vacuum, sink temperature, water temperature and flow rate). The conclusion was that no degradation of thermal resistance was observed after thermal cycling.
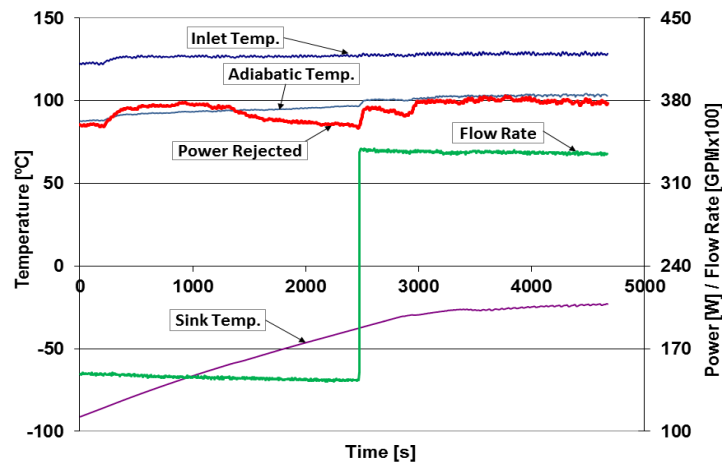

FIGURE 7. Power test after thermo-cycling test.

Module testing in ambient

Since all the radiator clusters tested at ACT must be in ambient conditions, the single radiator module was also tested in ambient. However, the results from the ambient testing are still helpful in determing how the radiator cluster will perform under vacuum conditions. The ambient testing results of the module are shown below in FIGURE 8a. The rejected power is 500W while the coolant temperature was 127°C and the flow rate was 3.4 GPM (12.9 L/min). As shown in the next section, radiator module testing in ambient also served for comparison between the performance of the module with the original evaporator of 5.5in (14 cm) and the module with an extended evaporator (7in (17.8 cm) long). The module in the new configuration was tested again in ambient and the results are shown in FIGURE 8b.
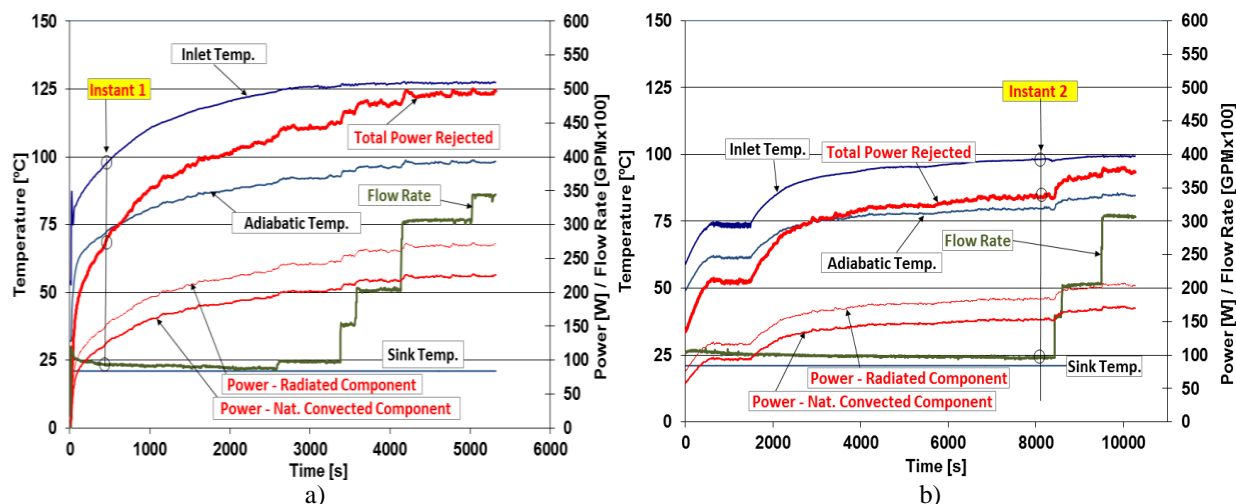

FIGURE 8. Module testing in ambient: a) initial evaporator length of 5.5in (13.7cm) b) final evaporator length of 7in (17.8 cm)

Large evaporator module testing in ambient

As mentioned previously, the module was also tested with a longer evaporator section to determine the effect on thermal performance. However, during testing of this module in ambient conditions the water heater had some technical problems, which prevented the water temperature from exceeding 100°C. To compare the heat rejection capability of the two configurations of the module (5.5 inch evaporator and 7 inch evaporator), instants where relevant parameters are similar (i.e.sink temperature, coolant flow rate and water inlet temperature) were chosen. As seen in FIGURE 8a and b parameters corresponding to Instants 1 and 2 in the two plots are: Coolant Flow rate = 1 GPM, Sink Temperature = 21°C and Coolant Inlet Temperature = 96°C. In the above conditions it was observed that:

- Power rejected by the module with a 5.5in (14.7 cm) evaporator was 275 W
- Power rejected by the module with a 7in (17.8 cm) evaporator was 345 W

In conclusion, the power rejected by the module with a 7in (17.8 cm) evaporator is approximately 25% higher than the one with a 5.5in (14 cm) evaporator. This percentage is expected to increase when the inlet temperature becomes nominal (127°C) because of the radiation component of the total power in ambient. In vacuum, this percentage would increase even more than in ambient simply because the radiation is the only heat rejection mode. It was decided that, although the performance of the 5.5in (13.7 cm) evaporator was satisfactory, the rest of 11 clusters will use 7in (17.8 cm) evaporators to increase the margin of performance of the TDU ultimate radiator.

HEAT PIPE RADIATOR CLUSTER DEVELOPMENT

The plan in the beginning of the program was that only the first radiator cluster will be tested in vacuum at NASA GRC's vacuum chamber. Since this cluster was the first one, it has short (5.5in, 13.7.cm) evaporators, as shown in FIGURE 9. As soon as the cluster arrived at ACT valves were installed on the heat pipes and the heat pipes were

charged with water. A flow meter was installed and RTDs were placed in the hot water supply stream before and after the cluster for calorimetric measurements.

FIGURE 9. First cluster a) Actual radiator cluster b) Detail showing the manifolds, the heat pipe evaporators and adiabatic sections.

Full Testing in Ambient at ACT

After a preliminary testing the cluster was fully instrumented and also charged with NCG. FIGURE 10 shows the thermocouple map used for both full ambient testing at ACT and future vacuum testing at NASA GRC. As it can be seen, each condenser was provided with 6 TCs marked as P1C1, P1C2 …P1C6 …P8C1…P8C6. The condenser TCs were installed on GFRC and not on the titanium pipe. The reservoirs had one TC each marked as P1R …P8R. The adiabatic sections also have one TC each marked as P1A …P8A. In addition to the two fluid "in" and "out" RTDs, 6 other TCs were installed on the manifold surfaces between the evaporators. These thermocouples are marked as CC1 …CC6.
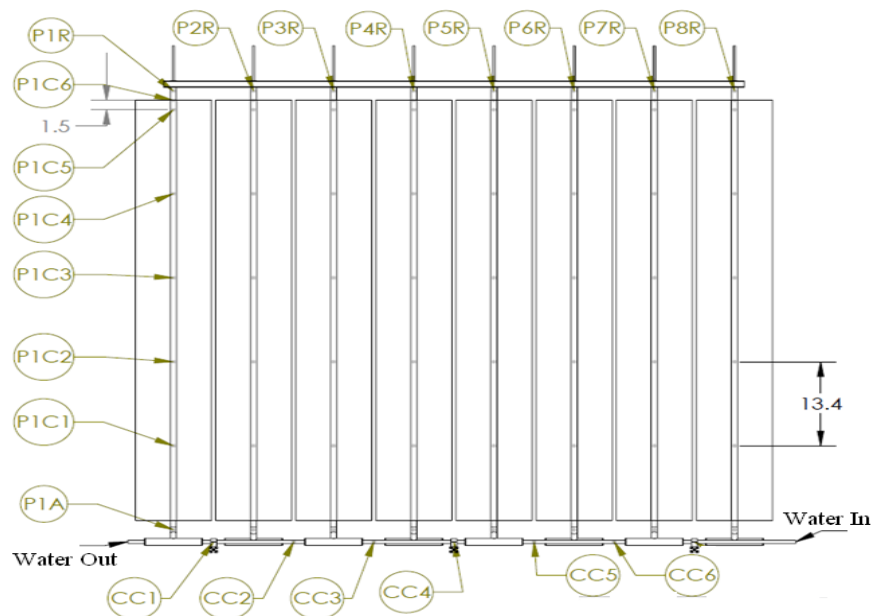

FIGURE 10. Thermocouple map on the First Cluster.

The actual testing consisted of a power test for various water inlet temperatures. The sink temperature was always ambient (21°C) and the flow rate was always 6 GPM (22.7 L/min). Since the two manifolds are connected in parallel, it was assumed that the flow rate per manifold was approximately 3 GPM (11.35 L/min).
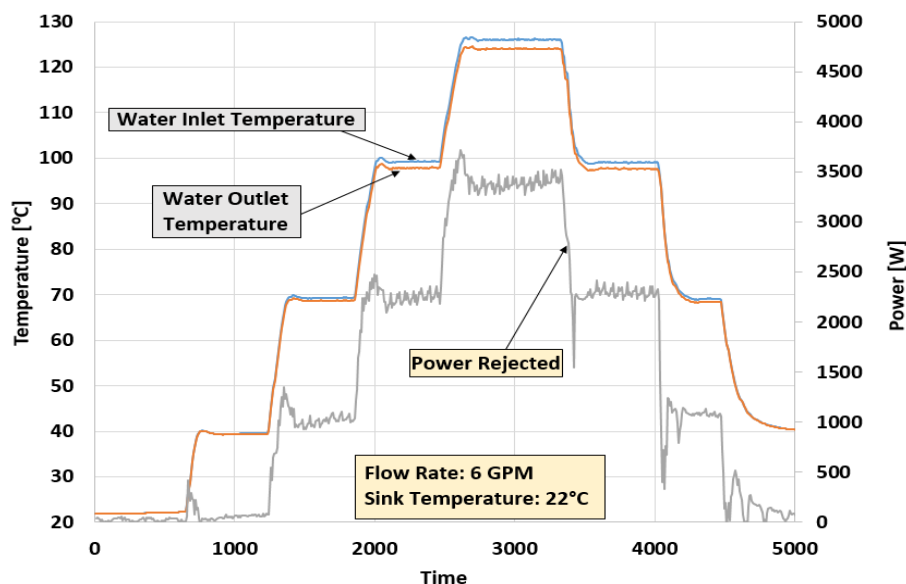

FIGURE 11. Power test: heat rejected for various water inlet temperatures

FIGURE 11 shows the power test results in ambient at ACT. As seen, the water inlet temperature was increased in steps from ambient all the way to the nominal value of 127°C. The intermediate steps were at 40°C, 70°C and 100°C. At each temperature step steady state was allowed to be reached. The maximum rejected power was again ~3.5 kW. However, there was conservative aspect of this test that is described in more detail below..

During this experiment the heat pipes worked as VCHPs and not as CCHPs. As the next plots will show, the NCG charge is slightly too large which preventedthe heat pipe condensers to be fully active at nominal water inlet temperature. As a consequence, it is expected that the panel would reject more than 3.5 kW in ambient conditions at nominal water inlet temperature and flow rate if the NCG amount is properly adjusted.
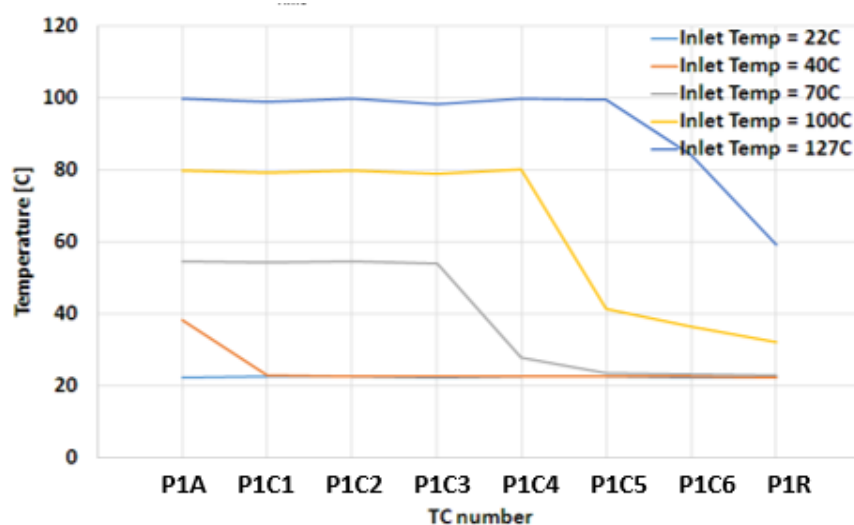

FIGURE 12. Steady state temperature profiles along Pipe No 1 corresponding to each water inlet temperature.

FIGURE 12 shows temperature profiles along the pipe number 1 during steady states at each water inlet temperature. This representation was necessary to evaluate the active length of the condenser. Indeed, it can be observed the NCG is slightly oversized. This is shown mainly by the temperature profile at the nominal water inlet temperature of 127°C where TCs P1C6 and P1R show lower temperatures when compared to the rest of the thermocouples. More complete analysis (not shown here) revealed similar temperature distributions in each pipe. The slight NCG apparent overcharge is due to the fact that the charge was calculated for a nominal sink temperature of -23°C rather than 22°C. As a consequence, the warmer reservoir caused a shorter active length of the condenser.

Cluster Testing in Vacuum at GRC

The first cluster was tested in vacuum in two rounds. During the first round the nominal parameters could not be used because of various reasons. In other words, sink temperature was 2°C (compared to the nominal value of -23°C), water inlet temperature and flow rate were 100°C and 3.9 GPM (14.8 L/min) respectively compared to the nominal values of 127°C and 6GPM (22.7 L/min), respectively. Therefore, a second round of testing where water inlet temperature was nominal was performed at a later time. Since the testing results obtained during the second round were very recent at the time of writing the paper, only the results of the first round of testing are presented in this paper.

The actual test consisted of a power test, followed by thermocycling and another power test to verify the status of the thermal resistance of the direct bond between GFRC and the titanium condenser. The water inlet temperatures during the two power tests were 40°C, 70°C and 100°C. During the thermal cycling sequence, the water inlet temperature was varied between 100°C and ambient. Water flow rate and sink temperature were always 3.88 GPM (14.7 L/min) and 2°C, respectively. As seen in FIGURE 13, two rejected powers are represented: one power resulted from calorimetric calculations and is represented by a highly scattered succession of data points, while the other power resulted from radiation calculations based on temperatures measured on each panel. As it can be observed, the agreement between the two power representations is good. It can be concluded that the power rejected by the radiator at 100°C water inlet temperature is 1.94 kW. Moreover, the rejected power after thermocycling did not change for all three water inlet temperatures. This fact confirms the integrity of the bond. Other conservative factors are discussed below in the conclusion section.
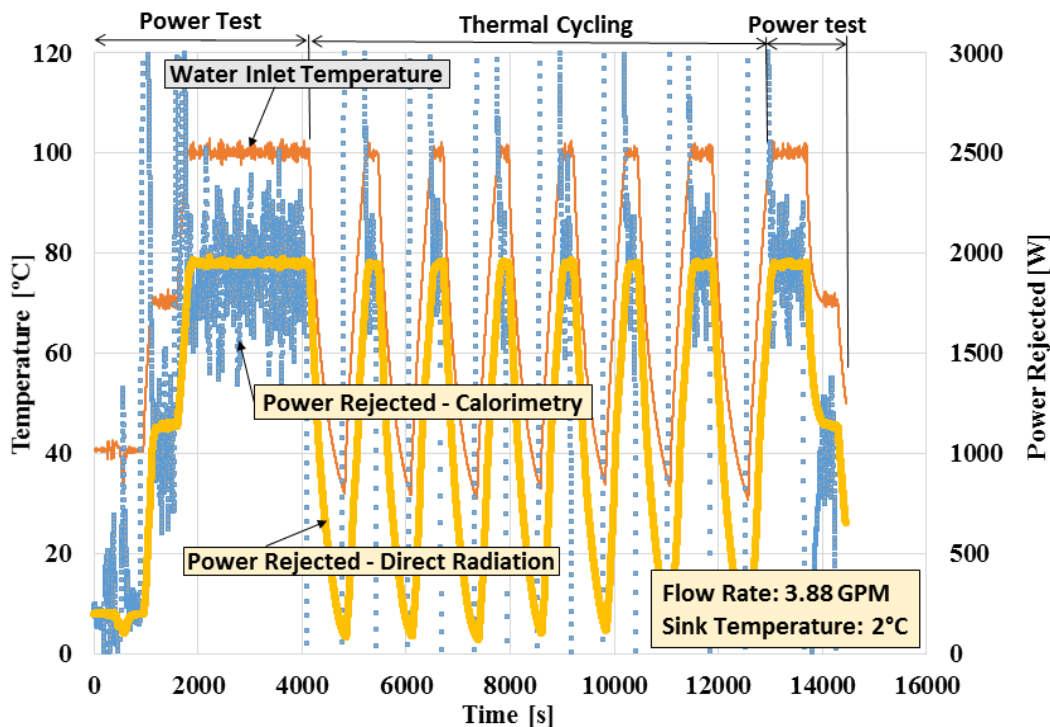

FIGURE 13. Radiator cluster testing in vacuum – first round. Testing was carried as power test, thermocycling and power test again.

CONCLUSION

The paper mainly presented testing results for the heat pipe radiator module and for the radiator cluster both in ambient and vacuum. The radiator module was tested in vacuum at nominal parameters where it rejected 380W, a power that is slightly less than the predicted 418W. However, the module initially had a short evaporator. After increasing the size of the evaporator, new ambient testing showed that the performance of the module increased by 25%. Also, thermal cycling in vacuum of the module showed that the direct bond was not affected by the repeated exposure to thermal stresses. The cluster was also tested in both ambient (at ACT) and vacuum (at GRC). Ambient testing showed a performance of 3.5 kW at nominal water temperature and flow rate. However, the sink temperature was ambient. In addition, an oversized NCG charge was observed in all 8 heat pipes of the cluster. In conclusion, several conservative factors influenced the performance of the radiator in ambient conditions. Vacuum testing of the cluster included an initial power test, thermocycling, and a second power test. None of the parameters were nominal. The power rejected by the radiator in vacuum was 1.94kW for the highest water inlet temperature. Again, the power test carried after thermocycling showed no degradation of the direct bond. In conclusion, it is expected that the performance of the cluster in vacuum would be significantly higher if all three parameters (water inlet temperature, flow rate and sink temperature) were at nominal conditions. In addition, other conservative factors during vacuum testing were: 1) the oversized amount of NCG, which even at nominal temperature would not allow a fully open condenser, 2) the fact that water inlet temperature was 27°C less than nominal, which further amplified the effects of the oversized amount of NCG, and lastly, the short evaporator. A second round of cluster testing was performed in vacuum where the water inlet temperature was raised to nominal values. These results will be presented in a future paper. Finally, it is also important to mention that all subsequent clusters will be fabricated with long evaporators.

ACKNOWLEDGMENTS

REFERENCES

[1] Briggs, M. H., Gibson, M., and Geng, S., "Development Status of the Fission Surface Power Technology Demonstration Unit," Nuclear and Emerging Technologies for Space (NETS-2015), Albuquerque, NM, February 23-26, 2015.
[2] Mason, L., Poston, D., and Qualls, L., "System Concepts for Affordable Fission Surface Power", NASA Technical Memorandum 215166 (2008).
[3] Mason, L. S., Oleson, S. R., Mercer, C. R., and Palac, D. T., "Nuclear Power System Concepts for Electric Propulsion Missions to Near Earth Objects and Mars," Nuclear and Emerging Technologies for Space (NETS-2012), The Woodlands, TX, March 21-23, 2012.
[4] Maxwell, T., Tarau, C., Anderson, W.G., Garner, S., Wrosch, M., and Briggs, M.H., "Status of the Low-Cost Radiator for Fission Surface Power - I," 14th International Energy Conversion Engineering Conference (IECEC), Orlando, FL, July 27-29, 2015.
[5] Maxwell, T., Tarau, C., Anderson, W.G., Hartenstine, J., Stern, T., Walmsley, N., and Briggs, M.H., "Low-Cost Radiator for Fission Power Thermal Control," 13th International Energy Conversion Engineering Conference (IECEC), Cleveland, OH, July 28-30, 2014. http://www.1-act.com/wp-content/uploads/2014/08/IECEC-2014-Low-Cost-Radiator-for-Fission-Surface-Power-Systems_Final.pdf
[6] William G. Anderson, et al., "Variable Conductance Heat Pipe Radiator for Lunar Fission Power Systems," 11th International Energy Conversion Engineering Conference (IECEC), San Jose, CA, July 15-17, 2013. http://www.1-act.com/variable-conductance-heat-pipe-radiator-for-lunar-fission-power-systems/

Multiphysics Analysis of Liquid Metal Annular Linear Induction Pumps: A Project Overview

Carlos O. Maidana [1,2,3] and Juha E. Nieminen[1,4]

[1]*MAIDANA RESEARCH, 2885 Sanford Ave SW #25601, Grandville, MI 49418, United States*
[2]*Idaho State University, Department of Mechanical Engineering, Pocatello, ID 83209, United States*
[3]*Chiang Mai University, Dept. of Mechanical Engineering, Chiang Mai 50200, Thailand*
[4]*University of Southern California, Department of Astronautical Engineering, Los Angeles, CA 90089, United States*
E-mail: carlos.omar.maidana@maidana-research.ch | +1 208 904-0401

Abstract. Liquid metal-cooled fission reactors are both moderated and cooled by a liquid metal solution. These reactors are typically very compact and they can be used in regular electric power production, for naval and space propulsion systems or in fission surface power systems for planetary exploration. The coupling between the electromagnetics and thermo-fluid mechanical phenomena observed in liquid metal thermo-magnetic systems for nuclear and space applications gives rise to complex engineering magnetohydrodynamics and numerical problems. It is known that electromagnetic pumps have a number of advantages over rotating mechanisms: absence of moving parts, low noise and vibration level, simplicity of flow rate regulation, easy maintenance and so on. However, while developing annular linear induction pumps, we are faced with a significant problem of magnetohydrodynamic instability arising in the device. The complex flow behavior in this type of devices includes a time-varying Lorentz force and pressure pulsation due to the time-varying electromagnetic fields and the induced convective currents that originates from the liquid metal flow, leading to instability problems along the device geometry. The determinations of the geometry and electrical configuration of liquid metal thermo-magnetic devices give rise to a complex inverse magnetohydrodynamic field problem were techniques for global optimization should be used, magnetohydrodynamics instabilities understood –or quantified- and multiphysics models developed and analyzed.

We present a project overview as well as a few computational models developed to study liquid metal annular linear induction pumps using first principles and the a few results of our multi-physics analysis.

Keywords: liquid metals, magneto-hydrodynamics, thermo-magnetic systems, electromagnetic pumps, ALIP.

INTRODUCTION

The coupling between the electromagnetics and thermo-fluid mechanical phenomena observed in liquid metal thermo-magnetic systems, and the determination of the device geometry and electrical configuration, gives rise to complex engineering magnetohydrodynamics and numerical problems that we aim to study, were techniques for global optimization has to be used, MHD instabilities understood, and multiphysics models developed and analyzed. The environment of operation adds even further complexity, i.e. vacuum, high temperature gradients and radiation, whilst the presence of external factors, such as the presence of time and space varying magnetic fields, also leads to the need of developing active flow control systems. The development of analytical models and predictive tools to model, characterize, design and build liquid metal thermo-magnetic systems and components for space, nuclear and industrial applications are of primordial importance and represent a cross-cutting technology that can provide unique design and development capabilities besides a better understanding of the physics behind the magneto-hydrodynamics of liquid metals and plasmas.

LIQUID METAL TECHNOLOGY FOR NUCLEAR FISSION REACTORS

Liquid metal-cooled reactors are both moderated and cooled by a liquid metal solution. These reactors are typically very compact and can be used for regular electric power generation in isolated places, for fission surface power units for planetary exploration, for naval propulsion and as part of space nuclear propulsion systems. Certain models of liquid metal reactors are also being considered as part of the Generation-IV nuclear reactor program. The liquid metal thermo-magnetic systems used in this type of reactors are MHD devices which design, optimization and fabrication represents a challenge due to the coupling of the thermo-fluids and the electromagnetics phenomena, the environment of operation, the materials needed and the computational complexity involved. This challenge we aim to solve.

A liquid metal cooled nuclear reactor is a type of nuclear reactor, usually a fast neutron reactor, where the primary coolant is a liquid metal. While pressurized water could theoretically be used for a fast reactor, it tends to slow down neutrons and absorb them. This limits the amount of water that can be allowed to flow through the reactor core, and since fast reactors have a high power density most designs use molten metals instead. The boiling point of water is also much lower than most metals demanding that the cooling system be kept at high pressure to effectively cool the core. Another benefit of using liquid metals for cooling and heat transport is its inherent heat absorption capability. Liquid metals also have the property of being very corrosive and bearing, seal, and cavitation damage problems associated with impeller pumps in liquid-metal systems make them not an option and electromagnetic pumps are used instead. In all electromagnetic pumps, a body forced is produced on a conducting fluid by the interaction of an electric current and magnetic field in the fluid. This body force results in a pressure rise in the fluid as it passes from the inlet to the outlet of the pump.

In space reactors as well as in other types of semi-transportable small modular reactors, weight, reliability and efficiency are of fundamental importance. Furthermore, for the former, liquid metals as working fluid are the only option due to the working environment characteristics that outer space provides. For space power systems, the induction electromagnetic pump, because it lacks electrodes, is inherently more reliable than the conduction electromagnetic pump. The annular linear induction pump, furthermore, has several advantages over its flat counterpart because it has greater structural integrity, is more adaptable to normal piping systems, and allows greater design freedom in the coil configuration. The annular design also has a basically greater output capability since the path followed by the induced currents has a lower resistance than the path followed in a corresponding flat pump.

LIQUID METAL TECHNOLOGY FOR NUCLEAR FUSION REACTORS

Research and development in nuclear fusion devices is increasing worldwide and experimental facilities and prototypes face new engineering magnetohydrodynamics challenges and needs. Among the latter are the use of liquid metals thermomagnetic systems such as electromagnetic pumps and the use of liquid metals as plasma facing material. Certain engineering MHD problems and solutions are shared by different fields but there are aspects specific to nuclear fusion devices that we aim to solve by developing mathematical, computational and experimental methods and tools useful in the design and multi-physics analysis of engineering components and in the understanding of the MHD phenomena in place.

Despite many differences between possible designs of power plant, there are several systems that are common to most. A fusion power plant, like a fission power plant, is customarily divided into the nuclear island and the balance of plant. The balance of plant converts heat into electricity via steam turbines; it is a conventional design area and in principle similar to any other power station that relies on heat generation, whether fusion, fission or fossil fuel based. The nuclear island has a plasma chamber with an associated vacuum system, surrounded by plasma-facing components (first wall and divertor) maintaining the vacuum boundary and absorbing the thermal radiation coming from the plasma, itself surrounded by a "blanket" where the neutrons are absorbed to breed tritium and heat a working fluid that transfers the power to the balance of plant. If magnetic confinement is used, a magnet system is needed, and usually systems for heating and refueling the plasma and for driving current. In inertial confinement, a driver (laser or accelerator) and a focusing system are needed, as well as a mean for forming and positioning the pellets.

The plasma-facing material is any material used to construct the plasma-facing components, those components exposed to the plasma within which nuclear fusion occurs, and particularly the material used for the lining or first wall of the reactor vessel. The plasma facing components in energy producing fusion devices will experience 5-15 MW/m^2 surface heat flux under normal operation (steady-state) and off-normal energy deposition up to 1 MJ/m^2 within 0.1 to 1.0 ms. Refractory solid surfaces represent one type of plasma facing component option. Another option is to use a flowing liquid metal surface as a plasma facing component, an approach which will require the production and control of thin, fast flowing, renewable films of liquid metals such as lithium, gallium, or tin for particle control at diverters.

FUNDAMENTAL EQUATIONS

The equations describing the liquid metal dynamics are given by:

$$J_i = \sigma(\mathbf{E} + \mathbf{u} \times \mathbf{B}) \tag{1}$$

$$\rho\left[\frac{\partial \mathbf{u}}{\partial t} + (\boldsymbol{u} \cdot \nabla)\mathbf{u}\right] + \nabla p - \rho v \nabla^2 \mathbf{u} = \mathbf{J} \times \mathbf{B} \tag{2}$$

where the current density is $\mathbf{J}=\mathbf{J}_s+\mathbf{J}_i$, s and n are the conductivity and kinematic viscosity (ratio of the viscous force to the inertial force) of the fluid, and **u** is the fluid velocity. Because the linear momentum of the fluid element could change not only by the pressure force, $-\nabla p$, viscous friction, $\rho v \nabla^2 \boldsymbol{u}$, and Lorentz force, $\boldsymbol{J} \times \boldsymbol{B}$, but also by volumetric forces of non-electromagnetic origin; then eq. (2) should be modified and it could be expressed with an additional term f in the right hand side,

$$\rho\left[\frac{\partial \mathbf{u}}{\partial t} + (\boldsymbol{u} \cdot \nabla)\mathbf{u}\right] + \nabla p - \rho v \nabla^2 \mathbf{u} - \mathbf{f} = \mathbf{J} \times \mathbf{B} \tag{3}$$

while the conservation of mass for liquid metals would be given by $\nabla \cdot \boldsymbol{u} = 0$, which expresses the incompressibility of the fluid. An induction equation, valid in the domain occupied by the fluid and generated by the mechanical stretching of the field lines due to the velocity field, can be written as,

$$\frac{\partial}{\partial t}\boldsymbol{B} + (\boldsymbol{u} \cdot \nabla)\boldsymbol{B} = \frac{1}{\mu\sigma}\nabla^2 \boldsymbol{B} + (\boldsymbol{B} \cdot \nabla)\boldsymbol{u} \tag{4}$$

describing the time evolution of the magnetic field, $\partial \boldsymbol{B}/\partial t$, due to advection $(\boldsymbol{u} \cdot \nabla)\boldsymbol{B}$, diffusion $\nabla^2 \boldsymbol{B}$ and field intensity sources $(\boldsymbol{B} \cdot \nabla)\boldsymbol{u}$. Sometimes the induction equation, eq. (4), is written dimensionless by the introduction of scale variables and as a function of the magnetic Reynolds number, $R_m = \mu\sigma L u_0$, where u_0 is the mean velocity and L the characteristic length. A relatively small R_m generates only small perturbations on the applied field; if R_m is relatively large then a small current creates a large induced magnetic field. For small magnetic Reynolds numbers ($R_m \ll 1$), the magnetic field will be dominated by diffusion and perturbative methods can be used accurately. Similarly, the equation for temperature is

$$\rho c_p \left[\frac{\partial}{\partial t}T + (\boldsymbol{u} \cdot \nabla)T\right] = \nabla \cdot (\lambda \nabla \boldsymbol{T}) + \frac{1}{\sigma}\boldsymbol{J}^2 + \Phi + Q \tag{5}$$

which is a convection-diffusion equation with l*: thermal conductivity, *Q:* other sources of volumetric energy release such as radiation or chemical reactions and thermal diffusivity $k= \lambda/\rho c_p$, c_p: constant pressure specific heat of the flow*; while the kinetic energy evolution is given by,

$$\frac{\partial}{\partial t}\left(\frac{1}{2}\rho u^2\right) = -\nabla \cdot \left[\boldsymbol{u}\left(p + \frac{1}{2}\rho u^2\right) - \boldsymbol{u} \cdot \boldsymbol{S}\right] + \boldsymbol{u} \cdot (\boldsymbol{J} \times \boldsymbol{B}) + \boldsymbol{u} \cdot \boldsymbol{f} - \Phi \tag{6}$$

where **S** is the viscous stress tensor. We deduce from the latter that due to the action of the Lorentz forces an increase of the kinetic energy leads to a decrease in the magnetic energy. From the temperature equation, eq. (5), one

can identify the temporal increase of enthalpy, $\rho c_p \frac{\partial T}{\partial t}$, which equals to the loss of magnetic energy due to joule dissipation, $\frac{1}{\sigma} J^2$, plus the loss of kinetic energy, F, due to viscous dissipation.

From the mathematical point of view, the coupling between Maxwell equations and Navier-Stokes equations induces an additional nonlinearity with respect to the ones already present, leading to unsolved questions of existence and uniqueness (mainly related to the hyperbolic nature of Maxwell equations). As explained by Gerbeau et al., simplified models can be analyzed but care should be taken with certain approximations:

A system coupling the time dependent incompressible Navier-Stokes equations with a simplified form of the Maxwell equations (low frequency approximation) is well-posed when the electromagnetic equation is taken to be time-dependent, i.e. parabolic form. In contrast, the same model is likely to be ill-posed when the electromagnetic equation is taken to be time-independent, i.e. elliptic form, while the hydrodynamic equations are still in a time dependent form.

The coupling of Maxwell equations with Navier-Stokes equations certainly represents a challenge.

ANNULAR LINEAR INDUCTION PUMPS

A special type of liquid metal thermo-magnetic device is the annular linear induction pump. It is known that electromagnetic pumps have a number of advantages over mechanical pumps: absence of moving parts, low noise and vibration level, simplicity of flow rate regulation, easy maintenance and so on. However, while developing a large-scale induction pump, in particular annular linear induction pumps (ALIPs), we are faced with a significant problem of magnetohydrodynamic instability arising in the device. The manifestation of the instability does not allow linear induction pump development in a certain range of flow rate or the development of high efficiencies under certain flow rates and dropping pressure conditions.
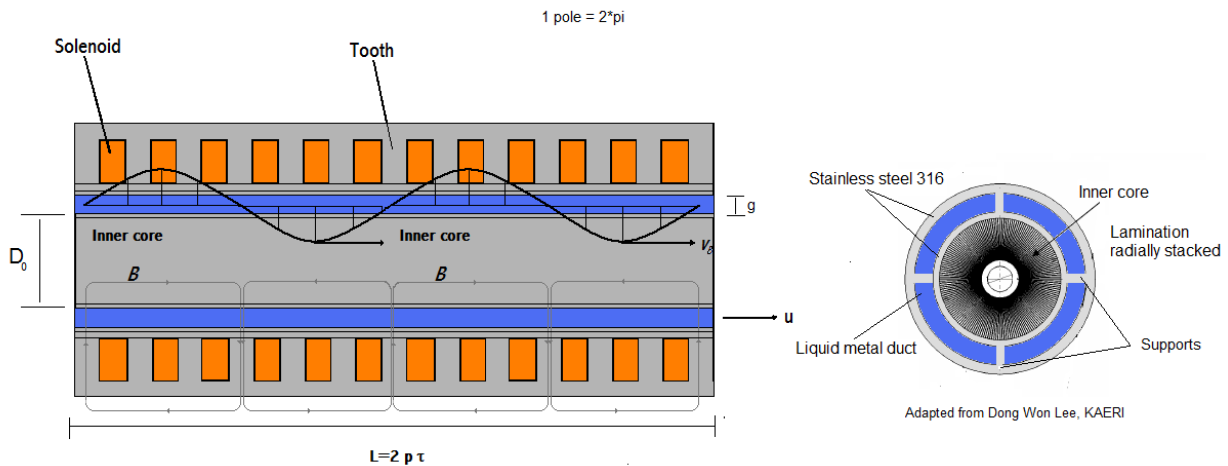

FIGURE 1. Cross sections of an annular linear induction pump (conceptual representation).

Linear induction pumps use a traveling magnetic field wave, Fig. 1, created by 3-phase currents, and the induced currents and their associated magnetic fields that generate a Lorentz force. The three-phase winding arrangement for the solenoids usually follows the sequence AA ZZ BB XX CC YY where A, B, C denote the balanced three-phase winding and X, Y, Z the opposite phase; for a direct balanced system, if A: 0°, B:120° and C:240° then X:180°, Y:300° and Z:60°. Arranging the sequence by rising phase, one obtain the correct winding sequence for the solenoids: AA ZZ BB XX CC YY. The complex flow behavior in this type of devices includes a time-varying Lorentz force and pressure pulsation due to the time-varying electromagnetic fields and the induced convective currents that originates from the liquid metal flow, leading to instability problems along the device geometry. The determination of the geometry and of the electrical configuration of a thermo-magnetic device gives rise to an

inverse magnetohydrodynamic field problem. When the requirements of the design are defined, this problem can be solved by an optimization technique. The objective function which has to be maximized in the optimization problem is derived from the main design requirement. Usually for a magnetohydrodynamic device, this is the efficiency. Other design requirements can be taken into account as constraints. For a non-linear system, such as for linear induction pumps, the main objective functions are low weight and high efficiency and so more than one maximum can exist. In this case a technique for the global optimization has to be used. Before any optimization method can be used, design approaches should be identified and understood while mathematical and computational models developed. This leads to the study of magnetohydrodynamics instabilities, usually with negative effects on the efficiency and working fluid behavior, as well as to the study of its individual components, its fabrication methods, assembly and system integration procedures.

PROJECT OBJECTIVES AND METHODOLOGY

The development of analytical models and predictive tools to model, characterize, design and build liquid metal thermo-magnetic systems and components for space, nuclear and industrial applications are of primordial importance and represent a cross-cutting technology that can provide unique design and development capabilities besides a better understanding of the physics behind the magneto-hydrodynamics of liquid metals and plasmas. The complexity of the MHD equations had made impossible to develop a design and optimization methodology using first-principles as well as to perform a true multi-physics analysis where the couple phenomena is studied as a whole. The approached used until today is to approximate the system behavior by using the electric-circuit-approach for electric machines which cannot give a realistic inside to the physics phenomena that takes place and can neither leads to a reliable design methodology nor to the determination of reliable operational working points by itself. The increased in computational power, at software and hardware level, as well as the theoretical, computational, and experimental effort performed during the last years by the principal investigator and a group of people in the United States, France, Japan and South Korea has led to advances in the understanding of the phenomenology and technical challenges that the engineering of MHD devices represent. We are for first time in conditions of performing this type of work designing and optimizing liquid metal thermo-magnetic systems. We aim to design liquid metal thermo-magnetic systems with emphasis in annular linear induction pumps as well as computational tools for analysis and CAE design of electromagnetic pumps of the ALIP type including measurement and control systems for diagnostics, operation and machine protection of the electrical and mechanical systems.
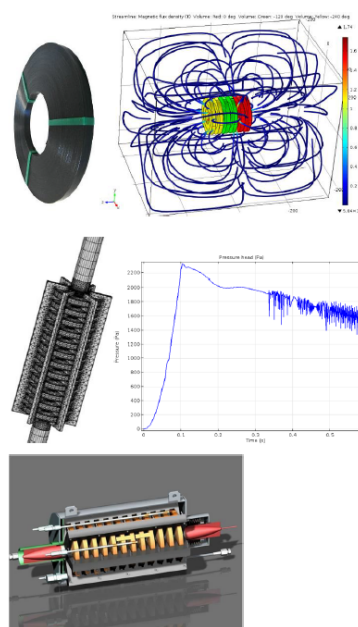

FIGURE 2. Modeling, simulation and analysis methodology.

For our project development we have selected COMSOL Multiphysics and MATLAB. COMSOL Multiphysics is a finite element analysis, solver and Simulation software / FEA Software package for various physics and engineering applications, especially coupled phenomena, or multiphysics. COMSOL Multiphysics also offers an extensive interface to MATLAB and its toolboxes for a large variety of programming, preprocessing and post-processing possibilities. The packages are cross-platform. In addition to conventional physics-based user interfaces, COMSOL Multiphysics also allows for entering coupled systems of partial differential equations (PDEs). The PDEs can be entered directly or using the so-called weak form (see finite element method for a description of weak formulation). MATLAB® is a high-level language and interactive environment for numerical computation, visualization, and programming. Using MATLAB, you can analyze data, develop algorithms, and create models and applications. The language, tools, and built-in math functions enable you to explore multiple approaches and reach a solution faster than with spreadsheets or traditional programming languages, such as C/C++ or Java. COMSOL Multiphysics is integrated with MATLAB via the LiveLink for MATLAB, which lets you generate a MATLAB file version of a simulation built with COMSOL Multiphysics. We can modify the model MATLAB file, extend it with MATLAB code, and run it from MATLAB which can allow the compilation of specific models that can be used independently as well as for the development of a low order model of the MHD flow. MATLAB can be used for the development of active flow control, machine   protection and   other   general   control systems using model-based design.

Once our analysts and researchers complete their simulation model we will be able to package it into an application using the Application Builder. This app will feature a custom made interface and control method designed by our analysts and researchers for our clients, co-workers, collaborators, students, and more. By using COMSOL Server as a hub that will enable the sharing and running of simulation applications. Apps can be run from anywhere in the world and on multiple computers, can save the end user's input changes directly through the server, and allow colleagues and customers   access   to   the   simulation   expertise   of design and engineering teams, Fig. 2.

Our modeling, simulation and analysis methodology can be divided in three parts: i) understanding the uncoupled physics phenomena, ii) understanding the coupled physics phenomena and iii) understanding of the engineering methodology to use. The first part can be sub-divided in modeling individual engineering components and simulating, analyzing and validating the results. After the main individual components where modeled, then the modeling, simulation and analysis of combined engineering components was performed analyzing the results of the integration process with uncoupled physical processes. The second part can be divided in simulating the coupled physical processes (multiphysics) and analyzing its behavior. Instabilities naturally come out of the coupling and validation with experimental data available can be performed. The third part is related to the construction of the ALIP where structural integrity issues, instrumentation type and location, and construction, assembly, operation and machine protection issues should be considered and used as constraints or feedback when needed.

PARTIAL RESULTS

We have studied, modeled and simulated the solenoids that represent the core of the annular linear induction pumps. A strong dependency on frequency has been found where the lower the frequency the higher the magnetic field available for Lorentz force pumping. A possible non-desired effect of working on lower frequency range is the increased of the edge effect on the solenoidal cell. Large fringe fields are found besides the excitation frequency of the system. These fringe fields should be minimize using a stator sections but they can be identified as a source of instabilities at the inlet and outlet of electromagnetic pumps, Fig. 3.
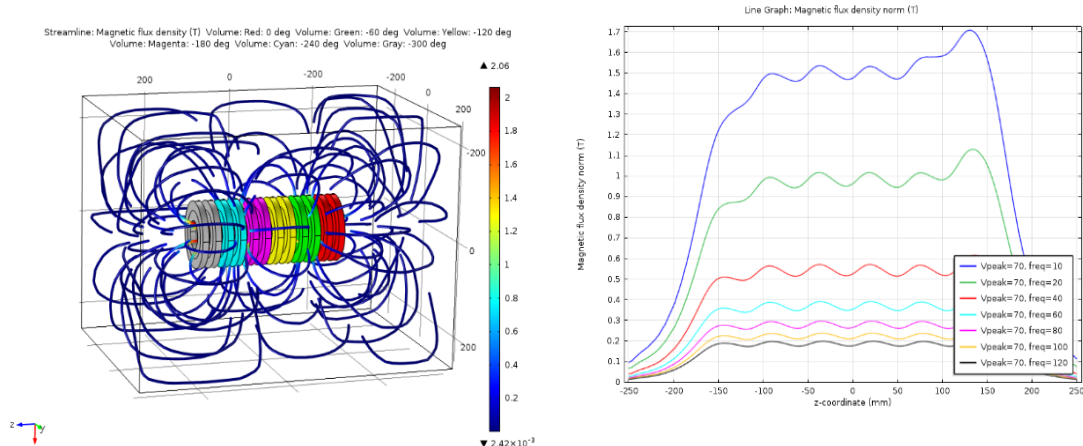
FIGURE 3. Model and simulations results for 12 solenoids powered by a 3-phase system. A strong frequency dependence on the magnetic field (average) is observed. The lower the frequency the largest the magnetic field.

After studying the individual components and some uncouple phenomena, we modeled, simulated and analyzed the behavior of a one pole pair, 6 solenoids, Sodium pump with different core sizes. The model employs the full 3D geometry of the pump and the cooling loop, and couples electromagnetic and turbulent fluid dynamics to simulate the flow in the closed system. A time-dependent study was used, time step being 1/16 of the full excitation voltage cycle to capture the temporal variation of Lorentz force that produces the pumping action. A study of the pressure head developed, shows the development of instabilities on a short period of time. The specific instability found as a result of our simulations is known as a double-frequency pulsation and it is found in most annular linear induction pumps in operation, Fig. 4. This result is useful for partial validation of the modeling work done.
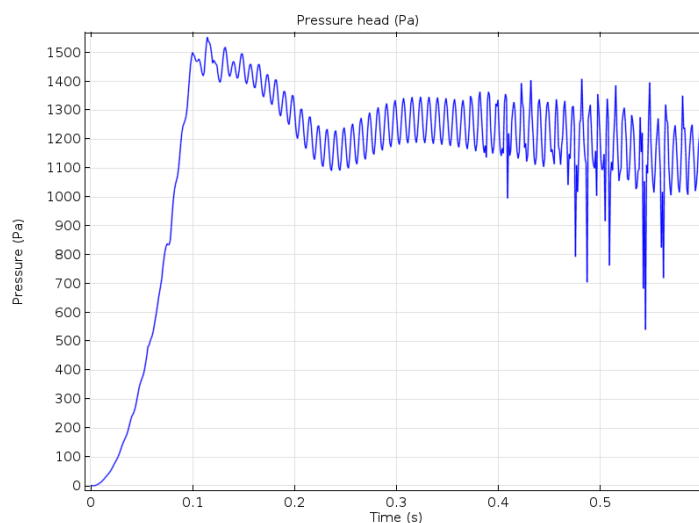

FIGURE 4. Pressure head versus time for a 6-coils annular linear induction pump model where the double-frequency pulsation instability can be easily seen.

Simulation of a 12 coils ALIP for different set of parameters represents a bigger computational challenge. Analysis of the pressure head for a 12 coils, 60 Hz, 70 V 3-phase system with a relatively large core shows the presence of two type of instabilities as expected, Fig. 5. The first instability is a low frequency (LF) instability which with time is superimposed to the double-frequency instability (DF). As a result of the combination of instabilities, and a complex pressure pattern is developed at inlet and outlet. But differences have been found when symmetry is wants to be exploited instead of using a full 3D model.

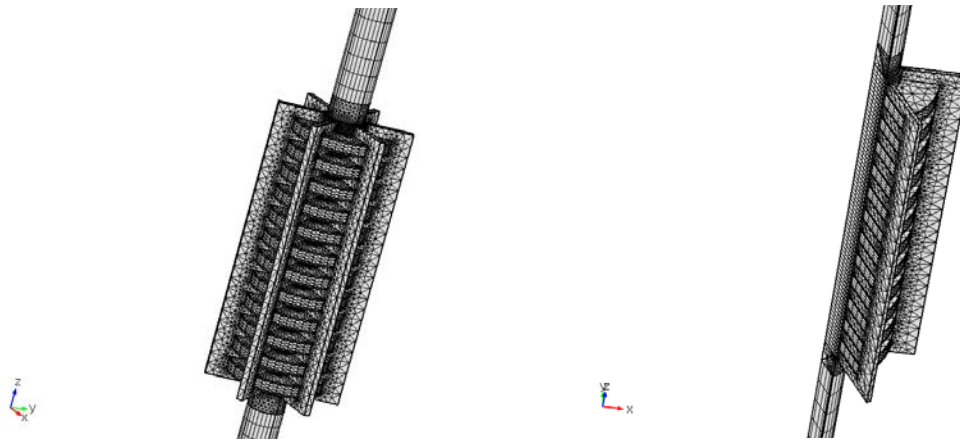**FIGURE 5.** 3D and sliced models of annular linear induction pumps. The sliced model tries to make use of symmetries to reduce the computations but it seems not applicable or partially applicable only.
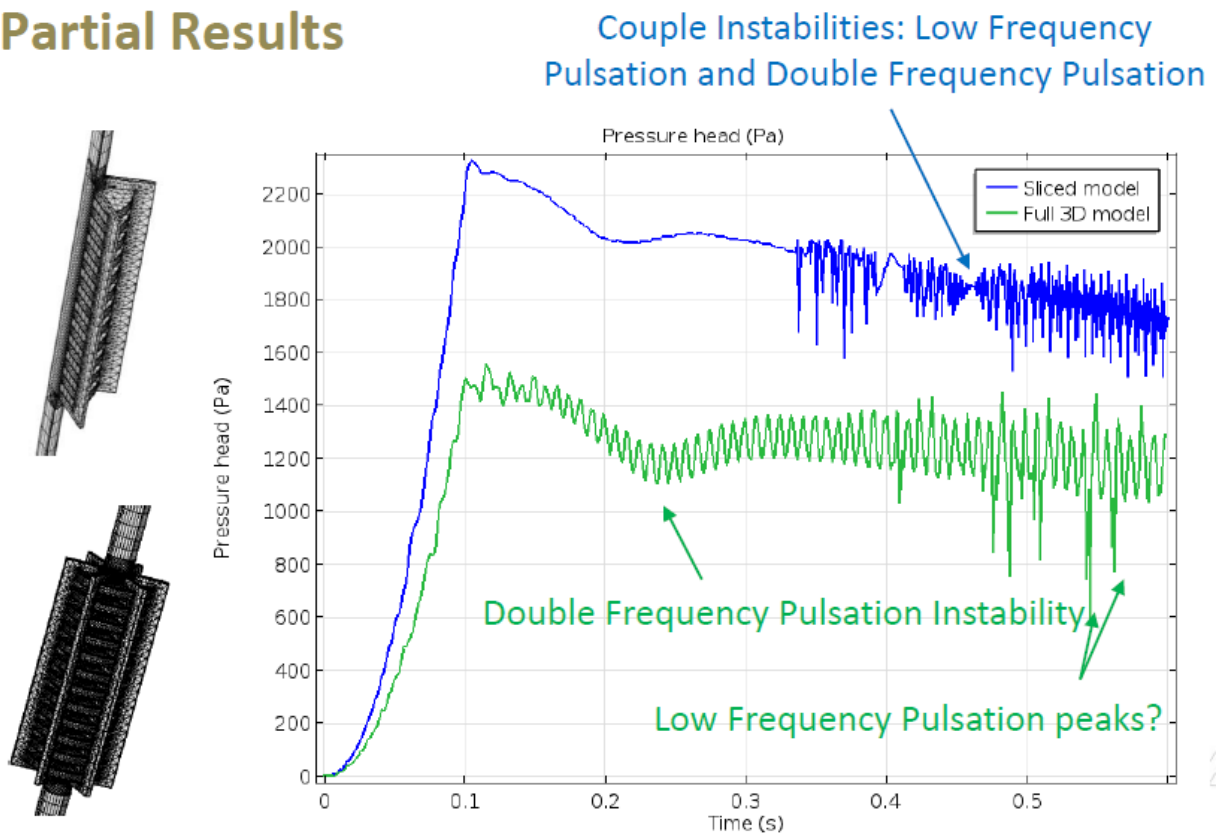

FIGURE 6. Comparison of pressure heads results for a 3D model simulation and a sliced model simulation. The sliced model using symmetries seems not to be able to resolve the presence of the double frequency instability by itself.
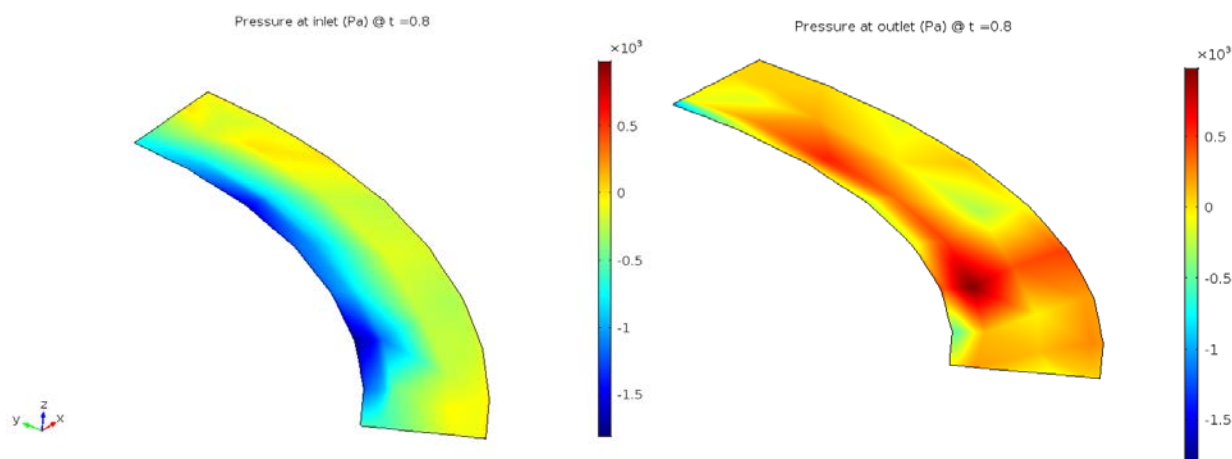
FIGURE 7. Pressure at inlet and outlet. It can be easily seen the inhomogeneous pressure distribution that prevent the use of symmetry.

The fringe fields generated by coils contain various nonlinearities due to the longitudinal dependence of the magnetic field. Due to the solenoids fringe fields, its finite core length and the induced currents, the ALIP has an *end effect* at both ends of the pump. A reduction on the developed force arises which is roughly equal to the product of the magnetic field and its perpendicular induced current. Theoretical calculations indicate a reduction of the end effects by controlling the input frequency; increasing the efficiency at the lower frequencies compared with results obtained at frequencies over 60 Hz. The inlet *end effect* force affects most of the pump while the outlet *end effect* domain is limited to the exit region. Considering the direct relationship between fluid velocity and *end effect*, low frequency operation is preferred as far as the developing force and the efficiency are not decreased too much. When the end effects are neglected, it is easy to show that the pump efficiency is given as the ratio of the flow velocity u to the synchronous velocity ω/κ of the fields (i.e. $n = \kappa u/\omega = 1-s$). But when the end effects are included its efficiency has to be computed using numerical integration and its maximum lies in the range $0.2 < s < 0.4$ where s is the slip factor, Fig. 7.

Instabilities usually arise when the three conditions hold true: $R_{ms} > 1$, $D/2\tau$ and N_{int} = *"large enough"*. An instability appears as a low frequency (LF) pulsation in the pressure head affecting the flow rate, liquid metal velocity and magnetic field distribution. As a consequence vortices are generated in the inlet region as well as fluctuations in the winding currents and voltages. The dominant frequency of this instability is in the range 0-10 Hz with amplitude that increases with the slip factor. This LF pressure pulsation is produced by vortices in the liquid metal generated by the no uniformity of the azimuthal component of the applied magnetic field when $R_{ms} > 1$. The magnetic Reynolds number, R_{ms}, often becomes greater than unity in the pump region where the slip is larger than 0.2 giving place to another instability known as double supply frequency (DSF) pressure pulsation. The vibration caused by the DSF pressure pulsation occurs in the pump outlet and propagates to the pipe when $R_{ms} < 1$ and *s* < 0.2.

The thickness of the duct walls affect the efficiency of the pump due to the magnetic resistivity that presents; but it must not be too thin as too risk its structural integrity. The width of the fluid channel should be limited to below the skin depth of the fluid for stable operation. A final diagram is shown in Fig. 8.
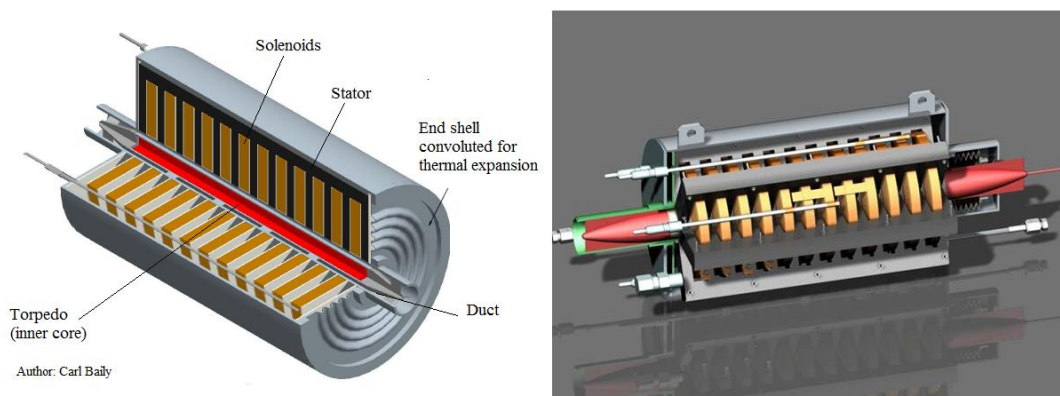
FIGURE 8. 3D model of the EM pump. Notice how the inner core, or torpedo, extends beyond the solenoid-stator section.

CONCLUSIONS

The complexity of the MHD equations had made impossible to develop a design and optimization methodology using first-principles as well as to perform a true multi-physics analysis where the couple phenomena is studied as a whole. The approached used until today is to approximate the system behavior by using the electric-circuit-approach for electric machines which cannot give a realistic inside to the physics phenomena that takes place and can neither leads to a reliable design methodology nor to the determination of reliable operational working points by itself. The increased in computational power, at software and hardware level, as well as the theoretical, computational, and experimental effort performed during the last years by this author and a group of people in the United States, France, Japan and South Korea has led to advances in the understanding of the phenomenology and technical challenges that the engineering of MHD devices represent. We are for first time in conditions of performing this type of work designing and optimizing liquid metal thermo-magnetic systems using first principles and multi-physics analysis.

The variety and importance of the topic leads to the need of i) developing computational tools for the study and analysis of the liquid metal MHD phenomena, ii) To a better understanding of the physics and engineering of liquid metal thermo-magnetic systems for better modeling, iii) To develop tools, procedures and CAE software for more accurate simulation of the device, iv) To develop procedures and tools for design optimization, and v) to develop control systems for active flow control.

We have shown a project overview as well as the first results. Further results will be discussed in other papers but the advances made are of fundamental importance.

ACKNOWLEDGMENTS

REFERENCES

[1] Maidana, C.O., "Thermo-magnetic Systems for Space Nuclear Reactors: An Introduction", Springer Briefs in Applied Science and Technology, ISBN-13 978-3319090290. (2014)

[2] Maidana, C.O. et al., "Design of an Annular Linear Induction Pump for Nuclear Space Applications", Proceedings of Nuclear and Emerging Technologies for Space Exploration 2011 (NETS2011), Albuquerque, NM, February 7-10 (2011).

[3] Maidana, C. O., Latina, A., Jonker, M., "Failure Studies at the Compact Linear Collider: Main Linac and Beam Delivery System", International Particle Accelerator Conference 2012 – USA. (2012)

[4] Maidana, C.O., Makino, K., Berz, M., "Muon Ring Cooler Simulations using COSY Infinity", Institute of Physics Conference Series N 175. (2004)

[5] Werner, J. et al., "An Overview of Facilities and Capabilities to Support the Development of Nuclear Thermal Propulsion", Proceedings of Nuclear and Emerging Technologies for Space Exploration 2011 (NETS2011), Albuquerque, NM, February 7-10 (2011).

[6] Maidana, C.O., "Nuclear Technologies for Space Exploration: an overview on nuclear thermal propulsion, radioisotope power generators and fission surface power", Mars Transactions N5 – Journal of the Italian Mars Society, ISSN: 2037-6928. (2014)

[7] Giordani, A., "Seven innovative ways to cool a scientific computer", International Science Grid this Week, e-Science Talk, 2/2012. Contributed Article / Scientific Consultant: Carlos O. Maidana. Selected as one of the most popular articles by Google Analytics. (2012)

[8] Kim, H. R., "Design and Experimental Characterization of an EM Pump", Journal of the Korean Physical Society, Vol. 35, No. 4, pp. 309-314. (1999)

[9] Schwirian, R. E., "Analysis of linear-induction or traveling wave electromagnetic pump of annular design", NASA TN D-2816 , NASA Lewis Research Center, Cleveland, Ohio, United States. (1965)

A Point Design for a LEU Composite NTP system: Superb Use of Low Enriched Uranium (SULEU)

Paolo F. Venneri*[1,2], Michael J. Eades[3], Yonghee Kim[2]

[1]Ultra-Safe Nuclear Corporation, Los Alamos, NM, 87544
[2]Department of Nuclear and Quantum Engineering, Korea Advanced Institute of Science and Technology, Daejeon, ROK, 64141
[3]Nuclear Engineering Program, The Ohio State University, Columbus, OH 43201
858-342-4837; pvenneri@ultrasafe-nuclear.com

Abstract. This work presents the initial point design and development of the Superb Use of Low Enriched Uranium (SULEU) nuclear thermal propulsion core. The core design is based off the heritage NERVA design, retaining the graphite-composite fuel elements (the only difference being the enrichment level), the presence of the moderator elements in the core (albeit with a varied configuration and an increase in the size of the moderator sleeve), and the core peripherals including the reflector, control drums, and axial components of the core. The core is unique at this point by the fact that is able to match the existing NASA DRA 5.0 style mission requirements while having a similar mass as existing NTP core designs. The performance parameters achieved by this preliminary design are as follows. It has a mass of 2498 kg (excluding the shield), a nominal Isp of 898 seconds, a nominal thrust of 155.7 kN (35,000 lbf.), and a peak fuel temperature of 2850 K. It should be noted that in order to achieve these performance values, the inlet pressure for the core is higher than other LEU-NTP designs, requiring 8 MPa at the core inlet and consequently higher pressure drop across the core of 3 MPa. Furthermore, SULEU, has a total fissile mass of ^{235}U that is well below that of other cores of the same class. In direct contrast with existing LEU-NTP cores, SULEU has only 18.1 kg of ^{235}U. This establishes it as the current best in class in terms of reduction of fissile material, particularly when compared with tungsten CERMET LEU-NTP cores. In this work we have done a basic neutronic and performance analysis of the core and identified various methods and areas where it can be further improved upon.

Keywords: LEU-NTP, graphite composite, SPOC.

INTRODUCTION

The present work presents a baseline reactor core, the Superb Use of Low Enriched Uranium (SULEU) core, as the reference LEU graphite composite core for NTP mission analysis and future design efforts. The importance of this core design lies in its simplicity, reliance on existing technology and NTP core design methodologies, and its ability to meet the desired performance requirements of a NASA DRA 5.0 style human Mars mission. This will enable side-by-side comparisons of different NTP system designs with the full knowledge that such a system is in fact based on a real design that is able to provide the specified performance values. Just as importantly, it allows the identification of the system requirements for the core to operate at the desired performance level as well as areas for future development needed for improving the system.

SULEU follows the well-known design philosophy of the heritage NERVA/ROVER programs that ran in the US from the 1960s through the 1970s. These programs established a baseline reactor and system design that have persisted today as the baseline design for most of the mainstream design efforts [1] [2] [3]. The advantage of persisting with this baseline design is the ability to rely on experimental and design data that has transcended project terminations and allowed the continual progression of the system. These designs all share a set of common components and configurations: hexagonal fuel elements with evenly space coolant channels, moderator elements to

hold the structural tie-tubes and protect a solid moderator, a radial beryllium reflector holding rotating control drums as the primary reactivity control system, and a hydrogen coolant. Within NERVA/ROVER based core designs, there are further categories based on the fuel type. These currently consist of two major types: graphite composites and tungsten CERMETS. SULEU, being a NERVA core, has all the above and implements the graphite composite fuel as there is already an existing tungsten CERMET point design [4] that has been developed jointly by the Center for Space Nuclear Research and NASA Marshall.

SULEU, as the name suggests, is a LEU NTP core. This is a major change from the baseline NERVA designs as they are fueled exclusively with HEU. This is in response to the growing need for the development of lower cost and high performance systems in support of NASA missions. The use of HEU in previous NTP design, while maximizing the performance of the propulsion system (particularly for the HEU tungsten CERMET designs), resulted in the significant increase of the development and implementation costs of the system. This has the further implication of limiting NTP use and development to government institutions in nuclear weapon states such as the United State and Russia. While this is justified, as HEU is a considerable nuclear weapon proliferation risk and needs to be subjected to significant safeguards requirements, they are significant roadblock to NTP development and implementation. The result, when combined with the extensive costs associated with HEU systems and the impressive security requirements, is the handicapping of NTR research when it should be a simple, affordable, and streamlined and process. This is especially important now that the propulsion system needs to be designed and built in time for the upcoming Mars missions in 2035.

In an effort to open the research and development of these crucial systems to non-government organizations (such as the private commercial sector) and reduce the R&D costs and complexity of the infrastructure needed for their implementation, there has been a recent push to develop low enriched uranium (LEU) fueled NTP systems. With LEU fuel the NTP system can be developed by institutions without direct government oversight (no more than any other civilian nuclear installation), reduced costs (material and operational), and offers the possibility of developing a commercial product. This research has been led by researchers at the Korea Advanced Institute of Science and Technology (KAIST) [4][5][6] and the Center for Space Nuclear Research (CSNR) in cooperation with Aerojet-Rocketdyne and NASA Marshall Space Flight Center [8][9][10].

DESIGN PROCESS

SULEU seeks to be the reference core to represent the baseline performance capabilities of LEU graphite composite cores in order to enable the proper comparison between HEU and other LEU NTP designs. As such, SULEU has been designed to provide the performance characteristics required for a NASA DRA 5.0 style mission. This allows it to be compared directly with other LEU NTP reference point designs, specifically the SCCTE design being developed by the Center for Space Nuclear Research in cooperation with a research group at NASA Marshall [9]. In this comparison, two aspects were addressed in order to make it a meaningful comparison: both were designed and analyzed using the same code system and methodology and both were designed to have the same thrust and specific impulse.

The design methodology used consists of generating a large number of core designs based on the NERVA core by varying a set number of parameters while leaving others constant. In this study, the constant parameters are the core components, the design of the fuel and moderator elements (radial geometry and material), core materials, and thrust level. The parameters varied were core length, core radius, active core arrangement, inlet pressure, and outlet temperature. Once these core designs are generated, they are each evaluated in terms of performance and the lowest mass core able to meet the desired requirements is selected. This was all done using SPACE, an in-house variant of the Space Propulsion Optimization Code (SPOC) [10]. SPACE derives a majority of its components from SPOC with the additional capabilities for Serpent 2 neutronic calculations, reactor burnup, and the implementation of multiple fuel materials. The result of this process is presented in Figure 1. In Figure 1, each point represents a critical core design that has been optimized to achieve its maximum specific impulse while providing 35 klbf of thrust. The key point is that each point represents the highest achievable performance level of each core at the specified thrust level. In Figure 1 these point designs have then been plotted in terms of core mass and specific impulse, the two explicit discriminators between each design in terms of performance given that they all operate at the same thrust level. As shown here, the number of core designs capable of operating at or above 900s is considerable, requiring a further down selection by finally choosing the core with the minimum mass and still able

to provide the desired 900 s specific impulse. The result is the identification of the core able to provide 900 s of specific impulse with the highest thrust to weight ratio. Once selected, the core design is then manually modified to flatten the radial power and remove any hot spots in the core. The result is a close approximation of the highest performance LEU graphite composite NTP core for a NASA DRA 5.0 mission: SULEU.
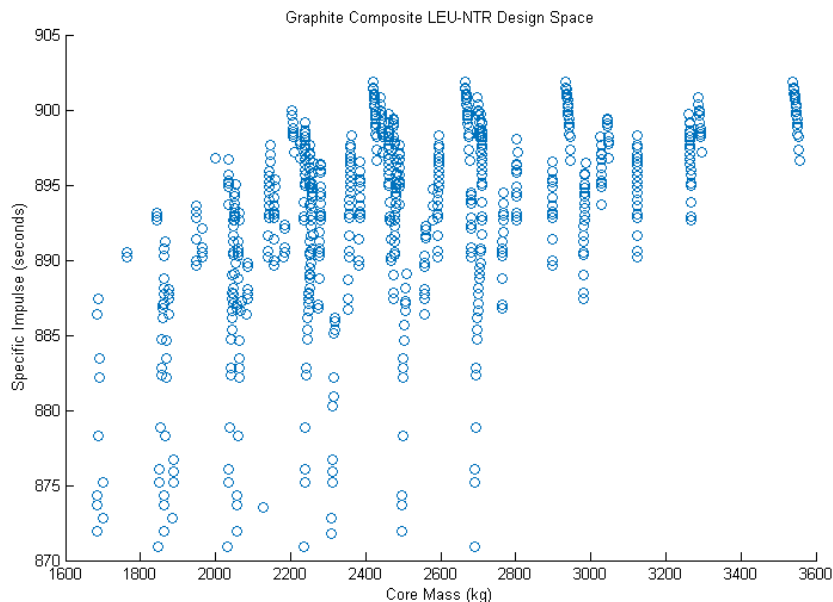

FIGURE 1. Design space for NERVA type LEU-NTP cores at 35k lbf.

CORE CONFIGURATION

The active core and fuel element configurations are provided in detail in Table 1 and Table 2. There are three points where the moderator element differs from the standard NERVA type moderator element. First is the significant enlargement of the moderator sleeve. Here, the thickness of the moderator sleeve has been significantly increased to maximize the moderation ability of the moderator element. This is key in enabling the use of LEU fuel. The second major change is the use of Zircaloy as the tie-tube material. During the original development of LEU NTP designs [3], it was found that the parasitic neutron absorption by the tie-tube material was a significant issue to be resolved. For now, this has been resolved by replacing the Inconel tie-tubes with Zircaloy tie-tubes. Preliminary calculations have argued that the strength of the Zircaloy tie-tubes is still sufficient to maintain structural strength during regular operation. This is, however, a point that requires further study. The final change in the moderator element design is the removal of the external ZrC coating. The removal of the ZrC coating was done in order to simplify the element design as it as judged to unnecessary as an interface between the moderator and fuel elements.

The fuel elements follow the exact same configuration as that of the SNRE core configuration. They measure 1.905 cm across and consist of the (U,Zr)C-Graphite composite described in detail by Taub [11]. The key points for this fuel are the combination of the benefits of a carbide network inside of a graphite matrix. Thanks to the extensive experiments and development work done in the 1960s and 70s, it has been shown that an optimum in terms of strength, fuel content, and thermal properties is achieved with a carbide volume fraction of 35 vol% and .64 g/cm uranium loading in the fuel.

The core configuration is a mixture of a 2:1 and 1:1 fuel element to moderator element ratio configurations. The use of two configurations has allowed the flattening of the radial power profile without resorting to the use of radial enrichment or fuel loading zones, both of which are problematic for LEU graphite cores due to their extremely low fissile loading. The axial and radial core geometries are presented in Figure 2 while the detail of the fuel elements and moderator elements are given in Figure 3. In the axial plot the active core has been divided into 10 axial zones,

each one divided into two radial zones. This was done in order to take into account the axial and radial variations in temperature of the active core components as well as the density changes in the coolant.

TABLE 1. SULEU tie-tube configuration

Component	Material	Inner Radius (cm)	Outer Radius (cm)
Inner Hydrogen	Hydrogen		0. 2030
Inner tie tube	Zircaloy	0.2030	0.2540
Moderator	$ZrH_{1.8}$	0.2540	0.6700
Outer Hydrogen	Hydrogen	0.6700	0.7605
Outer tie tube	Zircaloy	0.7605	0.7860
Insulator tube	ZrC (50%TD)	0.7860	0.9000
Hexagonal element body	Graphite	1.905 cm flat to flat	
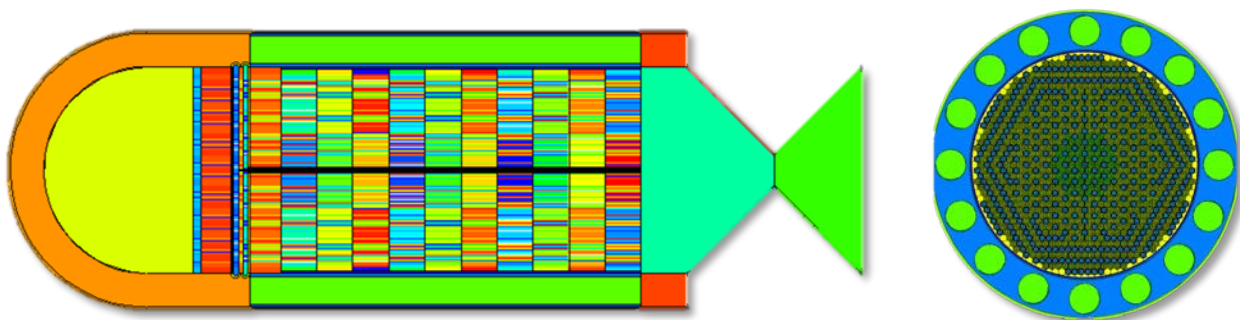
FIGURE 2. SULEU axial and radial geometry.

TABLE 2. SULEU active core details

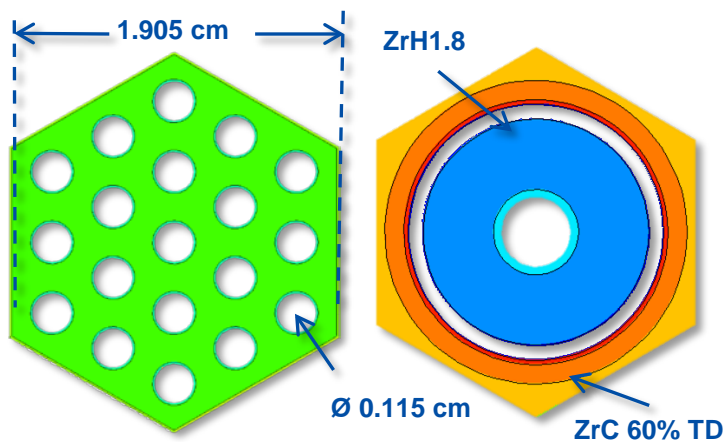| Parameter	Value
Mass (kg)	**2498**
Number of Fuel Elements	**600**
Number of Moderator Elements	**472**
Active Core Radius (cm)	**33**
Reflector Thickness (cm)	**11**
Active Core Length (cm)	**118**
Control Drum Worth ($)	**8**
Radial Power Peaking	**1.134**

FIGURE 3. SULEU fuel (left) and moderator element (right).

SULEU CORE CHARACTERIZATION

SULEU represents the typical values for a LEU graphite composite NTP core. It has a heavily thermalized spectrum and the typical sine-shaped control drum reactivity profile. It has negative temperature reactivity coefficients for the fuel and the moderator and a positive tie-tube hydrogen density reactivity coefficient. The neutron spectrum and the control drum reactivity profiles are shown in Figure 4 and the reactivity coefficients are reported in Table 3. The Moderator temperature coefficient was approximated by having the core at hot-zero power with the all the moderator elements having a single temperature. The moderator sleeve cross-section temperature was then varied for the whole core. The same was also done for the fuel as well. The tie-tube hydrogen density was determined by uniformly varying the density from nominal conditions in the core.
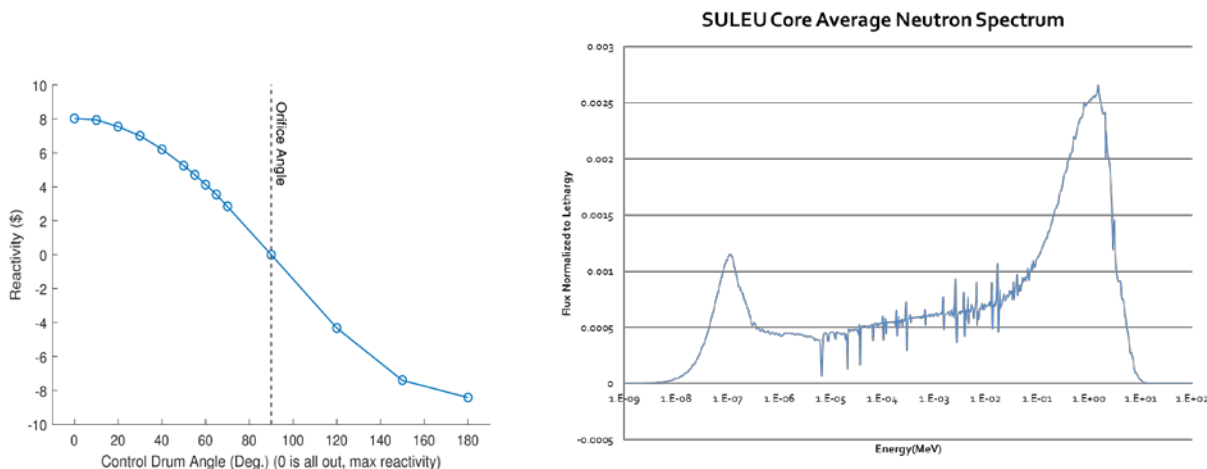

FIGURE 4. SULEU control drum reactivity profile (left) and core average neutron spectrum (right).

TABLE 3. SULEU active core details

Reactivity Coefficient SULEU	
Moderator Temperature ($/K)	- 0.0045
Fuel Temperature ($/K)	- 0.0032
Tie-Tube Hydrogen Density ($/%change)	0.0260

One of the impressive characteristics of SULEU is its radial power profile. This is shown along with the axial power profile in Figure 4. Without any radial enrichment zoning, the core is able to have an extremely low radial power peaking factor. This enables the core to have a relatively simple radial orificing scheme in order to ensure a maximized coolant outlet temperature. This is of note particularly because radial enrichment zoning is extremely difficult due to the already minimal amount of fissile material in the core. Further reduction of the fissile content has a drastic effect on the core reactivity. The axial power profile is a non-optimized profile which can be further improved in the future by following methodologies as those explored by Peter Husemeyer [12] and have been applied in the SCCTE reactor.
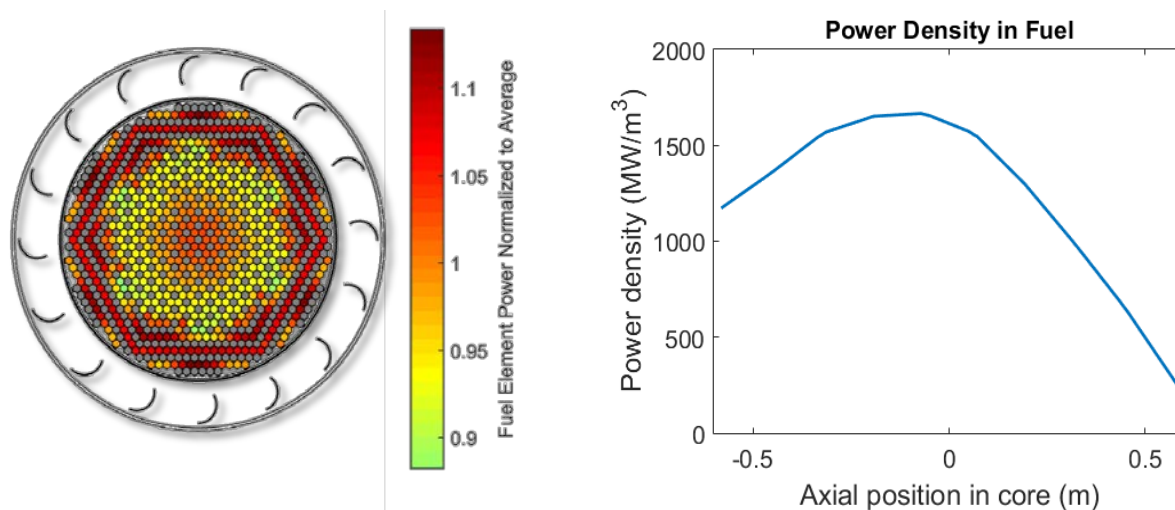

FIGURE 4. SULEU radial power profile and axial temperature.

SULEU AND SCCTE COMPARISON

The purpose behind the development of SULEU is to provide a baseline core fueled with LEU graphite composite with which to compare with other NTP systems, specifically the LEU-CERMET fueled SCCTE. In order to do so, the core was designed to operate in the same performance class as SCCTE. This will enable the fair comparison between the two fuel options in terms of their impact on operation, implementation of new reactor systems, and reactor mass. The performance values of the two are shown side by side in Table 4. As can be seen in Table 4, the two cores have almost the exact same performance characteristics. This makes them essentially equivalent in terms of their ability to meet the mission requirements of a NASA DRA 5.0 style mission.

The differences in core behavior are largely due to a combination of the fuel itself as well as the design of the fuel elements. For SULEU, the design is restricted to implementing the existing SNRE fuel element geometry and fuel. This results in a fuel element that has virtually no self-shielding, a highly thermalized spectrum (as shown in Figure 4) and necessitates a higher core inlet pressure to achieve the desired performance levels. This last is a consequence of the reduced number of fuel elements in the core due the increased number of moderator elements. These are in stark contrast with SCCTE which has a comparatively fast spectrum (yet still considered to be a thermalized core due to its thermal tail), large in-element power peaking, and lower core inlet pressure. These differences result in different requirements in terms of in-element orificing (SCCTE will require significantly more), the effect of xenon on the core reactivity (SULEU see a much larger negative reactivity insertion due to xenon build-up), and turbo-pump requirements.

The differences in core configurations and performance between the two cores is summarized in Table 4.

TABLE 4. Core configurations and performance comparison between SULEU and SCCTE.

Superb Use of Low Enriched Uranium (SULEU)				Space Capable Cryogenic Engine (SCCTE)			
SULEU is a Graphite Composite Fuel, $ZrH_{1.8}$ moderated LEU nuclear thermal propulsion concept relying largely on heritage design.				SCCTE is a LEU W-UO2, $ZrH_{1.8}$ moderated LEU nuclear thermal propulsion.			
Reactor System Mass				**Reactor System Mass**			
Fuel Mass (600 Elements) (kg)			800.1	Fuel Mass (151 Elements) (kg)			1029.8
Tie Tubes (427 Elements) (kg)			588.6	Tie Tubes (150 Elements) (kg)			700.4
Total Mass (Excluding Shield) (kg)			**2498.0**	**Total Mass (Excluding Shield) (kg)**			**2557.6**
Key Performance Parameters				**Key Performance Parameters**			
Nominal Isp (150:1 Nozzle)			897.9	Nominal Isp (150:1 Nozzle)			894
Nominal Thrust (kN)			155.7 (35k lbf)	Nominal Thrust (kN)			157.3 (35k lbf)
Whole Reactor Power(MW)			768.9	Whole Reactor Power(MW)			765.3
Fuel Temperature Max (K)			2850	Fuel Temperature Max (K)			2850
Engine System Interface Information				**Engine System Interface Information**			
Interface Point	Flow Rate (kg/s)	Pressure (MPa)	Temp. (K)	Interface Point	Flow Rate (kg/s)	Pressure (MPa)	Temp. (K)
Core inlet	17.68	8.0	300.0	Core inlet	17.76	6.93	291
Core outlet	17.68	5.0	2712.8	Core outlet	17.76	4.72	2694
Fuel Details				**Fuel Details**			
Fuel Composition			(U,Zr)C	Fuel Composition			W-UO2-ThO2
Carbide Fraction (vol%)			35	[184]W Enrichment (% atom)			98
Enrichment of [235]U (% atom)			19.75	Enrichment of [235]U (% atom)			13.13 to 19.75
Total [235]U (kg)			18.1	Total [235]U (kg)			45.9

CONCLUSION

This paper has presented the design and performance characteristics of the SULEU reactor. The reactor demonstrates the feasibility of a LEU graphite composite fuel NTP core and its ability to operate at the desired level of performance for a NASA DRA 5.0 style mission. In this paper SULEU has undergone a preliminary characterization that enables it to be used as a baseline core configuration for future work as well as a reference core for current and future mission planners as well as future development of the LEU graphite composite NTP concept.

Future work related to SULEU will involve its use in the development of passive reactivity control systems as well as full-submersion accident mitigation schemes.

ACKNOWLEDGMENTS

REFERENCES

[1] F. P. Durham, "Nuclear Engine Definition Study Preliminary Report I Volume I - Engine Description" 1972.

[2] F. P. Durham, "Nuclear Engine Definition Study Preliminary Report I Volume II – Supporting Studies" 1972.

[3] B.G. Schnitzler, "Small Reactor Designs Suitable for Direct Nuclear Thermal Propulsion: Interim Report", 2012.

[4] P. F. Venneri and Y. Kim, "A feasibility study on low-enriched uranium fuel for nuclear thermal rockets - I: Reactivity potential," Progress in Nuclear Energy, Vol.83. p-406-418, 2015.

[5] P. F. Venneri and Y. Kim, "A feasibility study on low-enriched uranium fuel for nuclear thermal rockets - II: Rocket and Reactor Performance," Progress in Nuclear Energy, Vol.87. p-156-167, 2016.

[6] S.H. Nam, P.F. Venneri, J.Y. Choi, Y.H. Jeong, S.H. Chang, "Innovative Nuclear Thermal Rocket Concept Utilizing Leu Fuel For Space Application", The 23rd International Conference on Nuclear Engineering(ICONE-23), Chiba, Japan, 2015.

[7] V. Patel, M. Eades, and W. Deason, "Center for Space Nuclear Research (CSNR) NTP Design Team Report", Idaho National Laboratory, INL/EXT-15-36810, 2015.

[8] W.R Deason, M.J. Eades, P.J. Husemeyer, and V.K. Patel, "Exploring the Design Space of CERMET LEU ZrH1.8 Moderated Nuclear Thermal Propulsion Systems", in "Nuclear and Emerging Technologies for Space", Albuquerque, NM, February 2015.

[9] M.J Eades, W.R. Deason, V.K. Patel, "SCCTE: An LEU NTP Concept with Tungsten Cermet Fuel" Winter American Nuclear Society Meeting 2015, Washington DC. November, 2015.

[10] P. Husemeyer, V. Patel, P. Venneri, W. Deason, M. Eades, S. Howe, "CSNR Space Propulsion Optimization Code: SPOC", in "Nuclear and Emerging Technologies for Space", Albuquerque, NM, February 2015.

[11] J. M. Taub, "A Review of Fuel Element Development for Nuclear Rocket Engines," *Los Alamos National Lab Report*, **LA-5931**, Los Alamos, United States, 1973.

[12] P. Husemeyer," Thermal-Hydraulically Optimal Power Profile for a Nuclear Thermal Rocket Engine Winter" American Nuclear Society Meeting 2015, Washington DC. November, 2014.

Effect of Sub-Sized Specimen Geometry and Orientation on High Strain-Rate Tensile Impact Ductilities of DOP-26 Iridium

Brian R. Friske and Cecil A. Carmichael, Jr.

Materials Science and Technology Division, Bldg. 2525-Rm. 108, Oak Ridge National Laboratory, 1 Bethel Valley Rd, Oak Ridge, TN 37831
(865) 576-1417; friskeb@ornl.gov

Abstract. There is a need to determine the tensile impact properties of the closure-weld zone of DOP-26 iridium alloy Clad Vent Sets (CVSs) used in General Purpose Heat Sources (GPHS). GPHS are used in Multi-Mission Radioisotope Thermoelectric Generators (MMRTG) to power missions such as Cassini and the Curiosity Mars Rover. A CVS is approximately 30 mm (1 3/16″) tall and consists of two DOP-26 cups, approximately 15 mm (0.59″) tall, with a 6 mm (0.24″) radius. These cups are gas tungsten arc welded to each other while oriented so that the cup blank (sheet) rolling direction of one cup is offset 90° from the rolling direction of the second cup. The dimensions of a full-sized tensile-impact specimen are too large to be removed from a CVS. The purpose of this work was to assess the relationship between the results obtained from tensile impact testing of sub-sized specimens with that obtained from tensile impact testing of full-sized specimens.

Keywords: Iridium, Clad Vent Set, High Strain-Rate Tensile Ductility.

INTRODUCTION

There is a need to determine the tensile impact properties of the closure-weld zone of DOP-26 iridium alloy Clad Vent Sets (CVSs). A CVS (Figure 1) is approximately 30 mm (1 3/16″) tall and consists of two DOP-26 cups, approximately 15 mm (0.59″) tall, with a 6 mm (0.24″) radius. These cups are gas tungsten arc welded to each other while oriented so that the cup blank (sheet) rolling direction of one cup is offset 90° from the rolling direction of the second cup. The dimensions of a full-sized tensile-impact specimen are too large to be removed from a CVS. The purpose of this work was to assess the relationship between the results obtained from tensile impact testing of sub-sized specimens with that obtained from tensile impact testing of full-sized specimens.
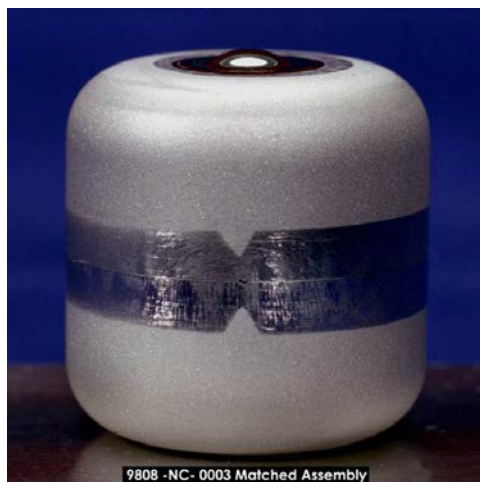
FIGURE 1. Photo of Clad Vent Set 9808-NC-0003 showing a Shield Cup (bottom) and Vent Cup (top) prior to gas tungsten arc welding.

For this work, both sub-sized and full-sized specimens were removed from flat sheet material used to make CVS. Attachments 1 and 2 show the dimensions of the sub-sized specimens and the full-sized specimens, respectively. The sub-sized specimen gauge sections were 4.83 mm (0.19″) long, 1.09 mm (0.043″) wide, and 0.64 mm (0.025″) thick while the full-sized specimens were 1.14 mm (0.45″) long, 2.54 mm (0.10″) wide, and 0.64 mm (0.025″) thick. The 57% reduction in gauge length and width of the sub-sized specimen allows the entire gauge section to be located within the closure-weld zone of a CVS, thus not involving the grit-blasted region. The specimen transition radius and grip section dimensions for the sub-sized specimens were identical to that of the full-sized specimen geometry. The sub-sized total specimen length and distance between the grip sections were modified to reflect the changed gauge length.

Sub-sized specimens were fabricated from non-prime sheets RS17-2, -3, -4, and RS10-6. Specimens were tested with the gauge section parallel (20 specimens), perpendicular (12 specimens), and at 45° (16 specimens) to the rolling direction of the sheet. The tensile elongations obtained from these sub-sized specimens were compared with values obtained from full-sized specimens fabricated from sheets RS17-2 and -4 with the gauge section parallel to the rolling direction (12 specimens). Sub-sized specimens with the gauge lengths perpendicular to and at 45° to the sheet rolling direction were also tested to determine whether there were any discernible orientation effects (with respect to sheet rolling direction) in the sub-sized specimens.

EXPERIMENTAL PROCEDURES

Three non-prime DOP-26 iridium sheets were fabricated using the approved RPS program procedures listed below.

1. Preparation of Iridium-0.3 wt % Tungsten Compacts: MET-MatP-SOP-72-10
2. Preparation of Master Alloys for Iridium Doping; MET-MatP-SOP-90-4
3. Electron Beam and Arc Melting of Iridium Alloys: MET MatP-SOP-82-11
4. Electron Beam Welding of Iridium Alloy Materials: MET-WB-SOP-31-2
5. Iridium Alloy Consumable Electrode Preparation: MET-MatP-SOP-98-6
6. Vacuum Arc Remelting of Iridium Alloy Electrodes: MET-MatP-SOP-99-4
7. Extrusion of Iridium Alloys: MET-MatP-SOP-100-6
8. Rolling Iridium DOP-26 Alloy to Sheet: MET-MatP-SOP-101-6

After the sheets were rolled, blanks (round or rectangular) were electric-discharge machined from the sheets and then ground to the final thickness of 2.54 mm (0.025″) following procedure MC-413-13 "Manufacturing Methods for Iridium Alloy Blanks."

Sub-sized specimens and full-sized specimens were fabricated from these ground blanks using procedure MET-MatP-SOP-81 "Tensile Impact Testing of DOP-26 Iridium Alloy Sheet." Once the specimens were fabricated, they were heat treated in vacuum at 1500 °C for 19 h. Vickers microhardness indents were made (using 1000 g load) at regular intervals along the specimen gage sections. The spacing between the indents were measured before tensile impact testing. Tabs, 2.54 mm (0.025″) thick, were welded to both sides of the 10.41 mm (0.410″) long grip section per procedure MAT-WB-SOP-31 "Electron Beam Welding of Iridium Alloy Electrodes and Tensile Specimen Tabs." Impact tests were performed at 980 ° C with a bullet velocity of 61±3 m s^{-1} (which corresponds to an engineering strain rate of +~10^3 s^{-1}). Once testing was complete, the distances between the microhardness indents were re-measured. The impact ductilities of the sub-size specimens were determined by using the equation,

$$\text{Impact Ductility (\%)} = [(D_{avg} - d_{avg})/d_{avg}] \times 100 \qquad (1)$$

where D_{avg} is the average spacing between microhardness indents after testing and d_{avg} is the average spacing between microhardness indents before testing. Fracture surfaces were also examined to evaluate the area fractions of transgranular and intergranular fracture.

RESULTS AND DISCUSSIONS

Tensile Impact Ductilities

Table 1 lists the tensile impact ductilities measured from 17 sub-sized specimens with their gauge sections machined parallel to the rolling direction.

Table 2 lists the tensile impact ductilities of 7 full-sized specimens fabricated from sheets RS17-2 and RS17-4 with the gauge section parallel to the rolling direction. The average tensile impact ductility of these specimens was 17.7%, which is lower than the average obtained from all sub-sized specimens tested with their gauge section parallel to the rolling direction (20.3% in Table 1). However, it is comparable to the 18.0% average elongation of the sub-sized specimens fabricated from the same sheets (TS-039 to TS-071 in Table 1) with the gauge section parallel to the rolling direction. Based on the similar elongations of sub-sized specimens and full-sized specimens in Tables 1 and 2, it was inferred that the specimen geometry had little or no effect on the elongations obtained during impact testing following a heat-treatment of 1500 °C for 19 h.

TABLE 1. Tensile ductilities of sub-sized specimens with gauge sections parallel to the rolling direction (heat treated at 1500 °C for 19 h and tested at 980 °C with a bullet velocity of 61±3 m s^{-1}).

Sheet Identity	Specimen Identity	Impact Ductility (%)
RS17-3	TS-003	23.0
RS17-3	TS-004	22.3
RS17-3	TS-005	21.1
RS17-3	TS-006	21.7
RS17-3	TS-007	23.3
RS17-3	TS-008	25.9
RS17-3	TS-010	25.7
RS17-4	TS-039	22.5
RS17-4	TS-040	18.6
RS17-4	TS-041	17.3
RS17-4	TS-042	15.6
RS17-2	TS-057	16.5

Sheet Identity	Specimen Identity	Impact Ductility (%)
RS17-2	TS-058	19.1
RS17-4	TS-069	15.4
RS17-4	TS-070	18.6
RS17-4	TS-071	18.4
	Avg	20.3
	Stdev	3.4
	Min	15.4
	Max	25.9

TABLE 2. Tensile ductilities of full-sized specimens with gauge section parallel to the rolling direction (heat treated at 1500 °C for 19 h and tested at 980 °C with a bullet velocity of 61 ± 3 m s^{-1}).

Sheet Identity	Specimen Identity	Impact Ductility (%)
RS17-2	TS-047	18.1
RS17-2	TS-048	20.7
RS17-4	TS-059	15.8
RS17-4	TS-060	18.9
RS17-4	TS-061	19.7
RS17-4	TS-062	15.3
RS17-4	TS-064	15.3
	Avg	17.7
	Stdev	2.2
	Min	15.3
	Max	20.7

Table 3 lists the tensile impact ductilities of 10 sub-sized specimens with the gauge section perpendicular to the rolling direction and 10 sub-sized specimens with the gauge section at 45° to the rolling direction with averages of 17.4% and 16.1%, respectively. The slightly lower average elongations of the sub-sized specimens with the gauge section oriented perpendicular and at 45° to the rolling direction when compared to the tensile ductilities obtained from the sub-sized specimens with the gauge section oriented parallel to the rolling direction (Table 1) indicates that the rolling direction anisotropy has an effect on the tensile impact ductilities.

TABLE 3. Tensile ductilities of sub-sized specimens with gauge sections perpendicular to the rolling direction and at 45° to the rolling direction heat treated at 1500 °C for 19 h and tested at 980 °C with a bullet velocity of 61 ± 3 m s^{-1}.

Perpendicular to Rolling Direction			45 Degrees to Rolling Direction		
Sheet identity	Specimen Identity	Impact Ductility (%)	Sheet Identity	Specimen Identity	Impact Ductility (%)
RS17-4	TS-011	18.3	RS17-3	TS-031	15.7
RS17-4	TS-012	17.5	RS17-3	TS-032	17.9
RS17-4	TS-013	18.9	RS17-3	TS-033	17.5
RS17-4	TS-014	17.2	RS17-3	TS-035	17.7
RS10-6	TS-022	16.0	RS17-3	TS-036	16.5
RS10-6	TS-023	16.2	RS17-3	TS-038	16.9
RS10-6	TS-025	15.7	RS17-4	TS-065	17.9
RS10-6	TS-027	16.9	RS17-4	TS-066	14.5

RS10-6	TS-028	17.9	RS17-4	TS-067	12.8
RS10-6	TS-029	19.5	RS17-4	TS-068	13.6
	Avg	17.4		Avg	16.1
	Stdev	1.3		Stdev	1.9
	Min	15.7		Min	12.8
	Max	19.5		Max	17.9

Analyses of Fracture Surfaces

Figure 2 shows scanning electron images of typical fracture surfaces of the sub-sized specimens with the gauge section parallel (a), perpendicular (c), and at 45° (d) to the rolling direction and the full-sized specimens with the gauge section parallel to the rolling direction (b).
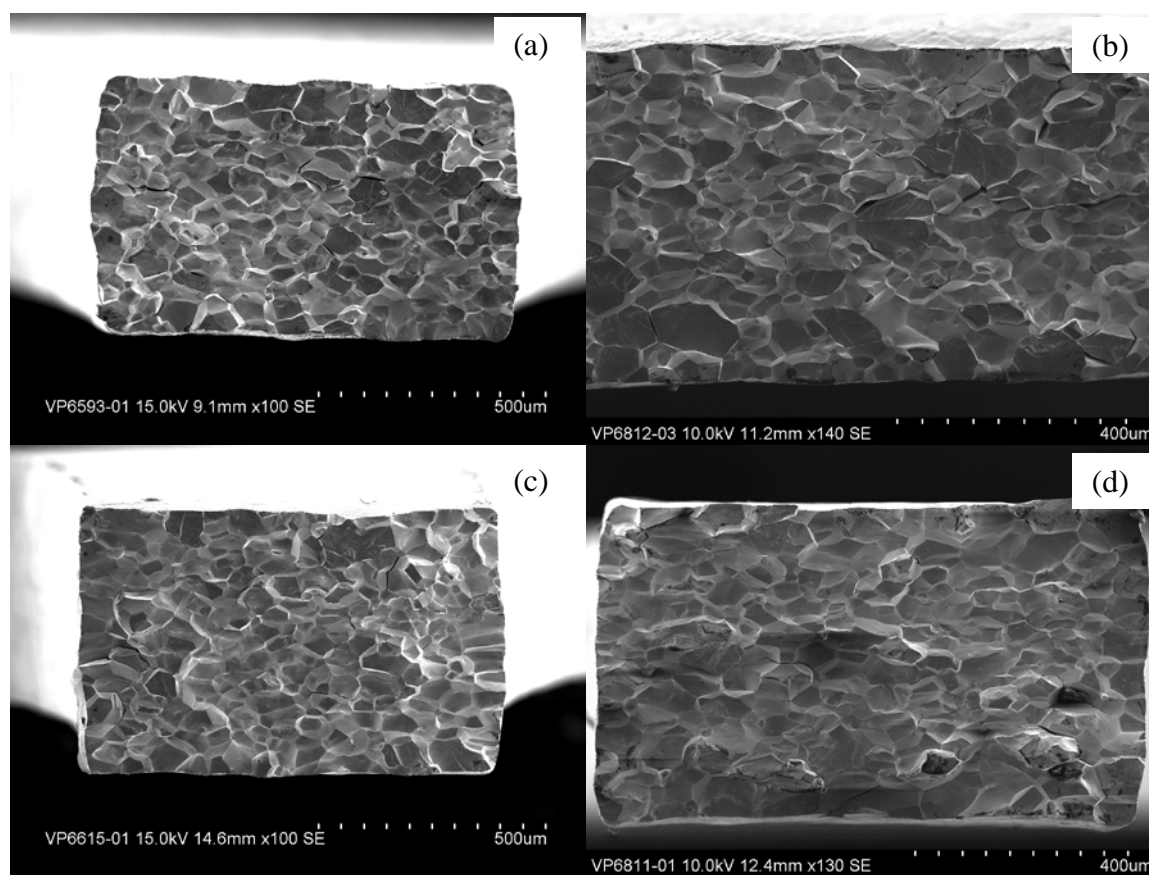

FIGURE 2. Scanning electron images of fracture surfaces, (a) sub-sized specimen TS-003 with gauge section parallel to the rolling direction, (b) full-sized specimen TS-063 with gauge section parallel to the rolling direction, (c) sub-sized specimen TS-027 with gauge section perpendicular to the rolling direction, and (d) sub-sized specimen TS-068 with gauge section 45° to the rolling direction.

The sub-sized specimens were first imaged at a magnification appropriate for viewing the whole fracture surface. Subsequently, higher magnification images were obtained to determine the fracture modes and transgranular fracture area percentages. Three sequential images were used to span the entire length of the fracture surface in full-sized specimens. Transgranular fracture area was quantified from these images. The results are summarized in Table 4 as fraction (%) of the total image area. The average transgranular fracture area measured for full-sized specimens, 13.1%, was similar to the average transgranular fracture area measured for sub-sized specimens with the gauge section parallel to the rolling direction, 15.8%. However, the transgranular fracture area for the sub-sized specimens

with the gauge section perpendicular and 45° to the rolling direction were approximately a third of the transgranular fracture surface on the sub-sized specimens tested with the gauge section parallel to the rolling direction. This difference in transgranular fracture area is consistent with rolling direction anisotropy having an effect on impact ductilities discussed above.

TABLE 4. Transgranular fracture areas (%) on sub-sized specimens and full-sized specimens heat treated at 1500 °C for 19 h and tested at 980 °C and a velocity of 61±3 m s^{-1}.

Specimen/Orientation	Average	Stdev.	Min.	Max.
Full-sized specimens parallel to rolling direction	13.1	2.6	9.1	16.3
Sub-sized specimen parallel to rolling direction	15.8	4.6	9.7	27.4
Sub-sized specimen perpendicular to rolling direction	6.6	1.9	4.4	10.1
Sub-sized specimen at 45° to rolling direction	5.0	1.9	1.9	7.8

SUMMARY AND CONCLUSIONS

There is a need to be able to determine the tensile impact properties of the closure weld zone of DOP-26 iridium alloy Clad Vent Sets (CVS). The thickness and geometry of CVS prohibit the use of full-size tensile-impact specimens. The purpose of this work was to evaluate the feasibility of using sub-size tensile-impact specimens to assess the weld zone properties of DOP-26 CVS. Comparison of results obtained from the testing of sub-sized specimens with the gauge section parallel, perpendicular, and at 45° to the sheet rolling direction with that obtained from full-sized specimens oriented parallel to the rolling direction shows:

1. The impact ductilities of sub-sized specimens with gauge sections oriented parallel to the rolling direction were found to be similar to those obtained from full-sized specimens fabricated from the same sheets. This indicates that specimen size had little effect on the elongation observed.

2. Sub-sized specimens with the gauge section oriented perpendicular to and at 45° to the rolling direction have lower average elongations when compared to the average elongations of full-sized specimens or sub-sized specimens oriented parallel to the rolling direction. This shows that impact ductility varies as a function of specimen orientation with respect to the rolling direction.

3. The anisotropy in ductility is also reflected in the fracture modes. The sub-sized specimens with their gauge section oriented perpendicular to and at 45° to the rolling direction show a lower, by ~1/3, transgranular fracture area compared to the transgranular fracture area of sub-sized specimens with their gauge sections parallel to the rolling direction.
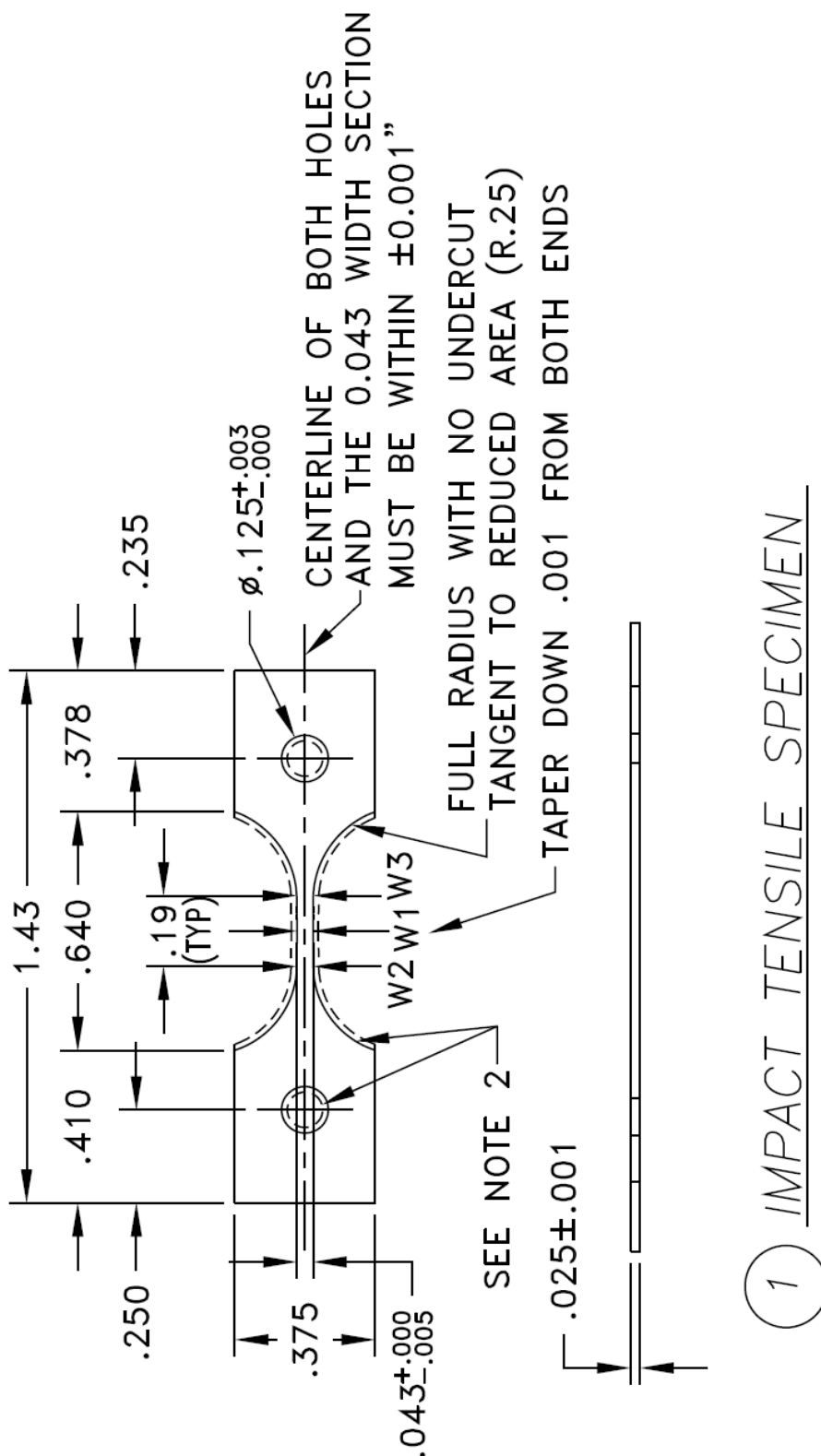
Future work should consider modifications to the shape of the grip sections and to the overall size of the specimens to allow the entire specimen to be extracted from the sidewall and transition radius of a CVS.

ACKNOWLEDGMENTS

ATTACHMENT 1: Sub-Size Tensile Impact Specimen Fabrication Drawing.

ATTACHMENT 2: Full-Size Tensile Impact Specimen Drawing.

IMPACT TENSILE SPECIMEN
SCALE: 2:1